Quantum Monte Carlo Studies of Novel Phases in Strongly Correlated Systems

Von der Fakultät Mathematik und Physik
der Universität Stuttgart
zur Erlangung der Würde eines Doktors der Naturwissenschaften
(Dr. rer. nat.) genehmigte Abhandlung

vorgelegt von
Zi Yang Meng
aus Xi'an, China

Hauptberichter:	Prof. Dr. Stefan Weßel	-	RWTH Aachen
Mitberichter:	Prof. Dr. Walter Metzner	-	Max-Planck-Institut für Festkörperforschung, Stuttgart
	Prof. Dr. Hans-Peter Büchler	-	Universität Stuttgart

Tag der mündlichen Prüfung: 19. 07. 2011

Institut für Theoretische Physik III
Universität Stuttgart
2011

Acknowledgements

Prof. Xian Lin Ji (1911 – 2009, vice president of Peking University) is a famous Chinese Indologist, linguist and historian. He received his Ph.D. majored in Sanskrit from Universität Göttingen in 1941, and returned to China after the second world war. In various recollecting essays he wrote about his gratitude towards the education he received in Germany, and one single point he kept emphasizing and appreciating is the "Gründlichkeit" (Thoroughness) of the German academic tradition. Upon finishing my own thesis, I become more and more convinced by his observation. I think it's a piece of luck that I, like Prof. Ji, also have the chance to receive such a "gründliche" education in Germany.

Many people from several places in Germany have helped and encouraged me throughout my Ph.D. years. Here at Universität Stuttgart, I would like to thank Prof. Stefan Wessel and Prof. Alejandro Muramatsu. Stefan is my Ph.D. advisor but more like a mentor and friend. Alejandro, with his deep insights and rich experience, always comes to help at the criticial moment of our research projects. Also I'm very grateful for Prof. Walter Metzner from Max Planck Insititut für Festkörperforschung, Stuttgart, Prof. Hans-Peter Büchler and Prof. Martin Dressel from Universität Stuttgart for their kind acceptance of being in my examination committee. I thank my colleagues from our institute, Alexander Moreno, Lars Bonnes, Thorsten Beck, Dr. Karim Bouadim, Adam Bühler for their help both inside and outside physics. Especially I would like to thank Alexander for being my landlord for two years, and Lars and Karim who spent their time on proofreading my thesis from the very beginning.

At Universität Würzburg, I would like to acknowledge Prof. Fakher F. Assaad, Dr. Thomas C. Lang, Dr. Martin Hohenadler and Martin Bercx. Fakher generously shared with us his codes and shared with us his years of experience with these codes, and he is always the cheerful figure at the downturns of our collaboration. Thomas, who helped me most in scientific world and real world, is indeed my mentor and becoming a brother to me throughout all these years. Martin and Martin are very helpful in proofreading my thesis.

At Universität Göttingen, where Prof. Xian Lin Ji's reflection about the German education is based on, I would like to express my appreciation to Priv.-Doz. Dr. Andreas Honecker and Helene Feldner, our collaboration is enjoyable and fruitful.

Three years of my work were financially supported by the Deutsche Forschungsgemeinschaft (DFG) through grants WE3649 and SFB/TRR21. Additionally, several stays in China and United States have been subsidized by the University of Hong Kong, Xi'an Xi Jing Group Co., Ltd. and the China Scholarship Council. The computation time allocated in John von Neumann Institute for Computing, Jülich; the Hochleistungsrechenzentrum, Stuttgart (HLRS); and the continuous technical supports from Martin Hecht, Shiqing Fan from HLRS are greatly appreciated.

Almost seventy years passed since Prof. Xian Lin Ji returned to China. Following his example, generations of Chinese students brought their knowledge and experience earned in Germany back home. I'm honored to become a member of such group

and glad to fulfill my responsibility as all my predecessors did. Hopefully in the near future, I will have the chance to tell my own students about the teachers and friends I met in Germany. And most important of all, I will inspire them with the "Gründlichkeit" of the German academic tradition.

Abstract

Three models of strongly correlated electron systems have been studied in this thesis: the Shastry-Sutherland quantum antiferromagnet, the quantum spin liquid emerging out of correlated Dirac fermions on the honeycomb lattice, and the edge-state magnetism in the graphene nanoribbons. The methods applied are quantum Monte Carlo simulations, namely, stochastic series expansion quantum Monte Carlo for bosonic (spin) systems and projector auxiliary field quantum Monte Carlo for fermionic systems.

The stochastic series expansion quantum Monte Carlo method is applied to study the ground state properties as well as the magnetization process of the spin-1/2 easy-axis Heisenberg model on the Shastry-Sutherland lattice. The quantum phase transitions between a Néel state, a dimer triplet state and a ferromagnetic XY phase have been characterized by finite size scaling analysis. The crystalline structures of the triplon magnetic excitations in the magnetic plateaus have been identified.

The projector auxiliary field quantum Monte Carlo is applied to explore the ground state phase diagram of the SU(2) Hubbard model on the honeycomb lattice. The interplay between the relativistic Dirac dispersion, the vanishing density of states at half-filling and the strong quantum fluctuations, drives the system from a semimetal at weak coupling to an antiferromagnetic Mott insulator in the strong coupling regime. In between these phases there emerges an unexpected quantum spin liquid with no symmetry breaking in any channel. After careful finite size scaling analysis of various correlation functions, the quantum spin liquid phase is characterized as a short-range resonating valence bond state with a finite spin gap to all magnetic excitations.

The study of edge-state magnetism in graphene nanoribbons is more experimentally motivated. The projector auxiliary field quantum Monte Carlo method is used to measure the static spin-spin correlation function, the single-particle spectral function, as well as the dynamic spin structure factor along the zigzag edge of graphene nanoribbons. A dominant low energy peak generated by the Coulomb interaction in the single-particle spectral function is identified as the dynamical signature of edge-state magnetism. The magnetic excitations along the zigzag edge show a linear dispersion at low energies due to the effective antiferromagnetic coupling of the edges across the ribbon. The magnetic excitations are damped by scattering processes into the particle-hole continuum at high energies.

Kurzbeschreibung

In dieser Arbeit wurden drei Systeme stark korrelierter Elektronen untersucht: der Shastry-Sutherland Quanten-Anitferromagnet, eine Spin-Flüssigkeit, welche aus korrelierten Dirac-Fermionen auf dem Honigwaben-Gitter hervorgeht und der Magnetismus der Randzustände von Graphen-Nano-Bändern. Die hierzu verwendeten Methoden sind die Stochastische-Reihenentwicklung-Quanten-Monte-Carlo-Methode für die Simulation von bosonischen (Spin-) Systemen und das Projektor-Determinanten-Quanten-Monte-Carlo-Verfahren für die Simulation fermionischer Systeme.

Mit Hilfe der Stochastischen-Reihenentwicklung-Quanten-Monte-Carlo-Methode wurden die Grundzustandseigenschaften und der Magnetisierungsprozess des Spin-1/2 Easy-Axis-Heisenberg Modells auf dem Shastry-Sutherland Gitter studiert. Die Quanten-Phasenübergänge zwischen einem Néel Antiferromagneten, einem Dimer-Triplet Zustand und einer XY-ferromagnetischen Phase wurden mittels der Finite-Size-Technik charakterisiert. Innerhalb der zwei magnetischen Plateaus wurde die kristalline Struktur der magnetischen Triplon-Anregungen bestimmt.

Das Projektor-Determinanten-Quanten-Monte-Carlo-Verfahren wurde zur Bestimmung der Grundzustandseigenschaften des SU(2) Hubbard-Modells auf dem Honigwaben-Gitter eingesetzt. Das Wechselspiel relativistischer Dirac-Elektronen, einer verschwindenden Zustandsdichte bei halber Füllung und starker Quanten-Fluktuationen führt zu dem unerwarteten Auftreten einer Quanten-Spin-Flüssigkeit zwischen einem Halb-Metall bei schwacher Kopplung und einem Antiferromagneten bei starker Kopplung. Eine sorgfältige Untersuchung verschiedener Korrelationsfunktionen bestätigt, dass die Quanten-Spin-Flüssigkeit durch das Fehlen jeglicher Symmetriebrechung, einer Lücke zu Spin-Anregungen und kurzreichweitiger Korrelationen ähnlich einer Resonanz-Valenzbond-Flüssigkeit gekennzeichnet ist.

Die Studie des Magnetismus von Randzustände in Graphen-Nano-Bändern war von experimentellen Interesse getrieben. Erneut wurde das Projektor-Determinanten-Quanten-Monte-Carlo-Verfahren verwendet, um die statischen Spin-Spin-Korrelationen, die Einteilchen-Spektralfunktion, sowie den dynamischen Spin-Strukturfaktor entlang der Zigzag-Kante von Graphen-Nano-Bändern zu bestimmen. Ein dominantes Signal bei niedriger Energie in der Einteilchen-Spektralfunktion konnte als Signatur der spontanen Magnetisierung der Randzustände identifiziert werden. Die magnetischen Anregungen weisen bei kleinen Energien eine lineare Dispersion auf, die mit der effektiven antiferromagnetischen Kopplung der beiden Ränder erklärt werden kann. Bei höheren Energien streuen die magnetischen Anregungen in das Teilchen-Loch Kontinuum.

List of Abbreviations

μSR	muon spin rotation
AF	Antiferromagnetic
AFMI	Antiferromagnetic Mott insulator
BEDT-TTF	Bis-(ethylene-dithio)-tetra-thia-fulvalene
CDW	Charge density wave
DMRG	Density matrix renormalization group
ED	Exact diagonalization
LDOS	local density of states
MFT	Mean field theory approximation
MI	Mott insulator
Pd(dmit)	Palladium-1,3-dithiole-2-thione-4,5-dithiolate
PQMC	Projector auxiliary field quantum Monte Carlo
QMC	Quantum Monte Carlo
QSH	Quantum spin Hall state
QSL	Quantum spin liquid
RVB	Resonating valence bond
SM	Semimetal
SOC	spin-orbit coupling
SSE QMC	Stochastic series expansion quantum Monte Carlo
STM	Scanning tunneling microscope
TBI	Topological band insulator
TDL	Thermodynamic limit
VBS	Valence bonds Solid

Contents

List of Abbreviations v

1 Introduction 1

2 Quantum Monte Carlo Methods 5
2.1 Stochastic Series Expansion Quantum Monte Carlo for Bosons 5
2.1.1 Basic Formulation 5
2.1.2 Update Schemes 7
2.1.3 From Heatbath to Directed Loops 14
2.1.4 Observables 17
2.2 Projector Auxiliary Field Quantum Monte Carlo for Fermions 18
2.2.1 Basic Formulation 18
2.2.2 Equal Time Green's Function 20
2.2.3 Stabilization Scheme 22
2.2.4 Sampling Procedure and Imaginary Time Green's Function . 23
2.2.5 Wick Theorem and Observables 25
2.3 Data Analysis and Scalability 27

3 Shastry-Sutherland Quantum Antiferromagnet 31
3.1 $SrCu_2(BO_3)_2$ and Shastry-Sutherland Model 31
3.2 Phase Diagram 35
3.2.1 Ising Limit 35
3.2.2 Quantum Phase Transitions 37
3.2.3 Degenerate Perturbation Theory 43
3.3 Magnetization Process 47
3.4 Summary and Outlook 50

4 Quantum Spin Liquid emerging in the Hubbard Model on the Honeycomb Lattice 55
4.1 Introduction to Quantum Spin Liquids 55
4.1.1 QSLs as Exotic States of Matter 57
4.1.2 Realization of QSLs in Models 59
4.1.3 Realization of QSLs in Materials 63
4.2 Quantum Spin Liquid emerging in the Hubbard Model on the Honeycomb Lattice 70
4.2.1 Hubbard Model on the Honeycomb Lattice 70
4.2.2 Phase Diagram from PQMC 72
4.2.3 Characterization of the Quantum Spin Liquid Phase 80
4.2.4 Further Insight into the RVB State 92
4.3 Summary and Outlook 95

5 Edge-State Magnetism in Graphene Nanoribbons **99**
5.1 Graphene Nanoribbons 99
5.2 MFT Results and Experimental Progress 102
5.3 Static Spin-Spin Correlation on the Edge 104
5.4 Spectral Functions: $A(\omega)$ and $A(q,\omega)$ 107
5.5 Spin Spectral Function $S(q,\omega)$ 111
5.6 Summary and Outlook 113

6 Conclusion **117**

Bibliography **119**

Curriculum Vitae **140**

List of publications **141**

Chapter 1

Introduction

Strongly correlated electron systems remain one of the central challenges in solid state physics. Due to their close relevance with quantum magnetism [Schollwöck 2004], unconventional superconductors [Norman 2011], heavy fermion compounds [Si 2010], and ultra-cold atomic gases in optical lattices [Schneider 2008], the investigations of these systems are important for understandings of a broad range of physical phenomena. Given that analytical methods have difficulties in treating strong correlation effects in a controlled level, in many occasions unbiased numerical simulations provide an essential source of information to test ideas and develop intuitions. In particular, for a given model describing a specific material we would ultimately like to carry out efficient numerical simulations to provide *exact* results on the thermodynamic, dynamic, transport as well as ground state properties. If the model shows a continuous quantum phase transition, we would like to characterize it by computing the critical exponents. Even further, at times there might be new states of matter emerging out of the simulation, for instance, supersolid [Balibar 2010] and quantum spin liquid [Balents 2010]. Such exotic states of matter greatly extend our knowledge of many-body physics, which controls the myriad aspects of the world around us.

Numerical techniques have already provided invaluable insights in strongly correlated electron systems and will continue to do so. This thesis is yet another attempt along this direction. We have applied two different Quantum Monte Carlo methods to three different strongly correlated electron systems. We wish to offer our humble contributions to the fields spanned over frustrated quantum magnets, quantum spin liquids and the electronic and magnetic properties of graphene nanoribbons.

In chapter 2, we describe the two different Quantum Monte Carlo (QMC) methods, namely, the stochastic series expansion quantum Monte Carlo (SSE QMC) and the projector auxiliary field quantum Monte Carlo (PQMC). While SSE QMC is the generic method to study non-frustrated quantum spin (or bosonic) systems [Syljuåsen 2002, Alet 2005], with the PQMC one can readily obtain ground state as well as dynamic properties for half-filled, non-frustrated, fermionic lattice models [Assaad 2008].

Having these two powerful methods at hand, we begin to apply them to microscopic models. In chapter 3, we employed the SSE QMC with directed loop update scheme to investigate the ground state phase diagram and the magnetization process of the spin-1/2 easy-axis Heisenberg model on the Shastry-Sutherland lattice. The

Hamiltonian is given by,

$$\begin{aligned} H &= J\sum_{\langle i,j\rangle}\left[-\Delta(S_i^xS_j^x+S_i^yS_j^y)+S_i^zS_j^z\right] \\ &\quad +J'\sum_{\langle\langle i,j\rangle\rangle}\left[-\Delta(S_i^xS_j^x+S_i^yS_j^y)+S_i^zS_j^z\right]-h\sum_i S_i^z. \end{aligned} \tag{1.1}$$

The geometry of this model resembles that of the frustrated quantum antiferromagnet $SrCu_2(BO_3)_2$ which has a dimer singlet ground state and develops a series of magnetization plateaus under strong external magnetic fields [Miyahara 2003b, Sebastian 2008]. To circumvent the QMC sign problem inherent to the frustrated nature of the lattice [Shastry 1981], we design the transverse spin exchange to be ferromagnetic ($\Delta > 0$) and keep the geometric frustration in the antiferromagnetic (AF) Ising exchange sector ($(J, J') > 0$). For vanishing transverse exchange, the model reduces to an antiferromagnetic Ising model that, besides Néel order, harbors regions of extensive ground state degeneracy. In the quantum regime, the system develops a *dimerized phase of triplet states* separated from the *Néel ordered phase* by a *superfluid phase*. We performed finite-size scaling analysis to characterize the quantum phase transitions between these three phases, and used a degenerate perturbation theory to capture the phase boundary close to the point where the ground state is most degenerate. The magnetization process of the system shows a magnetization plateau at 1/3 of the saturation value, persisting down to the Ising limit. A further plateau at 1/2 emerges in the quantum regime. This plateau provides a prototypical example of an order-by-disorder phenomena [Henley 1989, Chubukov 1992], i.e., quantum fluctuations select a specific crystalline phase of magnetic excitations and hence lift the extensive ground state degeneracy induced by the geometric frustration.

Next, in chapter 4, we move to a topic of strongly correlated fermions. We used the PQMC to study the physics of correlated Dirac fermions on the honeycomb lattice, the structure realized in graphene, in the SU(2) Hubbard model framework,

$$H = -t\sum_{\substack{\langle i,j\rangle \\ \alpha=\uparrow,\downarrow}}(c_{i\alpha}^\dagger c_{j\alpha}+c_{j\alpha}^\dagger c_{i\alpha})+U\sum_i n_{i\uparrow}n_{i\downarrow}. \tag{1.2}$$

To our surprise, upon close scanning of the controlling parameter of the electron correlation, U/t, the PQMC simulations revealed that within an intermediately correlated regime at an average density of one electron per site, an unexpected quantum spin liquid emerges between a state described by massless Dirac fermions and an antiferromagnetically ordered Mott insulator. In hindsight, to put our finding into perspective, we firstly in this chapter give a comprehensive survey of quantum spin liquid states in models and solid state materials. Such a survey bring us to the understanding that quantum spin liquids occupy a prominent place among the newly discovered exotic quantum states of matter, like the high temperature superconducting cuprates and pnictides or frustrated magnets. This is because they

are ubiquitous in the theoretical description of cuprates and frustrated quantum magnets, and yet elusive once models proposed to capture such phases are subjected to close examinations. With such understanding, we then focused on the nature of the quantum spin liquid phase found in our simulation. We measured the excitation gaps in the single particle, charge and spin sectors. We excluded various proposed symmetry breaking states such as valence bond solid, charge density wave [Honerkamp 2008], quantum spin Hall state [Raghu 2008], possible superconducting pairing channels [Uchoa 2007], et al., by measuring the corresponding correlation functions and performed careful finite size scaling analysis. Moreover, we found that this quantum-disordered state is a resonating valence bond (RVB) liquid, akin to the one proposed for high temperature superconductors [Anderson 1987]. Specifically, this RVB quantum spin liquid state is identified to possess a finite gap to all the magnetic excitations (spin gap). These results were rather unexpected, since quantum spin liquids were generically expected in geometrically frustrated quantum magnets [Balents 2010], while the honeycomb lattice is bipartite and hence magnetic order is not frustrated. It is expected that such exotic states of matter lead to unconventional order like topological order, where the ground-state displays a degeneracy not due to spontaneous symmetry breaking, but due to states in different topological sectors [Wen 1991]. In particular, for a gapped spin-liquid, the topological order implies an emerging ground-state degeneracy in the thermodynamic limit depending on the genus of the system's topology. For example, for a torus geometry, a four-fold degeneracy emerges.

Finally, in chapter 5, we further employed the PQMC to explore the electronic and magnetic properties of graphene nanoribbons, especially the correlation effects on the edge states, within a Hubbard model description. We compared our results to a self-consistent mean field approximation in the weak coupling regime. By examining the local density of states throughout finite ribbon samples with zigzag edges, we verified that the Coulomb interactions between electrons drive the system to an insulating ground state with a finite single particle gap. There is a dominant peak in the local spectral function at the gap energy. We propose that this dominant peak can be used as a *dynamical signature* to detect the edge-state magnetism in scanning tunneling microscopy experiments of graphene nanoribbons. In addition, we observed a drastic increase of the spin-spin correlation length along the zigzag edge with the ribbon width. As for the finite width ribbon samples, the interactions between electrons induce ferromagnetic order alone the zigzag edge. However, the conduction electrons inside the bulk will at the same time mediate an effective antiferromagnetic coupling between the two edges, such that in the dynamic spin structure factor, instead of having a simple quadratic ferromagnetic magnon mode at low energies, we observe a noticeable linear contribution in the magnon dispersion due to the antiferromagnetic coupling between the edges. Furthermore, when the energy of these magnetic excitations enters the regime of the particle-hole continuum, they abruptly decay into strongly damped Stoner modes.

The three systems studied in this thesis lead to various new investigations. Among them are the studies of the finite temperature behavior of the magnetiza-

tion plateaus on Shastry-Sutherland lattice [Suzuki 2010], a possible quantum spin liquid state in the J_1-J_2 antiferromagnetic Heisenberg model on the honeycomb lattice [Clark 2010, Reuther 2011], the SU(N) Hubbard Heisenberg model on the honeycomb lattice with a similar quantum spin liquid at SU(2) [Lang 2010], to name a few. At the end of each chapters, we give detailed description of all these upcoming investigations based on our works, and more importantly, we have also listed the new ideas inspired by our works. Some of these new ideas are currently being tested by ourselves. For instance, the competition between the quantum spin liquid and the topological band insulator in the context of the Kane-Mele model [Kane 2005] plus prominent electron-electron interactions, the effect of electron interactions on the AB stacked bilayer graphene, etc. Hopefully in the near future, these investigations will extend our understanding of the systems studied in this thesis.

Chapter 2

Quantum Monte Carlo Methods

In this chapter, we explain two quantum Monte Carlo methods in detail, both of them are approximation-free, and capable of reaching large system sizes (the computation effort scales as a power of the volume), and provide ground state, dynamical as well as thermodynamic quantities. The first section is devoted to the stochastic series expansion quantum Monte Carlo (hereafter referred to as SSE QMC), which is generically applicable to non-frustrated quantum spin (or bosons) system in arbitrary dimensions. The second section is about the projector auxiliary field quantum Monte Carlo method (hereafter referred to as PQMC), which is the standard method for fermionic lattice model where both spin and charge degree of freedoms are involved. We will apply the SSE QMC in chapter 3 to study the spin-1/2 XXZ model on the Shastry-Sutherland lattice, and apply the PQMC in chapter 4 and 5 to investigate the ground state phase diagram of the Hubbard model on the 2D honeycomb lattice as well as the edge-state properties of graphene nanoribbons.

2.1 Stochastic Series Expansion Quantum Monte Carlo for Bosons

2.1.1 Basic Formulation

The stochastic series expansion QMC technique [Sandvik 1991, Sandvik 1997, Sandvik 1999, Syljuåsen 2002] is based on a high temperature series expansion of the partition function of a quantum lattice model for bosonic (or spin) systems

$$Z = \mathrm{Tr}\{e^{-\beta H}\} = \sum_{|\alpha\rangle} \sum_{n=0}^{\infty} \frac{(-\beta)^n}{n!} \langle \alpha | \hat{H}^n | \alpha \rangle, \tag{2.1}$$

with inverse temperature $\beta = 1/(k_B T)$. The trace has been written as a sum over diagonal matrix elements in a complete basis $\{|\alpha\rangle\}$ of the Hamiltonian H. The weight for one configuration (α, n) in the configuration space $\{(\alpha, n)\}$ is

$$W(\alpha, n) = \frac{(-\beta)^n}{n!} \langle \alpha | H^n | \alpha \rangle. \tag{2.2}$$

Take the spin-1/2 XXZ model on the 2D square lattice as an example. The Hamiltonian is $H = \sum_{\langle i,j \rangle} \left[J_{xy}(S_i^x S_j^x + S_i^y S_j^y) + J_z S_i^z S_j^z \right] - h \sum_{i=1}^{N_s} S_i^z$, with nearest neighbor couplings. If $(J_{xy}, J_z) > 0$ the couplings are antiferromagnetic and if $(J_{xy}, J_z) < 0$ they are ferromagnetic. We choose the Ising basis

$|\alpha\rangle = \left|S_1^z, S_2^z, \cdots, S_N^z\right\rangle$, and rewrite the Hamiltonian in terms of bond operators $\hat{H}_b$, where b refers to a pair of spins $\langle i(b), j(b)\rangle$, and N_b is the number of bonds,

$$\begin{aligned} H &= \sum_{<i,j>} \left[J_{xy}(S_i^x S_j^x + S_i^y S_j^y) + J_z S_i^z S_j^z\right] - h\sum_{i=1}^{N_b} S_i^z - J_z N_b C = \\ &- \sum_{b=1}^{N_b}\{J_z \underbrace{\left(C - S_{i(b)}^z S_{j(b)}^z + \frac{h}{4J_z}[S_{i(b)}^z + S_{j(b)}^z]\right)}_{H_{1,b}} - J_{xy}\underbrace{\frac{1}{2}\left(S_{i(b)}^+ S_{j(b)}^- + S_{i(b)}^- S_{j(b)}^+\right)}_{H_{2,b}}\}. \end{aligned} \tag{2.3}$$

We name $H_{1,b}$ the diagonal bond operator and $H_{2,b}$ the off-diagonal bond operator. The powers of the Hamiltonian $\langle\alpha|H^n|\alpha\rangle$ in the partition function Eq. (2.1) can be readily expressed as sums of products of bond operators, $H_{1,b}$ and $H_{2,b}$, upon inserting the complete basis $|\alpha\rangle$ bewteen terms in the product. For a certain expansion order n, $\langle\alpha|H^n|\alpha\rangle$ can be written as,

$$\langle\alpha|(H)^n|\alpha\rangle = \sum_{S_n}^{(2N_b)^n} (-1)^n \cdot (-1)^{\text{number of } H_{2,b}} \cdot \langle\alpha| \prod_{p=1}^{n} H_{a(p),b(p)}|\alpha\rangle, \tag{2.4}$$

where the sum is performed over all the possible *operator string* S_n,

$$S_n = \left\{[a(n), b(n)], [a(n-1), b(n-1)], \ldots, [a(1), b(1)]\right\}, \tag{2.5}$$

with $a_i \in \{1, 2\}$ corresponding to the operator type ($1 \rightarrow$ diagonal; $2 \rightarrow$ off-diagonal) and $b_i \in \{1, 2, \ldots, N_b\}$ the bond index. For a certain expansion order n, the total number of different operator strings is $(2N_b)^n$.

The prefactor $(-1)^n$ in Eq. 2.4 comes from the minus sign before the bond sum in Eq. 2.3 and the prefactor $(-1)^{\text{number of } H_{2,b}}$ from the minus sign in the $-H_{2,b}$ term in Eq. 2.3. Note that the operators $H_{a(p),b(p)}$ do not all commute with each other, therefore the order of the operators in the string is important. Taking the descendent order: $\{n, n-1, \ldots, 2, 1\}$, the weight $W(\alpha, n)$ for one configuration (α, n) in the configuration space is given by

$$\begin{aligned} W(\alpha, n) &= \frac{(\beta)^n}{n!} \cdot (-1)^{\text{number of } H_{2,b}} \cdot \langle\alpha| \prod_{p=1}^{n} H_{a(p),b(p)}|\alpha\rangle \\ &= \frac{(\beta)^n}{n!} \cdot (-1)^{\text{number of } H_{2,b}} \cdot \langle\alpha(0)|H_{a(n),b(n)} \cdot \cdots \cdot H_{a(1),b(1)}|\alpha(0)\rangle. \end{aligned} \tag{2.6}$$

Within the local Ising basis we chose, the expectation value of the diagonal operator $H_{1,b(p)}$ is always positive with an appropriate constant $C \geq \frac{1}{4} + \frac{h}{4J_z}$, and for the off-diagonal operator $H_{2,b(p)}$, its expectation values are either 0 or 1. Hence if $J_{xy} < 0$ (ferromagnetic), even if the off-diagonal operator appears an odd number of times in the operator string, the $H_{2,b(p)}$ contribution in Eq. 2.6 is non-negative. The

Monte Carlo importance sampling of the partition function Z can thus be performed, even on a frustrated lattice geometry, i.g., triangle, kagome and Shastry-Sutherland lattices [1].

In practice we truncate the operator string at a cut-off M with an exponentially small truncation error. We also introduce a *unit operator* with indices $a = b = 0$, $H_{0,0} = \mathbf{1}$. It will do nothing to the spin states but fill up the operator string. We insert $M - n$ unit operators $H_{0,0}$ into every operator string with length $n < M$. There are $\binom{M}{n}$ such extended index sequences and therefore a factor $\binom{M}{n}^{-1}$ must be included in each weight to reduce this overweighting.

After the operator string is filled up to the length M, the weight

$$W(\alpha, S_M) = \frac{(\beta)^n (M-n)!}{M!} \langle \alpha | \prod_{p=1}^{M} H_{a(p),b(p)} | \alpha \rangle, \tag{2.7}$$

where n denotes the number of bond operators in the string, i.e., the number of elements $[a_i, b_i] \neq [0, 0]$, and p is the position of the operator in the string. For a bosonic or quantum spin systems, the partition function in SSE can thus be written as

$$Z = \sum_{\alpha} \sum_{S_M} \frac{\beta^n (M-n)!}{M!} \langle \alpha | \prod_{p=1}^{M} H_{a(p),b(p)} | \alpha \rangle. \tag{2.8}$$

In the configuration space $\{(\alpha, n)\}$ the SSE configurations are sampled according to the probability density

$$P(\alpha, S_M) = \frac{1}{Z} W(\sigma, S_M) = \frac{1}{Z} \frac{\beta^n (M-n)!}{M!} \langle \alpha | \prod_{p=1}^{M} H_{a(p),b(p)} | \alpha \rangle. \tag{2.9}$$

2.1.2 Update Schemes

Now we discuss how to update configurations according to the probability distribution $P(\alpha, S_M)$. In a Monte Carlo simulation, one starts with some arbitrary allowed configuration and generates a Markov chain of configurations by making changes. The update will be accepted or rejected according to the chosen probabilities, so that detailed balance is satisfied,

$$W(A) P(A \to B) = W(B) P(B \to A), \tag{2.10}$$

with

$$\underbrace{P(A \to B)}_{\text{transition probability}} = \underbrace{P_t(A \to B)}_{\text{trial probability}} \times \underbrace{P_a(A \to B)}_{\text{acceptance probability}} . \tag{2.11}$$

[1] For *bipartite* lattices, like square and honeycomb, J_{xy} can be both antiferromagnetic ($J_{xy} > 0$) and ferromagnetic ($J_{xy} < 0$). Because one needs to perform the off-diagonal operator an even number of times to bring the system back to the initial state $|\alpha(0)\rangle$. However, if the lattice is geometrically frustrated (e.g., triangle, Shastry-Sutherland lattice), one can also perform the off-diagonal operator an odd number of times and bring the system back to its initial state due to the existence of geometrical frustration. In this case the transverse coupling has to be ferromagnetic $J_{xy} < 0$ to avoid the *sign problem*.

Assuming the probability of making a tentative change from the current configuration A to new configuration B is equal to the probability of making the reverse transition, $P_t(A \to B) = P_t(B \to A)$, the probability to accept a trial change from the old configuration A to the new one B is given by the *Metropolis algorithm* [Metropolis 1953],

$$P_a(A \to B) = \min\left(\frac{W(B)}{W(A)}, 1\right). \tag{2.12}$$

However, if $P_t(A \to B) \neq P_t(B \to A)$, then the acceptance probability has to be modified in order to counterbalance the bias. In classical Monte Carlo simulations, e.g., of the Ising model, the condition $P_t(A \to B) = P_t(B \to A)$ usually holds, because the selection probability of randomly picking up a spin i to flip is always the same ($P_t(i) = \frac{1}{N}$). As we will see in next section, this is not always the case in QMC simulation.

In the SSE method, two types of updates are used: the *diagonal update* and the *operator loop update* [Syljuåsen 2002]. The diagonal update is carried out under the propagated state representation of the SSE configuration (using the operator string $opstring[\,]$ and spin configuration $spin[\,]$), whereas the operator loop update makes use of the linked vertices representation (using the linked vertex list $vertexlist[\,]$ which is constructed before the update is carried out) [2]. The simulation usually starts from an arbitrarily allowed configuration (α, S_M), a random spin configuration

$$spin[i] = \{1, -1, -1, -1, \ldots, 1\}, \quad i = 1, 2, \ldots, N \tag{2.13}$$

and an "empty" operator string

$$opstring[p] = 0, \quad p = 1, 2, \ldots, M \tag{2.14}$$

of arbitrary lenght M. The cut-off of the operator string length M will be adjusted during the thermalization part of the Monte Carlo simulation.

2.1.2.1 Diagonal Update

Diagonal updates are of the type $[0,0]_p \leftrightarrow [1,b]_p$. They are used to change the number n of bond operators ($[a_i, b_i] \neq [0,0]$) in the operator string S_M: we insert a diagonal operator at the position of a unit operator or remove a diagonal operator leaving a unit operator. The changes in n are given by $+1$ (insert), -1 (remove). If at the position p there is a unit operator, $opstring[p] = 0$, the acceptance probability for inserting a diagonal operator $P_a([0,0]_p \to [1,b]_p)$ can be calculated from the detailed balance equation, Eq. (2.10), as

$$\begin{aligned} &W\left([0,0]_p\right) P_t\left([0,0]_p \to [1,b]_p\right) P_a\left([0,0]_p \to [1,b]_p\right) = \\ &\quad W\left([1,b]_p\right) P_t\left([1,b]_p \to [0,0]_p\right) P_a\left([1,b]_p \to [0,0]_p\right). \end{aligned} \tag{2.15}$$

[2] The *propagated state* and *linked vertices* representations are two ways to save the information of spin configuration $\{\alpha\}$ and the operator string S_M in the SSE simulation. In the former case, all information of configurations are saved in arrays $spin[\,]$ and $opstring[\,]$; whereas in the latter, the actual information is saved by another bidirectional array $vertexlist[\,]$. Detailed description of their implementation can be found in Chapt. 3.4 of the Ref. [Meng 2007].

Here, $P_t(A \to B) \neq P_t(B \to A)$, because $P_t\left([0,0]_p \to [1,b]_p\right) = \frac{1}{N_b}$ taking the fact that there are N_b possible choices for b in the " $\to$ " direction into consideration, but $P_t\left([1,b]_p \to [0,0]_p\right) = 1$, since there is only one way to remove $[1,b]_p \to [0,0]_p$ when the bond b is given. Hence the trial probabilities now obey the ratio,

$$\frac{P_t\left([1,b]_p \to [0,0]_p\right)}{P_t\left([0,0]_p \to [1,b]_p\right)} = N_b. \tag{2.16}$$

The acceptance probability $P_a([0,0]_p \to [1,b]_p)$ is calculated by substituting the weight of the old and new configurations with Eq. (2.7) into the detailed balance equation Eq. (2.15),

$$\begin{aligned}
P_a([0,0]_p \to [1,b]_p) &= \min\left(\frac{W\left([1,b]_p\right)}{W\left([0,0]_p\right)} \cdot \frac{P_t\left([1,b]_p \to [0,0]_p\right)}{P_t\left([0,0]_p \to [1,b]_p\right)},\ 1\right) \\
&= \min\left(\frac{W([1,b]_p)}{W([0,0]_p)} \cdot N_b,\ 1\right) \\
&= \min\left(\frac{\frac{\beta^{n+1}\cdot(M-(n+1))!}{M!}\langle\alpha|\prod_{p=1}^{M} H_{a_p,bp}|\alpha\rangle \cdot N_b}{\frac{\beta^{n}\cdot(M-n)!}{M!}\langle\alpha|\prod_{p=1}^{M} H_{a_p,b_p}|\alpha\rangle},\ 1\right) \\
&= \min\left(\frac{\beta \cdot \langle\alpha(p+1)|H_{1,b}|\alpha(p)\rangle \cdot N_b}{(M-n)\cdot \underbrace{\langle\alpha(p+1)|H_{0,0}|\alpha(p)\rangle}_{=1}},\ 1\right) \\
&= \min\left(\frac{N_b\beta\langle\alpha(p+1)|H_{1,b}|\alpha(p)\rangle}{M-n},\ 1\right).
\end{aligned} \tag{2.17}$$

If we encounter a diagonal operator at bond b at position p, and will try to remove it, the detailed balance equation Eq. (2.10) turns out to be,

$$\begin{aligned}
&W\left([1,b]_p\right) P_t\left([1,b]_p \to [0,0]_p\right) P_a\left([1,b]_p \to [0,0]_p\right) = \\
&W\left([0,0]_p\right) P_t\left([0,0]_p \to [1,b]_p\right) P_a\left([0,0]_p \to [1,b]_p\right).
\end{aligned} \tag{2.18}$$

Taking Eq. (2.16) into account, the acceptance probability of removing one diagonal

operator $(P_a\left([1,b]_p \to [0,0]_p\right))$ can be derived as,

$$\begin{aligned} P_a([1,b]_p \to [0,0]_p) &= \min\left(\frac{W\left([0,0]_p\right)}{W\left([1,b]_p\right)} \cdot \frac{P_t\left([0,0]_p \to [1,b]_p\right)}{P_t\left([1,b]_p \to [0,0]_p\right)},\ 1\right) \\ &= \min\left(\frac{W([0,0]_p)}{W([1,b]_p)\cdot N_b},\ 1\right) \\ &= \min\left(\frac{\frac{\beta^{n-1}\cdot(M-(n-1))!}{M!}\langle\alpha|\prod_{p=1}^{M} H_{a_p,b_p}|\alpha\rangle}{\frac{\beta^{n}\cdot(M-n)!}{M!}\langle\alpha|\prod_{p=1}^{M} H_{a_p,b_p}|\alpha\rangle\cdot N_b},\ 1\right) \\ &= \min\left(\frac{(M-n+1)\cdot\overbrace{\langle\alpha(p+1)|H_{0,0}|\alpha(p)\rangle}^{=1}}{N_b\cdot\beta\langle\alpha(p+1)|H_{1,b}|\alpha(p)\rangle},\ 1\right) \\ &= \min\left(\frac{(M-n+1)}{N_b\cdot\beta\langle\alpha|H_{1,b}|\alpha\rangle},\ 1\right) \end{aligned} \tag{2.19}$$

again, N_b in the denominator reflects the fact that there is only one position to choose for each removal $[1,b]_p \to [0,0]_p$ when the bond b is given.

The diagonal updates are performed consecutively for all $p = 1, 2, \ldots, M$. When off-diagonal operators (spin-flip operators) $H_{2,b}(p)$ are encountered, the state $|\alpha(p-1)\rangle$ is propagated. The off-diagonal operator $H_{2,b}(p)$ at bond b acts on spins at sites $s1 = bsites[1,b]$ and $s2 = bsites[2,b]$. These two spins are flipped: $spin[s1] = -spin[s1], spin[s2] = -spin[s2]$ and because of the periodic boundary condition in the imaginary time, every spin can only be flipped an even number of times (including zero). When we complete the diagonal update until the last position $p = M$ in the operator string, the stored spins have been propagated back to the original state, $|\alpha(M)\rangle = |\alpha(0)\rangle$.

2.1.2.2 Operator Loop Update

The diagonal update cannot lead to any changes involving off-diagonal operators. It also cannot modify the spin configurations along the propagation path ($|\alpha(0)\rangle \to |\alpha(1)\rangle \to \ldots \to |\alpha(M-1)\rangle \to |\alpha(0)\rangle$). These are the task of the more efficient *operator loop updates* [Sandvik 1999, Syljuåsen 2002]. The operator loop update changes the types of bond operators, diagonal $\leftrightarrow$ off-diagonal, to a large scale in the operator string without changing their total number, i.e., the operator loop update is carried out with n fixed.

The idea of the operator loop update is to construct a closed path connecting vertex legs. Depending on the states of the two spins linked by bond b, and the type of operator that acts on b, there are six different vertices of a bond in the spin-1/2 XXZ model we considered here, as show in Fig. 2.1. Between different vertices, each vertex leg is linked to one leg of another vertex by the bidirectional link $vertexlist[\,]$ and these two form a segment of a path. Inside one vertex, we have one leg as the entrance and another as the exit, this part is also a segment of a path. Extending the path with these two types of segment until we go back to the original leg, a

closed loop is eventually formed. Once a path is closed, we flip all the spins the loop passes.

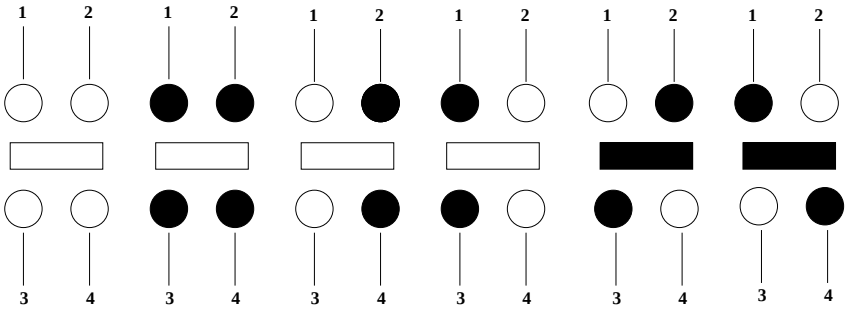

Figure 2.1: The six different vertices of a bond in spin-1/2 XXZ model: solid circles stand for spin-↑ and open circles stand for spin-↓; open horizontal bars represent the diagonal operators $H_{1,b}$ and the solid horizontal bars represent the off-diagonal operator $H_{2,b}$. Each vertex has four vertex legs $1, 2, 3, 4$.

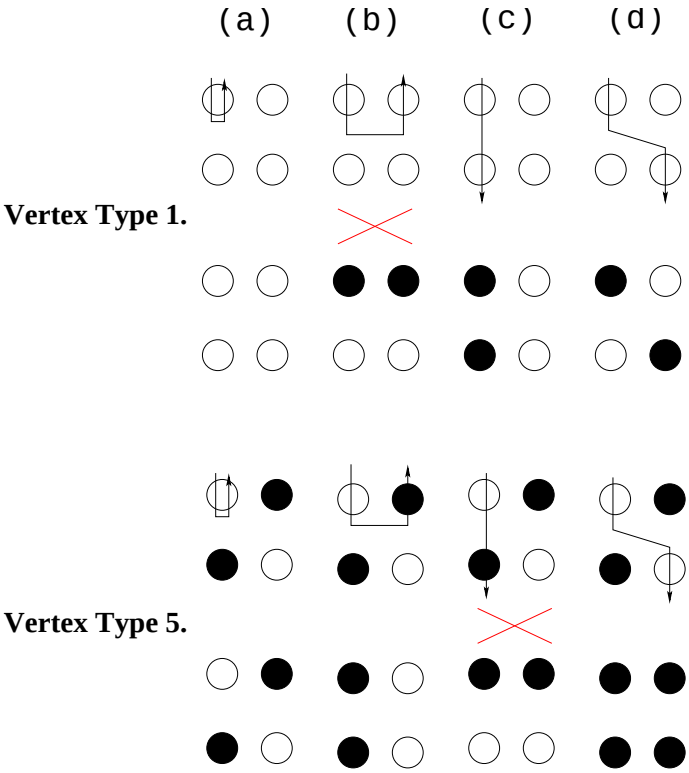

Figure 2.2: All four paths through vertices of type 1 and type 5, where the entrance leg is at the upper left (leg 1). The arrows indicate the direction of propagation. The updated vertices, with spins at entrance and exit flipped, are also shown. Note that the two cases marked with an red "X" are forbidden, because they violate conservation of magnetization. The four different processes are refered as (a) "Bounce", (b) "Switch and Reverse", (c) "Continue and Straight", and (d) "Switch and Continue".

Matrix Element	Value
$element[1] = \langle\downarrow,\downarrow\|H_{1,b}\|\downarrow,\downarrow\rangle$	$C - \frac{1}{4} - \frac{h}{4J_z}$
$element[2] = \langle\uparrow,\uparrow\|H_{1,b}\|\uparrow,\uparrow\rangle$	$C - \frac{1}{4} + \frac{h}{4J_z}$
$element[3] = \langle\downarrow,\uparrow\|H_{1,b}\|\downarrow,\uparrow\rangle$	$C + \frac{1}{4}$
$element[4] = \langle\uparrow,\downarrow\|H_{1,b}\|\uparrow,\downarrow\rangle$	$C + \frac{1}{4}$
$element[5] = \langle\downarrow,\uparrow\|H_{2,b}\|\uparrow,\downarrow\rangle$	$\frac{1}{2}$
$element[6] = \langle\uparrow,\downarrow\|H_{2,b}\|\downarrow,\uparrow\rangle$	$\frac{1}{2}$

Table 2.1: The 6 different matrix elements for the spin-1/2 XXZ model.

To construct an operator loop, one of the $4 \times n$ vertex legs is first selected randomly as an initial entrance leg. One of the four legs belonging to the same vertex is then chosen as the exit leg from the vertex: both the entrance and exit spins are flipped. In principle, there are four exits when the entrance is fixed, but due to the conservation of total magnetization — $\left[S^z_{tot}, H\right] = 0$, only three are possible. Taking vertices of type 1 and 5 as examples, Fig. 2.2 demonstrates how they can be changed in the four possible processes. The probability of exiting at a certain leg, given the extrance, is related to the matrix elements in Tab. 2.1. If the entrance and exit legs are at different sites ("Switch and Reverse" and "Switch and Continue"), the type of operator in that vertex will change: in the upper panel of Fig. 2.2 for vertex type 1, after "Switch and Continue", the operator changes from diagonal to off-diagonal. In the lower panel for vertex type 5, both processes "Switch and Reverse" and "Switch and Continue" change the operator from off-diagonal to diagonal. The "Bounce" processes in Fig. 2.2 for both vertex type 1 and vertex type 5 are always allowed and leave the vertex unaffected.

Fig. 2.3 demonstates the loop update scheme, from which we can clearly see how one operator loop is constructed and how this loop will change the SSE configuration. Here, we choose a 8-site 1D spin-1/2 chain with expansion cutoff $M = 13$ and bond operator number $n = 8$. We remove all those propagated spin states that have fixed spins between consecutive operations. The operator loop is denoted as the green path, the loop passes each vertex with the corresponding probabilities shown in Tab. 2.1. Once the construction of the loop is finished, all the spin states along the loop are flipped. In this way, we change some of the operator type along the loop, i.e., vertices at position $p = 1$ and $p = 8$, and made big change in the configuration. As the loop update can affect a very large number of operators, how many loops do we need to construct? (i) In case we have a deterministic loop construction, we can follow the *Swendsen-Wang* cluster algorithm for classical Ising model [Swendsen 1987] in the sense that we construct all the loops and flip each of them with probability 1/2; (ii) We can also follow the *Wolff* cluster algorithm [Wolff 1989], where we construct a certain number of loops, N_l, and each loop (cluster) is constructed at random (with different randomly chosen starting sites) and flipped with probability 1. The latter is more general and employed here.

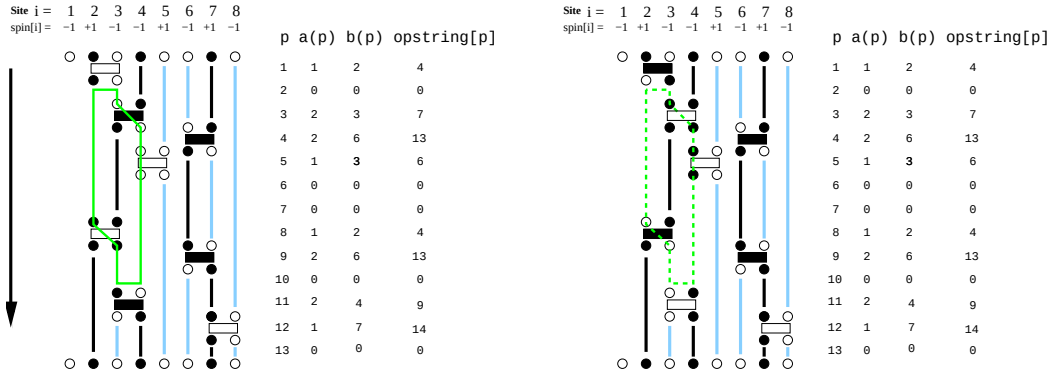

Figure 2.3: One operator loop in the SSE configuration for an 8-site 1D spin-1/2 chain with expansion cut-off $M = 13$ and operator number $n = 8$. Solid and open circles and bars have the same meaning as in Fig. 2.1. The arrow indicates the direction of propagation. The left panel is the path of this loop without spin flip, the right panel is the updated configuration when we flipped all the spins at vertex legs covered by this path. After the spin flip, in some vertices, the type of operators changed: for vertices at position $p = 1$ and $p = 8$, the operators change from diagonal to off-diagonal; while for vertices at position $p = 3$ and $p = 11$, the operators change from off-diagonal to diagonal; there are also vertices, whose operator remain the same after the spin flip, like the one at $p = 5$ in this case.

When the loop is constructed we need to mark the visited legs. The actual loop flip will be made after the loop has been constructed, and the intermediate information will only be recorded during the loop construction. Those spins in the state $|\alpha(p)\rangle, p = 0, 1, \ldots, M$ which are not acted on by any of the operators in operator string S_M are denoted as "free" spins. Such "free" spins can be flipped with probability 1/2 since they do not appear in the weight function. Since the average value of n, the number Hamiltonian operators in sequence S_M, grows linearly with inverse temperature β, free spins only appear frequently at high temperatures.

With the above information in mind, in SSE a Monte Carlo step is defined as following: Firstly, do a sweep of diagonal updates at all possible positions p in S_M. Then construct the linked list and complete a number N_l of operator loops. Finally flip the spin states of these N_l loops (mapping to a new operator string S_M and new spin configuration $|\alpha\rangle$) and flip the free spins with probability 1/2.

How many operator loops should be constructed in each MC simulation? There is usually no explicit value of N_l. However, to make sure that we visit a significant fraction of vertices, it is useful to record the loop sizes and adjust N_l during the equilibration of the simulation. Typically, in the equilibration part of the simulation, we determine N_l such that the average cumulative loop length (the number of visited vertices) in one QMC simulation is $\leq 10\langle n\rangle$ or $10\langle M\rangle$.

2.1.3 From Heatbath to Directed Loops

An important question when entering a vertex with a certain entrance leg, is, how to choose the exit leg? This question, which plays the key role in determining the efficiency of the SSE program, has several possible answers.

2.1.3.1 Heatbath

If the probability of selecting an exit leg is taken proportional to the corresponding matrix element in Tab.2.1, after the entrance and exit spins have been flipped. This is the *heatbath* scheme [Thijssen 2003]. Taking Fig. 2.2 as an example, the entrance leg on both vertices is the upper left (leg 1). The probability of taking the lower right leg (leg 4) as the exit for vertex type 1 is given by

$$P_{leg1.\to leg4.} = \frac{\langle\downarrow\uparrow |H_{2,b}| \uparrow\downarrow\rangle}{\langle\downarrow\downarrow |H_{1,b}| \downarrow\downarrow\rangle + \langle\uparrow\downarrow |H_{1,b}| \uparrow\downarrow\rangle + \langle\downarrow\uparrow |H_{2,b}| \uparrow\downarrow\rangle}, \tag{2.20}$$

which is the "Switch and Continue" process. The updated vertex now belongs to vertex type 6, and its bond operator changes from diagonal to off-diagonal ($H_{1,b} \to H_{2,b}$), the spin states at the entrance and exit leg are flipped. The probability of taking the upper left leg (leg 1) as the exit for vertex type 5 is given by

$$P_{leg1.\to leg1.} = \frac{\langle\uparrow\downarrow |H_{2,b}| \downarrow\uparrow\rangle}{\langle\downarrow\uparrow |H_{2,b}| \uparrow\downarrow\rangle + \langle\uparrow\downarrow |H_{1,b}| \uparrow\downarrow\rangle + \langle\uparrow\uparrow |H_{1,b}| \uparrow\uparrow\rangle}, \tag{2.21}$$

which is the "Bounce" process. The updated vertex still belongs to vertex type 5, and its bond operator remains off-diagonal ($H_{2,b} \to H_{2,b}$). Because the entrance and exit are the same leg, the spin state is flipped twice with the net effect of no change.

The "Bounce" process is unwanted in the simulation, as after such "Bounce" segments we are still in the same configuration. Unfortunately, in the heatbath algorithm, the probability of accepting the "Bounce" process is always finite except special cases.

2.1.3.2 Directed Loops

To overcome the drawback of the heatbath scheme, Syljuåsen and Sandvik designed a more powerful scheme to ensure the exclusion of "Bounce" during the construction of the operator loop [Syljuåsen 2002]. This new scheme is called the *directed loop scheme* in the sence that the construction of the path of vertices is directional, i.e., the probability of exiting from a particular leg, given the entrance leg, is not the same as the probability of the reverse process.

Directed loop Equations To explain the directed loop, we start again with the detailed balance equation, $W(A)P(A \to B) = W(B)P(B \to A)$, where A denotes a configuration having weight $W(A)$, and $P(A \to B) = P_t(A \to B) \cdot P_a(A \to B)$ is the transition probability of updating the configuration from A to B. Unlike the

weights which are given by the Hamiltonian (product of matrix elements Eq. (2.7)), the transition probability of how to update the configuration $P(A \to B)$ depends on the actual algorithm used.

In SSE, the probability for arriving at a new configuration B can be written as

$$\begin{aligned} P(A \to B) &= \sum_{\text{all possible loops}} P(l_0) \times P(A, l_0 \to A_1, l_1) \times P(A_1, l_1 \to A_2, l_2) \\ &\quad \times \ldots \times P(A_{n-1}, l_{n-1} \to B, l_0), \end{aligned} \tag{2.22}$$

where $P(l_0)$ is the probability for choosing the vertex leg l_0 as the starting entrance and $P(A_i, l_i \to A_{i+1}, l_{i+1})$ is the probability given a configuration A_i and entrance leg l_i and to exit that vertex at leg $vertexlist[l_{i+1}]$, which is connected to the next entrance leg l_{i+1} through the bidirectional $vertexlist[\,]$, resulting in a new configuration A_{i+1}. The exit leg $vertexlist[l_{i+1}]$ does not explicitly appear in the probabilities since they are uniquely linked to the following entrance leg l_{i+1}. The sum in Eq. (2.22) is over all possible closed loops which end up with the new configuration B. To find a efficient way of choosing the probabilities on the RHS of Eq. (2.22) one needs an expression for the inverse process where the SSE configuration B is transferred back into A. This can be achieved by realizing that for each of the terms in Eq. (2.22) there is a corresponding term that describes the "time-reversed" path, which contributes to the reverse probability,

$$\begin{aligned} P(B \to A) &= \sum_{\text{all possible loops}} P(l_0) \times P(B, l_0 \to A_{n-1}, l_{n-1}) \\ &\quad \times P(A_{n-1}, l_{n-1} \to A_{n-2}, l_{n-2}) \times \ldots \times P(A_1, l_1 \to A, l_0) \end{aligned} \tag{2.23}$$

where the sum is over exact the same closed loops as in Eq. (2.22).

Inserting the weight, Eq. (2.7), transition probabilities Eq. (2.22) and Eq. (2.23), into the detailed balance equation Eq. (2.10), we find that detailed balance is satisfied if

$$W(A_i)P(A_i, l_i \to A_{i+1}, l_{i+1}) = W(A_{i+1})P(A_{i+1}, l_{i+1} \to A_i, l_i) \tag{2.24}$$

for all possible intermediate SSE configurations A_i with corresponding entrance legs l_i. Because the update $(A_i, l_i \to A_{i+1}, l_{i+1})$ changes only one particular vertex, all except one of the factors in the product of vertex weights in Eq. (2.7) factor out. We then simplify our notation in such a way that

$$W(A_i)P(A_i, l_i \to A_{i+1}, e_i) \equiv W(A_i, l_i, e_i) \tag{2.25}$$

where $W(A_i)$ is the matrix element corresponding to a single vertex, l_i is the entrance leg, and e_i is the exit leg on the same vertex which is linked to the next entrance leg l_{i+1} in Eq. (2.24) by means of $vertexlist[e_i] = l_{i+1}$. With this notation, one can write Eq. (2.24) as

$$W(A_i; l_i, e_i) = W(A_{i+1}; l_{i+1}, e_{i+1}) \tag{2.26}$$

which must be valid for all possible vertex types that can be converted into each other by changing the states at the entrance and exit legs. This equation implies many relations between the unknown probabilities of how to choose an exit leg given a particular vertex and an entrance leg. Another relation which must be fulfilled is the path through a vertex always continues,

$$\sum_{e_i} P(A_i, l_i \to A_{i+1}, e_i) = 1 \tag{2.27}$$

where the sum is over all four legs on the vertex. The notation A_{i+1} means the resulting spin configuration depends on the exit leg e_i. Now we plug the weights $W(A_i, l_i, e_i)$ of Eq. (2.25) into Eq. (2.27). This requirement translates into

$$\sum_{e_i} W(A_i) P(A_i, l_i \to A_{i+1}, e_i) = W(A_i) \tag{2.28}$$

which must be valid for all vertices and entrance legs. Eq. (2.28) together with Eq. (2.26), form the *directed loop equations*, from which we can construct valid probability tables for an efficient loop update [Syljuåsen 2002]. To fulfill the detailed balance condition Eq. (2.26) we must relate vertices in which the two spins connected by the loop segment are flipped and the direction of the loop segment is reversed. One example of such related configurations is illustrated in Fig. 2.4.

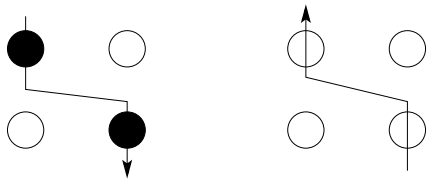

Figure 2.4: An example of two vertices with directed loop segments that transform into each other after a spin flip. Left: vertex type 6 with entrance at leg 1 and exit at leg 4; Right: vertex type 1 with entrance at leg 4 and exit at leg 1.

Furthermore, Eq. (2.28) relates vertices with different exit legs but the same entrance leg and the same spin configuration before the spin flip. We can make the key observation that *all possible vertex configurations can be divided into eight subsets that do not transform into each other*. All these eight subsets are listed in Fig. 2.5.

Now we can write down the eight sets of the directed loop equation for the eight subsets of vertex configuration in Fig. 2.5. We can "solve" these sets of equations to obtain the probability of choosing exit legs given the entrance leg and vertex type. Eventually, we found in a very broad parameter region, in terms of $\{J_{xy}/J_z, h/J_z\}$, for which we can simply set the probability of the "Bounce" process to zero without bringing non-valid (negative) probabitilities for the other three processes. Such exclusion of the "Bounce" in the parameter space by solving the directed loop equations lies at the heart directed loop scheme. With directed loops the efficiency of the operator loop update can be increased drastically. An explicit example of solving

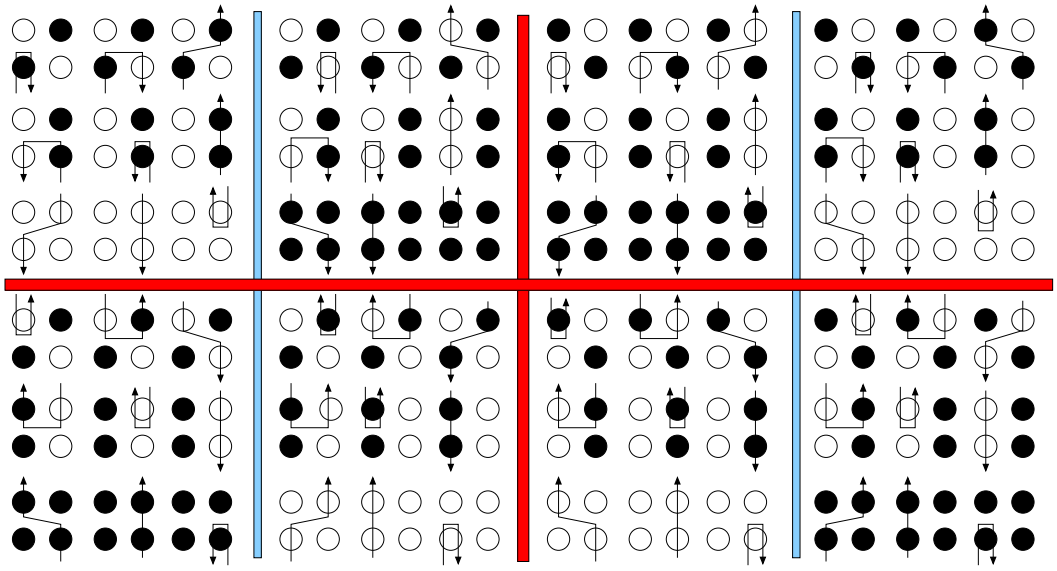

Figure 2.5: Possible assignments of directed-loop segments for different combinations of vertices and entrance legs. The lines with arrows are the directed-loop segments. Upon flipping the spins connected by the loop segment and reversing the direction of the arrow, only configurations within the same quadrant are transformed into each other.

the directed loop equations for the spin-1/2 XXZ model on square lattice is derived in Chap. 3.6 of the Ref. [Meng 2007].

Alet et al. have further generalized the above mentioned directed loop scheme [Alet 2005]. Their improvement is based on the observation that the directed loop equations can be extended by taking into account the matrix elements of the associated operator. The generalized directed loop algorithm uses a linear programming technniques to numerically solve the generalized directed loop equations, under the constraint of minimal "Bounce" processes, to ensure the SSE QMC to be more efficient.

2.1.4 Observables

Here we use the spin-1/2 XXZ model on the square lattice as an example, to demonstrate how observables are implemented in the SSE QMC simulations.

The energy is given by measuring the number of bond operators $\langle n \rangle$ in the operator string S_M,

$$\langle E \rangle = -\frac{\langle n \rangle}{N\beta} + C, \tag{2.29}$$

the AF structure factor S_{AF} is defined as

$$S_{AF} = \frac{1}{N} \sum_{i,j} \varepsilon_i \varepsilon_j \langle S_i^z S_j^z \rangle, \tag{2.30}$$

where $\varepsilon_i = \pm 1$ depending on the sublattice to which site i belongs, and it is directly measured since the simulation is performed in the S^z basis. The spin stiffness, or superfluid density, ρ_S, can be measured from the spin winding number,

$$\begin{aligned} \rho_S &= \frac{3}{J\beta N}\langle \frac{1}{2}(N_x^+ - N_x^-)^2 + \frac{1}{2}(N_y^+ - N_y^-)^2 \rangle \\ &= \frac{3}{4J\beta}\langle (\frac{N_x^+ - N_x^-}{2})^2 + (\frac{N_y^+ - N_y^-}{2})^2 \rangle \\ &= \frac{3}{4J\beta}\langle W^2 \rangle \end{aligned} \tag{2.31}$$

where N_x^+ and N_x^- are the occurrence of the off-diagonal operator $H_{2,b}$ in operator string S_M in the x direction of the lattice. Physically they correspond to the expectation values of the spin-flip part $\langle S_i^+ S_j^- \rangle$ and $\langle S_i^- S_j^+ \rangle$ in the Hamiltonian, in the x direction of the lattice, so as to N_y^+ and N_y^-. W is the net spin winding number [Pollock 1987].

In this way, we finally finished the detailed formulation of the SSE QMC method with the directed loop scheme. In Chapter 2, we have implemented it to simulate the spin-1/2 XXZ model on the Shastry-Sutherland lattice.

2.2 Projector Auxiliary Field Quantum Monte Carlo for Fermions

2.2.1 Basic Formulation

The projector auiliary field quantum Monte Carlo (PQMC) is a zero temperature version of the auxiliary field QMC introduced by Blankenbecler, Scalapino and Sugar (BSS) in 1981 [Blankenbecler 1981, Scalapino 1981] for fermionic systems. In this section we will describe the method in detail, based on the materials in the reviews by Assaad [Assaad 2002, Assaad 2008] and the corresponding chapters in the Diplom thesis of Bercx [Bercx 2008] and PhD thesis of Lang [Lang 2010].

Similar with the previous SSE QMC section, here we also demonstrate the implementation of the PQMC by example. The example we chose is the half-filled Hubbard model: $H = H_t + H_U$, with $H_t = -t\sum_{\langle i,j\rangle,\sigma} c_{i,\sigma}^\dagger c_{j,\sigma}$ and $H_U = \sum_i (n_{i,\uparrow} - \frac{1}{2})(n_{i,\downarrow} - \frac{1}{2})$. In the projective scheme of PQMC, an observable O is obtained by projecting a trial wavefunction $|\Psi_T\rangle = \sum_n |\Psi_n\rangle\langle\Psi_n|\Psi_0\rangle$ along the imaginary time axis

$$\frac{\langle\Psi_0|O|\Psi_0\rangle}{\langle\Psi_0|\Psi_0\rangle} = \lim_{\Theta\to\infty} \frac{\langle\Psi_T|e^{-\Theta H} O e^{-\Theta H}|\Psi_T\rangle}{\langle\Psi_T|e^{-2\Theta}|\Psi_T\rangle} \tag{2.32}$$

under the assumption of a finite overlap of the trial wave function with the ground state and a non-degenerate ground state,

$$\frac{\langle\Psi_0|O|\Psi_0\rangle}{\langle\Psi_0|\Psi_0\rangle} = \lim_{\Theta\to\infty} \frac{\sum_{m,n}\langle\Psi_T|\Psi_n\rangle\langle\Psi_m|\Psi_T\rangle e^{-\Theta(E_n - E_m - 2E_0)}\langle\Psi_n|O|\Psi_m\rangle}{\sum_n |\langle\Psi_T|\Psi_n\rangle|^2 e^{-2\Theta(E_n - E_0)}}. \tag{2.33}$$

According to the Trotter-Suzuki decomposition [Trotter 1959, Suzuki 1976], one can separate the H_t and H_U parts of the Hamiltonian and rewrite the partition function as

$$\begin{aligned} Z &= \mathrm{Tr}\{e^{-\beta H}\} = \mathrm{Tr}\{e^{-\beta(H_t+H_U)}\} = \lim_{L\to\infty} \mathrm{Tr}\Big\{\big(e^{-\frac{\beta}{L}H_t}e^{-\frac{\beta}{L}H_U}\big)^L\Big\} \\ &= \mathrm{Tr}\Big\{\prod_{i=1}^{L}\big(e^{-\Delta\tau H_t}e^{-\Delta\tau H_U} + \frac{\beta}{2}\Delta\tau[H_t,H_U] + \beta t U O(\Delta\tau^2)\big)\Big\}. \end{aligned} \tag{2.34}$$

where the Trotter slices are of length $\Delta\tau = \beta/L$. The term linear in $\Delta\tau$ will vanish since the trace over a commutator gives zero. So for a finite L the Trotter-Suzuki decomposition introduces a systematic error of $O(\Delta\tau^2)$ in the partition function. In the simulations of Chapter 4 and Chapter 5, we employed a finite imaginary time step $\Delta\tau = 0.05/t$ and verified upon extrapolating $\Delta\tau \to 0$, that this value produces no artifacts.

To evaluate the partition function of the non-interacting part of the Hamiltonian $H_t = \sum_{i,j} c_i^\dagger A_{i,j} c_j$, is straightforward. The first step is to diagonalize the Hamiltonian via a unitary transformation

$$H_t = \sum_{\langle i,j\rangle} c_i^\dagger A_{i,j} c_j = \sum_{\langle i,j\rangle} c_i^\dagger U U^\dagger A_{i,j} U U^\dagger c_j = \sum_\alpha a_\alpha c_\alpha^\dagger c_\alpha, \tag{2.35}$$

where $U^\dagger A U = \mathrm{diag}(a_1, ..., a_\alpha, ..., a_N)$, are the eigenenergies of the single-particle state, then,

$$\begin{aligned} Z &= \mathrm{Tr}\{e^{-\sum_{\langle i,j\rangle} c_i^\dagger A_{i,j} c_j}\} = \mathrm{Tr}\{e^{-\sum_\alpha a_\alpha c_\alpha^\dagger c_\alpha}\} = \mathrm{Tr}\{\prod_\alpha e^{-a_\alpha c_\alpha^\dagger c_\alpha}\} \\ &= \prod_\alpha \sum_{n_\alpha=0,1} e^{-a_\alpha n_\alpha} = \prod_\alpha (1 + e^{-a_\alpha}) = \det(\mathbf{1} + e^{-\mathbf{A}}). \end{aligned} \tag{2.36}$$

We see that the evolution of the non-interacting N-particle state is to propagate each particle independently, so as long as the the fermionic Hamiltonian can be represented in bilinear form (unitary transformed to the basis of single-particle state $|\alpha\rangle$ in which H is diagonal), one can always trace out the fermions and write the partition function in the form of a determinant. As for the interacting Hamiltonians, which cannot be simplified into bilinear form, e.g., the repulsion term is quartic, $n_{i,\uparrow} n_{i,\downarrow}$, we cannot arrive at the fermionic determinant directly. But we can introduce the Hubbard-Stratonovich (HS) transformation at each time step to transfer the higher order term into bilinear form [Hirsch 1985a]. The HS transformation is based on the Gaussian integral

$$e^{A^2/2} = \frac{1}{\sqrt{2\pi}} \int d\phi e^{-\phi^2/2 - A\phi}. \tag{2.37}$$

The Hubbard term can be written in squares $n_{i,\uparrow} n_{i,\downarrow} = \pm[(n_{i,\uparrow} \pm n_{i,\downarrow})^2 - (n_{i,\uparrow} + n_{i,\downarrow})]/2$, such that the transformation is given by

$$e^{\Delta\tau \frac{U}{2}(n_{i,\uparrow} \pm n_{i,\downarrow})^2} = (\frac{\Delta\tau}{2\pi})^{\frac{1}{2}} \int d\phi_i e^{-\frac{\Delta\tau}{2}\phi_i^2 + \Delta\tau\sqrt{U}(n_{i,\uparrow} \pm n_{i,\downarrow})\phi_i}. \tag{2.38}$$

In the numerical implementation of such a HS transformation, one usually introduces the discrete auxiliary field in the following way [Hirsch 1985b, White 1989]

$$e^{-\Delta\tau U\sum_i (n_{i,\uparrow}-\frac{1}{2})(n_{i,\downarrow}-\frac{1}{2})} = C \sum_{s_1,s_2,\ldots,s_N=\pm 1} e^{\alpha \sum_i s_i (n_{i,\uparrow}-n_{i,\downarrow})}, \tag{2.39}$$

where on an N sites square lattice the constant $C = e^{-(\Delta\tau UN/4)}/2^N$ and $\cosh(\alpha) = e^{-\Delta\tau U/2}$.

For the presented simulations, we use an SU(2) symmetric HS transformation which allows for a direct generalization to SU(N) symmetric models [Assaad 1998, Assaad 2005]. The interaction part of the imaginary time evolution operator is expressed as

$$e^{-\Delta\tau U(n_\uparrow+n_\downarrow-1)^2/2} = \sum_{l=\pm 1,\pm 2} \gamma(l) e^{i\sqrt{\Delta\tau U/2}\eta(l)(n_\uparrow+n_\downarrow-1)} + O(\Delta\tau^4), \tag{2.40}$$

with the four-valued auxiliary field $\gamma(l)$ and $\eta(l)$ parameterized as

$$\begin{aligned}
\gamma(1) &= 1+\sqrt{6}/3, & \eta(1) &= \sqrt{2(3-\sqrt{6})},\\
\gamma(-1) &= 1+\sqrt{6}/3, & \eta(-1) &= -\sqrt{2(3-\sqrt{6})},\\
\gamma(2) &= 1-\sqrt{6}/3, & \eta(2) &= \sqrt{2(3+\sqrt{6})},\\
\gamma(-2) &= 1-\sqrt{6}/3, & \eta(-2) &= -\sqrt{2(3+\sqrt{6})}.
\end{aligned} \tag{2.41}$$

Such a HS transformation produces an overall systematic error proportional to $\Delta\tau^3$ in the Monte Carlo estimate of observables, which will be buried into the $\Delta\tau^2$ Trotter-Suzuki error of the partition function, hence the transformation is as good as exact.

2.2.2 Equal Time Green's Function

The HS transformation left us with non-interacting fermions subject to time and space dependent auxiliary fields $\{\vec{\eta}_n\}$. By applying Wick's theorem [Mahan 1990], one can compute arbitrary observables with the PQMC by expressing them in terms of the single particle propagators – the Green's function. To further simplify the notation we introduce the index $x = (\mathbf{i}, \sigma)$ to define

$$\begin{aligned}
H_t &= \sum_{x,y} c_x^\dagger T_{x,y} c_y \equiv \mathbf{c}^\dagger \mathbf{T} \mathbf{c},\\
i\alpha \sum_i \eta_i (n_{i,\uparrow}+n_{i,\downarrow}) &= \sum_{x,y} c_x^\dagger V(\eta)_{x,y} c_y \equiv \mathbf{c}^\dagger \mathbf{V}(\vec{\eta}_n)\mathbf{c},
\end{aligned} \tag{2.42}$$

where $\vec{\eta}_n$ stands for the auxiliary field for all the lattice sites at the imaginary time slice n. One can define the imaginary time propagators,

$$\begin{aligned} U_{\vec{\eta}_n}(\tau_2,\tau_1) &= \prod_{n=n_1+1}^{n_2} e^{\mathbf{c}^\dagger V(\vec{\eta}_n)\mathbf{c}} e^{-\Delta\tau \mathbf{c}^\dagger \mathbf{T}\mathbf{c}}, \\ B_{\vec{\eta}_n}(\tau_2,\tau_1) &= \prod_{n=n_1+1}^{n_2} e^{\mathbf{V}(\vec{\eta}_n)} e^{-\Delta\tau \mathbf{T}}, \end{aligned} \tag{2.43}$$

where $n_1\Delta\tau = \tau_1$ and $n_2\Delta\tau = \tau_2$. For the PQMC algorithm, one still needs a trial wave function to begin the simulation. The trail wave function will be chosen as a Slater determinant [Ashcroft 1976], in practice the Slate determinant is constructed from the eigenvectors of the hopping matrix H_t. It is characterized by a column orthonormal matrix $\mathbf{P}$. For an non-interacting $N-$particle state it is expressed as

$$|\Psi_T\rangle = \prod_{y=1}^{N} \Big(\sum_x c_x^\dagger P_{x,y}\Big)|0\rangle = \prod_{y=1}^{N} \big(\mathbf{c}_\mathbf{x}^\dagger \mathbf{P}_y\big), \tag{2.44}$$

such that

$$\langle\Psi_T|e^{-2\Theta H}|\Psi_T\rangle = C^m \sum_{\vec{\eta}_1,\vec{\eta}_2,\ldots,\vec{\eta}_m} \det\left[\mathbf{P}^\dagger B_{\vec{\eta}}(2\Theta,0)\mathbf{P}\right], \tag{2.45}$$

with discretization in imaginary time implemented $m\Delta\tau = 2\Theta$. In this way, one can calculate expectation values

$$\frac{\langle\Psi_T|e^{-\Theta H} O e^{-\Theta H}|\Psi_T\rangle}{\langle\Psi_T|e^{-2\Theta H}|\Psi_T\rangle} = \sum_{\vec{\eta}} P_{\vec{\eta}}\langle O\rangle_{\vec{\eta}} + \mathcal{O}(\Delta\tau^2), \tag{2.46}$$

with $P_{\vec{\eta}}$ the Monte Carlo weight for each configuration of the auxiliary field $\{\vec{\eta}\}$ and $\langle O\rangle_{\vec{\eta}}$ the expectation value of operator O under that specific configuration,

$$\begin{aligned} P_{\vec{\eta}} &= \frac{\det\left[\mathbf{P}^\dagger B_{\vec{\eta}}(2\Theta,0)\mathbf{P}\right]}{\sum_{\vec{\eta}}\det\left[\mathbf{P}^\dagger B_{\vec{\eta}}(2\Theta,0)\mathbf{P}\right]}, \\ \langle O\rangle_{\vec{\eta}} &= \frac{\langle\Psi_T|U_{\vec{\eta}}(2\Theta,\Theta) O U_{\vec{\eta}}(\Theta,0)|\Psi_T\rangle}{\langle\Psi_T|U_{\vec{\eta}}(2\Theta,0)|\Psi_T\rangle}. \end{aligned} \tag{2.47}$$

Next step is to calculate the equal-time single-particle Green's function $O = c_x c_y^\dagger = \delta_{x,y} - \mathbf{c}^\dagger \mathbf{A}^{(y,x)}\mathbf{c}$, with $\mathbf{A}^{(y,x)}_{y_1,x_1} = \delta_{y_1,y}\delta_{x_1,x}$. Using the identity

$$\frac{\partial}{\partial\gamma}\ln\langle\Psi_T|U_1 e^{\gamma O} U_2|\Psi_T\rangle|_{\gamma=0} = \frac{\langle\Psi_T|U_1 O U_1|\Psi_T\rangle}{\langle\Psi_T|U_1 U_2|\Psi_T\rangle}, \tag{2.48}$$

the Green's function is obtained from

$$\begin{aligned}\langle c_x c_y^\dagger\rangle &= \delta_{x,y} - \frac{\partial}{\partial\gamma}\ln\langle\Psi_T|U_{\vec{\eta}}(2\Theta,\Theta)e^{\gamma\mathbf{c}^\dagger\mathbf{A}^{(y,x)}\mathbf{c}}U_{\vec{\eta}}(\Theta,0)|\Psi_T\rangle|_{\gamma=0}\\ &= \delta_{x,y} - \frac{\partial}{\partial\gamma}\ln\det\left[\mathbf{P}^\dagger B_{\vec{\eta}}(2\Theta,\Theta)e^{\gamma\mathbf{A}^{(y,x)}}B_{\vec{\eta}}(\Theta,0)\mathbf{P}\right]|_{\gamma=0}\\ &= \delta_{x,y} - \frac{\partial}{\partial\gamma}\mathrm{Tr}\ln\left[\mathbf{P}^\dagger B_{\vec{\eta}}(2\Theta,\Theta)e^{\gamma\mathbf{A}^{(y,x)}}B_{\vec{\eta}}(\Theta,0)\mathbf{P}\right]|_{\gamma=0}\\ &= \delta_{x,y} - \mathrm{Tr}\left[(\mathbf{P}^\dagger B_{\vec{\eta}}(2\Theta,0)\mathbf{P})^{-1}\mathbf{P}^\dagger B_{\vec{\eta}}(2\Theta,\Theta)\mathbf{A}^{(y,x)}B_{\vec{\eta}}(\Theta,0)\mathbf{P}\right]|_{\gamma=0},\end{aligned} \tag{2.49}$$

where we used the relation $\ln\det A = \mathrm{Tr}\ln A$ from the second to third equality. Operators within the trace can be cycled such that we arrive at the equal time Green's function at half-time Θ of the propagation length,

$$G_{\vec{\eta}}(\Theta)_{x,y} = \left(\mathbf{1} - B_{\vec{\eta}}(\Theta,0)\mathbf{P}(\mathbf{P}^\dagger B_{\vec{\eta}}(2\Theta,0)\mathbf{P})^{-1}\mathbf{P}^\dagger B_{\vec{\eta}}(2\Theta,\Theta)\right)_{x,y}. \tag{2.50}$$

2.2.3 Stabilization Scheme

For a given HS configuration of the auxiliary field $\{\vec{\eta}\}$, one can in principle calculate the equal time Green's function with Eq. 2.50. However, on finite precision computers, a direct calculation of Green's function as above will lead to numerical instabilities at large value of projection length Θ. To see this, note the trial wavefunction matrix $\mathbf{P}$ is a set of column orthonormal vectors (they are the eigenvectors of the tight-binding Hamiltonian). In the Hubbard model at weak coupling, the range of energy scale in the matrix $B_{\vec{\eta}}(2\Theta,0)$ is determined by the kinetic energy from $e^{6t\Theta}$ to $e^{-6t\Theta}$ in the 2D honeycomb lattice case (the non-interacting bandwidth is $6t$). When the set of orthonormal vectors in $\mathbf{P}$ are propagated, the large scales will wash out the small scales such that they would not be orthonormal any more and eventually yield ill-defined inversion of the matrix $\mathbf{P}^\dagger B_{\vec{\eta}}(2\Theta,0)\mathbf{P}$.

To circumvent this problem, several matrix decomposition techniques were employed. Earily works usually used the Gram-Schmidt orthogonalization procedure [Sorella 1989a, Sorella 1989b, White 1989] to decompose the N_p linearly independent vectors of the matrix

$$B^\rangle \equiv B_{\vec{\eta}}(\tau,0)\mathbf{P}, \tag{2.51}$$

to

$$B^\rangle \equiv (\mathbf{v}_1,\mathbf{v}_2,...,\mathbf{v}_{N_p}) = U^\rangle D_R V_R, \tag{2.52}$$

where $U^\rangle$ contains the orthonormal vectors $\{\mathbf{v}_1,\mathbf{v}_2,...,\mathbf{v}_{N_p}\}$, D_R is a diagonal matrix containing the scales, V_R is an upper unit triangular $N_p\times N_p$ matrix, whose diagonal elements are equal to unity.

Later, people realized that the Gram-Schmidt orthonormalization is itself unstable, hence nowadays the established method is to use singular value decompositions based on Housholder's scheme to obtain the above UDV form for the B matrices [Press 1992, Feldbacher 2001]. One can use the same procedure to obtain:

$$B^\langle \equiv \mathbf{P}^\dagger B_{\vec{\eta}}(2\Theta,\tau) = V_L D_L U^\langle. \tag{2.53}$$

The Green's function for the PQMC is now easy to compute:

$$\begin{aligned} 1 - G_{\vec{\eta}}(\tau) &= B_{\vec{\eta}}(\tau,0)\mathbf{P}(\mathbf{P}^\dagger B_{\vec{\eta}}(2\Theta,0)\mathbf{P})^{-1}\mathbf{P}^\dagger B_{\vec{\eta}}(2\Theta,\tau) \\ &= B^{\rangle}\big(B^{\langle}B^{\rangle}\big)^{-1}B^{\langle} \\ &= U^{\rangle}D_R V_R\big(V_L D_L U^{\langle}U^{\rangle}D_R V_R\big)^{-1}V_L D_L U^{\langle} \\ &= U^{\rangle}D_R V_R(D_R V_R)^{-1}(U^{\langle}U^{\rangle})^{-1}(V_L D_L)^{-1}V_L D_L U^{\langle} \\ &= U^{\rangle}(U^{\langle}U^{\rangle})^{-1}U^{\langle} \end{aligned} \tag{2.54}$$

thus, in the PQMC, different scales which are at the origin of the numerical instabilities are separated from the problem when computing Green's functions, and the above stabilization procedure leaves the physical results invariant. In practice, how often (the frequency) the stabilization is carried out is problem dependent. As for the Hubbard model on the Honeycomb lattice in chapter 4, with $\Delta\tau t = 0.05$, we can test the stabilization frequency as follow: take the Green's function at time τ, update and wrap it to next time slice τ_1

$$G(\tau_1) = B_{\vec{\eta}}(\tau_1,\tau)G_{\vec{\eta}}(\tau)B^{-1}_{\vec{\eta}}(\tau_1,\tau), \tag{2.55}$$

for the time interval $\tau_1 - \tau$ the involved scales should lie within the accuracy of the computer, say, 10^{-12} of the double precision numbers. The thus obtained Green's function at time τ_1 may be compared with the one computed from scratch using Eq. 2.54. For a 3x3 half-filled Hubbard model on the Honeycomb lattice at $U/t = 4$, $\Theta t = 50$, $\Delta\tau t = 0.05$ and $\tau_1 = 10\Delta\tau$, we obtain an maximal difference between the matrix elements of both Green's function of 10^{-12}, which is orders of magnitude smaller than the statistical uncertainty $(\Delta\tau t)^2 \sim 10^{-4}$. Hence, the frequency of appling stabilizatino at every 10th time slice is justified, and we will stick to this frequency of stablize at every 10th time slice throughout the simulations in Chapter 4 and 5.

2.2.4 Sampling Procedure and Imaginary Time Green's Function

The Monte Carlo sampling consists of creating a new auxiliary field configuration $\vec{\eta}'$ based on a single spin-flip scheme [Metropolis 1953]. The decision of updating the auxiliary spin is made by comparing $P_{acc} = \min[1, R]$. The ratio of the configuration weigths can be calculated as

$$R = \frac{w[\vec{\eta}']}{w[\vec{\eta}]} = \frac{P_{\vec{\eta}'}}{P_{\vec{\eta}}} = \frac{\det[\mathbf{P}^\dagger B_{\vec{\eta}'}(2\Theta,0)\mathbf{P}]}{\det[\mathbf{P}^\dagger B_{\vec{\eta}}(2\Theta,0)\mathbf{P}]}. \tag{2.56}$$

The change of a single spin will change the configuration and generate a new interaction matrix $\mathbf{V}(\vec{\eta}'_n)$

$$e^{\mathbf{V}(\vec{\eta}'_n)} = \big[1 + \underbrace{\big(e^{\mathbf{V}(\vec{\eta}'_n)}e^{-\mathbf{V}(\vec{\eta}_n)} - 1\big)}_{\Delta}\big]e^{\mathbf{V}(\vec{\eta}_n)}. \tag{2.57}$$

The matrix Δ has only one non-vanishing entry $\Delta_{x,y} = \delta_{x,x_1'}\delta_{y,y_1'}\vec{\eta}_n^{(x_1',y_1')}$. The propagator changes to $B_{\vec{\eta}'}(2\Theta,0) = B_{\vec{\eta}}(2\Theta,\tau)(1+\Delta)B_{\vec{\eta}}(\tau,0)$, accordingly. Let's remind us of the notation $B_{\vec{\eta}}^{\langle} = \mathbf{P}^\dagger B_{\vec{\eta}}(2\Theta,\tau)$, and $B_{\vec{\eta}}^{\rangle} = B_{\vec{\eta}}(\tau,0)\mathbf{P}$, to compute the ratio

$$\begin{aligned} R = \frac{\det\left[B_{\vec{\eta}}^{\langle}(1+\Delta^{(i)})B_{\vec{\eta}}^{\rangle}\right]}{\det\left[B_{\vec{\eta}}^{\langle}B_{\vec{\eta}}^{\rangle}\right]} &= \det\left[B_{\vec{\eta}}^{\langle}\left(1+\Delta^{(i)}\right)B_{\vec{\eta}}^{\rangle}\left(B_{\vec{\eta}}^{\langle}B_{\vec{\eta}}^{\rangle}\right)^{-1}\right] \\ &= \det\left[1+B_{\vec{\eta}}^{\langle}\Delta^{(i)}B_{\vec{\eta}}^{\rangle}\left(B_{\vec{\eta}}^{\langle}B_{\vec{\eta}}^{\rangle}\right)^{-1}\right] \\ &= \det\left[1+\Delta^{(i)}B_{\vec{\eta}}^{\rangle}\left(B_{\vec{\eta}}^{\langle}B_{\vec{\eta}}^{\rangle}\right)^{-1}B_{\vec{\eta}}^{\langle}\right]. \end{aligned} \tag{2.58}$$

If the proposed spin-flip is accepted, we need to update the Green's function according to the new auxiliary field $\vec{\eta}'$. To achieve this, one will first compute the matrix inversion:

$$\begin{aligned} (B_{\vec{\eta}'}^{\langle}B_{\vec{\eta}'}^{\rangle})^{-1} &= \left(B_{\vec{\eta}}^{\langle}(1+\Delta)B_{\vec{\eta}}^{\rangle}\right)^{-1} = \left(B_{\vec{\eta}}^{\langle}B_{\vec{\eta}}^{\rangle}+\mathbf{u}\otimes\mathbf{v}\right)^{-1} \\ &= (B_{\vec{\eta}}^{\langle}B_{\vec{\eta}}^{\rangle})^{-1} - \frac{(B_{\vec{\eta}}^{\langle}B_{\vec{\eta}}^{\rangle})^{-1}\mathbf{u}\otimes\mathbf{v}(B_{\vec{\eta}}^{\langle}B_{\vec{\eta}}^{\rangle})^{-1}}{1+\vec{\eta}^{(x_1',y_1')}[1-G_{\vec{\eta}}(\tau)]_{y_1',x_1'}} \end{aligned} \tag{2.59}$$

with $\mathbf{u}_x = [B_{\vec{\eta}}^{\langle}]_{x,x_1'}\vec{\eta}^{(x_1',y_1')}$ and $\mathbf{v}_x = [B_{\vec{\eta}}^{\rangle}]_{y_1',x}$. Note that we have used the Sherman-Morrison formula [Press 1992] from the second to the third equality. Here x runs over $1,...,N_p$ where N_p corresponds to the number of particles contained in the trial wave function. As shown in Eq. 2.54, the Green's function at imaginary time τ reads: $G_{\vec{\eta}}(\tau) = 1 - B_{\vec{\eta}}^{\rangle}(B_{\vec{\eta}}^{\langle}B_{\vec{\eta}}^{\rangle})^{-1}B_{\vec{\eta}}^{\langle}$, such that one can obtain the Green's function with the updated auxiliary field $\vec{\eta}'$

$$\begin{aligned} [G_{\vec{\eta}'}(\tau)]_{x,y} &= \left[1-(1+\Delta)B_{\vec{\eta}}^{\rangle}(B_{\vec{\eta}}^{\langle}(1+\Delta)B_{\vec{\eta}}^{\rangle})^{-1}B_{\vec{\eta}}^{\langle}\right]_{x,y} \\ &= [G_{\vec{\eta}}(\tau)]_{x,y} - \frac{[G_{\vec{\eta}}(\tau)]_{x,x_1'}\vec{\eta}^{x_1',y_1'}[1-G_{\vec{\eta}}(\tau)]_{y_1',y}}{1+\vec{\eta}^{x_1',y_1'}[1-G_{\vec{\eta}}(\tau)]_{y_1',x_1'}}, \end{aligned} \tag{2.60}$$

where again the Sherman-Morrison formula has been applied in the intermediate steps.

To calcualte the Green's function to an arbitrary, time displaced imaginary time $\tau > 0$, one will naively perform

$$G_{\vec{\eta}}\left(\Theta+\frac{\tau}{2},\Theta-\frac{\tau}{2}\right)_{x,y} = \left[B_{\vec{\eta}}(\Theta+\frac{\tau}{2},\Theta-\frac{\tau}{2})G_{\vec{\eta}}(\Theta-\frac{\tau}{2})\right]_{x,y}, \tag{2.61}$$

and

$$G_{\vec{\eta}}\left(\Theta-\frac{\tau}{2},\Theta+\frac{\tau}{2}\right)_{x,y} = -\left[(1-G_{\vec{\eta}}(\Theta-\frac{\tau}{2}))B_{\vec{\eta}}^{-1}(\Theta+\frac{\tau}{2},\Theta-\frac{\tau}{2})\right]_{x,y}. \tag{2.62}$$

But such calculations are not stable since the algorithm demands repeated matrix-matrix multiplications. As we have discussed in last section, due to the limited machine precision, the multiplication of matrix exponentials will mix the scales, and the roundoff error will be blown up exponentially. That is the reason why we

have to introduce the stabilization scheme in last section. A efficient implementation to overcome this problem rests on the observation that in the PQMC the Green's function is a projector [Feldbacher 2001],

$$\begin{aligned} G_{\vec{\eta}}(\tau)^2 &= G_{\vec{\eta}}(\tau), \\ (1-G_{\vec{\eta}}(\tau))^2 &= (1-G_{\vec{\eta}}(\tau)). \end{aligned} \tag{2.63}$$

This implies that propagators can be separated into several parts, as $\tau_1 > \tau_2 > \tau_3$,

$$\begin{aligned} G_{\vec{\eta}}(\tau_1,\tau_3) &= B_{\vec{\eta}}(\tau_1,\tau_3)G^2_{\vec{\eta}}(\tau_3) = G_{\vec{\eta}}(\tau_1,\tau_3)G_{\vec{\eta}}(\tau_3) \\ &= \underbrace{G_{\vec{\eta}}(\tau_1,\tau_3)B^{-1}_{\vec{\eta}}(\tau_2,\tau_3)}_{G_{\vec{\eta}}(\tau_1,\tau_2)} \underbrace{B_{\vec{\eta}}(\tau_2,\tau_3)G_{\vec{\eta}}(\tau_3)}_{G_{\vec{\eta}}(\tau_2,\tau_3)}. \end{aligned} \tag{2.64}$$

Using this property we can break up a large imaginary time propagation into a set of smaller intervals of length $\tau = N_\tau \Delta\tau$,

$$G_\tau(\Theta+\frac{\tau}{2},\Theta-\frac{\tau}{2}) = \prod_{n=0}^{N_\tau-1} G_{\vec{\eta}}\big(\Theta-\frac{\tau}{2}+[n+1]\Delta\tau,\Theta-\frac{\tau}{2}+n\Delta\tau\big), \tag{2.65}$$

In this way, we can obtain reliable imaginary time Green's function $G_\tau(\Theta+\frac{\tau}{2},\Theta-\frac{\tau}{2})$ even if the time displacement τ is large. Of course, while doing the imaginary time propagation in the above manner, we still keep the stabilization scheme at every 10th time slice (after every 10 $\Delta\tau$), and compare the imagniary time Green's function from the efficient propagation with that from scratch using $B(\tau,0)\mathbf{P}(\mathbf{P}^\dagger B(2\Theta,0)\mathbf{P})\mathbf{P}^\dagger B(2\Theta,\tau) = U^\rangle(U^\langle U^\rangle)^{-1}U^\langle$, at every 10 time slice. If the maximum difference between matrix elements is at the magnitude of the machine accuracy, and very small compare with the statistical uncertainty ($\sim(\Delta\tau)^2$) of the Monte Carlo simulations, we will keep using the efficient propagation scheme by multipling the Green's functions themselves, but if the maximum difference is larger than the statistical uncertainty, we will then reduce the time slice $\Delta\tau$, and restart the time propagation until we find a correct $\Delta\tau$ that will not induce the numerical instabilities and use that $\Delta\tau$ to continue the simulation.

2.2.5 Wick Theorem and Observables

Since we now have access to the single particle Green's function from PQMC simulations, we can apply the Wick's theorem [Mahan 1990] to each HS auxiliary-field configuration and obtain any arbitrary observables and correlation functions. Following the construction of the cumulants

$$\begin{aligned} \langle\langle O_n O_{n-1}\cdots O_1\rangle\rangle_{\vec{\eta}} &= \frac{\partial^n}{\partial\gamma_n\partial\gamma_{n-1}\cdots\partial\gamma_1} \\ &\ln\langle\Psi_T|U_{\vec{\eta}}(2\Theta,\Theta)e^{\gamma_n O_n}e^{\gamma_{n-1}O_{n-1}}\cdots e^{\gamma_1 O_1} \\ &U_{\vec{\eta}}(\Theta,0)|\Psi_T\rangle|_{\gamma_n,\gamma_{n-1},\cdots,\gamma_1=0}, \end{aligned} \tag{2.66}$$

with $O_i = \mathbf{c}^\dagger \mathbf{A}^{(\mathbf{i})} \mathbf{c}$, one can differentiate the above in different order to obtain

$$\begin{aligned}
\langle\langle O_1\rangle\rangle_{\vec{\eta}} &= \langle O_1\rangle_{\vec{\eta}} \\
\langle\langle O_2 O_1\rangle\rangle_{\vec{\eta}} &= \langle O_2 O_1\rangle_{\vec{\eta}} - \langle O_2\rangle_{\vec{\eta}}\langle O_1\rangle_{\vec{\eta}} \\
\langle\langle\langle O_3 O_2 O_1\rangle\rangle\rangle_{\vec{\eta}} &= \langle O_3 O_2 O_1\rangle_{\vec{\eta}} \\
&\quad -\langle O_3\rangle_{\vec{\eta}}\langle\langle O_2 O_1\rangle\rangle_{\vec{\eta}} - \langle O_2\rangle_{\vec{\eta}}\langle\langle O_3 O_1\rangle\rangle_{\vec{\eta}} \\
&\quad -\langle O_1\rangle_{\vec{\eta}}\langle\langle O_3 O_2\rangle\rangle_{\vec{\eta}} - \langle O_1\rangle_{\vec{\eta}}\langle O_2\rangle_{\vec{\eta}}\langle O_3\rangle_{\vec{\eta}} \\
\cdots &= \cdots
\end{aligned} \tag{2.67}$$

This leads to the following rule, which can be proven by induction, that we use to implement arbitrary correlation functions in the PQMC simulation,

$$\begin{aligned}
\langle O_n O_{n-1}\cdots O_1\rangle_{\vec{\eta}} = \langle\langle O_n O_{n-1}\cdots O_1\rangle\rangle_{\vec{\eta}} &+ \sum_{j=1}^{n}\langle\langle O_n\cdots\hat{O}_j\cdots O_1\rangle\rangle_{\vec{\eta}}\langle\langle O_j\rangle\rangle_{\vec{\eta}} \\
&+ \sum_{j>i}\langle\langle O_n\cdots\hat{O}_j\cdots\hat{O}_i\cdots O_1\rangle\rangle_{\vec{\eta}}\langle\langle O_j O_i\rangle\rangle_{\vec{\eta}} \\
&\cdots + \langle O_n\rangle_{\vec{\eta}}\langle O_{n-1}\rangle_{\vec{\eta}}\cdots\langle O_1\rangle_{\vec{\eta}}.
\end{aligned} \tag{2.68}$$

where $\hat{O}_j$ denotes the operator O_j has been omitted from the product. The cumulants can now be calculated order by order such that any multi-point correlation function will be decomposed into sum of multiproducts of the 2 point Green's function $\langle c_x c_y^\dagger\rangle$ or $\langle c_x^\dagger c_y\rangle$.

As an example, here we demonstrate the above decomposition scheme for a 6-point correlation function

$$\begin{aligned}
\langle c_{x_3}^\dagger c_{y_3} c_{x_2}^\dagger c_{y_2} c_{x_1}^\dagger c_{y_1}\rangle_{\vec{\eta}} &= \langle c_{x_3}^\dagger c_{y_3}\rangle_{\vec{\eta}}\langle c_{x_2}^\dagger c_{y_2} c_{x_1}^\dagger c_{y_1}\rangle_{\vec{\eta}} \\
&\quad +\langle c_{x_3}^\dagger c_{y_2}\rangle_{\vec{\eta}}\langle c_{y_3} c_{x_2}^\dagger c_{x_1}^\dagger c_{y_1}\rangle_{\vec{\eta}} \\
&\quad +\langle c_{x_3}^\dagger c_{y_1}\rangle_{\vec{\eta}}\langle c_{y_3} c_{x_2}^\dagger c_{y_2} c_{x_1}^\dagger\rangle_{\vec{\eta}} \\
&= \langle c_{x_3}^\dagger c_{y_3}\rangle_{\vec{\eta}}\big(\langle c_{x_2}^\dagger c_{y_2}\rangle_{\vec{\eta}}\langle c_{x_1}^\dagger c_{y_1}\rangle_{\vec{\eta}} + \langle c_{x_2}^\dagger c_{y_1}\rangle_{\vec{\eta}}\langle c_{y_2} c_{x_1}^\dagger\rangle_{\vec{\eta}}\big) \\
&\quad +\langle c_{x_3}^\dagger c_{y_2}\rangle_{\vec{\eta}}\big(\langle c_{y_3} c_{x_2}^\dagger\rangle_{\vec{\eta}}\langle c_{x_1}^\dagger c_{y_1}\rangle_{\vec{\eta}} - \langle c_{y_3} c_{x_1}^\dagger\rangle_{\vec{\eta}}\langle c_{x_2}^\dagger c_{y_1}\rangle_{\vec{\eta}}\big) \\
&\quad +\langle c_{x_3}^\dagger c_{y_1}\rangle_{\vec{\eta}}\big(\langle c_{y_3} c_{x_2}^\dagger\rangle_{\vec{\eta}}\langle c_{y_2} c_{x_1}^\dagger\rangle_{\vec{\eta}} + \langle c_{y_3} c_{x_1}^\dagger\rangle_{\vec{\eta}}\langle c_{x_2}^\dagger c_{y_2}\rangle_{\vec{\eta}}\big) \\
&\quad .
\end{aligned} \tag{2.69}$$

To derive the spin-spin correlation and density-density correlation, we have to reintroduce the site index $x = (i, \sigma)$. The equal time spin-spin correlation will be

$$\begin{aligned}
\langle S_i^z S_j^z\rangle &= \frac{1}{4}\langle(n_{i,\uparrow} - n_{i,\downarrow})(n_{j,\uparrow} - n_{j,\downarrow})\rangle \\
&= \frac{1}{4}\big(\langle c_{i,\uparrow}^\dagger c_{i,\uparrow} c_{j,\uparrow}^\dagger c_{j,\uparrow}\rangle - \langle c_{i,\uparrow}^\dagger c_{i,\uparrow} c_{j,\downarrow}^\dagger c_{j,\downarrow}\rangle - \langle c_{i,\downarrow}^\dagger c_{i,\downarrow} c_{j,\uparrow}^\dagger c_{j,\uparrow}\rangle + \langle c_{i,\downarrow}^\dagger c_{i,\downarrow} c_{j,\downarrow}^\dagger c_{j,\downarrow}\rangle\big) \\
&= \frac{1}{4}\big(\langle c_{i,\uparrow}^\dagger c_{i,\uparrow}\rangle\langle c_{j,\uparrow}^\dagger c_{j,\uparrow}\rangle + \langle c_{i,\uparrow}^\dagger c_{j,\uparrow}\rangle\langle c_{i,\uparrow} c_{j,\uparrow}^\dagger\rangle \\
&\quad -\langle c_{i,\uparrow}^\dagger c_{i,\uparrow}\rangle\langle c_{j,\downarrow}^\dagger c_{j,\downarrow}\rangle - \langle c_{i,\downarrow}^\dagger c_{i,\downarrow}\rangle\langle c_{j,\uparrow}^\dagger c_{j,\uparrow}\rangle \\
&\quad +\langle c_{i,\downarrow}^\dagger c_{i,\downarrow}\rangle\langle c_{j,\downarrow}^\dagger c_{j,\downarrow}\rangle + \langle c_{i,\downarrow}^\dagger c_{j,\downarrow}\rangle\langle c_{i,\downarrow} c_{j,\downarrow}^\dagger\rangle\big).
\end{aligned} \tag{2.70}$$

Between the second and third equality we have used to fact $\langle c^\dagger_{i,\uparrow} c_{j,\downarrow}\rangle = \langle c_{i,\uparrow} c^\dagger_{j,\downarrow}\rangle = \langle c^\dagger_{i,\downarrow} c_{j,\uparrow}\rangle = \langle c_{i,\downarrow} c^\dagger_{j,\uparrow}\rangle = 0$ since they do not conserve the total spin of the state. Similarly the density-density correlation

$$\begin{aligned}\langle n_i n_j\rangle &= \sum_{\alpha,\beta=\uparrow,\downarrow} \langle c^\dagger_{i,\alpha} c_{i,\alpha} c^\dagger_{j,\beta} c_{j,\beta}\rangle \\ &= \sum_{\alpha,\beta=\uparrow,\downarrow} \big(\langle c^\dagger_{i,\alpha} c_{i,\alpha}\rangle\langle c^\dagger_{j,\beta} c_{j,\beta}\rangle - \langle c^\dagger_{i,\alpha} c_{j,\beta}\rangle\langle c^\dagger_{j,\beta} c_{i,\alpha}\rangle\big). \end{aligned} \tag{2.71}$$

Here we use $n_i = n_{i,\uparrow} + n_{i,\downarrow}$.

2.3 Data Analysis and Scalability

To achieve a controlled estimation of the variance of any observables out of the QMC data series, we group the QMC measurements into bins. For instance, we put every k consecutive QMC measurements into one bin. If for any observable we have in total N QMC measurements, the number of bins is $N_B = N/k$. To compute the variance, we apply the Jackknife method [Shao 1996] to the data series that contains N_B elements. The overall average is $\overline{O} = \frac{1}{N}\sum_{i=1}^{N} O_i$, the bin average of the $n-th$ of the N_B bin is $O_{B,n} = \frac{1}{k}\sum_{i=1}^{k} O_{(n-1)k+i}$. The Jackknife-averages $O_{J,n}$ are generated with all the bin average included except the n-th bin average $O_{B,n}$

$$O_{J,n} = \frac{N\overline{O} - k\, O_{B,n}}{N-k} \qquad n = 1,\ldots,N_B\ . \tag{2.72}$$

The overall Jackknife-average is $\overline{O}_J = (1/N_B)\sum_{n=1}^{N_B} O_{J,n}$. The N_B Jackknife blocks contain $N-k$ data. They are very correlated since each of them originates from nearly the same $N_B - 1$ bins. Due to such correlations the variance has to be corrected by multiplying with a factor $(N_B-1)^2$, this leads us to the final estimation of the QMC variance for observable O

$$\sigma^2_O = \frac{N_B - 1}{N_B}\sum_{n=1}^{N_B}\left(O_{J,n} - \overline{O}_J\right)^2. \tag{2.73}$$

Based on the finite system QMC data, we usually like to extrapolate the behavior of the system to the thermodynamic limit (hereafter referred to as TDL). Especially in Chapter 4 of this thesis, we will have to extrapolate many observables like magnetic structure factors S_{AF}, single-particle gap Δ_{sp} and spin gap Δ_s, etc, to obtain a controlled TDL estimation. To estimate the errorbar of the extrapolated data, we have implemented the Bootstrap method [Press 1992, Shao 1996]. The idea is to generate data points randomly within the errorbar of each finite size data point, and perform finite size scaling with such a data set, if the number of the data set is large enough, according to the central limit theorem, we will obtain a Gaussian distribution of the extrapolated expectation values in the TDL. The variance of

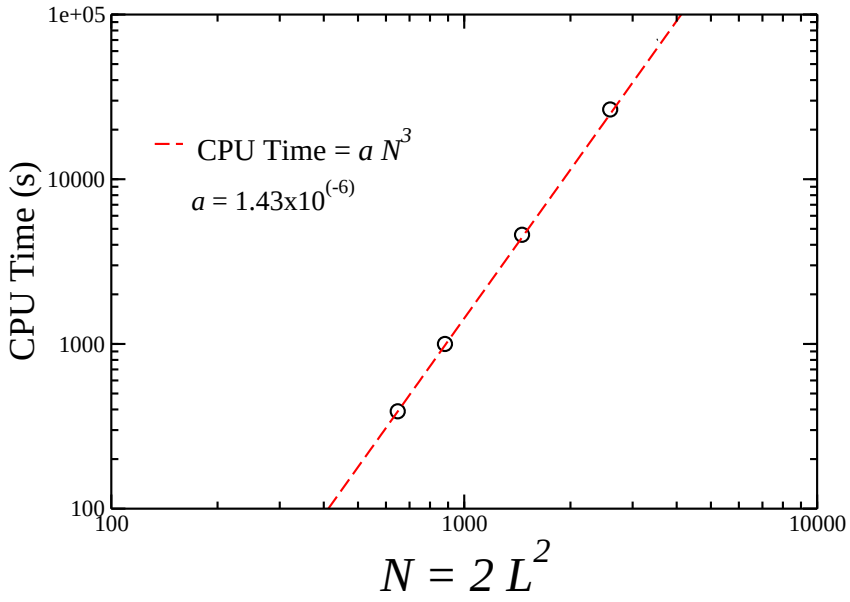

Figure 2.6: The computation effort of the PQMC grows as a power law of the system size. We choose the Hubbard model on the honeycomb lattice as testing example with the number of sites $N = 2L^2$ where L is the linear system size. On one computer core, the computational effort grows as N^3, in a log-log plot, it is a linear line.

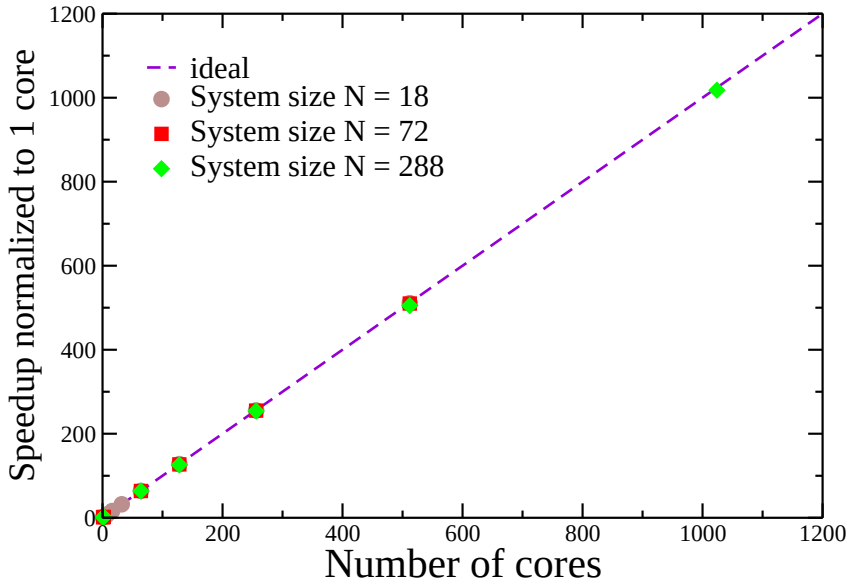

Figure 2.7: The speedup factor of the PQMC code as a function of cpu cores. Upon finishing the same number of simulations, for example, the fixed number of total measurements, the code speeds up linearly with the cpu cores.

such a distribution thus give us an estimate of the errorbar of the TDL expectation values.

The PQMC code used in this thesis is from the group of Prof. Fakher Assaad in Universität Würzburg, it has been developed mainly by Prof. Assaad over the years [Assaad 1993a, Assaad 1996, Feldbacher 2001, Assaad 2005, Assaad 2008]. Furthermore, we have also tested the scaling behavior of the PQMC code on the CRAY XE6 cluster in HLRS, Stuttgart, to obtain information about the scalability of the parallization of our code on supercomputers. Firstly we used one cpu core to test the computation effort of the PQMC code for different system sizes. We confirm that the effort indeed scales with system size as N^3, where N is the number of sites in the systema, as shown in Fig. 2.6. Note that in the case of SSE QMC, the time scales linearly with the system size, N, hence it is in general easier to obtain larger system sizes in the bosonic (or spin system) QMC simulations than the QMC for fermions.

Next, we increase the number of cpu cores in our simulation and measure the speedup factor upon finishing the same amount of tasks with more and more cpu cores. We found the speedup of the code is very linear, Fig. 2.7, as expected for a QMC simulation since each cpu core is performing its own QMC steps, and hence we have almost ideal scalability of our PQMC code.

Chapter 3

Shastry-Sutherland Quantum Antiferromagnet

3.1 $SrCu_2(BO_3)_2$ and Shastry-Sutherland Model

Quantum magnets exhibit a wealth of interesting phenomena, in particular on low-dimensional frustrated lattices, where both enhanced quantum fluctuations and geometric frustration can compete with or even destroy semi-classical magnetic order. Many compounds provide realizations of such paradigm. Recent examples include the valence bond solids state in $(C_2H_5)(CH_3)_3P[Pd(dmit)_2]_2$ [Tamura 2006] and $Zn_xCu_{4-x}(OD)_6Cl_2$ [Lee 2007]. Another material, that has been intensively studied is $SrCu_2(BO_3)_2$ [Kageyama 1999]. The crystal structure of $SrCu_2(BO_3)_2$ is tetragonal and is characterized by a layered structure of $CuBO_3$ and Sr planes. A sketch of a $CuBO_3$ layer is shown in Fig. 3.1 **(a)**. The effective linkage of the Cu^{2+} ions is illustrated in Fig. 3.1 **(b)**. The network of Cu^{2+} ions forms a 2D frustrated lattice which is topologically equivalent to an exact solvable model considered by Shastry and Sutherland three decades ago [Shastry 1981]. They proved the spin-1/2 antiferromagnetic Heisenberg model on the Shastry-Sutherland lattice has a dimer singlet ground state. In $SrCu_2(BO_3)_2$, a pair of nearest neighbor Cu^{2+} ions is connected via a O^{2-} ions of the BO_3 molecule and they indeed form a dimer singlet. A unit cell in the $CuBO_3$ plane contains two dimers which are mutually orthogonal, as shown in Fig. 3.1 **(a)**. Analysis of the experimental data shows that a dimer singlet ground state is realized in $SrCu_2(BO_3)_2$.

Fig. 3.2 **(a)** shows the temperature dependence of the magnetic susceptibility of $SrCu_2(BO_3)_2$. The susceptibility has a maximum around 20 K and then drops rapidly towards zero with decreasing temperature. By fitting the magnetic susceptibility with $\chi \propto \exp(-\Delta_s/T)$, the spin gap is obtained as $\Delta_s \sim 35K$ [Miyahara 2003b].

Early magnetization measurements in high fields revealed magnetization plateaus at 1/8, 1/4 and 1/3 of the saturated magnetization [Kageyama 1999, Onizuka 2000], refined measurements have suggested more plateaus at values of 1/9, 1/7, 1/6, 1/5, 2/9 and 1/2 of the saturated magnetization [Sebastian 2008], as shown in Fig. 3.2 **(b)**. The magnetic plateaus exhibit a crystalization of the itinerant triplet excitations. Due to the frustrated (orthogonal dimer) geometry of the Shastry-Sutherland lattice, hopping of the triplets is only possible through closed paths of dimer bonds, thus only from higher order in perturbation [Miyahara 1999]. Momoi and Totsuka [Momoi 2000a, Momoi 2000b] explained the appearence of plateau

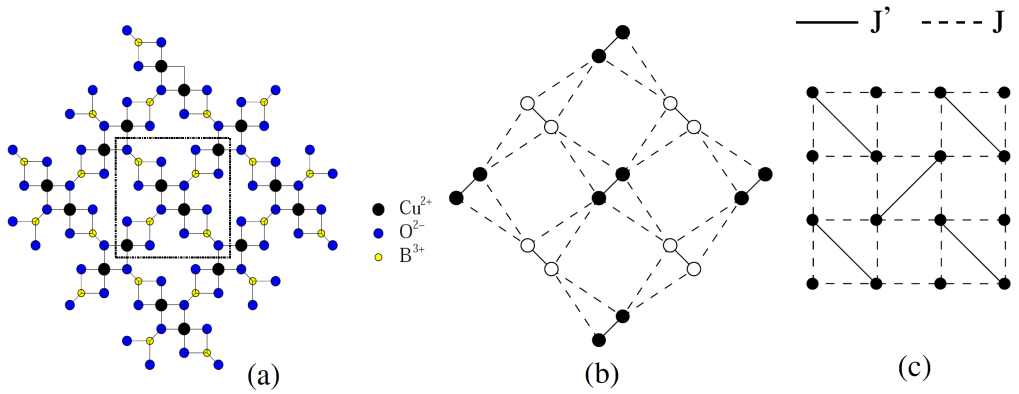

Figure 3.1: **(a)** Schematic view of the crystal structure of a $CuBO_3$ layer. The box contains a unit cell. **(b)** Two-dimensional orthogonal dimer model, which is equivalent to **(c)** the Shastry-Sutherland model with spin-1/2 degree of freedom on the square lattice vertices, and intradimer coupling J' (solid lines) and interdimer coupling J (dashed lines).

states through a scenario of metal to Mott-insulator transition where triplet excitations were treated as bosons interacting via various replusive interactions arising from higher order perturbations in the interdimer coupling J. They have also suggested supersolid phases at moderate fillings between plateaus. Under dominant repulsive interaction, the triplet excitations localize and crystallize in commensurate patterns developing plateau state [Misguich 2001, Isaev 2009]. In fact, NMR spectroscopy have directly demonstrated a superlattice sturcture at $m/m_{\text{sat}} = 1/8$ plateau [Kodama 2002, Takigawa 2008]. Recent theoretical work with nonperturbative Contractor-Renormalization [Abendschein 2008] have found magnetization pleteaus at 1/9, 1/6, and 2/9 of saturation, and an analysis using perturbative continuous unitary transformation [Dorier 2008] predicted, in addition to these, one more plateau at 2/15. It has also been shown in inelastic neutron scattering [Cépas 2001] and electron spin resonance [Nojiri 2003] measurements that $SrCu_2(BO_3)_2$ exhibits anisotropic behavior in spin space, hence the effects of inter and intra-dimer Dzyaloshinskii-Moriya interactions are needed to be considered in explaining the magnetization process of the the material [Romhányi 2011].

Another realization of the Shastry-Sutherland lattice is the rare earth tetraborid TmB_4 [Gabani 2007, Siemensmeyer 2008] which has recently been studied in finite magnetic fields. In contrast to $SrCu_2(BO_3)_2$, this metallic compound exhibits stable long-range antiferromagnetic order in zero field below about 9.8 K. Since full saturation can be obtained for magnetic fields parallel to the c-axis above 5T, TmB_4 allows for a complete scan of its magnetization process. For this compound magnetization plateaus have been observed e.g. at fractions 1/2, 1/7, 1/8 and 1/9 of magnetic saturation. Despite the metallic nature of TmB_4, its magnetism has been suggested to realize an easy-axis anisotropic version of the Shastry-

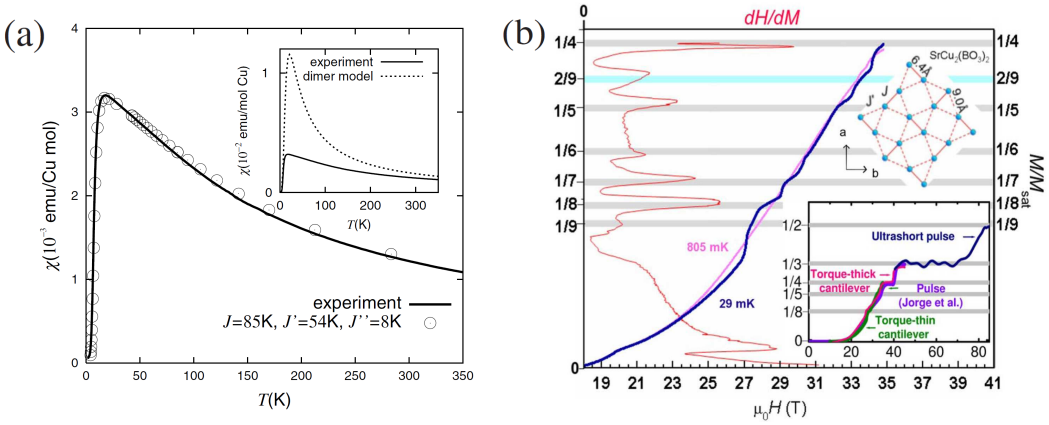

Figure 3.2: **(a)** The temperature dependence of the magnetic susceptibility of $SrCu_2(BO_3)_2$ (solid curve). Circles are the result of numerical calculation with the indicated parameter set. The inset is the result of fitting to an isolated dimer model. **(b)** Magnetization process of $SrCu_2(BO_3)_2$ for $H \parallel c$. Extracted from torque measured by using a 10-μm cantilever in static magnetic fields up to 35 T at representative temperatures. Plateaus are indicated by peaks in the inverse susceptibility dH/dM (red). (Upper inset) Couplings of Cu^{2+} ions within an $CuBO_2$ layer. (Lower inset) Magnetization data obtained by using a 10-μm cantilever up to 35 T (green), a 50-μm cantilever up to 45 T (pink), ultrashort pulsed-field magnetization from 38 T to 85 T (blue), all overlay well. Panel **(a)** is taken from [Miyahara 2003b], Panel **(b)** is adapted from [Sebastian 2008].

Sutherland model close to the Ising limit with similar intra- and inter-dimer coupling strengths [Siemensmeyer 2008].

In light of the rapid experimental progress in frustrated quantum magnets, it is important to explore in detail the interplay between geometric frustration and quantum fluctuations in such systems based on effective spin models. In many aspects, numerical techniques have become especially important as an unbiased approach to quantum magnetism. However, numerical studies of even simple models of frustrated spin systems suffer from severe restrictions on the finite sizes accessible to current simulation techniques. In particular, quantum Monte Carlo (QMC) simulations are hampered by the sign problem due to odd-length spin-exchange paths appearing on non-bipartite lattices [Troyer 2005], as we have discussed in Chapter 2.1. In this chapter, we employ a different approach. We studied a model of quantum magnetism in a parameter regime, where geometric frustration is restricted to the classical sector, hence does not lead to QMC sign problems. Using the SSE QMC method described in Chapter 2.1, we explored the ground state properties as well as the magnetization process of the spin-1/2 XXZ model on the Shastry-Sutherland

lattice with the Hamiltonian

$$\begin{aligned} H &= J\sum_{\langle i,j\rangle}\left[-\Delta(S_i^xS_j^x+S_i^yS_j^y)+S_i^zS_j^z\right] \\ &\quad +J'\sum_{\langle\langle i,j\rangle\rangle}\left[-\Delta(S_i^xS_j^x+S_i^yS_j^y)+S_i^zS_j^z\right]-h\sum_i S_i^z, \end{aligned} \tag{3.1}$$

the model is different from the original spin-1/2 antiferromagnetic (AF) Heisenberg model (Ref. [Shastry 1981]) in that the transverse exchange is ferromagnetic ($\Delta > 0$). Here, the first sum extends over all nearest neighbor bonds. The second sum runs over a staggered subset of the next-nearest neighbor bonds, as indicated in Fig. 3.1 **(c)**. h is the external magnetic field. The QMC results are obtained from finite size systems with lattice sites up to $N = 36 \times 36$, using period boundary conditions. In the simulations, we scaled the inverse temperature as $\beta = 1/T = 8L/\Delta J$ in order to access ground state properties, where L denotes the linear system size.

The model in Eq. 3.1 maintains the frustrated nature of the Shastry-Sutherland lattice in the antiferromagnetic Ising interactions. Appling the mapping between spin-1/2 degrees of freedom and hard-core bosons, the model can be mapped onto an extended bosonic Hubbard model of hard-core bosons hopping along the bonds of the Shastry-Sutherland lattice and experiencing repulsive interactions proportional to the strength of the Ising exchange,

$$\begin{aligned} H &= -t\sum_{\langle i,j\rangle}\left[b_i^\dagger b_j+b_ib_j^\dagger\right]+V_1\sum_{\langle i,j\rangle}n_in_j \\ &\quad -t'\sum_{\langle\langle i,j\rangle\rangle}\left[b_i^\dagger b_j+b_ib_j^\dagger\right]+V_2\sum_{\langle\langle i,j\rangle\rangle}n_in_j-\mu\sum_i n_i \end{aligned} \tag{3.2}$$

where $t = \frac{J\Delta}{2}$, $V_1 = J$, $t' = \frac{J'\Delta}{2}$, $V_2 = J'$, and $\mu = 2J + \frac{1}{2}J' + h$. Recently, similar hard-core boson models have been studied on different lattice geometries, and were found to exhibit interesting order-by-disorder phenomena when quantum fluctuations lift an extensive ground state degeneracy from the Ising limit $\Delta = 0$. Examples include a supersolid phase on the triangular lattice [Wessel 2005, Melko 2005, Heidarian 2005, Bonnes 2011], valence-bond-solids [Isakov 2006b, Damle 2006] and a Z_2 spin liquid [Balents 2002a, Sheng 2005, Isakov 2006a] on the Kagome lattice (will be discussed in more detail in chapter 4.1). In the limit of dominating kinetic terms, such models stabilize a superfluid phase, which in magnetic language corresponds to a transverse ferromagnetic spin alignment, driven by the ferromagnetic nature of the transverse spin exchange.

The content of this chapter has been published in Ref. [Meng 2008], and a detailed description of the ground state phase diagram can be found in Ref. [Meng 2007]. In the following section we will quickly flash through the ground state phase diagram of the model, as shown in Fig. 3.3. More attention will be paid to the quantum phase transitions between different phases, the magnetization process, the magnetization plateaus and their superstructures. Throughout this

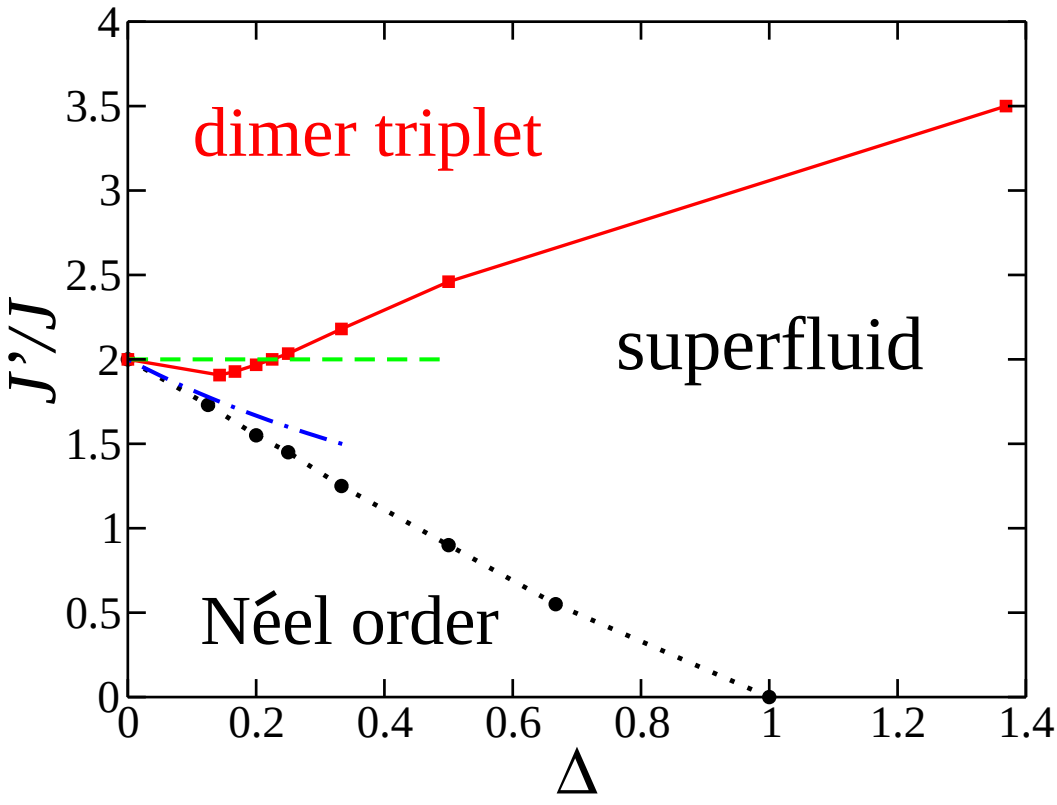

Figure 3.3: Ground state phase diagram of the spin-1/2 XXZ model on the Shastry-Sutherland lattice with ferromagnetic transverse spin exchange. The dotted (solid) line denotes a first-order (continuous) quantum phase transition. Uncertainties on the indicated phase boundaries are below the symbol size. The dashed line is a guide to the eye indicating a line of constant $J'/J = 2$. The dashed-dotted line gives the estimated phase boundary of the dimer triplet phase within perturbation theory around the point $(J'/J, \Delta) = (2, 0)$, discussed in Sec. 2.2.3.

chapter, we prefer using the spin language to describe the results, but occasionally find it convenient to also employ the bosonic notation.

3.2 Phase Diagram

3.2.1 Ising Limit

The Ising limit, $\Delta = 0$, of the phase diagram Fig. 3.3 provides a textbook example of the macroscopic ground state degeneracy induced by the geometric frustration of the lattice. As discussed by Shastry and Sutherland [Shastry 1981], at $\Delta = 0$, the model stabilizes an antiferromagnetic Néel phase for sufficiently weak J', up to $J'/J < 2$. The ground state has an intensive entropy $S = k_B \ln(2)$. For $J' > 2J$ the classical system has a macroscopically degenerate ground state manifold

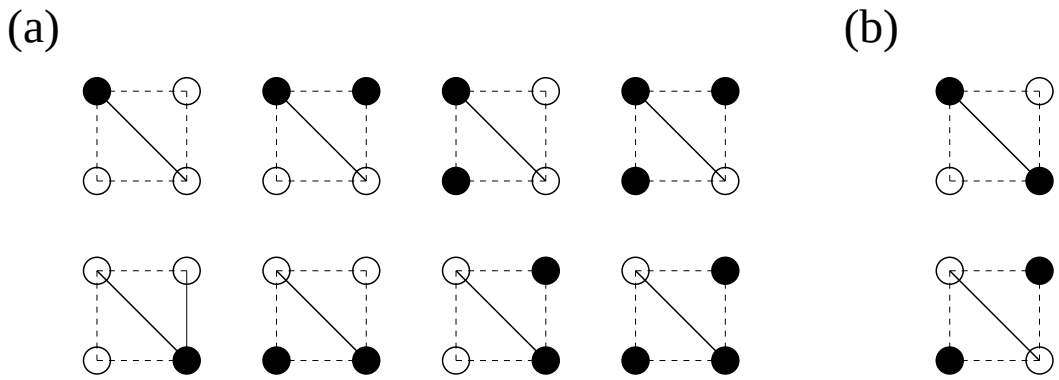

Figure 3.4: **(a)** Possible spin configurations in the Ising limit on a non-void plaquette for $J' > 2J$. **(b)** Additional configurations allowed on a non-void plaquette at $J' = 2J$. Full (open) circles denote spin up (down) states.

with an extensive ground state entropy $S = [\ln(2)/2]k_B N = 0.347 k_B N$. It can be understood as follows: consider one of the filled plaquettes on the lattice, the eight configurations shown in Fig. 3.4 **(a)** all provide the same lowest energy contribution of this plaquette to the total system, out of the $2^4 = 16$ possible configurations in the plaquette, these 8 are thus feasible, so the ground state entropy is $S = k_B \ln[2^N (\frac{8}{16})^{N/2}] = k_B \ln(2^{N/2}) = 0.347 k_B N$.

Exactly at $J' = 2J$, the degeneracy of the ground state manifold is enlarged further, as additional low-energy configurations emerge. Following the same arguement above, at $J' = 2J$, not only the eight configuration in Fig. 3.4 **(a)** provide mininal energy, the two configurations shown in Fig. 3.4 **(b)** also lead to a minimal energy contribution. Hence the ground state entropy can be estimated as $S \approx k_B \ln[2^N (\frac{10}{16})^{N/2}] = 0.458\ k_B N$. In fact, there are even more configurations allowed in the ground state at $J' = 2J$, Shastry and Sutherland proved a lower bound $S \geq 0.4812\ k_B N$ on the ground state entropy at $J' = 2J$, via mapping the model onto a 10-vertex model and using brading techniques [Shastry 1981].

The extensive ground state degeneracy is considered to be a key characteristic of frustration. Besides the Shastry-Sutherland Ising antiferromagnet, the triangular Ising antiferromagnet also has a extensive ground-state entropy $0.323 k_B N$ [Wannier 1950]. The 2D Shastry-Sutherland lattice (or triangular lattice) of Ising spins provide the prototypes of frustration. One can imagine at low temperatures, the spins continue to fluctuate within the macroscopic ground state manifold, there is no magnetic long range order developed.

Besides the Ising limit, Shastry and Sutherland considered the effects of antiferromagnetic transverse spin exchange ($\Delta < 0$ in our notation), and proved that the system possesses an exact dimer-singlet product eigenstate, $|\psi\rangle_D = \bigotimes_D \frac{1}{\sqrt{2}}(|\uparrow\downarrow\rangle - |\downarrow\uparrow\rangle)_D$, where the product extends over all J' dimer bond on the lattice. Remarkabley, for $J' > 2J$, $|\psi\rangle_D$ becomes the system's ground state [Shastry 1981],

and it is also generally accepted $|\psi\rangle_D$ captures the main feature of $SrCu_2(BO_3)_2$ in normal condition. Later studies by various groups considered the full quantum phase diagram of this model, which is not conclusively established till now (c.f. Ref. [Miyahara 2003b] for a review of the various theoretical and numerical proposals), even though numerical evidence has been put forward, that the $SU(2)$ symmetric model ($\Delta = -1$) features indeed three phases: (i) a low-J' antiferromagnetically ordered Néel phase, (ii) the large-J' dimer singlet phase, and (iii) an intermediate valence bond crystal (VBC) phase, which breaks the lattice symmetry by forming resonating plaquette singlet states on one of the subsets of the void plaquettes of the lattice [Läuchli 2002]. In our work, however, we study the quantum model in the region $\Delta > 0$, where large-scale QMC simulations are possible. Furthermore, our finding relates directly to a model of hard-core bosons, as shown in Eq. 3.2.

3.2.2 Quantum Phase Transitions

We find that upon increasing the ferromagnetic spin exchange Δ from 0 up to the Heisenberg point at $(\Delta, J'/J) = (1, 0)$, the extend of the Néel phase shrinks linearly[1]. In hard-core boson language, the Néel phase corresponds to a checkerboard solid with alternating occupation of the lattice sites. In our QMC simulations, we determine the corresponding structure factor S_{AF} for antiferromagnetic order, $S_{AF} = \frac{1}{N}\sum_{i,j} \varepsilon_i \varepsilon_j \langle S_i^z S_j^z \rangle$, as introduced in Chap. 2.1.4. If in the thermodynamic limit S_{AF}/N scales to a finite value, the Néel order is present. For dominant transverse exchange, $\Delta \gg 1$, the model reduces to an ferromagnetic XY model on the Shastry-Sutherland lattice, which in bosonic language relates to an non-frustrated tight-binding hopping model. Hence, the system is expected to exhibit a superfluid phase for large values of $\Delta > 0$, which in spin language relates to a ferromagnetic ordering within the XY plane. Such a phase is characterized by a finite value of the superfluid density, or spin stiffness, which in the SSE QMC simulations can be obtained from measuring the spin winding number fluctuation [Pollock 1987] $\langle W^2 \rangle$ as $\rho_S = \frac{T}{\Delta J}\langle W^2 \rangle$.

As an example, we show in Fig. 3.5 the behavior of ρ_S for different system sizes as a function of J'/J for fixed $\Delta = 1/2$. A region with finite spin stiffness is found for $0.9 \lesssim J'/J \lesssim 2.5$. The strong discontinuity of ρ_S at $J'/J = 0.9$ indicates that the quantum phase transition between the Néel ordered phase and the superfluid is first order. Such behavior is also seen by monitoring the antiferromagnetic structure factor S_{AF} upon crossing the phase boundary, as shown in Fig. 3.6, again for $\Delta = 1/2$. Combining the results for S_{AF} and ρ_S, we obtain no indication for an intermediate region exhibiting both finite superfluidity and diagonal long-range order as inside a supersolid phase, expected from the commensurate half-filling of the lattice. For dominant J' (e.g., $J'/J > 2.5$ at $\Delta = 1/2$), both S_{AF} and ρ_S eventually vanish. We explicitly verified that inside this regime the model does not exhibit long-ranged

[1] For $J' = 0$, the model reduces to a spin model on the bipartite square lattice, and the sign of Δ can be inverted by an unitary transformation , thus relating the point $(\Delta, J'/J) = (1, 0)$ to the isotropic antiferromagnetic Heisenberg model at $(\Delta, J'/J) = (-1, 0)$.

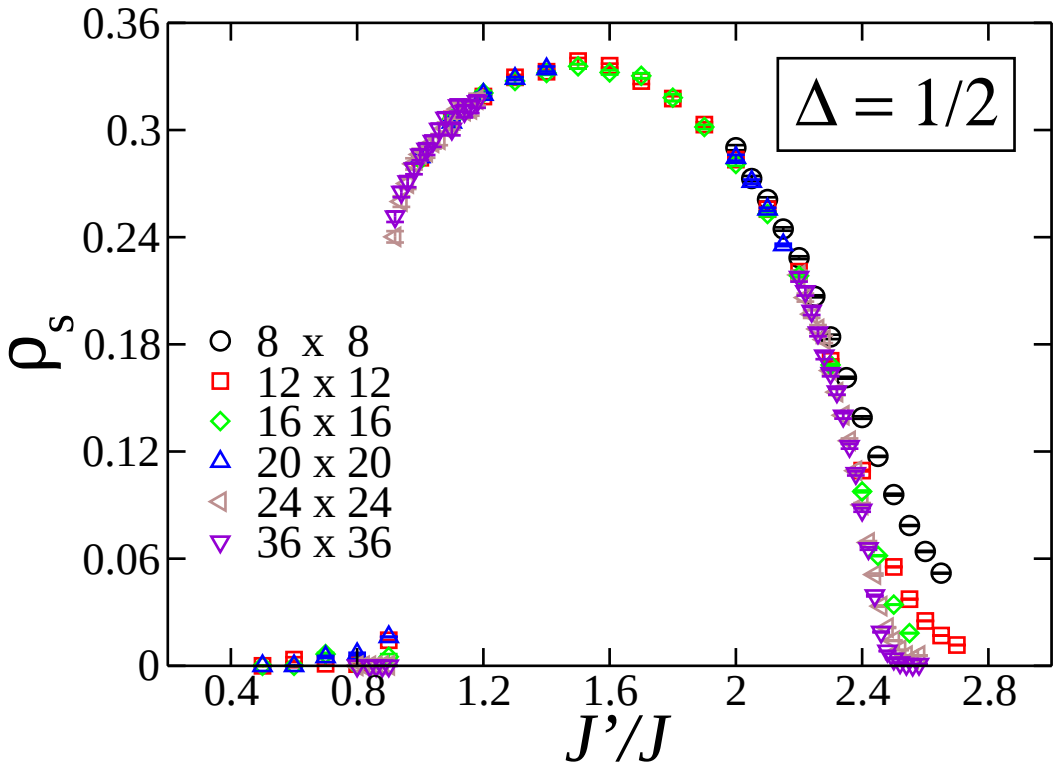

Figure 3.5: Spin stiffness ρ_S at fixed $\Delta = 1/2$ as a function of J'/J for different system sizes.

correlations in the longitudinal nor the transverse spin-spin correlation function. In addition, also the bond-order-wave structure factors do not exhibit long-ranged order in the spin exchange correlation function (corresponding to kinetic energy correlations in the bosonic model).

Since the parameter region with $J' > 2J$ approaches the degenerate region of the Ising limit for $\Delta \to 0$, quantum fluctuations indeed select a unique phase from this degenerate ground state manifold. In particular, for small values of $\Delta \ll 1$, the ground state in this large-J' regime can be obtained using degenerate perturbation theory around the Ising limit. Within first-order perturbation theory in Δ one then finds that for $J' > 2J$ quantum fluctuations select the following dimerized state of localized $S^z_{tot} = 0$ triplet states on each dimer: $|\psi\rangle_D = \bigotimes_D \frac{1}{\sqrt{2}}(|\uparrow\downarrow\rangle + |\downarrow\uparrow\rangle)_D$, where the direct product extends over all J' dimer bonds on the lattice. Obviously, this symmetric linear local combination results from the ferromagnetic nature of the transverse spin exchange ($\Delta > 0$) considered here. In contrast to the dimer singlet state however, the above state $|\psi_D\rangle$ is not an eigenstate of the Hamiltonian for finite values of J. As discussed in our degenerate perturbation calculations (next section), processes in higher order perturbation theory lead to local correlations between the dominant resonances on the dimers. Hence, the ground state in the large-J' region

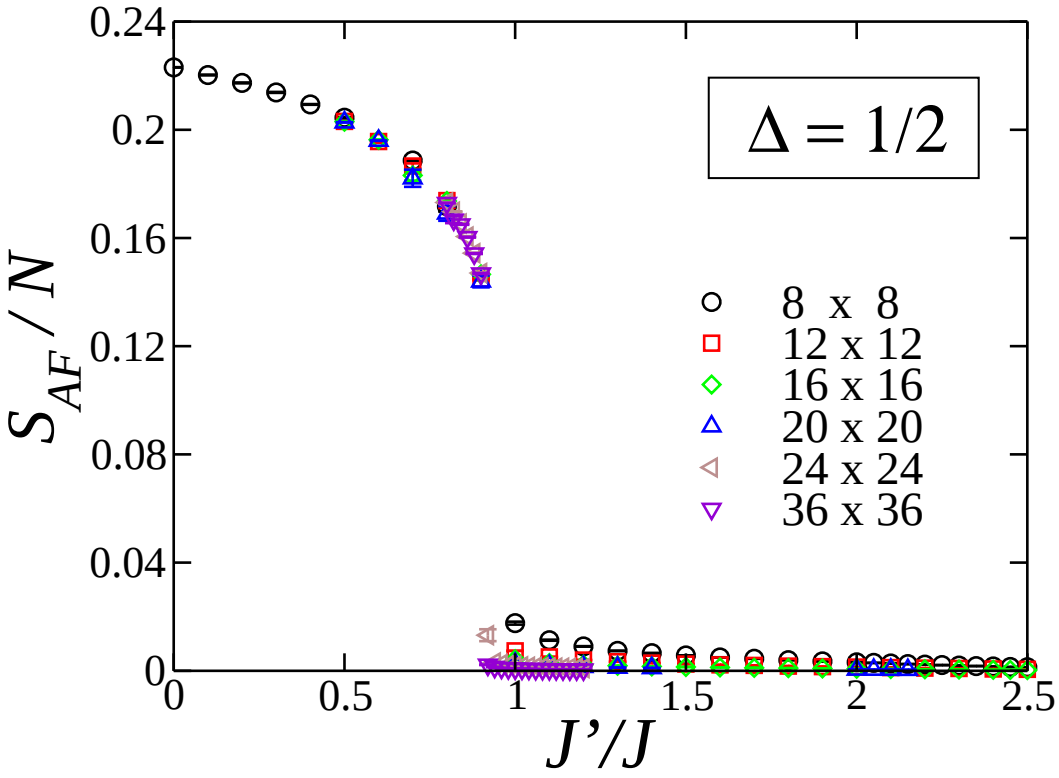

Figure 3.6: Antiferromagnetic structure factor S_{AF} across the phase boundary between the Néel ordered phase and the superfluid regime at fixed $\Delta = 1/2$ as a function of J'/J for different system sizes.

of the quantum phase diagram does not take the above direct product form, but approaches it for $J/J' \to 0$. From the ground state energy, we still find that the state $|\psi\rangle_D$ provides a appropriate variational state for the true ground state in the large-J' regime. This can be seen even at $\Delta = 1/2$, i.e. significantly away from the Ising limit, from a comparison between the system's ground state energy E and the variational energy of $|\psi_D\rangle$, $E_D = \langle\psi_D|H|\psi_D\rangle = -\frac{NJ'}{8}(1+2\Delta)$, shown in Fig. 3.7. The dominant formation of $S^z_{tot} = 0$ triplet states on the dimer bonds motivates us to name this magnetically disordered phase dimer triplet phase.

Since no spatial symmetry is broken in the dimer triplet phase, we expect the quantum phase transition from the superfluid with broken $U(1)$ symmetry to the dimer triplet phase to be continuous, and belongs to the universality class of the three-dimensional (3D) $O(2)$ model, with a dynamical critical exponent $z = 1$. In order to verify this prediction, we scanned the transition region at fixed values of either Δ or J'/J, varying the other parameter through the phase boundary. Denoting the varied parameter by X, at a continuous quantum phase transition the

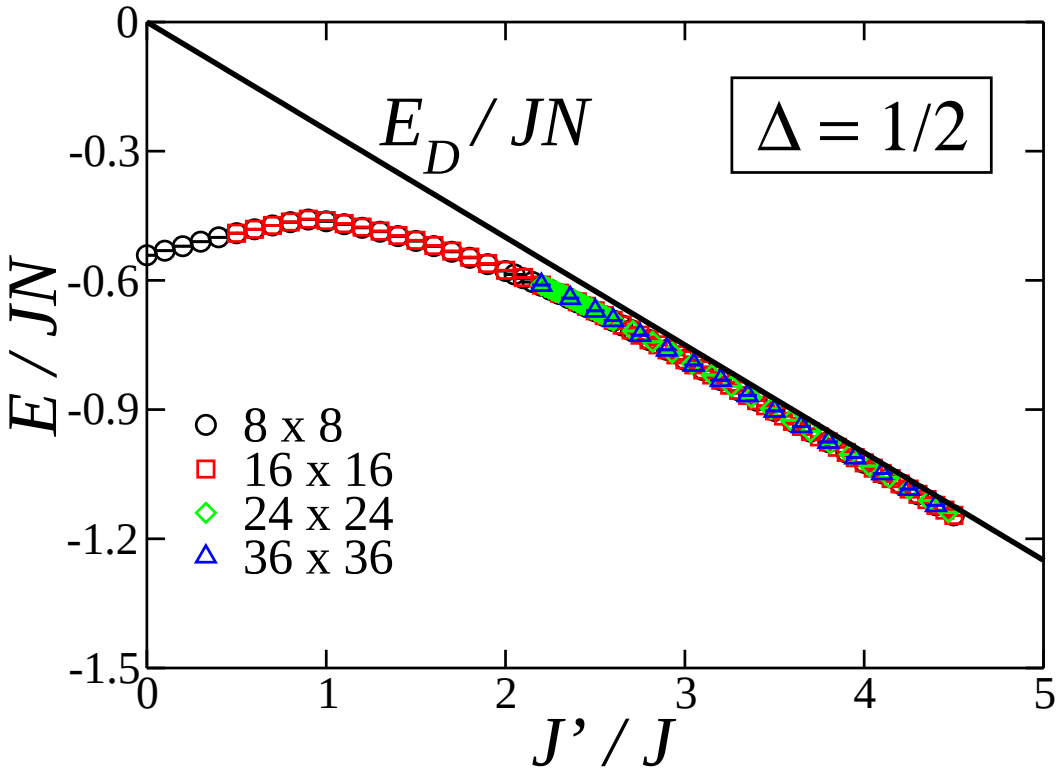

Figure 3.7: Comparison of the ground state energy E as a function of J'/J for $\Delta = 1/2$ and the variational energy of the dimerized state of localized $S^z_{tot} = 0$ triplet states, $E_D = \langle\psi_D|H|\psi_D\rangle$.

spin stiffness scales as

$$\rho_S(X, L) = L^{-z} f\left(t_X L^{1/\nu}, \beta/L^z\right) \tag{3.3}$$

with a scaling function f, and the correlations length exponent ν. Here $t_X = \frac{X - X_c}{X_c}$ denotes the relative distance away from the critical point at $X = X_c$. From the above scaling relation, it follows that X_c can be determined as the crossing point of finite size data for the rescaled spin stiffness $L^z\rho_S$. Furthermore, with appropriate values of the critical exponents z and ν, the scaling function $f(\cdot, A)$ is then obtained by plotting $L^z\rho_S$ vs. $t_X L^{1/\nu}$ for a fixed value of $\beta/L^z = A$. As an example, we consider a scan in $X = J'/J$ at a fixed value of $\Delta = 1/2$, for which the finite size data of ρ_S is shown in Fig. 3.8 **(a)**. For $z = 1$, we obtain $X_c = 2.46(2)$ from a clear crossing point in Fig 3.8 **(b)**, and a clear data collapse within a finite critical region, taking $\nu = 0.6723$ for the 3D $O(2)$ model [Hasenbusch 1999], as shown in Fig. 3.8 **(c)**.

We have also studied other values of Δ, and obtained the phase boundary shown in Fig. 3.3. From this analysis, we find that at low values of $\Delta \lesssim 0.225$, the dimer triplet phase extends below the line $J'/J = 2$, indicated by the dashed line in

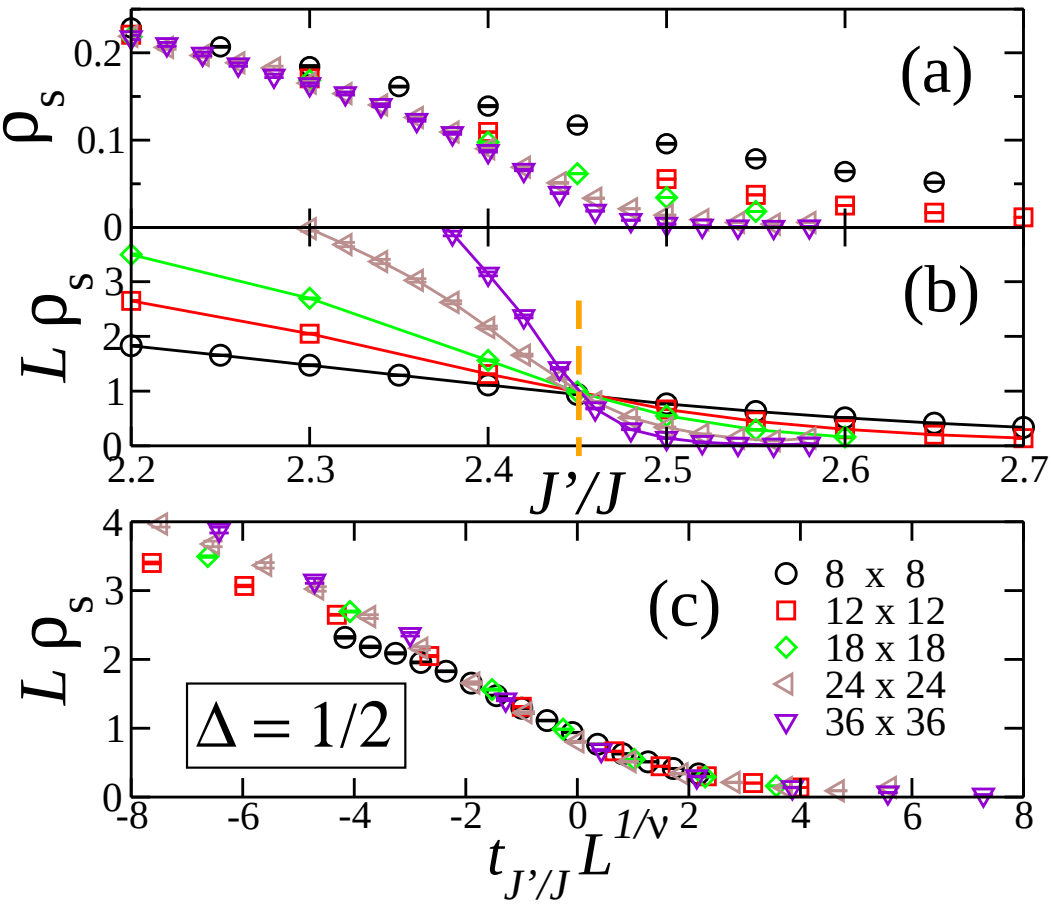

Figure 3.8: Spin stiffness ρ_S at fixed $\Delta = 1/2$ as a function of J'/J for different system sizes **(a)**, and rescaled with linear system size L **(b)**, with $J'/J = 2.46$ marked by the dashed line. Part **(c)** shows the data collapse expected from a finite size scaling analysis for the 3D $O(2)$ universality class.

Fig. 3.3. In order to illustrate this explicitly, we show in the left panels of Fig. 3.9 the results of the finite size scaling analysis at $\Delta = 1/6$, where the transition point is located at $J'/J = 1.928(5) < 2$. As a crosscheck, the right panel of Fig. 3.9 shows the data of the finite size scaling analysis at fixed $J'/J = 1.928$, where the transition is indeed observed at $\Delta = 1/6$. Similarly, when varying Δ at fixed $J'/J = 2$ a transition point between the dimer triplet phase and the superfluid regime is found at $\Delta = 0.225(1)$ (not shown). These results suggest that either (i) the superfluid region persists down to the Ising limit separating the Néel ordered phase and the dimer triplet phase, or (ii) the first order transition line and the second order transition line meet at a finite value of Δ, or (iii) an additional phase appears near $J' = 2J$ for even smaller values of $\Delta < 0.1$.

Such an additional phase might be selected by quantum fluctuations from the macroscopically degenerate Ising limit at $J' = 2J$. The QMC simulations could

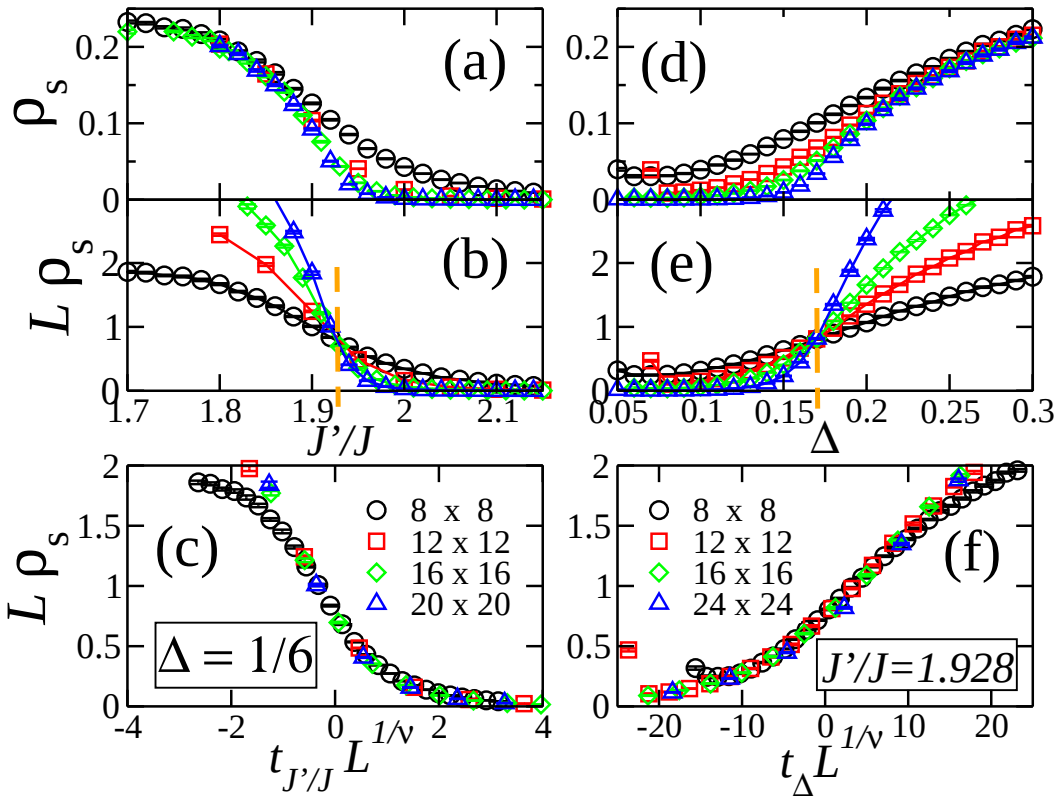

Figure 3.9: Left panel: Spin stiffness ρ_S at fixed $\Delta = 1/6$ as a function of J'/J for different system sizes **(a)**, and rescaled with linear system size L **(b)**, with $J'/J = 1.928$ marked by the dashed line. **(c)** shows the data collapse for the 3D $O(2)$ universality class. Right panel: Spin stiffness ρ_S at fixed $J'/J = 1.928$ as a function of Δ for different system sizes **(d)**, and rescaled with linear system size L **(e)**, with $\Delta = 1/6$ marked by the dashed line. **(f)** shows the data collapse for the 3D $O(2)$ universality class.

not be extended to significantly smaller values of Δ, due to an reduced efficiency in parameter regions dominated by the frustrated diagonal part of the Hamiltonian. However, as discussed in the following section, degenerate perturbation theory in Δ indicates that at $J' = 2J$ the dominant effect of a finite Δ is to drive the system away from $J' = 2J$ towards the region $J' > 2J$. This leads us to exclude option (iii) from the above list. Scenario (ii) would imply a direct first order transition between the Néel ordered phase and the dimer triplet state for sufficiently low values of $\Delta > 0$, whereas within scenario (i) the superfluid phase would always separate the two phases.

3.2.3 Degenerate Perturbation Theory

In order to study more closely the emergence of the dimer triplet phase from the Ising limit upon introducing transverse exchange interactions, we employed degenerate perturbation theory, starting from the degenerate ground state manifold in the Ising limit $\Delta = 0$. First, we consider the region $J' > 2J$, where the degenerate ground state manifold is spanned by independently placing two opposite spins on each J'-dimer. For each such J'-dimer d, we denote these two lowest energy states as

$$\begin{aligned} |\Downarrow\rangle_d &= |\uparrow\downarrow\rangle_d, \\ |\Uparrow\rangle_d &= |\downarrow\uparrow\rangle_d, \end{aligned} \tag{3.4}$$

which form an effective spin-1/2 degree of freedom on the dimer d. We separate the full Hilbert space of the system into the model space M, spanned by these ground state configurations, and the orthogonal space O. A basis of M is given by the orthonormal states

$$|\psi_a\rangle = \bigotimes_d |\psi_a\rangle_d, \text{ with } |\psi_a\rangle_d \in \{|\Downarrow\rangle_d, |\Uparrow\rangle_d\}. \tag{3.5}$$

The orthogonal space O is spanned by all states of the Ising model, that do not belong to this set. We denote these orthonormal basis states by $|\psi_b\rangle$, for which at least one dimer d has both spins equal, i.e. $|\uparrow\uparrow\rangle_d$ or $|\downarrow\downarrow\rangle_d$. The full Hamiltonian is thus split into the model Hamiltonian H_0 and a perturbation part $H_1 \propto \Delta$,

$$\begin{aligned} H_0 &= J\sum_{\langle i,j\rangle} S_i^z S_j^z + J'\sum_{\langle\langle i,j\rangle\rangle} S_i^z S_j^z; \\ H_1 &= J\sum_{\langle i,j\rangle} \left[-\Delta(S_i^x S_j^x + S_i^y S_j^y)\right] + J'\sum_{\langle\langle i,j\rangle\rangle} \left[-\Delta(S_i^x S_j^x + S_i^y S_j^y)\right], \end{aligned} \tag{3.6}$$

where H_0 is diagonal in the basis of M and O. The effective Hamiltonian H_{eff} describes the effective dynamics induced by H_1 within the model space M, it can be derived in degenerate perturbation theory up to third order in Δ as [Lindgren 1974]

$$\begin{aligned} H_{eff} &= PH_0P + \underbrace{PH_1P}_{\text{1st order}} + \underbrace{PH_1RH_1P}_{\text{2nd order}} \\ &\quad + \underbrace{PH_1RH_1RH_1P - PH_1RRH_1PH_1P}_{\text{3rd order}} + O(\Delta^4), \end{aligned} \tag{3.7}$$

where $P = \sum_a |\psi_a\rangle\langle\psi_a|$ is the projection operator onto the model space, and $R = \sum_b \frac{|\psi_b\rangle\langle\psi_b|}{E_0 - E_0^b}$ is the resolvent operator with $E_0 = -NJ'/8$ the degenerate ground state energy of H_0, and $E_0^b = \langle\psi_b|H_0|\psi_b\rangle$ the energy of the basis state $|\psi_b\rangle$ of the orthogonal space O.

In the first order contribution, the only possible process in this case is a single spin-flip along a diagonal bond, graphically represented in Fig. 3.10. In terms of

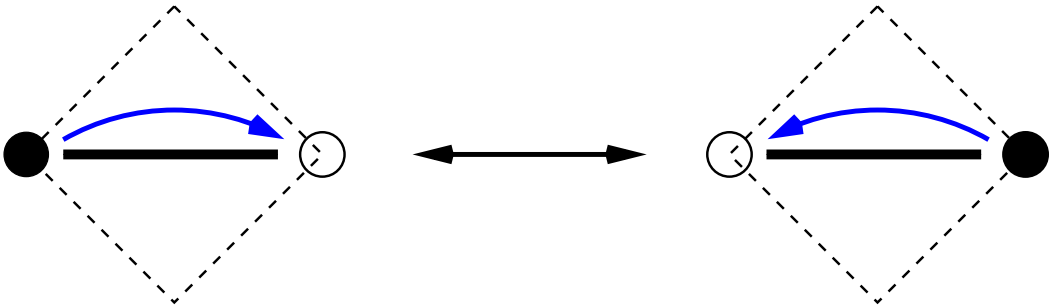

Figure 3.10: Spin exchange processes contributing to the effective Hamiltonian $H_{eff}^{(1)}$ in first order perturbation theory. Full (open) circles denote spin up (down) states.

effective spin operators $\widetilde{S}_d^+, \widetilde{S}_d^-$ and $\widetilde{S}_d^z$, that act on the effective dimer spin states $|\Uparrow\rangle_d, |\Downarrow\rangle_d$, the effective Hamiltonian in first order perturbation thus reads,

$$H_{eff}^{(1)} = -\frac{\Delta J'}{2}\sum_d (\widetilde{S}_d^+ + \widetilde{S}_d^-) = -\Delta J' \sum_d \widetilde{S}_d^x, \tag{3.8}$$

corresponding to a uniform transverse magnetic field acting on the effective dimer spins. The lowest-energy eigenstate of H_{eff} for $\Delta > 0$ is the direct product state

$$|\psi_D\rangle = \bigotimes_d \frac{1}{\sqrt{2}}(|\Uparrow\rangle_d + |\Downarrow\rangle_d) = \bigotimes_d \frac{1}{\sqrt{2}}(|\uparrow\downarrow\rangle + |\downarrow\uparrow\rangle)_d\,,$$

corresponding to the decoupled dimer state with each dimer forming a $S_{tot}^z = 0$ triplet state. However, $|\psi_D\rangle$ is not an eigenstate of the full Hamiltonian, and correlations between the effective dimer spins are introduced in higher order perturbation theory.

In second order perturbation, we need to consider two spin exchanges along axial bonds. Apart from diagonal terms, the result of such processes is again to flip the effective spin on one of the dimers, as shown in Fig. 3.11. The matrix element of each such process depends in detail on the specific local spin configuration on the dimers neighboring the dimer that undergoes the spin flip. Among the various possibilities, one with the largest amplitude is shown in Fig. 3.11 (a). In the second order effective Hamiltonian $H_{eff}^{(2)}$, this process contributes a term

$$\frac{2(\Delta J)^2}{2J - J'}\widetilde{S}_d^x(\frac{1}{2} - \widetilde{S}_i^z)(\frac{1}{2} - \widetilde{S}_j^z)(\frac{1}{2} - \widetilde{S}_k^z)(\frac{1}{2} + \widetilde{S}_l^z), \tag{3.9}$$

which provides a further contribution to the transverse field operator at site d, dressed by diagonal operators from the neighboring dimers, that project out the specific configuration of dimer spin states according to the configuration shown in Fig. 3.11. The dressed transverse field operators deriving from $H_{eff}^{(2)}$ lead to correlations among nearest neighbor dimer spins.

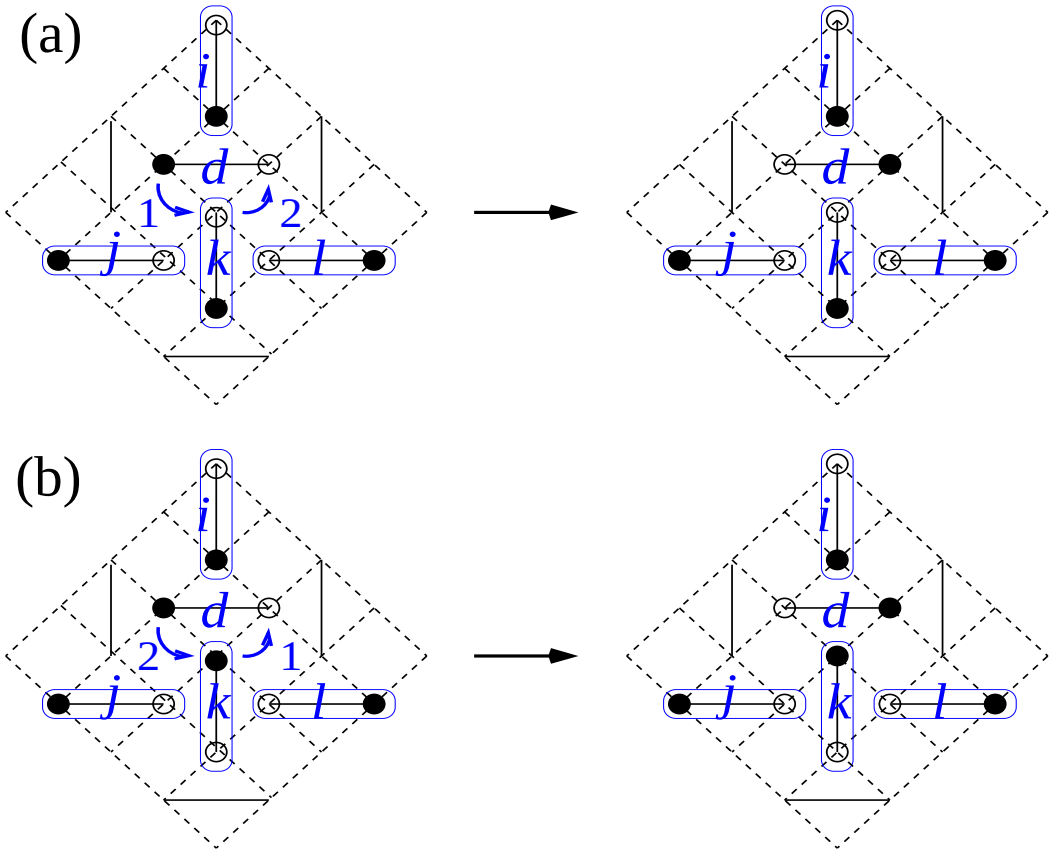

Figure 3.11: Two different spin exchange processes contributing to the effective Hamiltonian $H_{eff}^{(2)}$ in second order perturbation theory. These processes mediate the formation of an $S_{tot}^z = 0$ triplet state on the corresponding dimer, while blocking its formation on the neighboring dimers (inside ellipses). Full (open) circles denote spin up (down) states. Numbers indicate the order of the spin exchange in the processes.

The explicit form of the total effective Hamiltonian up to second order in Δ involves several terms, containing products of up to five effective spin operators, such as the term given explicitly in Eq. (3.9). While the ground state of this effective Hamiltonian is not directly accessible, the general structure of these terms indicate that it will be a dressed version of $|\psi_D\rangle$, with local inter-dimer correlations induced by the above virtual spin exchange processes. This reflects the QMC result, that the true ground state is close in energy to $|\psi_D\rangle$, and does not exhibit long ranged correlations.

As the process shown in Fig. 3.12, transverse spin exchange terms, that contain products of off-diagonal effective spin operators such as $\widetilde{S}_d^+ \widetilde{S}_k^- + \widetilde{S}_d^- \widetilde{S}_k^+$ on two neighboring dimers d and k, only appear in third order of the degenerate perturbation theory. Similar to the transverse magnetic field operator in second order, the matrix elements depend on the details of the spin configuration on the neighbors of the

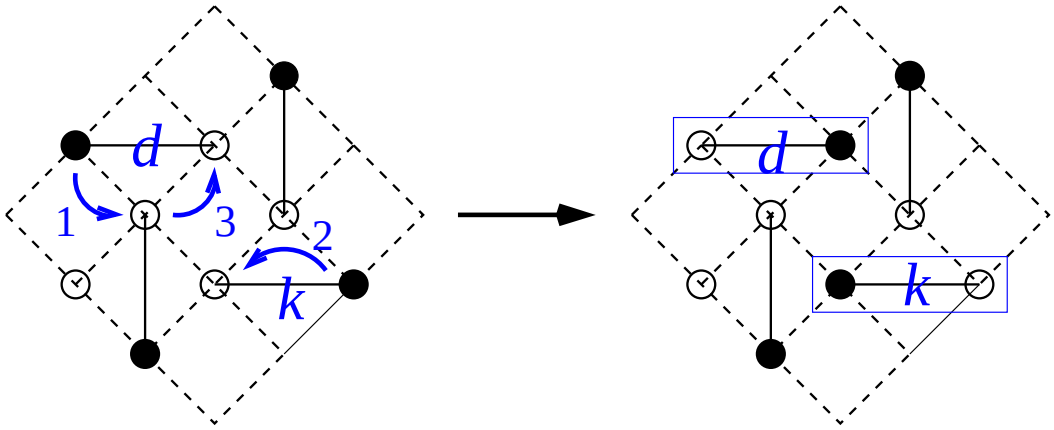

Figure 3.12: Spin exchange process contributing to the effective Hamiltonian $H_{eff}^{(3)}$ in third order perturbation theory. This process leads to a flip of the effective spins on two neighboring dimers (inside boxes). As a result of this process, the effective spins inside the boxes have been exchanged. Full (open) circles denote spin up (down) states. Numbers indicate the order of the spin exchange processes.

two dimers that undergo an effective spin exchange. The transverse effective spin exchange operators are thus similarly dressed by additional projection operators. Becoming more relevant at large values of Δ, we expect that such exchange terms eventually drive the transition from the dimer triplet phase to the superfluid region, that was observed in the QMC simulations (c.f. Fig. 3.3).

We now turn to the special point $J' = 2J$, where the ground state in the Ising limit has an enhanced degeneracy, as discussed in Chap. 2.2.1. Consider one of the J'-dimer of the Shastry-Sutherland lattice in the Ising limit $\Delta = 0$. For $J' = 2J$, this dimer can be either in one of the local configurations of Fig. 3.4 **(a)**, which are also allowed configurations for $J' > 2J$, or it is part of one of the local configurations shown in Fig. 3.4 **(b)**. Introducing a finite $\Delta > 0$ in first order perturbation theory, a splitting in the energy between the configurations of Fig. 3.4 **(a)** and those of Fig. 3.4 **(b)** results, since the configurations of Fig. 3.4 **(b)** cannot gain exchange energy by a transverse spin exchange along the dominant J' bonds, in contrast to the configurations of Fig. 3.4 **(a)**. To first order in Δ, this energy difference equals

$$\delta E = -J + \frac{J'}{2} + \frac{\Delta J'}{2}, \tag{3.10}$$

near the point $(\Delta, J'/J) = (0, 2)$. A finite $\delta E > 0$ thus leads to a partial lifting of the ground state degeneracy, and only the local configurations of Fig. 3.4 **(a)** remain to span the low-energy sector. The configurations of Fig. 3.4 **(b)** are split-off by a finite energy difference $\delta E > 0$ from the ground state manifold. Since this energy difference remains positive for

$$\delta E > 0 \Longleftrightarrow \frac{J'}{J} > \frac{2}{1+\Delta} \tag{3.11}$$

we expect that as long as $J'/J \gtrsim 2/(1+\Delta)$ close to $(\Delta, J'/J) = (0, 2)$, the system is driven by quantum effects towards the same phase as for $J' > 2J$. In fact, this expectation is in agreement with the QMC phase diagram of Fig. 3.3, where we found that (i) for small $\Delta > 0$ at $J' = 2J$, the system enters the dimer triplet state as it does for $J' > 2J$, and (ii) the phase boundary of the dimer triplet phase closely follows the limiting line $J'/J = 2/(1+\Delta)$ according to $\delta E = 0$ for small Δ (compare to the dashed-dotted line in Fig.3.3). The above argument was based on energy considerations on an isolated dimer. Due to this restriction, we are not able here to discern, if the superfluid phase indeed terminates at a small, but finite values of Δ, or if it persists down to any finite value of $\Delta > 0$. But we will leave this question aside, and move on to study the magnetization process in the model under consideration.

3.3 Magnetization Process

Now we consider the model of Eq. 3.1 in the presence of a finite magnetic field h, which couples to the spins by the standard Zeeman term, $h\sum_i S_i^z$. From considering a singly flipped spin with respect to the fully polarized state, one finds that the system is fully polarized for magnetic fields h beyond $h_s = (2J + J'/2)(1+\Delta)$.

Before discussing the magnetization process of the full quantum model, it is again useful to consider first the Ising limit. We have measured the magnetization process at the Ising limit in the Néel phase and the degenerate region of $J' > J$. Using classical Monte Carlo simulations on the lattice upto 18×18 spin in the canonical ensemble, we found there is only one plateau at $m/m_s = 1/3$, as shown in Fig. 3.13 **(a)** and **(b)**. We verified that an earlier statement of a $m/m_s = 1/2$ plateau by the authors of Ref. [Siemensmeyer 2008] is not correct, their observation in the first version of their paper is an artifact of the usage of inappropriate finite lattice sizes, as shown in the inset of Fig. 3.13 **(a)**.

In fact, a plateau at $m/m_s = 1/2$, not obtained in the Ising limit, emerges in the quantum model at finite values of $\Delta > 0$. Fig. 3.14 shows the magnetization process for $J' = 2.4J$ and $\Delta = 1/4$ from QMC simulations. Adding a transverse exchange to the Ising model leads to a softening of the large magnetization jump from $m/m_s = 1/3$ to 1 in the Ising limit, and an additional plateau region appears with $m/m_s = 1/2$. In hard-core boson language, the transverse exchange maps onto a non-frustrating hopping amplitude. In the current situation, this finite boson hopping does not lead always to superfluidity, but drives the system into a crystalline phase at filling $\rho = 3/4$, corresponding to $m/m_s = 1/2$[2]. Indeed, we find from Fig. 3.14, that the spin stiffness ρ_s vanishes inside both plateau regions. Long-range crystalline ordering of magnetic excitations inside magnetic plateau regions has previously been analyzed for the isotropic spin-1/2 Heisenberg model on the Shastry-Sutherland model based on different approximative schemes [Momoi 2000a,

[2] due to particle-hole symmetry, a similar insulating region emerges also for $\rho = 1/4$, corresponding to $m/m_s = -1/2$.

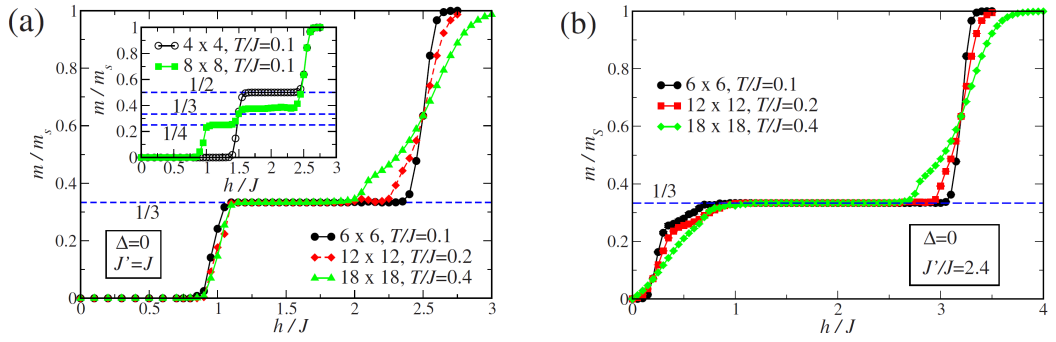

Figure 3.13: **(a)** Magnetization curves m/m_s as functions of h for the Ising model on the Shastry-Sutherland lattice at $J' = J$ for different system sizes, obtained from classical Monte Carlo simulations. The inset shows the results for the 4×4 and 8×8 lattices. The $m/m_s = 1/2$ plateau only develops in the 4×4 system, but is absent in the TDL. **(b)** Magnetization curves m/m_s as functions of h for the Ising model on the Shastry-Sutherland lattice at $J' = 2.4J$ for different system sizes, obtained from classical Monte Carlo simulations. Again only the $m/m_s = 1/3$ plateau is present.

Momoi 2000b, Miyahara 2000, Misguich 2001, Miyahara 2003a, Abendschein 2008, Sebastian 2008, Dorier 2008, Isaev 2009]. The relevant structures expected from these studies are shown in the inset of Fig. 3.15 for the 1/3 (upper panel), and the 1/2 (lower panel) plateau, respectively. They are expressed in terms of periodic arrangements of $S^z_{tot} = 1$ dimer triplet states $|\uparrow\uparrow\rangle_d$, denoted by dumbbells, in a background of less polarized, e.g. $S^z_{tot} = 0$ states on the remaining dimers.

In a QMC simulation, one can probe exactly for these magnetic superstructures by measuring an appropriate structure factor. Hence, we analyze the ordering pattern of the magnetic excitations by measuring the triplet excitation structure factor

$$S(\mathbf{q}) = \frac{1}{N_d}\sum_{d,k} e^{i\mathbf{q}(\mathbf{r}_d-\mathbf{r}_k)}\langle P_d P_k\rangle, \tag{3.12}$$

where P_d is a projector on the $S^z_{tot} = 1$ dimer triplet state $|\uparrow\uparrow\rangle_d$ on dimer d. $N_d = N/2$ equals the number of dimers in the finite system of N sites. The positions $\mathbf{r}_d$ of the dimers and the momentum space vector $\mathbf{q}$ are defined with respect to the convenient coordinate system formed by the square lattice of dimers, with the distance between the centers of two neighboring dimers taken as unity. In this way, the solid order shown in the upper panel of Fig. 3.15 for $m/m_s = 1/3$ corresponds to a peak in $S(\mathbf{q}) \propto N_d$ at $\mathbf{q} = (2\pi/3, 2\pi/3)$, and at $\mathbf{q} = (\pi, \pi)$ for the order shown in the lower panel of Fig. 3.15 for $m/m_s = 1/2$. The main panels of Fig. 3.15 show these components of the structure factor for different system sizes, respectively. We checked, that no other signal in $S(\mathbf{q})$ appeared. From these data we conclude, that indeed the crystalline orders of the magnetic excitations shown in Fig. 3.15 are stabilized within the two magnetization plateau regions, respectively.

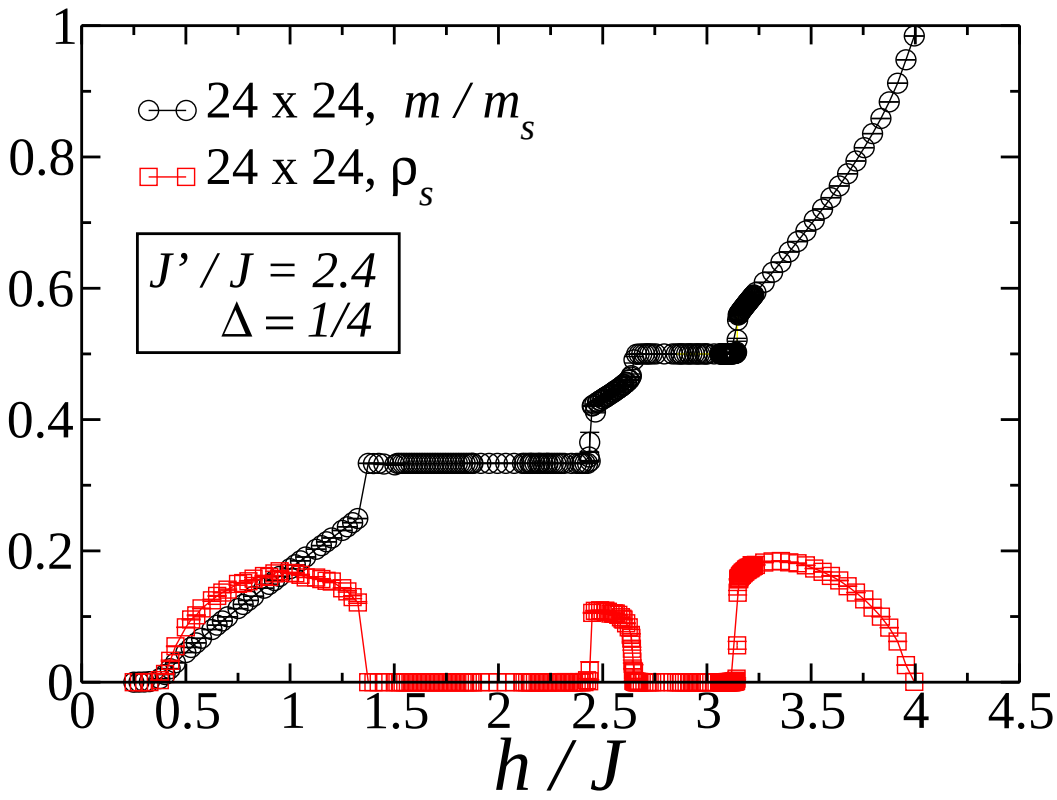

Figure 3.14: Magnetization m/m_s and spin stiffness ρ_S for $J' = 2.4J$ and $\Delta = 1/4$ as functions of the applied magnetic field h. Results are shown for a 24×24 lattice.

Upon varying h beyond these wide magnetization plateaus, the magnetization undergoes discontinuous jumps, as seen in Fig. 3.14. But when entering the 1/2 plateau from below, the jump appears not that well resolved. The spin stiffness ρ_s exhibits a similar behavior. Apart from this case, the superfluid-insulator transitions are thus clearly first order. Concerning the region below the 1/2 plateau, one might instead consider the presence of a supersolid state of magnetic excitations, with both a finite superfluid density and a crystalline superstructure. In order to assess the existence of supersolid in this regime, we show in Fig. 3.16 the finite size scaling of both the superfluid density ρ_s and the relevant structure factors from the neighboring magnetization plateaus at a magnetic field of $h = 2.6J$. From the finite size scaling we can exclude the presence of a supersolid phase in this parameter regime. Between the two magnetization plateaus, the system is thus in a uniform superfluid state.

Our analysis of the magnetization process at $J'/J = 2.4$ and $\Delta = 1/4$ did not exhibit the presence of any additional plateaus at lower values of m.

Finally, we present our results for the magnetization process upon varying over a wider range of parameters space. The results of QMC simulations similar to those discussed in detail above are summarized in Fig. 3.17, which shows the magnetic

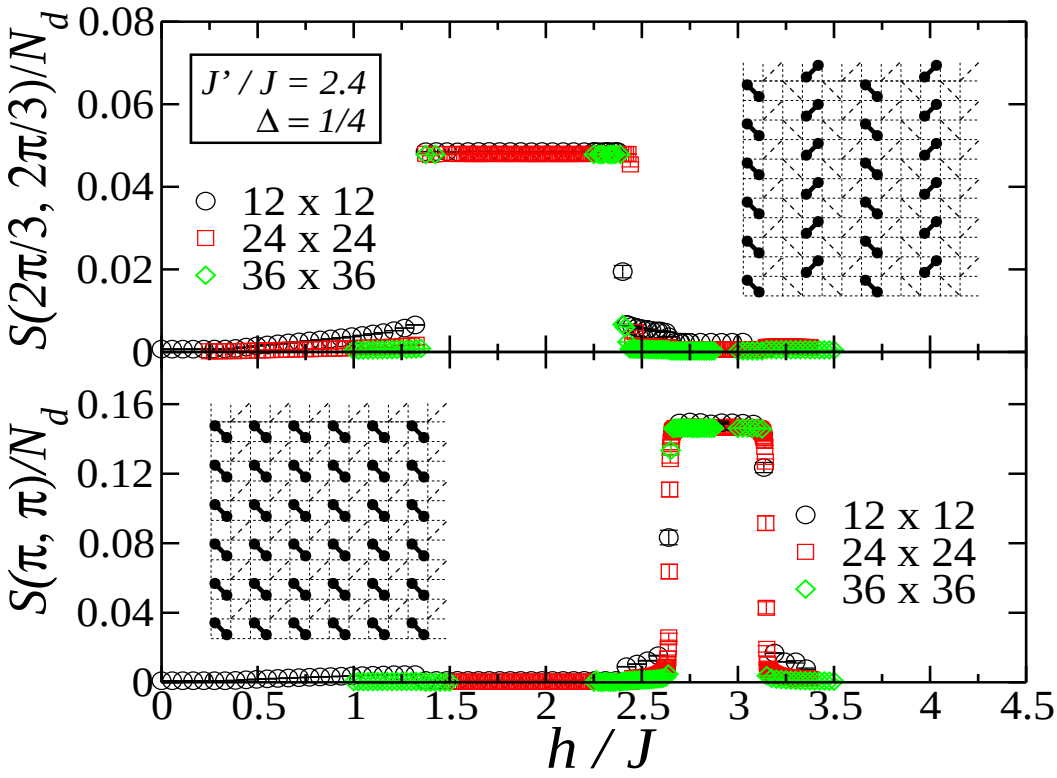

Figure 3.15: Dimer super structure factors $S(2\pi/3, 2\pi/3)$ (upper panel) and $S(\pi, \pi)$ (lower panel) at $J' = 2.4J$ and $\Delta = 1/4$ as functions of the applied magnetic field h. The insets illustrate the corresponding magnetic superstructures, where a dumbbell denotes a fully polarized dimer. $N_d = N/2$ is the number of dimers.

phase diagram for a generic fixed ratio of $J'/J = 2.4$. The figure shows both the $m/m_s = 1/3$ magnetization lobe that extends from the Ising limit up to $\Delta = 0.32(2)$, as well as the emergent $m/m_s = 1/2$ lobe, that extends up to a similar value of Δ, but shrinks upon approaching the Ising limit, where no 1/2 plateau persists.

3.4 Summary and Outlook

In this chapter, we studied the ground state phase diagram and the magnetization process of the spin-1/2 easy-axis Heisenberg model Eq. 3.1 with ferromagnetic transverse spin exchange on the Shastry-Sutherland lattice. The model exhibits a Néel ordered phase for small values of J'/J and Δ, and a superfluid phase for dominant Δ. For sufficiently large values of J'/J, a dimerized phase with the dominant formation of $S^z_{tot} = 0$ triplet states on the J'-dimer bonds is stabilized, that connects to the degenerate phase of the model in the Ising limit.

Using classical Monte Carlo simulations to assess the magnetization process in the Ising limit, we could exclude a magnetization plateau at 1/2 of the full satura-

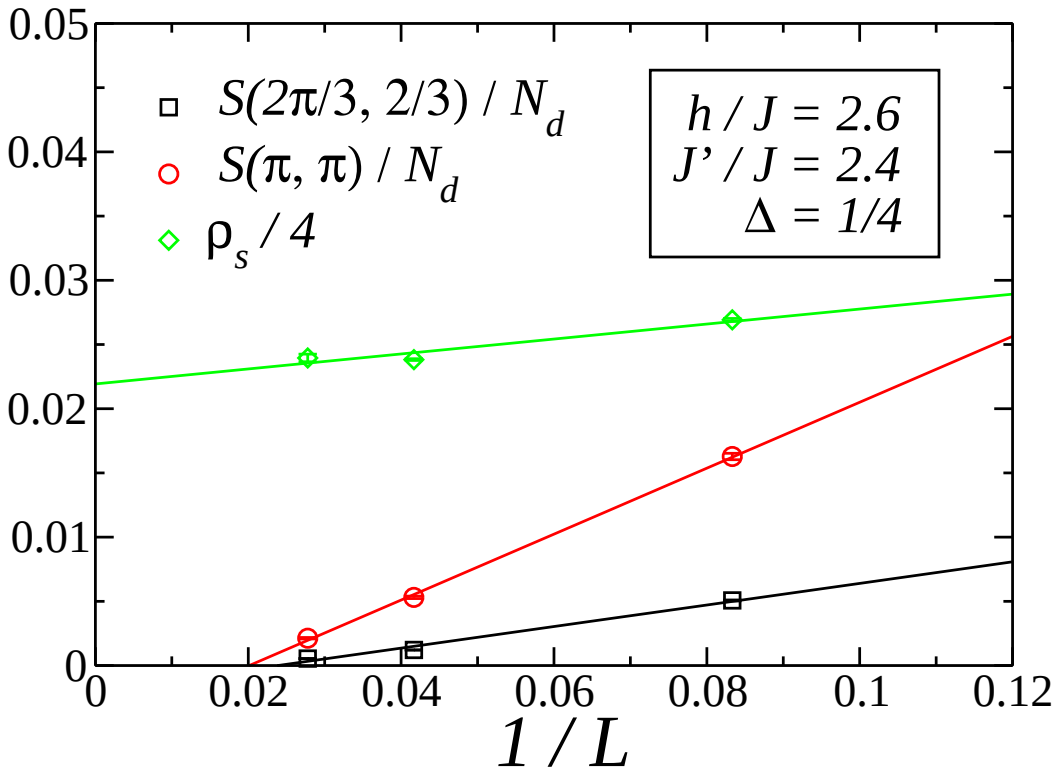

Figure 3.16: Finite size scaling of the superfluid density ρ_S and the dimer superstructure factors of the neighboring plateaus at $h = 2.6J$ for $J' = 2.4J$ and $\Delta = 1/4$.

tion [Siemensmeyer 2008], and instead found a 1/3 plateau, with a magnetization jump towards full magnetic saturation. The quantum model shows the presence of a 1/2 plateau in addition to the 1/3 plateau. This emergence of a magnetization plateau upon adding quantum fluctuations (via a finite Δ) to the Ising model reminds of previously observed emergences of magnetization plateaus via thermal fluctuations as e.g. in the classical Heisenberg model on the kagome lattice [Zhitomirsky 2002]. While we examined the case of a ferromagnetic transverse spin exchange, the experimental observation of a 1/2 plateau in the compounds TmB_4 and $SrCu_2(BO_3)_2$ can be taken as indication, that such a plateau also emerges for antiferromagnetic transverse exchange. Indeed, a 1/2 plateau is consistently reported also in the studies on the magnetization process of the isotropic Heisenberg model on the Shastry-Sutherland lattice [Miyahara 2003b].

With respect to other reported magnetization plateaus both from experiments and in recent theoretical work, we did not obtain evidence from our quantum Monte Carlo simulations, that they are stabilized in the current model. In particular, the pronounced 1/6 plateau, consistently reported in recent theoretical work [Sebastian 2008, Dorier 2008, Abendschein 2008, Isaev 2009], has not been found for the parameter region we examined in our simulations (we performed var-

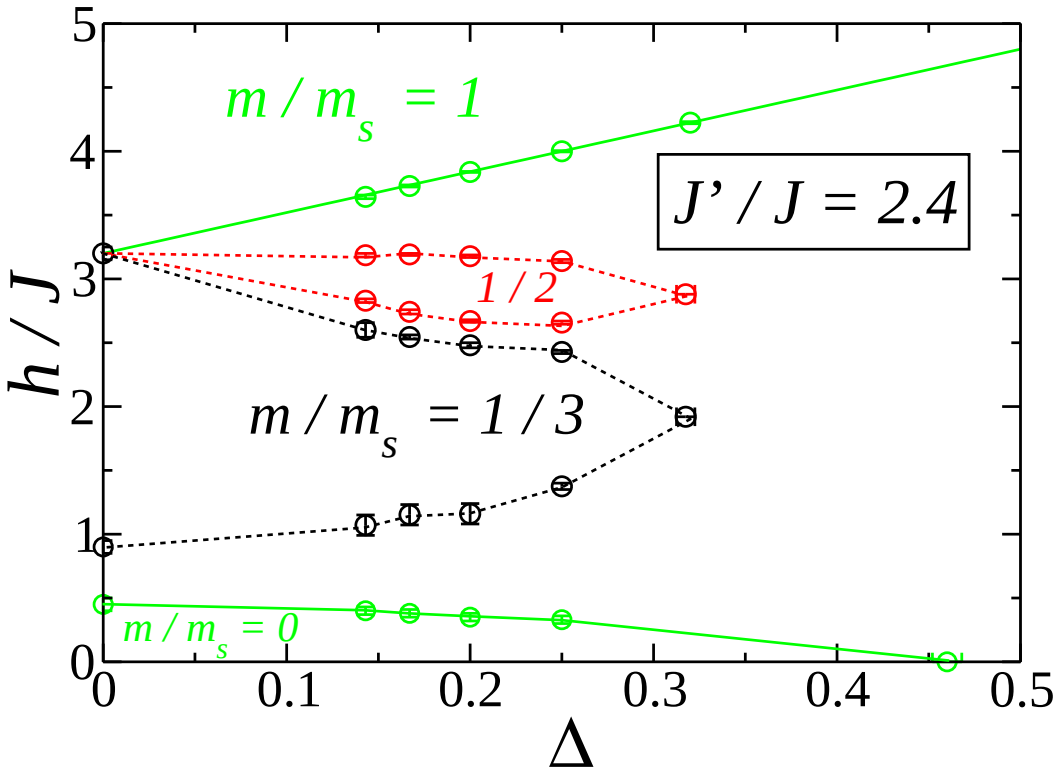

Figure 3.17: Magnetic phase diagram of the spin-1/2 XXZ model on the Shastry-Sutherland lattice with ferromagnetic transverse spin exchange at $J'/J = 2.4$ depending on the anisotropy Δ and the applied magnetic field h.

ious scans inside the range $2 < J'/J < 3$, down to $\Delta = 1/7$, with results similar to those presented in detail above), even though the proposed magnetic unit cell [Sebastian 2008, Dorier 2008, Abendschein 2008, Isaev 2009] is commensurate with the finite lattices that we employed in our simulations. We explicitly checked that no signal in the relevant component of $S(\mathbf{q})$ at $\mathbf{q} = (\pi, \pi/3)$ appears near $m/m_s = 1/6$ in this model. Hence, we conclude that the model considered here exhibits magnetization plateaus at 1/2 and 1/3 of the full saturation, only.

Future work could explore in more detail the magnetization process in the Ising model inside the low-field region using extended ensemble methods, similar to the approach taken in Ref. [Hwang 2007]. It would be interesting to apply the theoretical approaches employed in Refs. [Dorier 2008], [Abendschein 2008] and [Isaev 2009] to the current model, in order to to check their predictions against the unbiased large-scale quantum Monte Carlo present here. Furthermove, Suzuki et al. have included longer range couplings into the current model. From their SSE QMC simulations, they found that the 1/3 and 1/2 plateaus are stable against long range interactions [Suzuki 2009, Suzuki 2010]. They also studied the finite temperature phase transition to the 1/2 plateau and concluded that in the Ising limit, the finite

temperature transition to the 1/2 plateau is continuous and of the four-states Potts model universality class; in the quantum regime, there is a two-step phase transition with an intervening intermediate phase. Both the transitions are of the 2D Ising universality class. The intermediate phase is characterized by the retaining 180°-rotation symmetry on individual triplets with $m_z = 0$.

Chapter 4

Quantum Spin Liquid emerging in the Hubbard Model on the Honeycomb Lattice

In this chapter, we employ the PQMC to study the ground state phase diagram of correlated Dirac fermions on the honeycomb lattice, the structure of graphene. Before explaining our numeric results in detail, we would like to begin this chapter with an introduction to quantum spin liquids (QSL), with the purpose that one can put our finding of a quantum spin liquid phase emerging in the spin-1/2 Hubbard model on the honeycomb lattice into perspective.

4.1 Introduction to Quantum Spin Liquids

At sufficiently low temperatures, condensed matter systems tend to develop order. A notable exception to this behavior is the case of quantum spin liquids, in which quantum fluctuations prevent a magnetic system to an ordered state down to the lowest temperatures, e.g., the ground state of the system has no preferred spin orientations, and no frozen valence bond patterns. In a QSL, the constituent spins are highly correlated but still fluctuate strongly, strong quantum fluctuations give rise to remarkable collective phenomena such as emergent gauge fields and fractional particle excitations [Lee 2008b]. Besides being exotic forms of matter, quantum spin liquids have been suggested as a possible route towards high temperature superconductivity [Anderson 1987, Lee 2006], and their unusual topological properties may be useful in building quantum computers [Kitaev 2006].

The absence of order down to zero temperature, or the spin-liquid-like behavior, is actually common in one dimension (1D), since the lower the dimension is, the stronger the quantum fluctuations are [Fazekas 1999]. Taking the spin-1/2 1D antiferromagnetic (AF) Heisenberg chain as an example, the Bethe ansatz solution rules out a magnetically ordered ground state [Karbach 1997, Karbach 1998]. The strong zero point fluctuations drive the true ground state away from the classical Néel state (see Fig. 4.1), it exhibits critical AF correlations (power-law decay) and hence lacks true long range order [Fazekas 1999].

Furthermore, spin-1/2 AF Heisenberg ladder systems also have the spin-liquid-like ground state [Dagotto 1994]. Ladders made from an even number of legs have purely short range spin correlations – an exponential decay of the spin-spin correlation is produced by a finite spin gap [Dagotto 1996]. Ladders with an odd

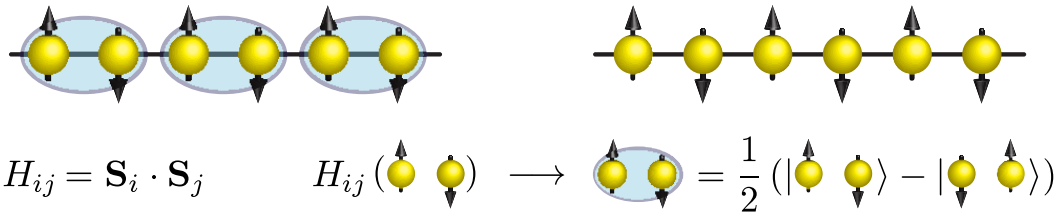

Figure 4.1: In a spin-1/2 AF Heisenberg chain, the classical Néel state is not the ground state of the Hamiltonian: for a pair of neighboring sites $\langle i, j \rangle$, the Hamiltonian H_{ij} favors the formation of the a spin singlet.

number of legs display properties similar to those of a single chain, namely, gapless spin excitations and a power-law decay of the spin-spin correlations, apart from logarithmic corrections. In fact, one can derive a path-integral expression of the effective action of the AF Heisenberg spin ladder system, and map it onto an O(3) nonlinear σ model in the continuum limit [Dell'Aringa 1997]. In case of even-leg ladders the nonlinear σ model does not have a topological term and is therefore gapped, whereas odd-leg ladders have a topological term, and are gapless. Spin liquid ground states in ladder systems have been confirmed by various simulations with quantum Monte Carlo [Dagotto 1994, Syljuåsen 1997, Wessel 2001] and density matrix renormalization group (DMRG) [White 1994]. Experimentalists also succeeded in finding ladder compounds, vanadyl pyrophosphate $(VO)_2P_2O_7$ (two leg ladder) [Eccleston 1994], $SrCu_2O_3$ (two leg ladder) [Azuma 1994], and $Sr_2Cu_3O_5$ (three leg ladder) [Azuma 1994], to name a few, that host spin liquid ground states.

In two dimensions (2D), the ground states of the nearest neighbor antiferromagnetic (AF) Heisenberg model in square, honeycomb and triangular lattices are truly ordered, but due to strong quantum fluctuations, the local moment is far from the saturation value of 1/2 per site. For example, on the square lattice, large-scale quantum Monte Carlo simulations give the local staggered magnetization $m_s = 0.3070(3)$ [Sandvik 1997], 60% of its classical value 0.5; on the honeycomb lattice, $m_s = 0.2681(8)$ [Löw 2009], 53% of its classical value 0.5; and on the triangular lattice, exact diagonalization with variational quantum Monte Carlo give $m_s = 0.21(1)$ [Capriotti 1999], only 41% of its classical value.

Currently, the consensus of having a QSL ground state in two or higher dimensions is the following: as for purely quantum spin models, the geometric frustrations induced by the lattice (triangular, Kagome), by longer range exchange interactions ($J_1 - J_2$ AF Heisenberg model), and by strong multispin interactions (such as ring exchange), are crucial to enforce a quantum spin liquid ground state; and if the charge degrees of freedom of the electron are also involved, such as in fermionic Hubbard models, the strong charge fluctuations close to the Mott insulator to metal transition, past which there are no localized spins, are important ingredients for the emergence of a QSL.

The materials of the following summary mainly come from the nice reviews by

Alet et. al. [Alet 2006], Balents [Balents 2010], and Powell et. al. [Powell 2011], as well as the corresponding chapter in the Ph.D. thesis of my collaborator Thomas Lang [Lang 2010].

4.1.1 QSLs as Exotic States of Matter

In quantum spin models, to construct a non-magnetic state, a natural building block is the valence bond – a pair of spins forms a $S = 0$ singlet due to the antiferromagnetic coupling between them. If all the spins in the system are subject to valence bonds, then the ground state has total spin $S = 0$ and is hence non-magnetic. One way in which this can occur is to partition the spins into static and localized valence bond patterns. Such a ground state can be formulated into a direct product of the valence bonds, so that each spin is maximally entangled with its valence-bond partner. This kind of state is known as a valence-bond solid (VBS) [Fazekas 1999]. We have discussed VBS in detail in Chapter 3, the plateaux compound $SrCu_2(BO_3)_2$ has a VBS ground state (the dimer singlet state). If one expose it to a (strong) magnetic field, the singlet valence bond can be excited into triplet (triplons). Due to the density and interaction strength between them, these triplons can be either itinerant or localized, and the magnetization process of the compound can be understand as the Bose-Einstein condensation or crystallization of these triplons. Besides $SrCu_2(BO_3)_2$, the dimerized compounds $TlCuCl_3$, and the 'Han purple' $BaCuSi_2O_6$, are the experimental realizations of the triplon condensation scenario discussed here [Giamarchi 2008].

However, as its name stands, a VBS is a solid, but not a quantum spin liquid, because it typically breaks the translation or rotation symmetries of the underlying lattice. In order to build a true quantum spin liquid, the valence bonds must be allowed to undergo quantum fluctuations. The ground state may then be expressed as a superposition of different partitionings of spins into valence bonds, not only one specific pattern as in a VBS. Under the superposition of these various partitionings, for each individual spin, there is then no preference for any specific valence bond partner. And such states can be regarded as a valence-bond 'liquid' rather than a solid. This type of wavefunction is indeed a quantum spin liquid and is generally named as resonating valence bond (RVB) state. The RVB state was originally introduced by Anderson and Fazekas [Anderson 1973, Fazekas 1974] as the possible ground state wavefunction of the AF Heisenberg model on the triangular lattice, and became subject of intense theoretical interest since 1987, when Anderson further proposed that the RVB state might describe the physics of high-temperature superconductivity [Anderson 1987]. Since then, the RVB wavefunction has been gradually shown to be the ground states for specific model Hamiltonians [Moessner 2001a].

There are different types of QSL, and we can differentiate them by looking at their low energy excitations [Alet 2006]. For example, in the superposition of different valence bond partitionings, the valence bonds need not to be formed by neighboring spins. If a valence bond is formed from spins that are far apart, then those spins are only weakly bound into a singlet and the valence bond can be broken

to form free spins with only a small energy cost. Such type of QSL will have a significant contribution from long-range valence bonds and will have more low energy spin excitations than those QSL in which the valence bonds are mainly short ranged. There are also other excitations that do not break the valence bonds but simply rearrange them. Such excitations can be low energy excitations even in short-range RVB states [Balents 2010].

Considering different types of QSLs, it is interesting to try to classify them. The problem is far from solved at the moment, but after the efforts of theorists for decades, it is clear now that the number of possible QSLs is huge. For instance, Xiao-Gang Wen has classified hundreds of different 'symmetrical spin liquids' (QSLs with the full space-group symmetry) for spin-1/2 antiferromagnets on the square lattice, alone! [Wen 2002]. However, one feature that many people expected QSLs to have in common is that they have exotic excitations. Here 'exotic' means these excitations are not the elementary excitations in most condensed matter systems that are either electron-like (spin $S = 1/2$, and charge e) or magnon-like (spin $S = 1$ and charge neutral), but are carrying fractional quantum numbers such as those in the fractional quantum Hall states [Jain 2000]. In QSLs, the most prominent exotic excitations are spinons, which are neutral and carry spin $S = 1/2$. Spinons are well established in 1D systems, in which they occur as domain walls (Fig. 4.2 **a**). In 1D, a spinon can be created by flipping a semi-infinite string of spins, so the only boundary of such a string is its end point, and hence the string is guaranteed to cost only intensive energy from this boundary. By contrast, in 2D or higher dimensions, the boundary of a string extends along its full length. A string will then naturally be expected to have a tension, because the energy cost is now proportional to its length. String tension represents confinement of the spinons, similar in spirit to quarks in quantum chromodynamics.

But QSLs provide the possibility to liberate the confined spinons (deconfinement) [Senthil 2004]. At zero temperature, in a 2D or 3D QSL, the string associated with a spinon can become tensionless. This is due to the strong quantum fluctuations (Fig. 4.2 **c**), and can be understood from the quantum superposition principle: rearranging the spins along the string simply reshuffles the various spin or valence bond configurations that are already superposed in the ground state. Detailed studies of QSL states have shown that higher-dimensional spinons can have different character. They may obey Fermi-Dirac statistics [Read 1991], Bose-Einstein statistics [Affleck 1988] or even anyonic statistics [Stern 2010]. They might be gapped, or gapless, or they may even be so strongly interacting that there are no sharp excitations of any kind [Rantner 2002]. Furthermore, these spinons cannot live by themselves but are generally accompanied by gauge fields, just as electrons are always accompanied by electromagnetic gauge fields. This is a dramatic example of emergent phenomena, where new particles and fields emerge at low-energy scales but are totally absent in the Hamiltonian that describes the initial system [Lee 2008b].

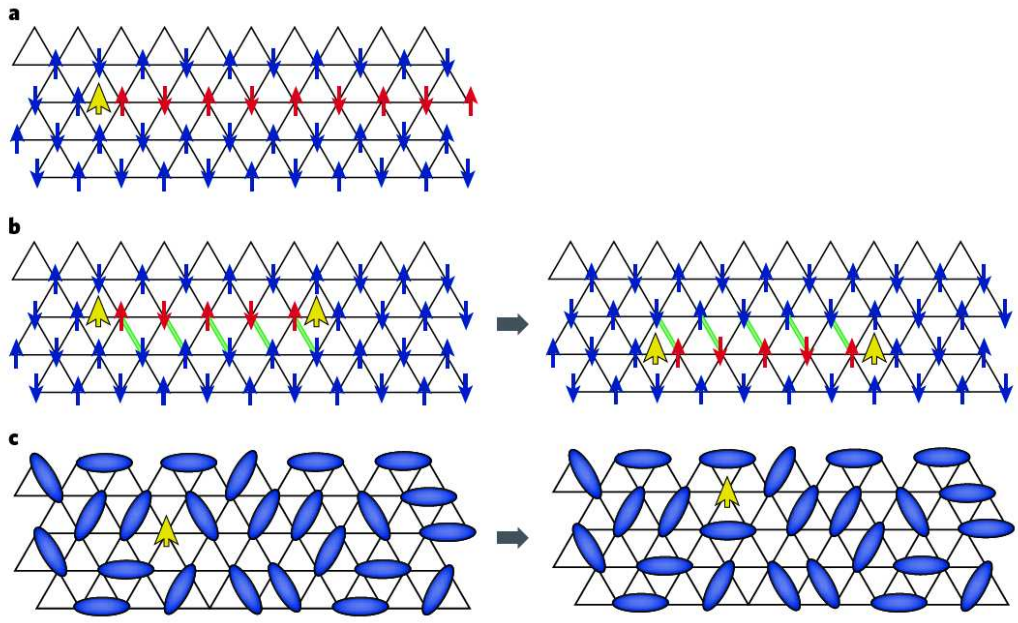

Figure 4.2: **a**, In a quasi-1D system (such as the triangular ribbon depicted), spinons are formed as a domain wall between two antiferromagnetic ground states. Creating a spinon (yellow arrow) thus requires the flipping of a semi-infinite line of spins (red arrows). The spinon cannot hop between chains, because to do so would require the coherent flipping of an infinite number of spins, here would mean to flip all the red spins and their counterparts on the next chain. **b**, A bound pair of 1D spinons forms a triplon. Because a finite number of spins are flipped (red arrows) between the two domain walls (yellow arrow), the triplon can coherently move between chains, by the flipping of spins along the green bonds. **c**, In a 2D QSL, a spinon is created simply as an unpaired spin, which can then move by locally adjusting the valence bonds. Figures and caption are adapted from Ref. [Balents 2010].

4.1.2 Realization of QSLs in Models

The number of microscopic models that host a QSL ground state has been increasing steadily in recent years. Our work of the Hubbard model on the honeycomb lattice is among them, and will be discussed in detail in the next section. There is also theoretical consensus that the Hubbard model on a triangular lattice has a QSL ground state for intermediate-strength Hubbard repulsion near the Mott transition [Lee 2008a, Yoshioka 2009, Yang 2010].

Besides the Hubbard model on the honeycomb and triangular lattices, one of the earliest microscopic models hosting QSL ground state are the **hard-core bosons on the Kagome lattice** with short-range hopping and repulsive interac-

tions [Balents 2002b, Isakov 2006a, Isakov 2007],

$$H = -t\sum_{(i,j)}(b_i^\dagger b_j + \text{h.c.}) + V\sum_{\hexagon}(n_{\hexagon})^2 - \mu\sum_i n_i, \tag{4.1}$$

where $b_i^\dagger$ (b_j) is the boson creation (annihilation) operators. $t > 0$ is the hopping amplitude, $V > 0$ is the repulsion strength, $n_i = b_i^\dagger b_i$ is the number operator. The hopping term (i, j) connects the first, second, and third neighbors. By the mapping between hard-core bosons and $S = 1/2$ spins (see the Chapter 3.1), this model is equivalent to a short range XXZ model

$$H = -J_\perp\sum_{\hexagon}[(S^x_{\hexagon})^2 + (S^y_{\hexagon})^2 - 3] + J_z\sum_{\hexagon}(S^z_{\hexagon})^2, \tag{4.2}$$

where $J_\perp = t$ and $J_z = V$, $S^x_{\hexagon} = \sum_{i\in\hexagon} S^x_i$ is a sum over six spins on each hexagon of the Kagome lattice unit cell, and $\sum_{\hexagon}$ denotes a sum over all hexagons on the lattice. Isakov et al. explored the ground state phase diagram of this model using SSE QMC simulations (see the Chapter 2.1). They found a continuous quantum phase transition between a ferromagnet and a quantum spin liquid as the ratio of longitudinal over transverse coupling $J_z/J_\perp$ increases. The transition is of the 3D XY universality class. The spin liquid state in this model has been characterized as having topological order with four-fold topological degeneracy in the ground state. The excitations in this spin liquid phase are visons, which are gapped Z_2 vortices in the effective field theory description.

More recently, Levin and Wen proposed to measure the topological order directly by looking at the topological entanglement entropy 2γ [Levin 2006]. The topological entanglement entropy is designed to pick up non-local correlations in the ground state wavefunction that are not manifest as conventional long-range order, such as the Z_2 topological degeneracy. The entanglement entropy between different subregions of the system A and its complement B (where $A\cup B$ is the entire system) can be quantified by the Renyi entropies [Renyi 1961]

$$S_n(A) = \frac{1}{1-n}\ln[\text{Tr}(\rho_A^n)], \tag{4.3}$$

where ρ_A is the reduced density matrix of region A. Isakov et al. successfully implemented the idea of Levin and Wen by considering separately the Renyi entropies on four differently shaped subregions of the 2D Kagome lattice on a torus (with periodic boundary conditions in both directions), with the help of the replica trick, which allows direct access to $S_n(A)$ for $n \geq 2$ in quantum Monte Carlo simulations [Melko 2010]. They found out that as temperature $T \to 0$, the topological entanglement entropy 2γ indeed approaches two distinct plateaus $2\gamma = \ln(2)$ and $2\gamma = 2\ln(2)$, as expected for a state with Z_2 topological order [Isakov 2011].

Another example of a QSL ground state is the **AF Heisenberg model on the Kagome lattice**. The Hamiltonian of the system, $H = J\sum_{\langle i,j\rangle}\mathbf{S_i}\cdot\mathbf{S_j}$, is isotropic in both space and spin directions, Yan et al. performed extensive DMRG simulations on the Kagome cylinders with circumferences as large as

$L = 12$ lattice spacings, and applied carefully designed finite size analysis to their data [Yan 2011]. They found the ground state of this simple system is a singlet-gapped spin liquid with substantially lower energy than previously proposed valence bond solids [Nikolic 2003, Singh 2007, Singh 2008]. The spin liquid ground state is likely to have Z_2 topological order [Yan 2011]. Figure 4.3 shows the geometry of the cylinders they studied and the energy comparison with previous proposals.

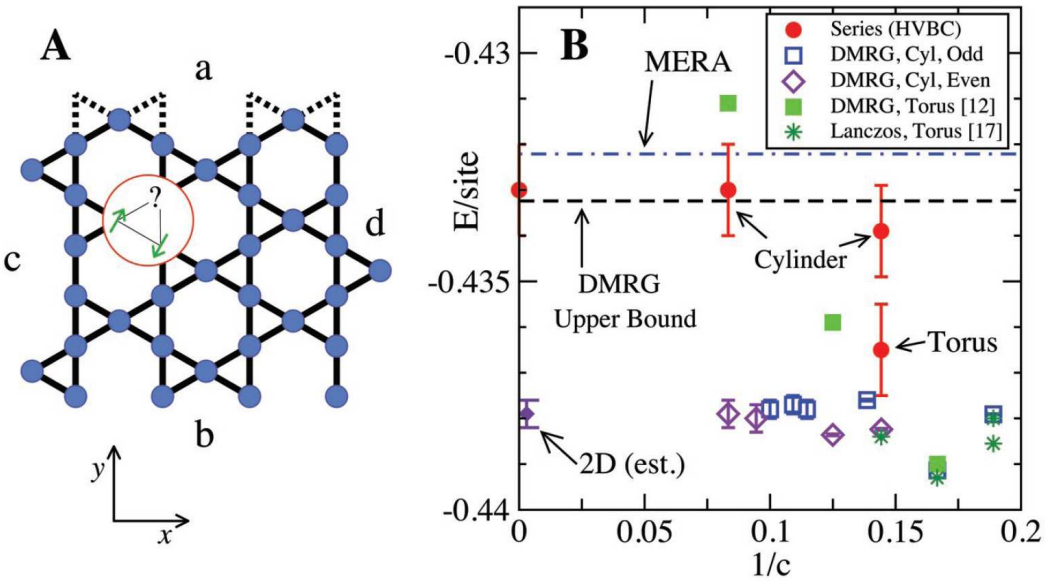

Figure 4.3: **(A)** A section of Kagome lattice. The frustration is indicated by the spins shown on one triangle. To make a cylinder the top (a) is connected to the bottom (b) by the dotted bonds. To further make a torus, similarly connect sides (c) and (d). **(B)** Comparison of energies per site for various lattice geometries and methods. For cylinders, the horizontal axis is the inverse circumference in units of inverse lattice spacings. For tori [Jiang 2008a, Läuchli 2011], the smallest circumference is used. The MERA [Evenbly 2010] and DMRG upper bound results apply directly to an infinite 2D system as does the series HVBC result [Singh 2007, Singh 2008]. Figures and caption are adapted from Ref. [Yan 2011].

In this tour-de-force DMRG work, Yan et al. firstly demonstrated that the so called honeycomb valence bond crystal (HVBC) obtained from perturbative series expansion [Nikolic 2003, Singh 2007, Singh 2008] with a large 36-site unit cell, is not the true ground state. They purposely chose geometries that accommodate the HVBC state, as shown in Fig. 4.4. They even begin the calculation with the HVBC initial state. But these biases towards the HVBC state demonstrate that the HVBC is a metastable up to $m \approx 2400$, where m is the number of states kept per block in DMRG simulation. When m increases even further, the system transitions to a quantum spin liquid state. In this way, the possibility of the HVBC ground state is completely ruled out.

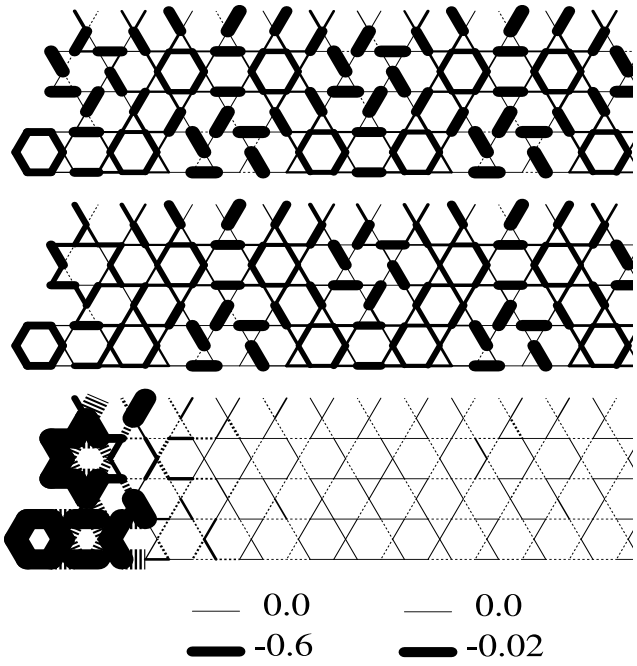

Figure 4.4: Valence bond pattern for the left two-thirds of a 208 sites cylinder. The width of the lines is proportional to $|\langle \mathbf{S_i} \cdot \mathbf{S_j} \rangle|$ (up and middle panels and the left key) or $|\langle \mathbf{S_i} \cdot \mathbf{S_j} - e_\alpha \rangle|$ (bottom panel and the right key), with dashed lines indicating the quantity is positive. Here α signifies bond direction and the approximate bulk bond correlations are $e_\alpha = -0.223$ for horizontal bonds and $e_\alpha = -0.217$ for diagonal bonds. The top panel shows sweep 6 with $m = 200$, with HVBC as initial ground state. The middle panel sweep 14 with $m = 600$, the HVBC state is still visible. The bottom panel the final sweep 34 with $m = 8000$. Between middle and bottom panel, near $m = 2400$ (not shown), the energy drops abruptly by about 0.1%, the HVBC is replaced by a spin liquid state. Figures and caption are adapted from Ref. [Yan 2011].

Yan et al. found the ground state has only short-range correlations, with a finite energy gap for any excitations, including the spin singlet ($S = 0$) excitations. The singlet gap, Δ_0, separating the ground state from the lowest $S = 0$ excited state, is approximately $0.05J$, with uncertain errorbars on this estimate. Such a state can be represented as short-range RVB state, and they furthermore found this RVB appears to substantially prefer certain 8-site loops of a diamond shape. As shown in Fig. 4.5, they probe the response of the ground state to enhancing possible elementary resonant loops, by slightly increasing the exchange couplings along the bonds of such a loop at the center of a cylinder, and measured how much this enhancement will affect the spin-spin correlations along the loop and elsewhere. Fig. 4.5 **B** clearly shows it is the 8-site diamond loop that elicits the strongest response. The 6-site "perfect hexagon" loop (Fig. 4.5 **A**) shows a much smaller response, suggesting that this resonant loop is actually underweighted in

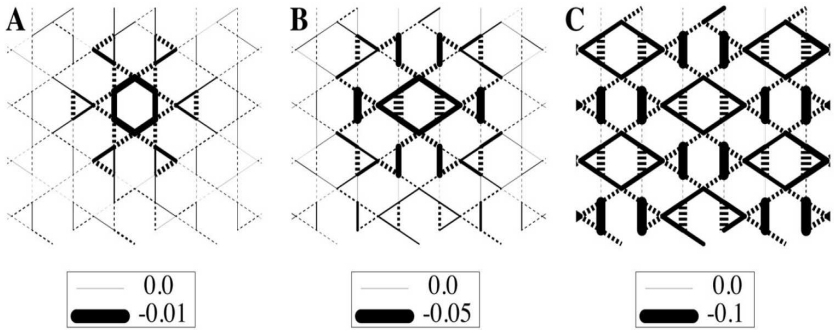

Figure 4.5: Response of the spin liquid to small perturbation. In each case certain bonds have been strengthened: **(A)** the bonds in the 6 site hexagon have been strengthened by 1%; **(B)** the bonds in the 8 site diamond have been strengthened by 1%; **(C)** the wide strong and weak vertical bonds have been strengthened by ±0.5%. Line width indicates the subtracted bond spin-spin correlations, $|\langle \mathbf{S_i} \cdot \mathbf{S_j} - e_\alpha \rangle|$, with dashed lines indicating the quantity is positive and e_α s have the same meaning and values as in Fig. 4.4. The response increases strongly from **(A)** to **(B)** to **(C)**, surrounding dimers arise in response to the diamond pinning in **(B)** and diamonds arise in response to dimmer pinning in **(C)**. Figures and caption are adapted from Ref. [Yan 2011].

the ground state. Moreover, there is suggestive evidence that the ground state is two-fold degenerate on extrapolation to large system sizes, as expected for a spin liquid with Z_2 topological order.

4.1.3 Realization of QSLs in Materials

Experimental confirmation of the existence of the spin liquid state has been elusive, and only recently have several promising examples surfaced. In this section, we will introduce several materials considered to be possible candidates for QSLs. According to their degree of electron localization, we classify them into two categories: the first category contains those materials regarded as strong Mott insulators, in which the exchange coupling is small relative to the Mott charge gap. For these materials, a microscopic description in terms of Heisenberg spins is justified. These materials are highly-frustrated quantum magnets such as the Herbertsmithite [1] $ZnCu_3(OH)_6Cl_2$ [Keren 1994, Mendels 2007, Helton 2007, Imai 2008], Vesignietite [2] $BaCu_3V_2O_8(OH)_2$ [Okamoto 2009], and $Na_4Ir_3O_8$ [Okamoto 2007], their structures are the highly frustrated Kagome- (2D) and Hyper-Kagome-lattices (3D). By contrast, the second category mainly contains the organic compounds κ-(BEDT-TTF)$_2$X [Shimizu 2003, Kurosaki 2005, Yamashita 2008, Yamashita 2009, Pratt 2011] and β'-Z[Pd(dmit)]$_2$ [Itou 2007, Yamashita 2010]. In these compounds

[1] A mineral discovered in Chile in 1972 and named after Herbert Smith.

[2] Named after Louis Vésignié (1870-1954), mineral collector, President of the Mineralogical Society of France.

the exchange energies are larger and the charge gaps are smaller, these materials are therefore weak Mott insulators, in which the electronic spins are much less localized. In the organic compounds, charge fluctuations play an important role. The Hubbard repulsion U is much smaller than in inorganic compounds, owing to the extended nature of the molecular orbital constituting each spin. In fact it is believed that in the proximity of an insulator-to-metal transition implies that the spins interact with a more complicated Hamiltonian such as the anisotropic Hubbard models [Powell 2011].

4.1.3.1 QSLs in Frustrated Magnets

$\mathbf{ZnCu_3(OH)_6Cl_2}$ (Herbertsmithite) is a layered material whose Cu^{2+} ions in each layer constitute a Kagome lattice [Mendels 2007, Helton 2007, Imai 2008], see the upper panels (left and right) of Fig. 4.6. Although the exchange energy is as large as $\sim$ 200K, inelastic neutron scattering [Helton 2007] and muon spin rotation (μSR) [Mendels 2007] measurements demonstrate the material does not show any magnetic ordering down to 50 mK. In terms of spin dynamcis, inelastic neutron scattering and μSR reveal a spectrum of low energy spin excitations with no observable gap down to 0.1 meV. The specific heat at low temperatures also follows a power law temperature dependence.

$\mathbf{Na_4Ir_3O_8}$ is a spin-1/2 hyperkagome lattce in 3D. The spins come from low spin $5d^5$ Ir^{4+} ions and form a 3D network of cornered shared triangles. This gives rise to a $S = 1/2$ antiferromagnetically coupled spin system on a geometrically frustrated Hyper-Kagome lattice [Okamoto 2007], see lower left and right panels of Fig. 4.6. It should be realized that because of the large atomic number, spin-orbit coupling in Ir is expected to be strong. This question is recently addressed by Chen and Balents [Chen 2008]. Temperature dependent spin susceptibility around room temperature yields an antiferromagnetic Curie-Weiss constant $\theta_w \sim 650$K, and there is no anomaly indicative of long range order down to 2 K. Some kind of phase transition or crossover seems to occur at a temperature $T_c \sim 20$K where the specific heat C_V divided by T shows a sharp peak. But the spin susceptibility $\chi(T)$ is almost temperature independent at low temperatures. Based on these experimental data, Zhou et al. suggested a fermionic spin liquid theory that explains the transition at 20 K as a transition between a $U(1)$ spinon Fermi liquid and a Z_2 spin liquid where spinons are paired at low temperatures. At high temperatures, $T_c < T < \theta_w$, however, the system is a Fermi liquid of spinons with a spinon Fermi surface [Zhou 2008].

4.1.3.2 QSLs close to Mott transition

Now we turn to the second category of the QSL materials – the weak Mott insulators – in which electrons are more itinerant. These materials are mainly the organic charge-transfer salts κ-(BEDT-TTF)$_2$X [Shimizu 2003] and β'-Z[Pd(dmit)]$_2$ [Itou 2007]. Since the exchange energies are larger and the charge gaps

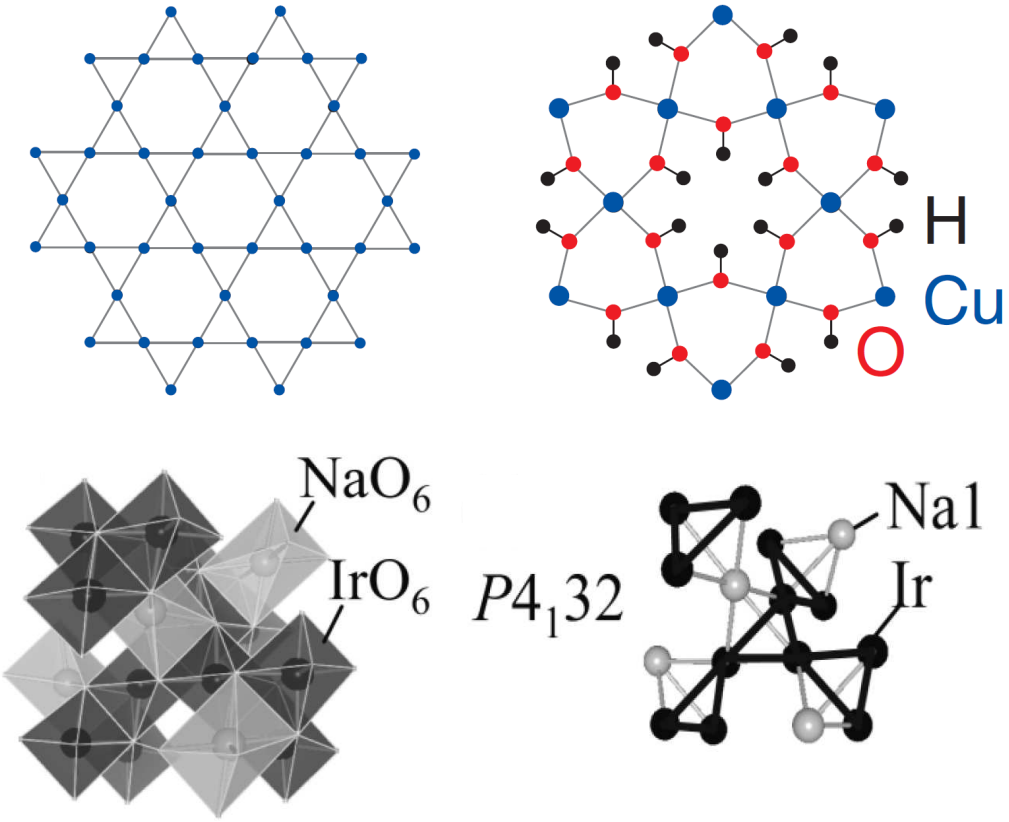

Figure 4.6: **Upper left** A Kagome lattice. **Upper right** Cu^{2+} Kagome layer in $ZnCu_3(OH)_6Cl_2$. Cl^- sites are above or below the middle of the Cu^{2+} triangles. Figures and caption are adapted from Ref. [Imai 2008]. **Lower left** Crystal structure of $Na_4Ir_3O_8$. Among the three Na sites, only Na1 site is shown for clarity. Black and gray octahedra represent IrO_6 and NaO_6, respectively. The spheres inside the octahedra represent Ir and Na atoms and oxygens occupy all the corners. **Lower right** HyperKagome Ir and Na sublattice derived from the structure of $Na_4Ir_3O_8$. Figures and caption are adapted from Ref. [Okamoto 2007].

are smaller in the weak Mott insulators, one can drive them through metal to Mott insulator transition by appling magnetic field, hydrostatic or chemical pressures. And if the temperature is lower than 10 K, an Mott insulator to superconductor transition occurs upon increasing pressure [Nam 2007], resembling the similar phenonema in cuprates and pnictides, as shown in Fig. 4.8 **(b)**. The organic charge-transfer salts can be synthesized in ultra-pure single crystals. Hydrostatic pressure of the order of kbars, chemical pressure by substitution of anion, **X**, layers and external magnetic field provide means of tuning the materials through different ground states [Powell 2011].

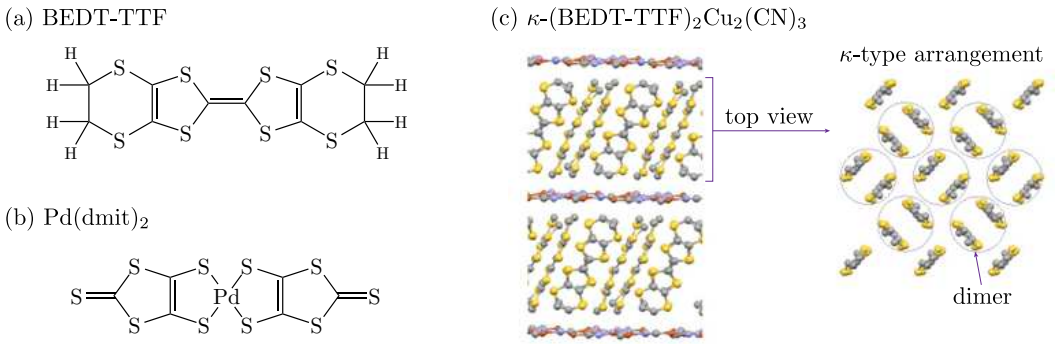

Figure 4.7: The molecules bis-(ethylene-dithio)-tetra-thia-fulvalene (BEDT-TTF) **(a)** and Palladium-1,3-dithiole-2-thione-4,5-dithiolate (Pd(dmit)$_2$) **(b)**, which form the charge transfer salts with frustrated triangular lattices. The quasi-two-dimensional layers of organic molecules are separated by the anion-layer, here formed by $Cu_2(CN)_3$ **(c)**. In the crystallographic κ-phase the organic molecules arrange themselves in dimers which form slightly distorted triangular lattice. **(a)** and **(b)** are adapted from Ref. [Powell 2011], **(c)** is adapted from Ref. [Lang 2010].

κ-(BEDT-TTF)$_2$X are a class of organic charge transfer salts. They form crystal with alternating layers of the electron donor BEDT-TTF molecules (shown in Fig. 4.7 **(a)**), and the electron acceptors, anion **X**, leading to a quasi-two-dimensional band structure. Charge is transferred from the organic (BEDT-TTF) layer to the anion (**X**) layer. The frontier molecular orbitals of the BEDT-TTF molecule are π orbitals, these orbitals overlap strongly with the equivalent orbitals on the other molecule in the same dimer (see Fig. 4.7 **(c)**), this suggests to treat the dimers as single units in a lattice model of a slightly anisotropic triangular lattice,

$$H = -t \sum_{\langle i,j\rangle,\sigma} c^\dagger_{i,\sigma} c_{j,\sigma} - t' \sum_{(i,j),\sigma} c^\dagger_{i,\sigma} c_{j,\sigma} + U \sum_i n_{i,\uparrow} n_{i,\downarrow}, \tag{4.4}$$

where $c^\dagger_{i,\sigma}$ ($c_{i,\sigma}$) creates (destroys) an electron with spin σ on site (dimer) i, t and t' are the hopping amplitudes between neighboring dimers, as shown in the inset of Fig. 4.9 **(a)**, and U is the effective Coulomb repulsion between two electrons on the same site (dimer).

The values of the hopping amplitudes, t and t', are still under debate, and their ratio t'/t sets the strength of the frustration in the system. Quanutum oscillation or angle-dependent magnetoresistance oscillation measurements [Kartsovnik 2004], suggest the hopping t to be of the order of tens of eV. The ratio t'/t, depending on the anion **X**, is in the range of $[0.75, 1.1]$, which yields significant frustration effects [Pratt 2010, Powell 2011]. The local Coulomb repulsion U is estimated to be of the order of the hopping such that the system can be understood in terms of a half-filled Hubbard model on the (anisotropic) triangular lattice [Motrunich 2005, Lee 2005, Lee 2008a, Tocchio 2009, Yoshioka 2009, Powell 2011].

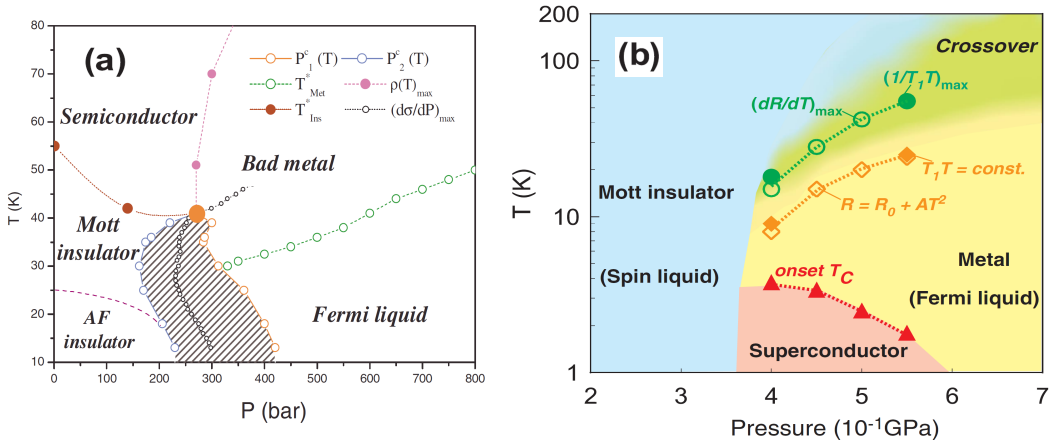

Figure 4.8: **(a)** Pressure-temperature phase diagram of κ-(BEDT-TTF)$_2$Cu[N(CN)$_2$]Cl. At low temperatures it undergoes a first-order Mott transition from an antiferromagnetic (AF) insulator to a metal when hydrostatic pressure is applied. In the insulating phase raising the temperature destroys the AF order. **(b)** Pressure-temperature phase diagram of κ-(BEDT TTF)$_2$Cu$_2$(CN)$_3$. Similar to that of **(a)**, but has important differences. Most importantly the Mott insulating phase does not show any signs of long-range magnetic order down to 20 mK. Thus, κ-(BEDT TTF)$_2$Cu$_2$(CN)$_3$ is believed to be a spin liquid at ambient and low pressures. Upon increasing pressure at low temperatures, the system undergoes transition from a QSL to a superconductor. The geometrical frustration of κ-(BEDT TTF)$_2$Cu$_2$(CN)$_3$ is the greatest among the κ salts. Panel **(a)** is adapted from Ref. [Limelette 2003], panel **(b)** is adapted from Ref. [Kurosaki 2005].

The strength of the electronic correlations and the degree of frustration is determined by the choice of anion, X, and the applied hydrostatic pressure. For example, κ-(BEDT-TTF)$_2$Cu[N(CN)$_2$]Cl [Limelette 2003] is an antiferromagnetic Mott insulator at ambient pressure (Fig. 4.8 **(a)**); changing the the anion to X=Cu[N(CN)$_2$]Br or Cu(NCS)$_2$, the compounds become superconducting below ∼10 K [Powell 2011]. The most frustrated κ-(BEDT TTF)$_2$Cu$_2$(CN)$_3$ [Kurosaki 2005] probably has a spin liquid ground state (Fig. 4.8 **(b)**) at ambient pressure. Shiziumi et al. [Shimizu 2003] measured its spin susceptibilities: in the Mott insulating phase the spin degrees of freedom are described by a Heisenberg model with an AF exchange coupling of $J \sim 250$ K close to the Mott transition, and κ-(BEDT-TTF)$_2$Cu$_2$(CN)$_3$ lacks signatures of magnetic transition in the susceptibility down to 32 mK. This temperature is four orders of magnitude smaller than the exchange coupling which led the conclusion of κ-(BEDT-TTF)$_2$Cu$_2$(CN)$_3$ being a QSL. The absence of evidence for long-range magnetic order is supported by NMR spectra at temperatures as low as 20 mK!

Three recent experiments have attempted to reveal the nature of the quantum spin liquid phase in κ-(BEDT-TTF)$_2$Cu$_2$(CN)$_3$. S. Yamashita et al. measured the

tempearture dependence of the heat capacity [Yamashita 2008]. By fitting the low temperature heat capacity data to the formula $C_p = A/T^2 + \gamma T + \beta T^2$, they found a large T-linear contribution (finite γ). By making a analogy with the electronic heat capacity in metals, which is also linear in T, S. Yamashita et al. conclude the spin excitations in the QSL phase is *gapless*. However, shortly afterwards, M. Yamashita et al. performed the thermal transport measurement down to 80 mK, and found out "unambiguous evidence for the absence of a gapless excitation", indicating a *spin-gapped* QSL phase [Yamashita 2009]. Figures 4.9 **(a)** show the temperature dependence of the in-plane thermal conductivity κ(T) in zero field for two different single crystals of deuterated κ-(BEDT-TTF)$_2$Cu$_2$(CN)$_3$. As the temperature is lowered, the thermal conductivity decreases and exhibits a broad hump around $T^* \sim 6\ K$. Futhermore, Figure 4.9 **(b)** shows the thermal conductivity at low temperatures, measured in two samples and under different magnetic fields. For a metal one expects the thermal conductivity to behave as $\kappa(T) = \alpha T + \beta T^3 + \ldots$, where electrons give rise to the linear term, and phonons contribute to the cubic term [Ashcroft 1976]. But as shown in Fig. 4.9 **(b)**, a striking deviation of κ/T from a T^2 dependence is observed for both samples. Therefore, such clear non-T^2 dependence, together with the fact that κ is enhanced by magnetic field give indication of a substantial magnetic contribution in κ in low temperatures. Moreover, both curves in Fig. 4.9 **(b)** exhibit a convex trend, the authors found the extrapolation of κ/T to $T \to 0$ give zero residue of thermal conductivity. The vanishing κ/T indicates the absence of low-lying fermionic excitations, which led M. Yamashita et. al. to conclude that the spin liquid state of κ-(BEDT-TTF)$_2$Cu$_2$(CN)$_3$ is *gapped* [Yamashita 2009]. The estimated spin gap from the κ via $1/T$ Arrhenius plot is of the magnitude of $\Delta \sim J/500$.

More recently, Pratt et al. [Pratt 2011] used muon spin rotation (μSR) to study the field-induced phase transition of κ-(BEDT-TTF)$_2$Cu$_2$(CN)$_3$. With such a exquisitely sensitive technique, Pratt et al. show that the naive QSL state of κ-(BEDT-TTF)$_2$Cu$_2$(CN)$_3$ can be frozen and become ordered by the application of a magnetic field of 14 millitesla, which is only a few hundred times stronger than the magnetic field of Earth. The ordered phase is a weak-moment antiferromagnetic (WAF) insulator with strongly suppressed magnetic moment, and it can be described as Bose-Einstein condensation of spin excitations. The spin gap in the QSL phase, deduced from the μSR data, is extremely small, $\Delta = 3.5(1)$ mK, nearly five magnitudes weaker than the exchange coupling $J \sim 250$ K.

Clearly, the experimental efforts in κ-(BEDT-TTF)$_2$Cu$_2$(CN)$_3$ raise a number of profound questions about the nature of QSL in this material, further investigations are in urgent need.

β'-Z[Pd(dmit)$_2$]$_2$ is the second class organic charge transfer salts with a potentially QSL ground state [Itou 2008, Itou 2009, Yamashita 2010]. It is based on Pd(dmit)$_2$ molecules (see Fig. 4.7 **(b)**), and the compound is usually simply referred to as dmit. The Z denotes the anions which form layers separating the quasi two di-

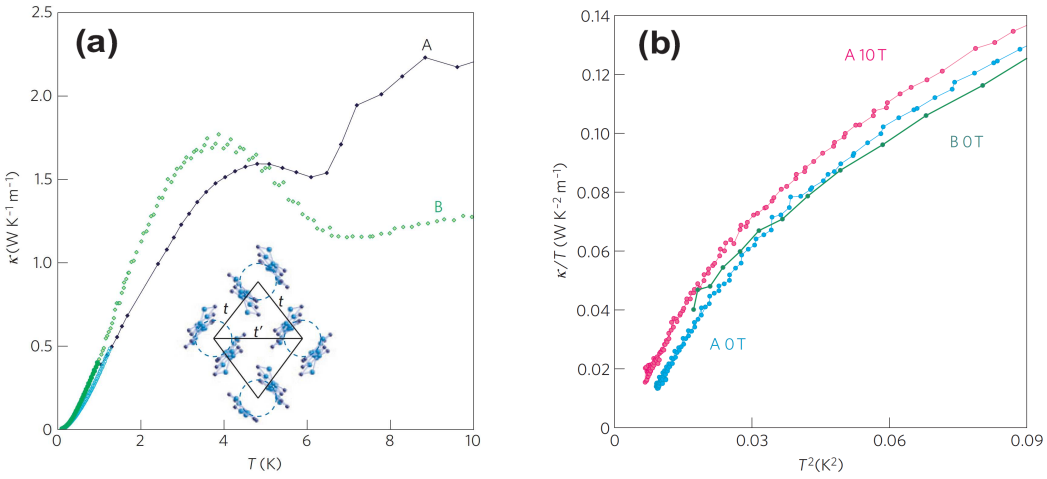

Figure 4.9: **(a)** Temperature dependence of the in-plane thermal conductivity κ(T) for two different single crystals of deuterated κ-(BEDT-TTF)$_2$Cu$_2$(CN)$_3$. As the temperature is lowered, κ(T) decreases and exhibits a broad hump starting to increase at around $T^* \sim 6\ K$. Inset: The crystal structure of a BEDT-TTF layer of κ-(BEDT-TTF)$_2$Cu$_2$(CN)$_3$ viewed along the long axes of BEDT-TTF molecules. Pairs of BEDT-TTF molecules form dimers arranged in a triangular lattice. t and t' are the hopping amplitudes between dimers. **(b)** Thermal conductivity divided by temperature $\kappa(T)/T$ of κ-(BEDT-TTF)$_2$Cu$_2$(CN)$_3$ plotted as a function of T^2 below 300 mK in zero field (blue for sample A and green form sample B) and at $H = 10T$ (red, sample A) applied perpendicular to the basal plane. κ/T for all data vanishes as extrapolating to $T \to 0$ K, indicating the absence of the gapless fermionic excitations. Panels were adapted from Ref. [Yamashita 2009].

mensional organic molecules. Of particular interest is the QSL candidate compound EtMe$_3$Sb[Pd(dmit)$_2$]$_2$ (dmit-131). In the β' crystal phase two Pd(dmit)$_2$ molecules form a dimer, and the dimers arrange themselves in an anisotropic half-filled triangular lattice, more anisotropic than the κ-salts. The AF exchange coupling is also large $J \sim 250$ K and again no magnetic order could be found down to temperature of 1.37 K – two orders of magnitude smaller than J [Itou 2008]. Recent thermal conductivity experiments reveal a sizable linear temperature dependence of the thermal conductivity in the $T \to 0$ limit, indicating the presence of gapless excitations with long mean free path, analogous to excitations near the Fermi surface in metal. However, the magnetic field dependence of the thermal conductivity suggests a concomitant appearance of spin-gap-like excitations at low temperatures [Yamashita 2010]. The coexistence of two kinds of excitations impose new challenge to QSL theories and future experiments.

4.2 Quantum Spin Liquid emerging in the Hubbard Model on the Honeycomb Lattice

With the introduction of the QSLs in theoretical models and solid state materials, now we are ready to discuss the quantum spin liquid phase we found in the Hubbard model on the Honeycomb lattice by large scale PQMC simulations. This work has been published in Ref. [Meng 2010], on which the materials of this section are based, the essential finding of this chapter are at the same time published in the Ph.D. thesis of my collaborator Thomas Lang [Lang 2010].

4.2.1 Hubbard Model on the Honeycomb Lattice

The quantum mechanical description of the relativistic electron was attained by Dirac, who revealed both its intrinsic angular momentum ($S = 1/2$), and the existence of its antiparticle, positron [Weinberg 2005]. In case of a vanishing rest mass, the energy of Dirac fermions is a linear function of momentum. Such massless Dirac fermions were recently observed in 2D solid state system like graphene [Castro Neto 2009] and surfaces of bismuth based compounds [Zhang 2009, Chen 2009, Herbut 2009]. For graphene, a single layer of carbon atoms with honeycomb structure, unusual electronic behavior is anticipated, and partly verified in experiments, due to the 2D Dirac-like dispersion of the electrons at low energies. As shown in Fig. 4.10, the tight-binding dispersion of electron on the graphene honeycomb lattice, has a linear dispersion close to the K (and K') point on the edge of its Brillouin zone (left and middle panels of Fig. 4.10). So at half-filling, free electrons with momentum close to K and K' in the honeycomb lattice behave as massless, relativistic, Dirac fermions. And since the density of states is vanishing linearly close to the Fermi energy (right panel of Fig. 4.10), the system can be described as a semimetal (SM).

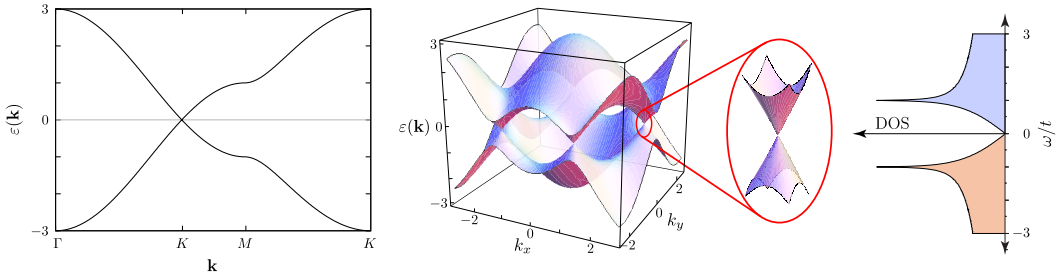

Figure 4.10: Left: Band structure along the high symmetry path, $\Gamma \to K \to M \to \Gamma$, in the first Brillouin zone of graphene honeycomb lattice. Middle: a 3D plot of the graphene honeycomb dispersion, with zoom-in of the energy bands close to one of the Dirac point K. Right: the density of states (DOS) of the nearest neighbor tight binding model on the honeycomb lattice. Close to the half-filled Fermi energy, $\omega/t = 0$, the DOS can be approximated by $\rho(\omega) \propto |\omega|$.

The interplay between a relativistic dispersion and electron interactions at half-filling is expected to lead to a quantum phase transition between the semimetal (SM) at low interaction strength and a Mott insulator (MI) at high interaction strength [Hermele 2007, Drut 2009]. A Mott insulating state is one that results not from the band structure alone but is due to the effects of electron interactions. Such correlation effects can be displayed by the Hubbard model in its most basic form, as exemplified in high temperature superconductivity [Lee 2006], or with ultra-cold fermionic atoms loaded in optical lattices [Jordens 2008, Schneider 2008]. Studies of Hubbard-like models on the honeycomb lattice suggested the emergence of exotic phases such as gapless QSL [Lee 2005, Hermele 2005, Hermele 2007], charge density waves [Raghu 2008, Honerkamp 2008], quantum spin Hall states [Kane 2005, Raghu 2008], or superconductivity [Uchoa 2007, Honerkamp 2008] at or near a density of one fermion per site (half-filling for the two-species case).

Given the various phases proposed for fermions on a honeycomb lattice based on Hubbard-like models, it is important to explore the ground state properties in the intermediate coupling regime of the original lattice model with an unbiased method. In this section, we apply the PQMC method described in Chapter 2.2 to the spin-1/2 Hubbard model at half-filling on the honeycomb lattice, due to the absence of a sign-problem in the PQMC simulations in the half-filled case, it is the method of choice for extrapolations to the thermodynamic limit (TDL), leading to essentially exact results limited only by the statistical noise. Our large-scale QMC simulations reveals that for intermediate interactions a gapped non-magnetic phase destroys the semimetal (SM) before the transition to an antiferromagnetically ordered Mott insulator (AF MI) at strong interactions sets in. This quantum spin liquid phase is characterized by local correlations that correspond to a resonating valence-bond (RVB) state [Anderson 1973, Fazekas 1974] as proposed in the context of high temperature superconductivity [Anderson 1987, Kivelson 1987, Lee 2006].

From the general introduction of QSL in the first part of this chapter, we understand there are two possible routes towards realization of quantum spin liquid state: i), geometric frustration induced macroscopic degeneracy of the classical ground state such as Heisenberg spins on a Kagome lattice [Yan 2011]; and ii), strong charge fluctuations sufficiently close to the Mott transition melting the magnetic long range order while at the same time maintianing the charge gap, such as the Hubbard model on the triangular lattice [Lee 2008a, Yang 2010] and its experimental realization κ-(BEDT-TTF)$_2$Cu$_2$(CN)$_3$ [Shimizu 2003, Powell 2011]. Our results follow the second category and show that RVB states are realized in a microscopic model of correlated electrons, bringing closer their observation in experiments. Honeycomb lattices of group IV elements [Cahangirov 2009], ultra-cold fermionic atoms loaded in optical lattices [Duan 2003, Jordens 2008, Schneider 2008], and nanofabricated honeycomb lattice on the surface of GaAs heterostructure [Singha 2011], appear as promising candidate systems to realize the RVB state out of Dirac fermions.

4.2.2 Phase Diagram from PQMC

Previous numerical studies of the Hubbard model on the honeycomb lattice [Sorella 1992, Scalettar 1993, Paiva 2005] suggested that a direct quantum phase transition separates the weak-coupling, paramagnetic semimetal phase from a strong-coupling, antiferromagnetic Mott insulator. When the repulsion is sufficiently strong, antiferromagnetism is certainly possible since the honeycomb lattice is bipartite, meaning that antiferromagnetic order is not geometrically frustrated, similar as that of the square lattice we have discussed in Chap. 3. However, the honeycomb lattice has the smallest coordination number in two dimensions ($z = 3$), such that the effect of quantum fluctuations is the strongest. Moreover, as shown in Fig. 4.10 (right panel), at half-filling the density of state is linearly vanishing close to the Fermi energy, this will render the strong antiferromagnetic instability caused by the nesting effect inact in the honeycomb lattice, different from that in the square lattice . Hence, the competition between the tendency to order and quantum fluctuations requires a detailed analysis of correlations and a careful finite size extrapolation to the TDL in order to characterize the possible phases. In order to assess the transition and the emergence of possible exotic phases [Lee 2005, Hermele 2005, Kane 2005, Hermele 2007, Uchoa 2007, Raghu 2008, Honerkamp 2008] mentioned above, we performed the PQMC simulation with particular focus near the region of the Mott transition.

The Hamiltonian of the spin-$\frac{1}{2}$ Hubbard model on the honeycomb lattice reads

$$H = -t \sum_{\substack{\langle i,j \rangle \\ \alpha=\uparrow,\downarrow}} (c^\dagger_{i\alpha} c_{j\alpha} + c^\dagger_{j\alpha} c_{i\alpha}) + U \sum_i n_{i\uparrow} n_{i\downarrow} \,, \tag{4.5}$$

where $c^\dagger_{i\alpha}$ ($c_{i\alpha}$) denotes the creation (annihilation) operator for fermions of spin $\alpha = \uparrow, \downarrow$ on lattice site i, and $n_{i\alpha} = c^\dagger_{i\alpha} c_{i\alpha}$. Here, t denotes the nearest-neighbor hopping amplitude, and $U \geq 0$ the strength of the onsite repulsion. The sum $\langle i, j \rangle$ runs over all nearest neighbor pairs. Our notation for points and vectors in real and momentum space is shown in the inset of Fig. 4.11. At $U = 0$, as discussed in the previous section, the tight-binding Hamiltonian has a linear dispersion near the Dirac pionts K and K', where the conduction and valence bands touch at half-filling, corresponding to a density $\sum_\alpha \langle n_{i,\alpha} \rangle = 1$. The PQMC simulation, discussed in Chap. 2.2, can be applied in the finite-U region to obtain ground state expectation values of any physical observable. The phases described in the following correspond to extrapolations to the TDL. For that purpose we study lattices of $N = 2L^2$ sites with periodic boundary conditions, and linear size L is always a multiple of 3 such that the Dirac points are under monitor in each system sizes, we have studied the system size up to $L = 18$. Also we found the projection parameter $\Theta = 40/t$ and an imaginary-time step $\Delta\tau = 0.05/t$ in the second-order Trotter decomposition to lead to converged quantities.

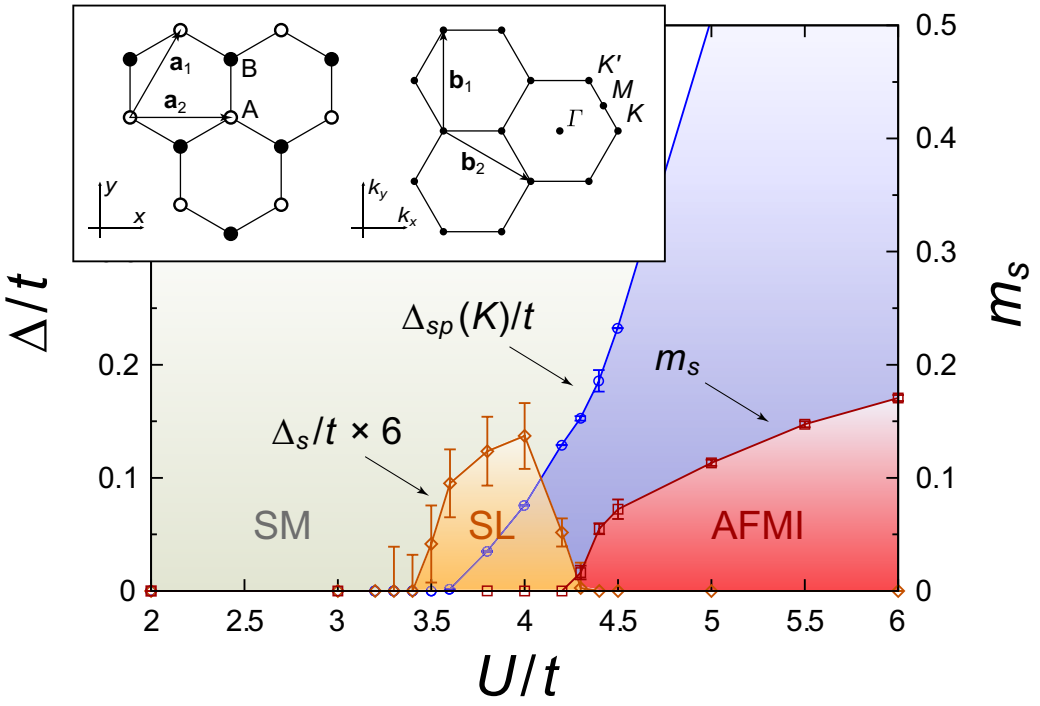

Figure 4.11: Phase diagram for the Hubbard model on the honeycomb lattice at half-filling. The semimetal (SM) and the AF Mott insulator (AFMI) are separated by a gapped quantum spin liquid (QSL) phase in an intermediate coupling regime. $\Delta_{sp}(K)$ denotes the single-particle gap at the Dirac point K and Δ_s the spin gap. m_s denotes the staggered magnetization whose saturation value is 1/2. Inset, the honeycomb lattice with primitive vectors $\mathbf{a}_1$ and $\mathbf{a}_2$, and the reciprocal lattice with primitive vectors $\mathbf{b}_1$ and $\mathbf{b}_2$. The Dirac points K and K' and the M and Γ points are marked.

4.2.2.1 Green's Function and Single-Particle Gap

To monitor the electronic properties of the system upon increasing U, we extracted the single-particle excitation gap $\Delta_{sp}(\mathbf{k})$ from the imaginary time displaced Green's function, as discussed in Chap. 2.2.4,

$$G(\mathbf{k},\tau) = \frac{1}{2}\sum_a \langle c^\dagger_{\mathbf{k}a\uparrow}(\tau) c_{\mathbf{k}a\uparrow}(0)\rangle = \frac{1}{2}\sum_a \langle c^\dagger_{\mathbf{k}a\downarrow}(\tau) c_{\mathbf{k}a\downarrow}(0)\rangle,$$

with $c^\dagger_{\mathbf{k}a\alpha}(\tau) = e^{\tau H} c^\dagger_{\mathbf{k}a\alpha} e^{-\tau H}$, here subscript $\mathbf{k}$ denotes the momentum, a denote the two sublattices A and B, and α is the spin flavor index $\uparrow$ and $\downarrow$. At large imaginary time τ,

$$G(\mathbf{k},\tau) \propto \exp(-\tau\Delta_{sp}(\mathbf{k})),$$

and $\Delta_{sp}(\mathbf{k})$ corresponds to the lowest-lying particle (or hole) excitation energy. At $U = 0$, the single-particle gap vanishes at the Dirac points K and K', and we thus

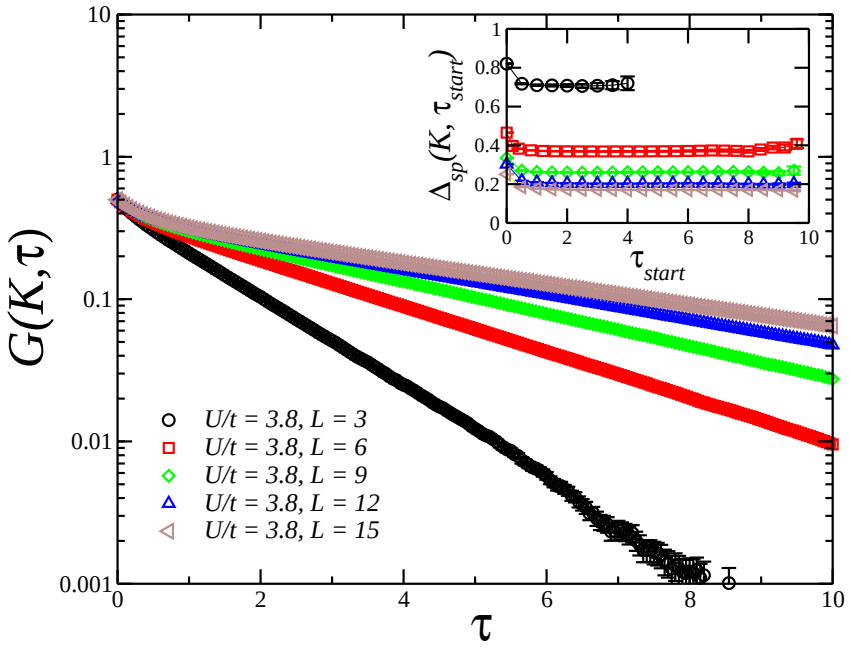

Figure 4.12: Green's function at the Dirac point $G(K,\tau)$ for different system sizes at $U/t = 3.8$. The inset shows the determination of $\Delta_{sp}(K)$ as a function of the starting point of the fitting range τ_{start} with the covariance matrix of the Green's function taken into account.

consider $\Delta_{sp}(K)$ in the following. To obtain a robust estimate of $\Delta_{sp}(K)$ for each value of U and each linear system size L, we diagonalized the covariance matrix of the $G(K,\tau)$ data to minimize the correlation among QMC data before fitting the lowest exponential decay of the QMC data (main panel of Fig. 4.12). Then we extrapolated $\Delta_{sp}(K)$ for various fitting ranges in terms of varying the starting point τ_{start}, as seen in the inset of Fig. 4.12. Finally, we took the converged values of $\Delta_{sp}(K)$ and perform the finite size scaling to obtain the thermodynamic limit estimation of the gaps for different U values, note that the finite size scaling is accompanied by bootstrap analyses, discussed in Chap. 2.3, such that we have controlled errorbars of the TDL value of the gaps. As for the staggered and uniform spin excitation gaps $\Delta_s(\Gamma)$ and $\Delta_u(\Gamma)$, we performed the same data analysis procedure.

$\Delta_{sp}(\mathbf{K})$ gives the minimal energy necessary to extract one fermion from the system, and corresponds to the gap that can be observed in photoemission experiments [Damascelli 2003]. As shown in the phase digram Fig. 4.11, $\Delta_{sp}(K) = 0$ for U/t below about 3.5, as expected for a SM. Fig. 4.13 **a** shows the finite size scaling of the single-particle gap for different U values. Clearly, a single-particle gap opens beyond $U/t \approx 3.6$, signaling the break-down of the weak-coupling SM.

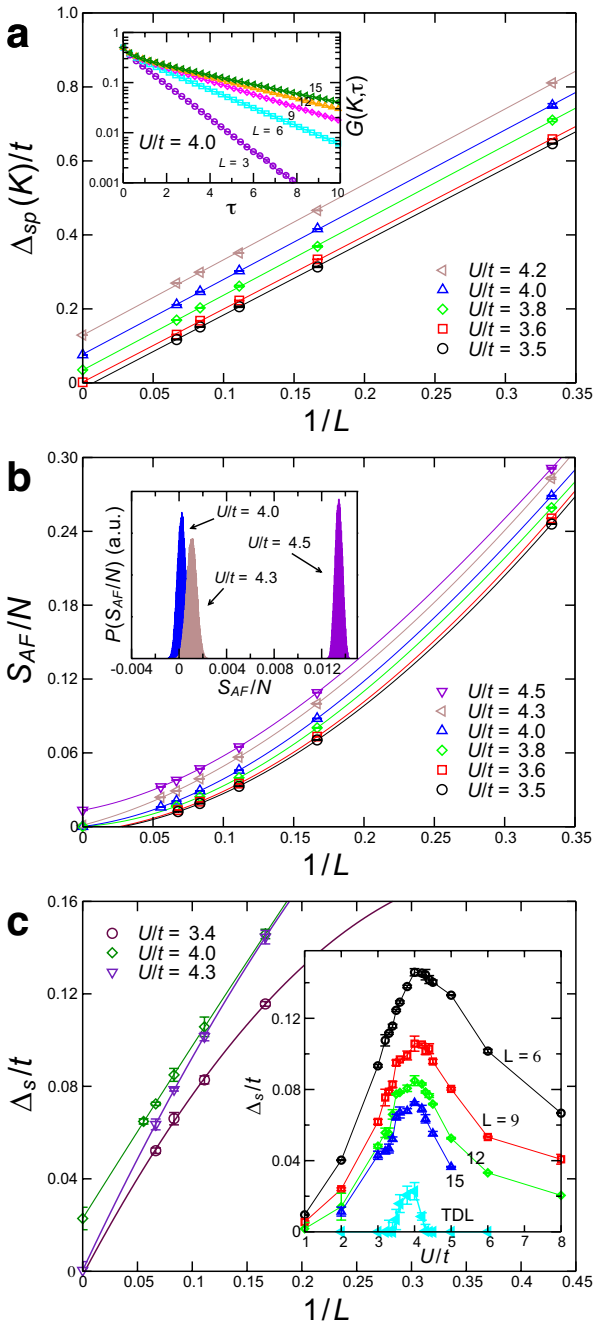

Figure 4.13: Finite size extrapolations of the excitation gaps and the antiferromagnetic structure factor. **a**, Single-particle gap at the Dirac point, $\Delta_{sp}(K)$, shown here for different values of U/t, is linear in $1/L$. $\Delta_{sp}(K)$ is obtained by fitting the tail of the Green's function, $G(K,\tau)$ (inset), to the form $e^{-\tau\Delta_{sp}(K)}$. **b**, Antiferromagnetic structure factor, S_{AF}, for various values of U/t, fitted with 3rd order polynomials in $1/L$. AF order appears beyond $U/t = 4.3$, as seen in the histograms from a Monte Carlo bootstrap analysis (inset). a.u. arbitrary units. **c**, Spin gap, Δ_s, for different values of U/t, fitted using 2nd order polynomials in $1/L$. Inset shows a pronounced dome in the finite size data, that sharpens to a region with finite spin gap between $U/t \sim 3.5$ and $U/t \sim 4.3$ in the TDL.

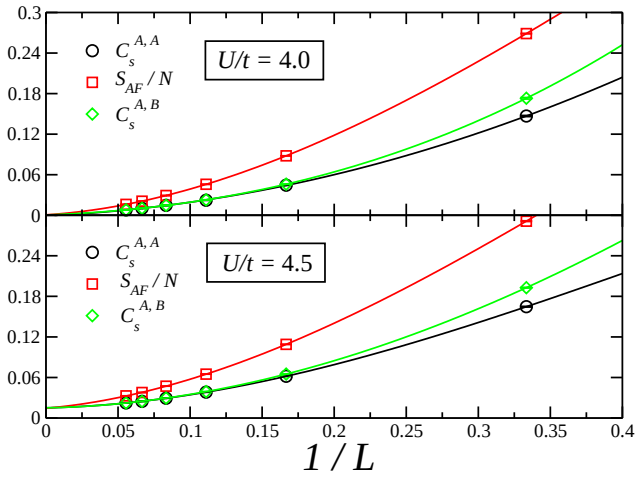

Figure 4.14: Comparison of the finite size scaling between the spin correlations $C_s^{A,A}$ and $C_s^{A,B}$ at the largest available distance and the staggered structure factor S_{AF} at $U/t = 4$ (upper panel) and $U/t = 4.5$ (lower panel), using 3rd order polynomials in $1/L$.

4.2.2.2 Spin Correlations

From previous analyses of the model [Sorella 1992, Scalettar 1993, Paiva 2005], one expects long range AF correlations when the MI appears. We therefore measured the AF spin structure factor S_{AF} that reveals long range AF order if $m_s^2 = \lim_{N\to\infty} S_{AF}/N > 0$. The AF order at large values of U/t resides within the unit cell of the honeycomb lattice. Hence, the spin structure factor for AF order relates to the staggered spin correlations at the Γ point of the Brillouin zone,

$$S_{AF} = \frac{1}{N}\Big\langle \Big[\sum_{\mathbf{x}} (\mathbf{S}_{\mathbf{x}A} - \mathbf{S}_{\mathbf{x}B})\Big]^2 \Big\rangle, \tag{4.6}$$

where the sum runs through all the unit cell $\mathbf{x}$ of the lattice.

In addition to the above structure factor, we also probed the spin-spin correlation functions in real space. To simplify the notation, as for the correlation between two local operators O_1 and O_2, we define the cumulant in the following way,

$$\langle\langle O_1 O_2 \rangle\rangle := \langle O_1 O_2 \rangle - \langle O_1 \rangle \langle O_2 \rangle \ . \tag{4.7}$$

The real-space spin-spin correlations

$$C_s^{a,b}(\mathbf{x},\mathbf{y}) = \langle\langle \mathbf{S}_{\mathbf{x}a} \cdot \mathbf{S}_{\mathbf{y}b} \rangle\rangle \ , \tag{4.8}$$

are measured at the largest available distance $\mathbf{d}_L = ([L/2+1]-1)\ \mathbf{a}_1 + ([L/2+1]-1)\ \mathbf{a}_2$ for different system sizes, and performed a finite size scaling of both $C_s^{A,A} = C_s^{A,A}(0,\mathbf{d}_L)$ and $C_s^{A,B} = -C_s^{A,B}(0,\mathbf{d}_L)$. In the TDL, $C_s^{a,b}(\mathbf{x},\mathbf{y})$ will scale to the same value as the structure factor S_{AF}/N, where N is the lattice site. A comparison of the scaling of these quantities with S_{AF} is shown for both $U/t = 4$ and

$U/t = 4.5$ in Fig. 4.14, exhibiting the consistency between these different approaches to quantify the spin correlations in the ground state.

Figure 4.13 **(b)** shows the QMC results of AF spin structure factor together with a finite size extrapolation, the TDL S_{AF}/N are obtained from bootstrap analysis with errorbars (see the histogram in the inset of Fig. 4.13 **b**). The TDL values of the staggerd magnetization ($m_s^2 = lim_{N\to\infty} S_{AF}/N$) are also presented in the phase diagram of Fig. 4.11. AF order appears beyond $U/t = 4.3$, a value that is consistent with previous estimates for the onset of long ranged AF order [Sorella 1992, Furukawa 2001, Paiva 2005, Lee 2009]. This leaves an extended window $3.5 < U/t < 4.3$, within which the system is neither a SM, nor an AF MI.

4.2.2.3 Spin Excitation Gaps

Further details on the nature of this intermediate region are obtained by examining the spin excitation gap, extracted from the long-time behavior of the imaginary-time displaced spin-spin correlation function at momentum vector $\mathbf{k}$ for both the staggered sector,

$$S_s(\mathbf{k},\tau) = \langle\langle(\mathbf{S}_{\mathbf{k}A}(\tau) - \mathbf{S}_{\mathbf{k}B}(\tau)) \cdot (\mathbf{S}_{\mathbf{k}A}(0) - \mathbf{S}_{\mathbf{k}B}(0))\rangle\rangle \ , \tag{4.9}$$

as well as the uniform sector,

$$S_u(\mathbf{k},\tau) = \langle\langle(\mathbf{S}_{\mathbf{k}A}(\tau) + \mathbf{S}_{\mathbf{k}B}(\tau)) \cdot (\mathbf{S}_{\mathbf{k}A}(0) + \mathbf{S}_{\mathbf{k}B}(0))\rangle\rangle \ , \tag{4.10}$$

where $\mathbf{S}_{\mathbf{k},a}(\tau) = e^{\tau H}\mathbf{S}_{\mathbf{k},a}e^{-\tau H}$. Similarly as for the single-particle gap, the spin excitation gaps are obtained from $S_s(\mathbf{k},\tau) \propto \exp(-\tau\Delta_s(\mathbf{k}))$, and $S_u(\mathbf{k},\tau) \propto \exp(-\tau\Delta_u(\mathbf{k}))$ at large imaginary time τ. The staggered spin gap $\Delta_s = \Delta_s(\Gamma)$ can be calculated directly via the staggered spin-spin correlations at the Γ point. However, since the total magnetization $\mathbf{S}_{tot} = \mathbf{S}_{\Gamma A} + \mathbf{S}_{\Gamma B}$ commutes with the Hamiltonian of the system, $[\mathbf{S}_{tot}, H] = 0$, the uniform spin gap Δ_u cannot be extracted from the uniform spin-spin correlations at the Γ point in a canonical QMC simulation, because the total uniform magnetization is always zero since the ground state of the system is a singlet. Instead, one obtains $\Delta_u = \lim_{\mathbf{k}\to\Gamma} \Delta_u(\mathbf{k})$ from measurements performed at the finite momenta closest to the Γ point for each finite system.

We consider first the spin gap Δ_s, which vanishes inside the AF phase due to the emergence of two Goldstone modes, as well as in the gapless SM phase. Figure 4.13 **c** shows finite size estimates of Δ_s for different values of U/t, along with an extrapolation to the TDL. A finite value of Δ_s persists within an intermediate parameter regime $3.5 < U/t < 4.3$, while it vanishes both within the SM and the AF phase. This dome in the spin gap is also seen in the inset of Fig. 4.13 **c**, that displays both the finite-size data and the extrapolated values of Δ_s as a function of U/t.

The uniform gap Δ_u is found to be even larger (four times) than Δ_s inside the intermediate region (e.g., $\Delta_u = 0.099 \pm 0.001$ at $U/t = 4$), and vanishes in the

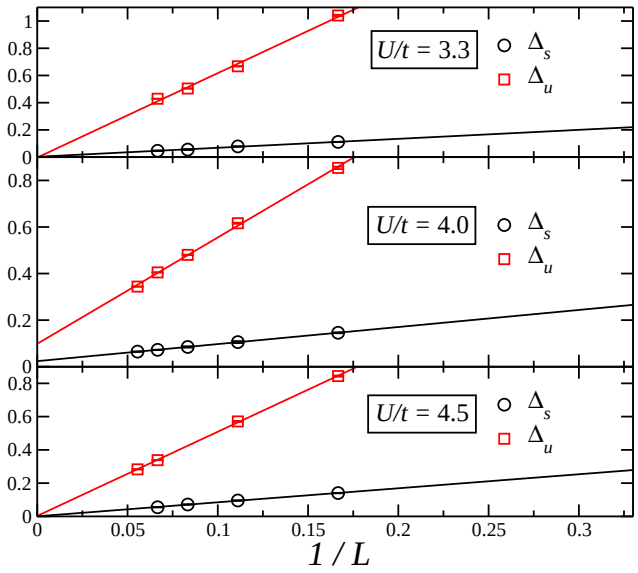

Figure 4.15: Comparison of the finite size scaling between the staggered spin gap Δ_s and the uniform spin gap Δ_u at $U/t = 3.3, 4$ and 4.5 (top to bottom). The extrapolated values in the thermodynamic limit for $U/t = 4$ are $\Delta_s = 0.023 \pm 0.007$ and $\Delta_u = 0.099 \pm 0.001$.

SM and the AF phase. Hence, this intermediate insulating region corresponds to a spin-gap phase. Figure 4.15 shows the finite size data for these gaps at $U/t = 3.3, 4$ and 4.5. For $U/t = 4$, both gaps scale to finite values in the thermodynamic limit, with Δ_u being about four times as large as Δ_s. For the other two values of U/t, both gaps clearly vanish in the thermodynamic limit.

4.2.2.4 Kinetic Energy Density and Double Occupation

From analyzing the U-dependence of the kinetic energy density,

$$E_{kin} = \frac{1}{N}\langle -t \sum_{\substack{\langle i,j\rangle \\ \alpha=\uparrow,\downarrow}} (c^\dagger_{i\alpha} c_{j\alpha} + c^\dagger_{j\alpha} c_{i\alpha})\rangle \ , \tag{4.11}$$

we obtain further insight into these different regimes and the emergence of local moments. As shown in Fig. 4.16, the curvature d^2E_{kin}/dU^2 changes sign near $U/t = 4.3$. This marks a characteristic change from the weak-coupling region of positive curvature with delocalized electrons to the strong-coupling AF region with negative curvature. In the latter region, localized spins form and order in an AF state. In the intermediate spin-gap region, fluctuations are large enough to prevent the formation of well-localized magnetic moments. We note that around $U/t = 3.5$, a change in the curvature can be observed, that adds to the already presented evidence for an intermediate phase.

Similarly, we also monitor how the evolution of the double occupation D as a

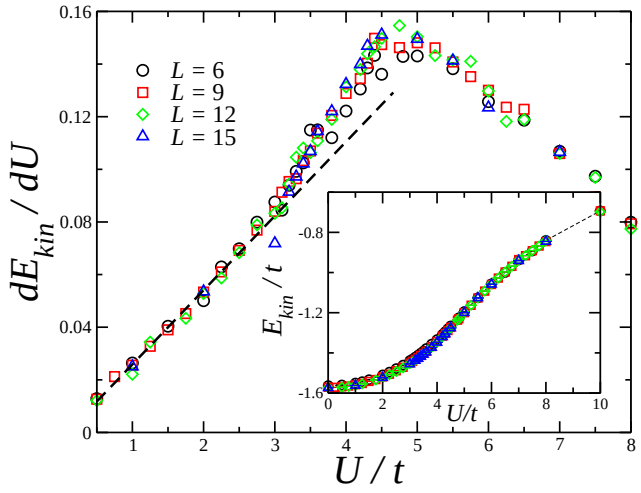

Figure 4.16: Derivative dE_{kin}/dU of the kinetic energy density as a function of U/t for systems of different sizes. The dashed line is a fit to the low-U behavior. The inset shows the QMC data for the kinetic energy density E_{kin} from which the derivative is obtained by numerical differentiation. Statistical errors are smaller than the symbol size.

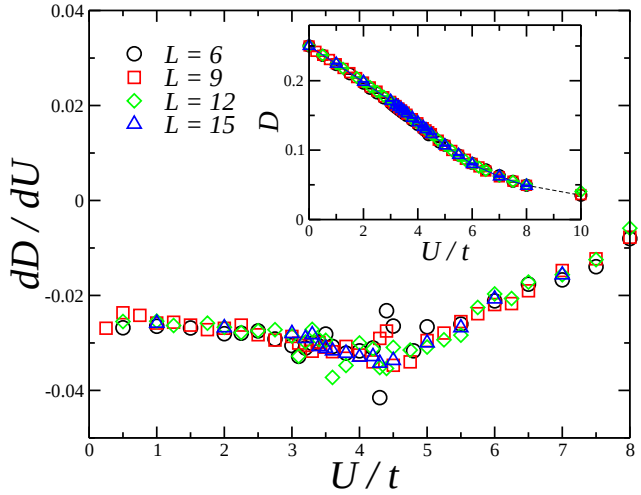

Figure 4.17: Derivative dD/dU of the double occupation as a function of U/t for systems of different sizes. The inset shows the QMC data for the double occupation D from which the derivative is obtained by numerical differentiation. Statistical errors are smaller than the symbol size.

function of U/t, with

$$D = \frac{1}{N}\langle \sum_{\langle i \rangle} (n_{i,\uparrow} n_{i,\downarrow}) \rangle. \tag{4.12}$$

As shown in the inset of Fig. 4.17, in non-interacting limit $U = 0$, $D = 0.25$ for all the system sizes, and it reduces as U/t increases, however, in the spin-gap region, the double occupation still has a well-defined value $D \sim 0.15$, meaning that the charge fluctuations are not negligible. In the main panel of Fig. 4.17, the same observation obtained from the kinetic energy density above could also be applied by looking the first derivative of the double occupations $dD/dU = d(n_\uparrow n_\downarrow)/dU$, that the curvature d^2D/dU^2 will change sign near $U/t = 4.3$.

4.2.3 Characterization of the Quantum Spin Liquid Phase

The observation of a finite spin gap rules out a gapless spin liquid [Lee 2005, Hermele 2005, Hermele 2007], quantum spin Hall states [Raghu 2008], as well as triplet superconductivity [Uchoa 2007]. The remaining possibilities can be enumerated by considering the coupling to order parameters that lead to the opening of a mass gap in Dirac fermions [Ryu 2009], and hence account for the single-particle gap observed in the QMC data: (i) singlet superconductivity, (ii) a quantum Hall state (QHS) [Haldane 1988], (iii) charge density wave (CDW) order [Raghu 2008, Honerkamp 2008] and (iv) a valence bond solid (VBS).

4.2.3.1 Flux Quantization Measurements to test Superconductivity

In order to assess the possibility of superconductivity arising in the vicinity of the Mott transition, we first used the method of flux quantization to probe the superfluid density. This method can directly address the off-diagonal long range order and is hence independent of the specific symmetry of the pair wave function [Byers 1961, Assaad 1993b, Assaad 1994].

To introduce the flux quantization scheme, let's introduce a Peierls factor into the kinetic part of the Hamiltonian

$$H(\Phi) = (-t) \sum_{\mathbf{x}} \sum_{i=1,2,3} \left(e^{\frac{2\pi \mathrm{i}}{\Phi_0} \int \mathbf{A}\cdot d\mathbf{l}} a^\dagger_{\mathbf{x}} b_{\mathbf{x}+\delta_\mathbf{i}} + e^{-\frac{2\pi \mathrm{i}}{\Phi_0} \int \mathbf{A}\cdot d\mathbf{l}} b^\dagger_{\mathbf{x}+\delta_\mathbf{i}} a_{\mathbf{x}} \right), \tag{4.13}$$

where $\mathbf{x}$ runs for unit cells, the integrals inside the Peierls factor are performed **along** the direction of hopping (i.e. from $\mathbf{x} + \delta_\mathbf{i}$ to $\mathbf{x}$ in the first part), within our notation of the honeycomb lattice

$$\mathbf{a_1} = (\sqrt{3}, 0), \qquad \mathbf{a_2} = (\frac{\sqrt{3}}{2}, \frac{3}{2}). \tag{4.14}$$

The $\delta_\mathbf{i}$-s are the three nearest-neighbour vectors

$$\delta_\mathbf{1} = (0, 1), \quad \delta_\mathbf{2} = (-\frac{\sqrt{3}}{2}, -\frac{1}{2}), \quad \delta_\mathbf{3} = (\frac{\sqrt{3}}{2}, -\frac{1}{2}). \tag{4.15}$$

The vector field $\mathbf{A} = \frac{\Phi}{\frac{\sqrt{3}}{2}L}\frac{\mathbf{a_1}}{|\mathbf{a_1}|}$ is implemented along the direction of $\mathbf{a_1}$ such that a particle that goes once around the flux line acquires a phase $\exp(2\pi \mathrm{i}\frac{\Phi}{\Phi_0})$. In the case of a superconducting ground state with Cooper pairs, $\Phi_0/2$ will be the period within which the groundstate energy climbs up an energy barrier. Here, $\Phi_0 = \frac{hc}{e}$ and $\frac{\Phi}{\Phi_0}$ is parameterized as a "TWIST" in our PQMC code. Now we perform the Fourier transformations

$$a^\dagger_{\mathbf{x}} = \frac{1}{L}\sum_{\mathbf{x}} e^{-\mathrm{i}\mathbf{k}\cdot\mathbf{x}} a^\dagger_{\mathbf{k}}, \quad a_{\mathbf{x}} = \frac{1}{L}\sum_{\mathbf{x}} e^{\mathrm{i}\mathbf{k}\cdot\mathbf{x}} a_{\mathbf{k}}, \tag{4.16}$$

to obtain the Hamiltonian in momentum space

$$\begin{aligned} H_K(\Phi) &= (-t)\frac{1}{N}\sum_{\mathbf{x}}\sum_{\mathbf{k},\mathbf{k'}}\sum_{i=1,2,3}\Big(\underbrace{e^{-\mathrm{i}\mathbf{x}\cdot(\mathbf{k}-\mathbf{k'})}}_{\delta_{\mathbf{k},\mathbf{k'}}} e^{\mathrm{i}\mathbf{k'}\cdot\delta_{\mathbf{i}}} e^{2\pi\mathrm{i}\frac{\Phi}{\Phi_0}\frac{\delta_{\mathbf{i}}\cdot\mathbf{a_1}}{\frac{\sqrt{3}}{2}L|\mathbf{a_1}|}}\ a^\dagger_{\mathbf{k}} b_{\mathbf{k'}} + \mathrm{h.c.}\Big) \\ &= (-t)\sum_{\mathbf{k}}\sum_{i=1,2,3}\big(e^{\mathrm{i}\mathbf{k}\cdot\delta_{\mathbf{i}}} e^{2\pi\mathrm{i}\frac{\Phi}{\Phi_0}\frac{\delta_{\mathbf{i}}\cdot\mathbf{a_1}}{\frac{\sqrt{3}}{2}L|\mathbf{a_1}|}}\ a^\dagger_{\mathbf{k}} b_{\mathbf{k}} + h.c.\big) \\ &= (-t)\sum_{\mathbf{k}}\begin{pmatrix} a^\dagger_{\mathbf{k}} & b^\dagger_{\mathbf{k}}\end{pmatrix}\begin{pmatrix} 0 & f(\mathbf{k}) \\ f^*(\mathbf{k}) & 0\end{pmatrix}\begin{pmatrix} a_{\mathbf{k}} \\ b_{\mathbf{k}}\end{pmatrix}, \end{aligned} \tag{4.17}$$

where

$$\begin{aligned} f(\mathbf{k}) &= e^{\mathrm{i}\mathbf{k}\cdot\delta_{\mathbf{1}}} e^{2\pi\mathrm{i}\frac{\Phi}{\Phi_0}\frac{\delta_{\mathbf{1}}\cdot\mathbf{a_1}}{\frac{\sqrt{3}}{2}L|\mathbf{a_1}|}} + e^{\mathrm{i}\mathbf{k}\cdot\delta_{\mathbf{2}}} e^{2\pi\mathrm{i}\frac{\Phi}{\Phi_0}\frac{\delta_{\mathbf{2}}\cdot\mathbf{a_1}}{\frac{\sqrt{3}}{2}L|\mathbf{a_1}|}} + e^{\mathrm{i}\mathbf{k}\cdot\delta_{\mathbf{3}}} e^{2\pi\mathrm{i}\frac{\Phi}{\Phi_0}\frac{\delta_{\mathbf{3}}\cdot\mathbf{a_1}}{\frac{\sqrt{3}}{2}L|\mathbf{a_1}|}} \\ &= e^{\mathrm{i}\mathbf{k}\cdot\delta_{\mathbf{1}}} + e^{\mathrm{i}\mathbf{k}\cdot\delta_{\mathbf{2}}} e^{\frac{2\pi\mathrm{i}}{L}\frac{\Phi}{\Phi_0}} + e^{\mathrm{i}\mathbf{k}\cdot\delta_{\mathbf{3}}} e^{\frac{2\pi\mathrm{i}}{L}\frac{\Phi}{\Phi_0}}. \end{aligned} \tag{4.18}$$

Diagonalizing the 2×2 matrix inside $H_K(\Phi)$, one obtains the two bands free dispersion,

$$\varepsilon^{\pm}_1(\mathbf{k}) = \pm t\sqrt{f(\mathbf{k})f^*(\mathbf{k})} =$$

$$\pm\, t\sqrt{3 + 2\big(\cos(\mathbf{k}\cdot(\mathbf{a_1}-\mathbf{a_2}) - \frac{2\pi}{L}\frac{\Phi}{\Phi_0}) + \cos(\mathbf{k}\cdot\mathbf{a_2} - \frac{2\pi}{L}\frac{\Phi}{\Phi_0}) + \cos(\mathbf{k}\cdot\mathbf{a_1} - \frac{2\pi}{L}\frac{2\Phi}{\Phi_0})\big)}. \tag{4.19}$$

In a finite $L\times L$ lattice, the momentum $\mathbf{k} = \frac{m}{L}\mathbf{b_1} + \frac{n}{L}\mathbf{b_2}$, where integer $(m,n) \in \big(-\frac{L}{2}, -(\frac{L}{2}-1), ..., 0, ..., (\frac{L}{2}-1), \frac{L}{2}\big)$. Since the primitive vectors in reciprocal space and direct space obey the relation $\mathbf{a_i}\cdot\mathbf{b_j} = 2\pi\delta_{i,j}$, one can readily obtain the quantized dispersion on a finite lattice

$$\varepsilon^{\pm}_1(m,n) =$$

$$\pm\, t\sqrt{3 + 2\big(\cos(\frac{2\pi}{L}(m-n-\frac{\Phi}{\Phi_0})) + \cos(\frac{2\pi}{L}(n-\frac{\Phi}{\Phi_0})) + \cos(\frac{2\pi}{L}(m-2\frac{\Phi}{\Phi_0}))\big)}. \tag{4.20}$$

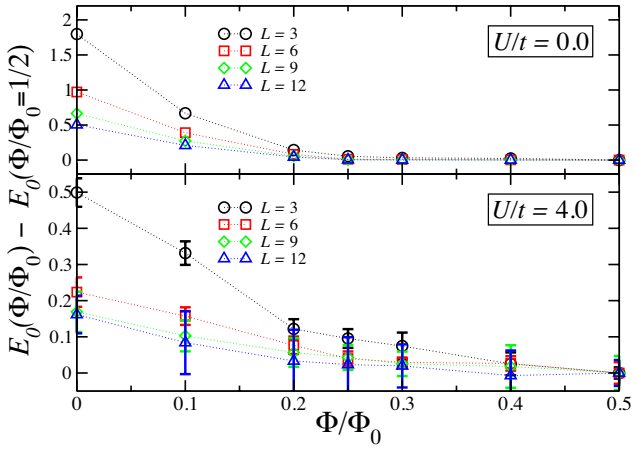

Figure 4.18: The energy difference of $E_0(\Phi/\Phi_0) - E(\Phi/\Phi_0 = 1/2)$ for different system sizes at $U/t = 0$ and $U/t = 4$. Note that the scale for $U/t = 4$ is four times smaller than for $U/t = 0$. The flattening of the energy differences exclude the superconducting ground state at both $U/t = 0$ and $U/t = 4$.

Here one sees the effect of the flux is to shift the momentum by factor $\frac{2\pi}{L}\frac{\Phi}{\Phi_0}$.

Physically speaking, as one tunes the flux Φ/Φ_0 through the center of a torus on which the electronic system lies, one can monitor the functional form of the ground state energy with respect to the threaded flux, $E_0(\Phi/\Phi_0)$, and furthermore one can distinguish between normal and superconducting ground states of the system. The signature of the latter requires that the macroscopic energy difference $E_0(\Phi/\Phi_0) - E_0(\Phi/\Phi_0 = 1/2)$ scales in the thermodynamic limit to a periodic function of period 1/2, and hence the occurrence of an energy barrier between $\Phi/\Phi_0 = 0$ and $\Phi/\Phi_0 = 1/2$. In contrast, a metallic phase is characterized by the energy difference $E_0(\Phi/\Phi_0) - E_0(\Phi/\Phi_0 = 1/2)$ vanishing as a power law as a function of system size, while in an insulating phase, it would vanish exponentially.

Figure 4.18 compares the QMC results of the macroscopic energy difference at $U = 0$ with that at $U/t = 4$. In both cases one clearly observes the vanishing of this quantity in the thermodynamic limit. Hence, no signal for superconductivity is obtained from these flux quantization measurements.

4.2.3.2 Pairing Amplitude Measurements to test Superconductivity

In addition to the flux quantization measurement, we also measured pair correlations in real space. The results in these measurements rule out superconductivity in (extended) s-, p-, d-, and f-wave channels. Order parameters for superconductivity are in principle obtained from considering the irreducible representations of the D_6 point group of the honeycomb lattice, which can be described as a triangular lattice with a basis of two atoms in the sublattices A and B, respectively. For the following, it is convenient to repeat the three lattice vectors related to the three

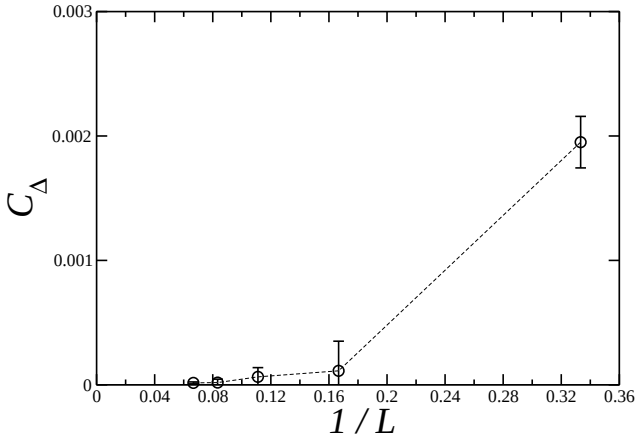

Figure 4.19: Finite size scaling of on-site s-wave pairing correlation C_Δ at $U/t = 4$.

nearest neighbor bonds $\boldsymbol{\delta} = \{\mathbf{0}, -\mathbf{a}_2, \mathbf{a}_1 - \mathbf{a}_2\}$, and introduce the vectors

$$\mathbf{r}_1 = \mathbf{a}_2, \quad \mathbf{r}_2 = \mathbf{a}_2 - \mathbf{a}_1, \quad \mathbf{r}_3 = -\mathbf{a}_1, \quad \mathbf{r}_4 = -\mathbf{r}_1, \quad \mathbf{r}_5 = -\mathbf{r}_2, \quad \mathbf{r}_6 = -\mathbf{r}_3,$$

connecting a given lattice site to its six next-nearest neighboring lattice sites.

The Cooper pair wave function of a superconducting state is a product of a spin, orbital and a sublattice components. Since Pauli's principle requires the wave function to be antisymmetric under particle exchange, we obtain the following possibilities for spin-singlet pairing: for an even (odd) orbital part, the wave function must be symmetric (antisymmetric) under sublattice exchange. It is convenient to introduce pair creation operators in the singlet channel

$$\Delta^\dagger(\mathbf{x}, a; \mathbf{y}, b) = c^\dagger_{\mathbf{x}a\uparrow} c^\dagger_{\mathbf{y}b\downarrow} - c^\dagger_{\mathbf{x}a\downarrow} c^\dagger_{\mathbf{y}b\uparrow} \ , \tag{4.21}$$

where $a, b \in \{A, B\}$ and $\mathbf{x}, \mathbf{y}$ are the unit cell labels. The operator

$$\Delta^\dagger_s(\mathbf{x}) = \frac{1}{2}(\Delta^\dagger(\mathbf{x}, A; \mathbf{x}, A) + \Delta^\dagger(\mathbf{x}, B; \mathbf{x}, B)) \ , \tag{4.22}$$

describes on-site s-wave pairing, which is symmetric under sublattice exchange. In Fig. 4.19, we show the s-wave pair-pair correlation function $C_\Delta = |\langle \Delta_s(0)\Delta^\dagger_s(\mathbf{d}_L)\rangle|$ at the largest distance $\mathbf{d}_L$ at $U/t = 4$. No long-ranged pairing correlation sustains to the thermodynamic limit; instead, the on-site pair-pair correlation function decreases rapidly.

Extended pair creation operators based on nearest neighbor pairing can be expressed in terms of phase factors f^a_1, f^a_2, f^a_3, $a \in \{A, B\}$,

$$\Delta^\dagger(\mathbf{x}, f^A_1, f^A_2, f^A_3, f^B_1, f^B_2, f^B_3) = \sum_{i=1}^{3} [f^A_i \Delta^\dagger(\mathbf{x}, A; \mathbf{x}+\boldsymbol{\delta}_i, B) + f^B_i \Delta^\dagger(\mathbf{x}, B; \mathbf{x}-\boldsymbol{\delta}_i, A)] \ . \tag{4.23}$$

For an extended s-wave,

$$\Delta^\dagger_{\text{ext-}s}(\mathbf{x}) = \Delta^\dagger(\mathbf{x}, 1, 1, 1, 1, 1, 1) \ . \tag{4.24}$$

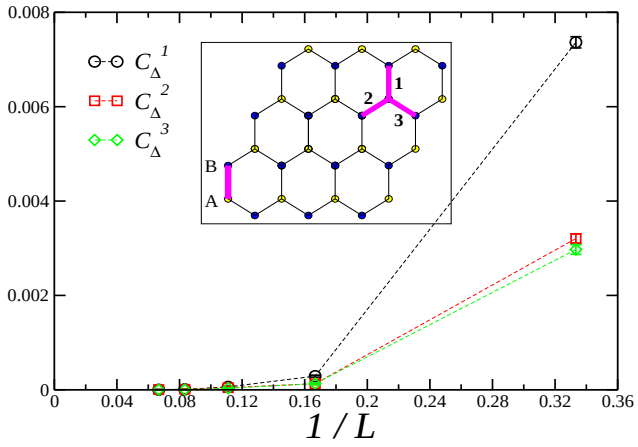

Figure 4.20: Finite size scaling of nearest neighbor pair correlation C^i_Δ at $U/t = 4$. The inset illustrates the three inequivalent directions with respect to the reference bond marked by AB.

Nearest neighbor p-wave states relate to

$$\Delta^\dagger_{p_x}(\mathbf{x}) = \Delta^\dagger(\mathbf{x}, 0, +1, -1, 0, -1, +1) \ , \tag{4.25}$$

$$\Delta^\dagger_{p_y}(\mathbf{x}) = \Delta^\dagger(\mathbf{x}, 0, +1, +1, 0, -1, -1) \ , \tag{4.26}$$

and nearest neighbor d-wave states to

$$\Delta^\dagger_{d_{xy}}(\mathbf{x}) = \Delta^\dagger(\mathbf{x}, 0, +1, -1, 0, +1, -1) \ , \tag{4.27}$$

$$\Delta^\dagger_{d_{x^2-y^2}}(\mathbf{x}) = \Delta^\dagger(\mathbf{x}, -2, +1, +1, -2, +1, +1) \ . \tag{4.28}$$

In terms of next-nearest neighbors, one furthermore obtains the singlet f-wave state

$$\Delta^\dagger_f(\mathbf{x}) = \sum_{i=1}^{6} (-1)^i [\Delta^\dagger(\mathbf{x}, A; \mathbf{x} + \mathbf{r}_i, A) - \Delta^\dagger(\mathbf{x}, B; \mathbf{x} + \mathbf{r}_i, B)] \ . \tag{4.29}$$

In order to probe for superconductivity based on nearest neighbor or next-nearest neighbor pairing in the above symmetry sectors, we directly measured in real-space the various inequivalent pair-pair correlation functions at the largest distances on the finite lattices,

$$C^i_\Delta = |\langle\langle \Delta(0, A; 0, B) \Delta^\dagger(\mathbf{d}_L, A; \mathbf{d}_L + \boldsymbol{\delta}_i, B)\rangle\rangle| \ , \quad i = 1, 2, 3, \tag{4.30}$$

for the nearest neighbor pairing states, and

$$C^{AA,i}_\Delta = |\langle\langle \Delta(0, A; \mathbf{r}_1, A) \Delta^\dagger(\mathbf{d}_L, A; \mathbf{d}_L + \mathbf{r}_i, A)\rangle\rangle| \tag{4.31}$$

$$C^{AB,i}_\Delta = |\langle\langle \Delta(0, A; \mathbf{r}_1, A) \Delta^\dagger(\mathbf{d}_L, B; \mathbf{d}_L + \mathbf{r}_i, B)\rangle\rangle| \ , \quad i = 1, ..., 6, \tag{4.32}$$

for next-nearest neighbor pairing states both within the same sublattice and between the two sublattices. As shown in Fig. 4.20 and Fig. 4.21, both nearest neighbor and

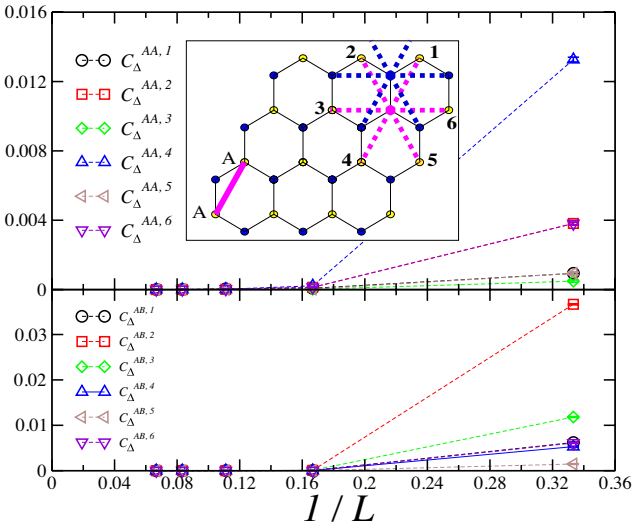

Figure 4.21: Finite size scaling of the next-nearest neighbor pair correlations $C_\Delta^{AA,j}$ and $C_\Delta^{AB,j}$ at $U/t = 4$. The inset illustrates the inequivalent directions with respect to the reference bond marked by AA, with the lower (upper) star corresponding to equal (different) sublattices.

next-nearest neighbor pair-pair correlation functions are very weak, even reaching zero within statistical errors for $L \geq 9$. From this, we exclude pairing in all the above symmetry sectors, since the full Cooper pair correlations $\langle \Delta_{ext.-s}(0)\Delta^\dagger_{ext.-s}(\mathbf{d}_L)\rangle$, $\langle \Delta_{p_x}(0)\Delta^\dagger_{p_x}(\mathbf{d}_L)\rangle$, $\langle \Delta_{p_y}(0)\Delta^\dagger_{p_y}(\mathbf{d}_L)\rangle$, $\langle \Delta_{d_{xy}}(0)\Delta^\dagger_{d_{xy}}(\mathbf{d}_L)\rangle$, $\langle \Delta_{d_{x^2-y^2}}(0)\Delta^\dagger_{d_{x^2-y^2}}(\mathbf{d}_L)\rangle$, and $\langle \Delta_f(0)\Delta^\dagger_f(\mathbf{d}_L)\rangle$ are linear superpositions of the above pair-pair correlation functions, and hence vanish in the thermodynamic limit.

Both, flux quantization as well as a direct measurement of pair correlations lead to no sign of superconductivity. We can thus exclude superconductivity in the half-filled Hubbard model on the honeycomb lattice in the quantum spin liquid phase.

4.2.3.3 Density, Currents and Bond Correlations in the Charge Sector

Charge density wave (CDW) [Honerkamp 2008] and quantum Hall states (QHS), or charge currents [Raghu 2008], trigger a breaking of the sub-lattice symmetry and thereby open a mass gap at the mean-field level. To exclude these effects as the cause for the spin-gapped phase we first measure the density-density correlation function, which is given by

$$C_d^{a,b}(\mathbf{x},\mathbf{y}) = \langle\langle n_{\mathbf{x}a} n_{\mathbf{y}b}\rangle\rangle \,, \tag{4.33}$$

where $a, b \in \{A, B\}$. At half-filling, $\langle n_{\mathbf{x}a}\rangle = \langle n_{\mathbf{x}b}\rangle = 1$. Figure 4.22 shows the finite size scaling of the density correlations at the largest distance, $C_d^{A,A} = |C_d^{A,A}(0,\mathbf{d}_L)|$ and $C_d^{A,B} = |C_d^{A,B}(0,\mathbf{d}_L)|$ at $U/t = 4$. Both scale to zero in the thermodynamic limit, and no long-range density correlations persist. Furthermore, in comparison

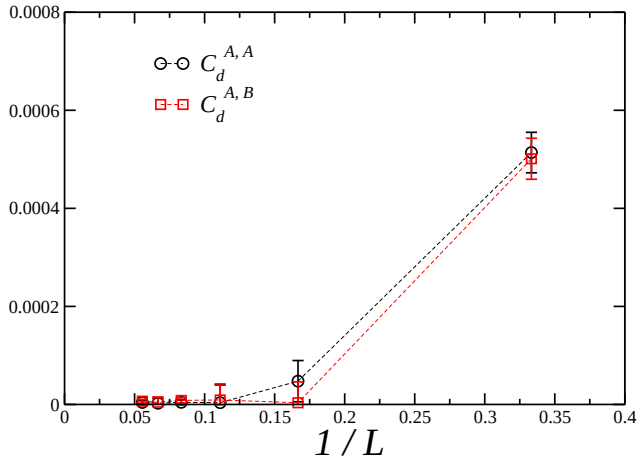

Figure 4.22: Finite size scaling of the density correlation functions $C_d^{A,A}$ and $C_d^{A,B}$ at $U/t = 4$.

with the spin correlations, the density correlations are seen to be significantly weaker and essentially zero within the statistical error for system sizes $L \geq 9$.

Next, we present our results on the dimer-dimer correlations in the charge sector. We measured both the correlations between the kinetic energy bond operators and the current operators. Correlations between the kinetic energy bond operators

$$k(\mathbf{x}, a; \mathbf{y}, b) = \sum_{\alpha} (c^{\dagger}_{\mathbf{x}a\alpha} c_{\mathbf{y}b\alpha} + c^{\dagger}_{\mathbf{y}b\alpha} c_{\mathbf{x}a\alpha}) \,, \tag{4.34}$$

and the current operators

$$j(\mathbf{x}, a; \mathbf{y}, b) = -i \sum_{\alpha} (c^{\dagger}_{\mathbf{x}a\alpha} c_{\mathbf{y}b\alpha} - c^{\dagger}_{\mathbf{y}b\alpha} c_{\mathbf{x}a\alpha}) \,, \tag{4.35}$$

can be defined between both nearest-neighbor and next-nearest neighbor sites on the honeycomb lattice.

To probe for VBC-like order in the kinetic energy sector, we measured the three inequivalent dimer-dimer correlation functions

$$C_k^i = |\langle\langle k(0, A; 0, B) k(\mathbf{d}_L, A; \mathbf{d}_L + \boldsymbol{\delta}_i, B)\rangle\rangle| \,, \quad i = 1, 2, 3, \tag{4.36}$$

at the largest distance $\mathbf{d}_L$ on the finite lattices. For an illustration of the different relative bond orientations, see the inset of Fig. 4.23. The upper panel of Fig. 4.23 shows the finite size scaling of the C_k^i at $U/t = 4$. These correlations scale to zero in the thermodynamic limit, hence no long-ranged bond order in the kinetic energy persists. Furthermore, in comparison with the spin correlations, these correlations are also seen to be significantly weaker.

To probe for the persistence of nearest-neighbor currents in the ground state, we measured the current-current correlation functions between the bonds of the honeycomb lattice

$$C_j^i = |\langle\langle j(0, A; 0, B) j(\mathbf{d}_L, A; \mathbf{d}_L + \boldsymbol{\delta}_i, B)\rangle\rangle| \,, \quad i = 1, 2, 3, \tag{4.37}$$

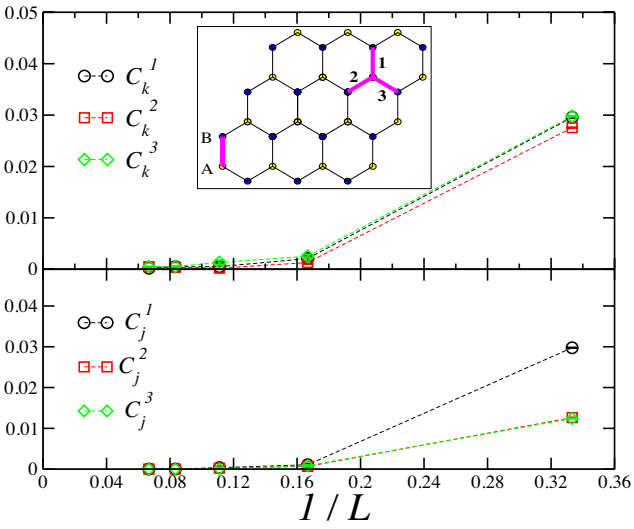

Figure 4.23: Finite size scaling of the nearest-neighbor correlations C_k^i and C_j^i at $U/t = 4$. The inset illustrates the three inequivalent directions with respect to the reference bond marked by AB.

at the largest distance $\mathbf{d}_L$ on the finite lattices. The corresponding finite size scalings are shown in the lower panel of Fig. 4.23. Again, long range correlations in the thermodynamic limit can be clearly excluded, indicating the absence of currents between nearest neighbor sites in the ground state.

To probe for bond order and currents between next-nearest neighbor sites, we measured all inequivalent next-nearest neighbor bond-bond and current-current correlation functions at the largest distances both within the same sublattice and between the two sublattices,

$$C_k^{AA,i} = |\langle\langle k(0,A;\mathbf{r}_1,A)k(\mathbf{d}_L,A;\mathbf{d}_L+\mathbf{r}_i,A)\rangle\rangle| \,, \tag{4.38}$$

$$C_j^{AA,i} = |\langle\langle j(0,A;\mathbf{r}_1,A)j(\mathbf{d}_L,A;\mathbf{d}_L+\mathbf{r}_i,A)\rangle\rangle| \,, \tag{4.39}$$

$$C_k^{AB,i} = |\langle\langle k(0,A;\mathbf{r}_1,A)k(\mathbf{d}_L,B;\mathbf{d}_L+\mathbf{r}_i,B)\rangle\rangle| \,, \tag{4.40}$$

$$C_j^{AB,i} = |\langle\langle j(0,A;\mathbf{r}_1,A)j(\mathbf{d}_L,B;\mathbf{d}_L+\mathbf{r}_i,B)\rangle\rangle| \,, \quad i=1,...,6. \tag{4.41}$$

The QMC data for the correlations within the same sublattice at $U/t = 4$ are shown in Fig. 4.24. Both $C_k^{AA,i}$ and $C_j^{AA,i}$ all scale to zero in the thermodynamic limit. Thus neither bond ordering nor currents persist between next-nearest neighbor sites in the ground state at $U/t = 4$.

The lack of order in the charge sector rules out the breaking of sublattice and time reversal symmetries, as required for the QHS, in the pristine Hubbard model. Possibly, extensions in the form of next-nearest neighbor Coulomb interactions, or spin-orbit coupling are necessary to reach such a state [Haldane 1988, Kane 2005, Raghu 2008].

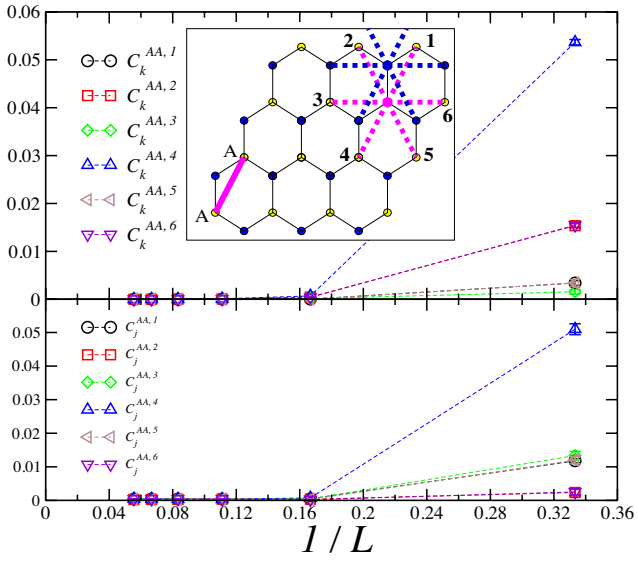

Figure 4.24: Finite size scaling of the next-nearest neighbor correlations $C_k^{AA,i}$ and $C_j^{AA,i}$ at the largest distance at $U/t = 4$. The inset illustrates the inequivalent directions with respect to the reference bond marked by AA, with the lower (upper) star corresponding to equal (different) sublattices.

4.2.3.4 Dimer-Dimer, Spin-Currents and Spin-Bond Correlations in Spin Sector

To examine the occurrence of a VBC in spin sector, we probed for dimer-dimer correlations between separated dimers formed by nearest neighbor bonds $\langle ij \rangle$ and $\langle kl \rangle$. The dimer-dimer correlation function is defined as

$$D_{ij,kl} = \langle\langle (\mathbf{S}_i \cdot \mathbf{S}_j - \frac{1}{4})(\mathbf{S}_k \cdot \mathbf{S}_l - \frac{1}{4}) \rangle\rangle \ , \tag{4.42}$$

Figure 4.25 shows the results of the correlation between singlet dimers at $U/t = 4.0$. The striped bond is the one with respect to which correlations were determined. Positively correlated bonds will be more likely to present with the reference bond and negative correlated bonds are unlikely to exist when there is a singlet at the reference location. The correlations are found to be short-ranged, and consistent with the dominance of a RVB state within the hexagons of the honeycomb lattice [Fouet 2001, Sun 2009, Clark 2010, Albuquerque 2011, Reuther 2011]. This can be seen by comparing the singlet-correlations with those of an isolated hexagon (inset Fig. 4.25), the classical example of the resonance phenomenon in conjugated π-electrons [Pauling 1960]. Accordingly, we find no long-ranged order from the dimer-dimer structure factors in Fourier space. Our results thus reveal a genuinely exotic state of matter, where no spontaneous symmetry breaking is observed, while a spin-gap is present. It corresponds to a quantum spin liquid state characterized by a RVB in the intermediate coupling regime in the vicinity of the Mott transition.

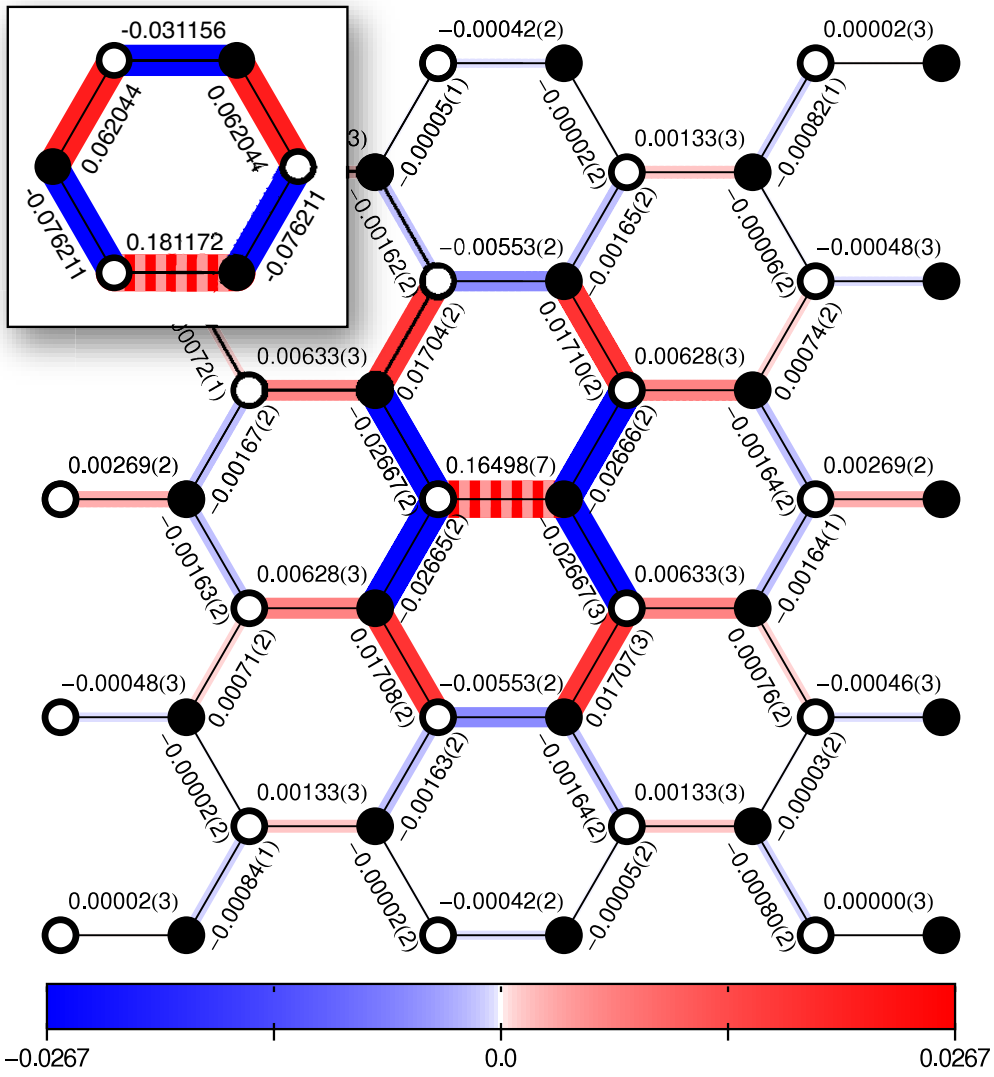

Figure 4.25: Real space plot of the spin dimer-dimer correlations. The correlation function $D_{ij,kl}$ for a $L = 6$ system at $U/t = 4$, together with the same correlation for the isolated Hubbard hexagon also at $U/t = 4$ (inset). The reference bonds are dressed with stripes. Numbers in parenthesis indicate the standard error of the last digit.

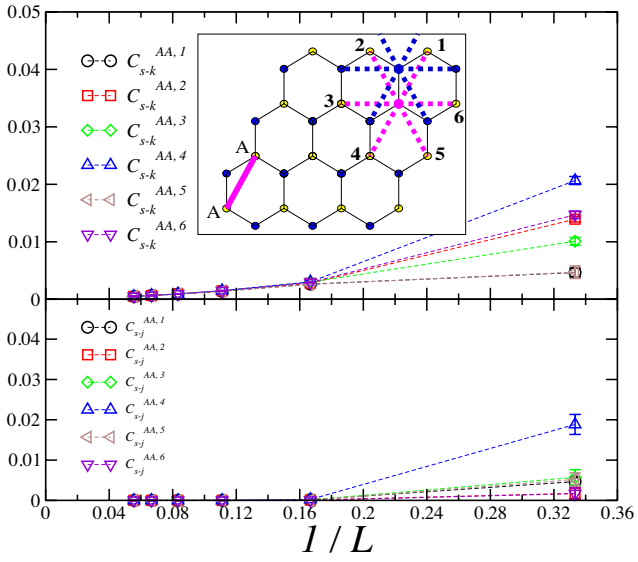

Figure 4.26: Finite size scaling of the next-nearest neighbor correlations $C_{s-k}^{AA,i}$ and $C_{s-j}^{AA,i}$ at the largest distance at $U/t = 4$. The inset illustrates the inequivalent directions with respect to the reference bond marked by AA, with the lower (upper) star corresponding to equal (different) sublattices.

We furthermore measured correlations between the spin-current operators

$$j_s(\mathbf{x}, a; \mathbf{y}, b) = -i \sum_\alpha (-1)^\alpha (c^\dagger_{\mathbf{x}a\alpha} c_{\mathbf{y}b\alpha} - c^\dagger_{\mathbf{y}b\alpha} c_{\mathbf{x}a\alpha}) \,, \tag{4.43}$$

as well as the spin-bond operators

$$k_s(\mathbf{x}, a; \mathbf{y}, b) = \sum_\alpha (-1)^\alpha (c^\dagger_{\mathbf{x}a\alpha} c_{\mathbf{y}b\alpha} + c^\dagger_{\mathbf{y}b\alpha} c_{\mathbf{x}a\alpha}) \,, \tag{4.44}$$

for next-nearest neighbor sites, where the α sum over the two spin flavors. We measured these correlations between all inequivalent pairs of next-nearest neighbor sites both within the same sublattice and between the two sublattices at the largest distance on the finite lattices,

$$C_{s-k}^{AA,i} = |\langle\langle k_s(0, A; \mathbf{r}_1, A) k_s(\mathbf{d}_L, A; \mathbf{d}_L + \mathbf{r}_i, A)\rangle\rangle| \,, \tag{4.45}$$

$$C_{s-j}^{AA,i} = |\langle\langle j_s(0, A; \mathbf{r}_1, A) j_s(\mathbf{d}_L, A; \mathbf{d}_L + \mathbf{r}_i, A)\rangle\rangle| \,, \tag{4.46}$$

$$C_{s-k}^{AB,i} = |\langle\langle k_s(0, A; \mathbf{r}_1, A) k_s(\mathbf{d}_L, B; \mathbf{d}_L + \mathbf{r}_i, B)\rangle\rangle| \,, \tag{4.47}$$

$$C_{s-j}^{AB,i} = |\langle\langle j_s(0, A; \mathbf{r}_1, A) j_s(\mathbf{d}_L, B; \mathbf{d}_L + \mathbf{r}_i, B)\rangle\rangle| \,, \quad i = 1, .., 6. \tag{4.48}$$

Figure 4.26 shows the finite size scaling of the correlations within the same sublattice at $U/t = 4$. They all decay to zero in the thermodynamic limit. The corresponding correlations between different sublattices show a similar behavior (not shown). Thus neither spin-bond order nor spin-currents persist between next-nearest neighbor sites in the ground state at $U/t = 4$.

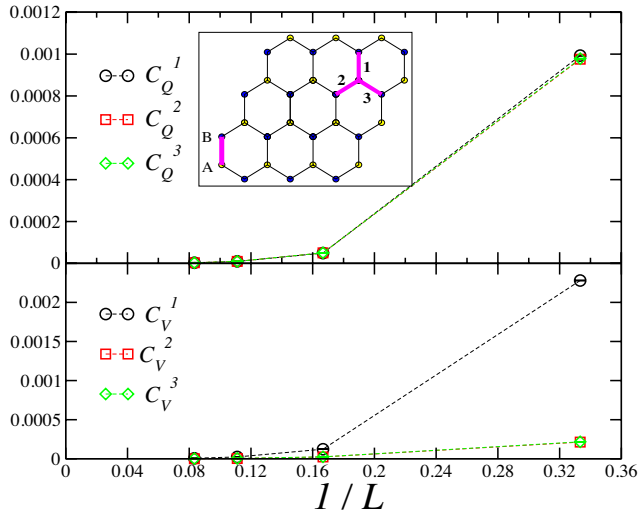

Figure 4.27: Finite size scaling of the nearest neighbor correlations C_Q^i and C_V^i at the largest distance at $U/t = 4$. The inset illustrates the inequivalent directions with respect to the reference bond marked by AB.

4.2.3.5 Order Parameters for Spin-nematic Order

The spin-nematic phase was introduced by Andreev and Grishchuk [Andreev 1984]. Such phase has no net magnetic moment, but nevertheless breaks the SU(2) spin-rotation symmetry, as individual spins are correlated in a plane and remain disordered. To probe for a possible spin-nematic order in the spin-gapped phase, we measured the correlations of the operators

$$Q^{xy}(\mathbf{x}, a; \mathbf{y}, b) = \frac{1}{2}(S^x_{\mathbf{x}a} S^y_{\mathbf{x}b} + S^y_{\mathbf{y}a} S^x_{\mathbf{y}b}) \,, \tag{4.49}$$

for the n-type nematics and

$$V(\mathbf{x}, a; \mathbf{y}, b) = \mathbf{S}_{\mathbf{x},a} \times \mathbf{S}_{\mathbf{y},b} \,, \tag{4.50}$$

for the p-type nematics in real-space at the largest distance on the finite lattices,

$$\begin{aligned} C_Q^i &= |\langle\langle Q^{xy}(0, A; 0, B) Q^{xy}(\mathbf{d_L}, A; \mathbf{d_L} + \boldsymbol{\delta_i}, B)\rangle\rangle| \,, \\ C_V^i &= |\langle V(0, A; 0, B) V(\mathbf{d_L}, A; \mathbf{d_L} + \boldsymbol{\delta_i}, B)\rangle| \qquad (4.51) \\ &= |\langle (\mathbf{S}_{0,A} \cdot \mathbf{S}_{\mathbf{d_L},A})(\mathbf{S}_{0,B} \cdot \mathbf{S}_{\mathbf{d_L}+\boldsymbol{\delta}_i,B}) - (\mathbf{S}_{0,A} \cdot \mathbf{S}_{\mathbf{d_L}+\boldsymbol{\delta}_i,B})(\mathbf{S}_{0,B} \cdot \mathbf{S}_{\mathbf{d_L},A})\rangle| \,, \\ & \qquad i = 1, 2, 3, \qquad (4.52) \end{aligned}$$

and performed similar finite-size scaling as in previous sections. The upper panel of Fig. 4.27 displays the behavior of C_Q^i and the lower panel displays that of C_V^i, for system size $L = 3, 6, 9, 12$ at $U/t = 4$. These correlations are very weak, reaching zero within statistical errors for $L \geq 12$. Thus, we exclude the possibility of spin-nematic states inside the intermediate coupling regime.

Recently, based on Schwinger-fermion approaches, Lu and Ran [Lu 2010a, Lu 2010b] proposed that the quantum spin liquid phase in our model is adjacent to a chiral-antiferromagnetic (CAF) phase. The chiral-antiferromagnetic phase breaks the SU(2) spin-rotation symmetry completely and has a vector-chirality spin order parameter. The quantum spin liquid phase connects to the CAF phase through an $O(4)$ critical point. According to Lu and Ran, the CAF phase coexists with the Néel AFMI phase, upto the point U/t is very large. Hence, to check the existence of the CAF phase in the vicinity of the transition point $U/t \sim 4.3$, and to verify the transition between the CAF phase and the Néel AFMI phase at large U/t, one should pin the Néel order by an infinitesimally small (in the TDL) staggered magnetic field along S^z direction, and then measure the order parameter of the CAF phase by correlation functions. We will address this question in future investigations.

4.2.4 Further Insight into the RVB State

The QMC results presented above uncover the realization of a quantum spin liquid state with short-range RVB correlations in correlated fermions on a non-frustrated, bipartite lattice. The observation of a finite spin-gap is consistent with the characterization of the observed spin-liquid in terms of short-range RVB states [Anderson 1973, Fazekas 1974, Kivelson 1987, Rokhsar 1988, Moessner 2001b], also in accordance with the observed short-ranged dimer-dimer correlations. Short-range RVB states are modeled in general by quantum dimer models [Rokhsar 1988, Moessner 2001b, Moessner 2008], which fall into the class of Z_2 spin liquids. Fully gapped phases of quantum dimer models are furthermore characterized by a non-trivial topological order, implying e.g., an emerging ground state degeneracy of two-dimensional systems with periodic boundary conditions in the TDL [Wen 1991, Moessner 2008]. Recently, a generalization of the Lieb-Schultz-Mattis theorem beyond 1D was presented, which states that systems with a half-integer spin per unit cell either exhibit long range order or, in case of short range order, topological degeneracy is present [Hastings 2004]. However, since the honeycomb lattice has two sites per unit cell, our quantum spin liquid is not covered by this theorem, thus leaving the presence of topological order a open question.

In order to assess this question, here we examined the low-energy singlet excitations. As proven in an exact theorem by Lieb [Lieb 1989], the finite systems used in our numerical simulations have a non-degenerate singlet ground state for any finite value of $U > 0$. Hence, degeneracy can only appear in the TDL. If so, low-energy singlet states should be present, with decreasing excitation energy as the system size increases. Since our QMC method projects out the finite system's ground state from a singlet trial wavefunction, we can monitor the expectation value of the internal energy $E(\Theta)$, where Θ is the projection parameter of PQMC. Here all contributions from singlet states with the same quantum numbers as the ground state are included, that have a finite overlap with the trial wave function.

We consider the internal energy as a function of the projection parameter Θ,

$$E(\Theta) = \frac{\langle \Psi_T | \mathrm{e}^{-\Theta H/2} H \mathrm{e}^{-\Theta H/2} | \Psi_T \rangle}{\langle \Psi_T | \mathrm{e}^{-\Theta H} | \Psi_T \rangle} , \tag{4.53}$$

where $|\Psi_T\rangle$ is the trial wave function. Let $\{|n\rangle\}$ be the set of eigenstates of H. Then, we have

$$E(\Theta) - E_0 = \frac{1}{1 + R(\Theta)} \sum_{n>0} \mathrm{e}^{-(E_n - E_0)\Theta} (E_n - E_0) \frac{|\langle n|\Psi_T\rangle|^2}{|\langle 0|\Psi_T\rangle|^2} , \tag{4.54}$$

where E_0 is the ground state energy, $|0\rangle$ the ground state, and define

$$R(\Theta) = \sum_{n>0} \mathrm{e}^{-(E_n - E_0)\Theta} \frac{|\langle n|\Psi_T\rangle|^2}{|\langle 0|\Psi_T\rangle|^2} . \tag{4.55}$$

Next, we consider an energy scale

$$\varepsilon \ll (E_1 - E_0)/N , \tag{4.56}$$

where E_1 is the energy of the first excited singlet and the singlet gap $\Delta_{\mathrm{singlet}} = (E_1 - E_0)$, with the same quantum numbers as the ground state, and define Θ^*, such that for $\Theta > \Theta^*$, $(E(\Theta) - E_0)/N < \varepsilon$. Typically, ε can be taken of the order of the statistical error in the energy, such that the condition on ε is clearly fulfilled. However, ε is not defined in terms of the statistical errors; the only defining condition on ε is (4.56). With such a definition we have

$$\varepsilon = \frac{1}{N} \sum_{n>0} \frac{\mathrm{e}^{-(E_n - E_0)\Theta^*}}{1 + R(\Theta^*)} (E_n - E_0) \frac{|\langle n|\Psi_T\rangle|^2}{|\langle 0|\Psi_T\rangle|^2} \ll \Delta_{\mathrm{singlet}}/N , \tag{4.57}$$

such that

$$\frac{R(\Theta^*)}{1 + R(\Theta^*)} < \sum_{n>0} \frac{\mathrm{e}^{-(E_n - E_0)\Theta^*}}{1 + R(\Theta^*)} \frac{(E_n - E_0)}{\Delta_{\mathrm{singlet}}} \frac{|\langle n|\psi_T\rangle|^2}{|\langle 0|\psi_T\rangle|^2} \ll 1 , \tag{4.58}$$

so that it also holds that $R(\Theta^*) \ll 1$. The last inequality also implies that

$$\mathrm{e}^{-\Delta_{\mathrm{singlet}}\Theta^*} \frac{|\langle 1|\Psi_T\rangle|^2}{|\langle 0|\Psi_T\rangle|^2} \ll 1 , \tag{4.59}$$

since the sum in $R(\Theta)$ consists of positive definite terms.In case the overlaps in the last inequality are finite,

$$\Delta_{\mathrm{singlet}}\Theta^* \gg 1 , \tag{4.60}$$

such that $1/\Theta^*$ provides a lower bound for the singlet gap. In case $|\langle 1|\Psi_T\rangle|^2/|\langle 0|\Psi_T\rangle|^2 \ll 1$ such that the inequality (4.59) is fulfilled due to a vanishing overlap, we miss the lowest excited singlet state, and $1/\Theta^*$ provides a lower bound for the next lowest singlet with a finite overlap with the trial wave function.

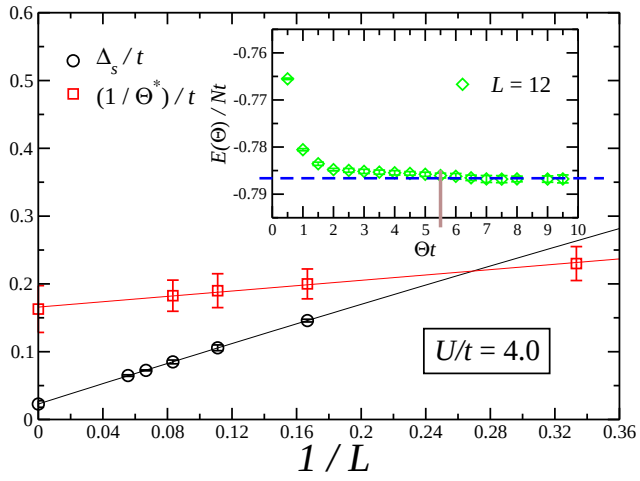

Figure 4.28: Lower bound $1/\Theta^* \sim \Delta_{\text{singlet}}$ for $L = 3$, 6, 9, and 12 at $U/t = 4$. For comparison, the values of the spin-gap are reproduced. The inset shows the internal energy $E(\Theta)$ as a function of the projection parameter Θ for the $L = 12$ system. The vertical bar gives the position of Θ^*. Error bars in Δ_s and $E(\Theta)$ denote standard errors. For the determination of the error bars in $1/\Theta^*$, see the text.

For the determination of the lower bound for singlet states we concentrated on the value $U/t = 4$, centered in the RVB phase. We verified that in the case $L = 2$, where the system can be fully diagonalized, setting $\varepsilon = 10^{-3}t$, $1/\Theta^* = (0.74 \pm 0.04)t$ is a lower bound. Namely, for this system size, $\Delta_{\text{singlet}} = 1.84t$ for the first excited singlet state of momentum $\mathbf{k} = 0$. We also verified that this state has an overlap of 0.22 with the trial wave function. The above value of ε corresponds to the maximal error for all system sizes. The uncertainty in the determination of Θ^* is taken as the maximum between (i) the distance from Θ^* to the value of Θ for $E(\Theta)/N = E(\Theta^*)/N - \varepsilon$ and (ii) the distance between two consecutive values of Θ around Θ^*. By means of error propagation, we then estimate the error in $1/\Theta^*$.

In Fig. 4.28 we display $1/\Theta^*$ for $L = 3$, 6, 9, and 12, and an extrapolation to the TDL. In all these cases, the lower bound is above the spin-gap, as well as the extrapolation to the TDL. Hence, we find no evidence for singlet states with the same quantum numbers as the ground state, that may become degenerate with it in the thermodynamic limit. However, we cannot definitely exclude topological order, if the relevant singlet states happen to have a vanishing overlap with our trial wave function. For the future investigations, it will be interesting to explore the low-energy singlets beyond the projective scheme, and probe for soft modes similarly as the construction of finite momentum trial states in quantum dimer models [Rokhsar 1988, Moessner 2008].

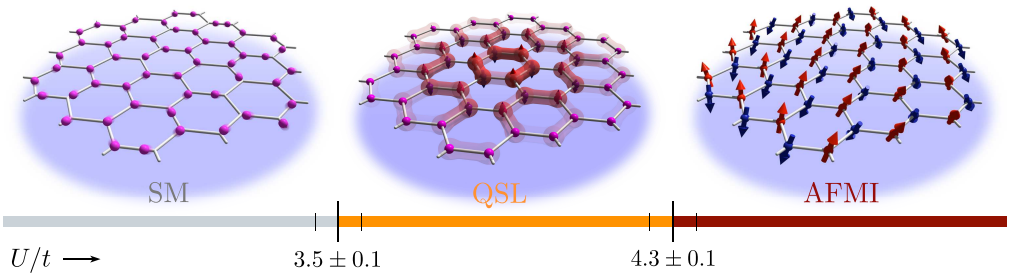

Figure 4.29: Schematic phase diagram of the finding in this chapter.

4.3 Summary and Outlook

Figure 4.29 provides an artistic summary of our finding in this chapter. The presence of a quantum spin liquid in the Hubbard model on the bipartite honeycomb lattice close to an AF Mott insulator resembles the situation in the organic charge transfer salt κ-(BEDT-TTF)$_2$Cu$_2$(CN)$_3$, which has been discussed in the first part of this chapter, and argued to display a quantum spin liquid ground state down to 20 mK [Shimizu 2003, Yamashita 2009, Pratt 2011]. Although the organic salt is on a triangular lattice and is hence frustrated, the difference can be reconciled starting from the strong-coupling limit of the Hubbard model, that is, a nearest-neighbor Heisenberg model, which close to the Mott transition acquires corrections that induce efficient frustrations to the spin degrees of freedom (next-nearest neighbor exchange, ring exchange, etc.). In fact, a Klein Hamiltonian for a spin-liquid state on the honeycomb lattice was constructed, including extended exchange interactions [Chayes 1989]. In the strong coupling regime it is reasonable to describe the low energy physics by an effective $S = 1/2$ Heisenberg Hamiltonian, which can be derived from the Hubbard model in the large-U limit [MacDonald 1988, MacDonald 1990]. The antiferromagnetic J_1-J_2 Heisenberg model on the honeycomb lattice would be the first guess. Recent works on the AF J_1-J_2 Heisenberg model on the honeycomb lattice, by means of variational Monte Carlo [Clark 2010] and pseudofermion functional renormalization group [Reuther 2011], all point to the physical picture that a small next-nearest neighbor coupling J_2 will destabilize the AF Néel order and drive the system to a QSL phase. Furthermore, a recent applicaiton of the continuous unitary transformations, which systematically derive the effective low-energy model from strong coupling limit, on the honeycomb latice [Yang 2010] even suggests upto the point of $U/t = 4.3$, J_2 is not the only contribution to destabilize the J_1, but other higher order terms, including ring exchange, which make the system even more frustrated, all contribute in the same magitude as J_2.

The reason of the absence of superconductivity in our QSL phase is also interesting. As we have discussed in Chap. 4.1, in the organic charge transfer salts, the superconductivity appears upon appling pressure [Nam 2007]. This is equivalent to a reduction of the ratio U/t in the Hubbard model. The absence of superconduc-

tivity in our system could be due to the vanishing density of states at the Fermi energy. In this situation, a finite coupling strength is needed, at least in the BCS-frame [Kopnin 2008]. However, having an unexpected realization of a short-range RVB state, it would be highly interesting to explore the consequences of doping, in a spirit rather close to the original scenario proposed by Anderson [Anderson 1987] and Kivelson et. al. [Kivelson 1987] for the cuprates. In particular, for the fully gapped short-range RVB state, the finite spin gap sets the energy scale of pairing in the superconducting state [Kivelson 1987]. In this respect, the value obtained for the spin gap is rather promising. The largest value attained is $\Delta_s \sim 0.025t$, that for t in the range of 1.5 to 2.5 eV (in graphene is $t = 2.8$ eV [Castro Neto 2009]) corresponds to a temperature scale ranging from 400 to 700 K. Although studies of doping are beyond the power of our PQMC approach due to the sign problem, they could open interesting perspectives e.g. in future experiments with ultra-cold atoms on a honeycomb optical lattice, or with honeycomb lattices based on group IV elements like expanded graphene (to enhance the ratio U/t) or Si, where the nearest neighbour distance is expected to be approximately 50% larger than in graphene [Cahangirov 2009], such that correlations effects are enhanced. More recently, people have also succeeded in nanofabricating artificial crystal lattice with honeycomb geometry [Singha 2011]. Singha et al. trapped electrons, confined as a 2D gas in a gallium arsenide quantum well, in a nanofabricated artificial honeycomb lattice. By tuning the repulsive Coulomb interactions between electrons, they probed the excitation spectrum in a magnetic field, identified the Hubbard gap due to electron interactions. Their setup offers new playground for the realization of QSL on the honeycomb lattice.

The subject of topological insulator has attracted considerable attentions recently. The topological band insulator (TBI) arises from spin-orbit coupling (SOC) and is invariant under time reveral symmetry [Hasan 2010]. The bulk of TBI is insulating, and on the edge there are counter propagating helical states, that are topologically protected, render gapless charge and spin excitations. An explicit realization of TBI in 2D is given by the Kane-Mele Hamiltonian [Kane 2005] on the honeycomb lattice. The model contains the nearest neighbor hopping with strength t (kinetic energy) and imaginary, spin dependent, next-nearest neighbor hopping with strength λ (spin-orbit coupling). The interaction effects on the TBI phase is a open question under intense debate, and the interplay between spin-orbit coupling λ and the Coulomb repulsion U may introduce new physics at the phase transitions between TBI, AF MI and even the QSL state. We will address this question with our PQMC simultaions, and the first set of results has already shown that the QSL phase is robust against small perturbation of spin-orbit coupling [Hohenadler 2011].

Going back to the question of topological degeneracy in our quantum spin liquid phase. A definite numerical assessment of the topological order will have immediate impact on the current exploration of topologically non-trivial state of matter. Our attempt in previous section (Chap. 4.2.4) is actually very restricted, as we can only check the possible low-lying states within the zero-momentum, singlet sector of the trial wave function. And even there we are hampered by our current, limited com-

putational power. The spin gap is at the order of $0.25t$, so the magnetic correlation length will be around 40 unit cells, whereas we can only access 18 at the moment. Now we are proposing massive CPU time on one of Europe's Tier-0 high performance system. Once the proposal is accepted, we will be able to perform PQMC simulation up to 42^2 unit cells, that will allow us to directly determine the spin-spin correlation length, and the relevant energy scale of the quantum spin liquid phase. After that we can proceed with two complementary approaches to identify the presence of topological order. Firstly, we can devise a probe for the breakdown of adiabatic continuity of the QSL to a topologically trivial band insulator. In particular, we consider honeycomb lattice with varying modulations in hopping integrals based on a Kekule pattern that connects the non-interacting semimetal with a trivial band insulator. Performing PQMC simulations for the modulated system starting from the QSL phase, a breakdown of adiabatic continuity to the band insulator via an intermediate quantum phase transition will provide direct evidence for non-trivial topological order in the QSL. Second, we will continue the attempt in Chap. 4.2.4 of looking for low-lying states that go below the spin gap in the TDL, but we will begin in the lattice symmetry sectors different from the $k = 0$, $S = 0$ sector considered so far. By an appropriate construction of the trial wave function, we can target in our PQMC simulations any given sector within the system's representations of the space-group symmetry.

Our findings in this chapter, based on a controlled numerical framework, open a new facet of quantum spin liquids, where an appreciable amount of doubly-occupied sites are present, extending well beyond the regime of localized spin physics. This result will inspire us and others to study a QSL in a non-frustrated, realistic model under controlled approximations. In response to the publication of our results, a number of papers has emerged aiming to shed further lights on the quantum spin liquid phase [Xu 2010, Lu 2010b, Wang 2010, Vaezi 2010, Clark 2010, Vaezi 2011, Albuquerque 2011, Reuther 2011, Xu 2011], to list a few. We are looking forward to, and will also contribute, further efforts in this direction.

Chapter 5

Edge-State Magnetism in Graphene Nanoribbons

5.1 Graphene Nanoribbons

Graphene, the 2D carbon flatland, carries the great expectation of being a promising candidate for future electronics [Castro Neto 2009]. Graphene nanoribbons, the 1D strip of graphene with open edges, are considered as the building block for nanoelectronics and spintronics [Yazyev 2008]. The properties of graphene nanoribbons, and other nanodevices such as flakes and dots, are in large part governed by their edge structures [Son 2006a, Son 2006b, Trauzettel 2007, Yazyev 2008, Muñoz-Rojas 2009]. In this chapter, we will address the electronic and magnetic properties of graphene ribbons with PQMC simulations.

Graphene nanoribbons exhibit a remarkable interplay of low dimensionality, bipartite geometry and electron-electron interactions. One of the most fundamental predictions for graphene nanoribbons (with zigzag edges) is the possibility of spontaneous edge-state magnetism [Fujita 1996, Nakada 1996, Wakabayashi 1998, Wakabayashi 1999, Hikihara 2003, Fernández-Rossier 2007, Bhowmick 2008, Jiang 2008b, Yazyev 2010]. In contrast, as we know from previous chapters, bulk graphene is expected to be non-magnetic.

Historically, the interests in the edge states of graphene nanoribbon begin even earlier than the interests in graphene itself. During the time of carbon nanotubes, people have already noticed the special properties of the edges in zigzag and armchair ribbons (geometry shown in Fig. 5.1 **a** and **b**). Fujita et al. [Fujita 1996] performed the tight-binding calculation on graphene ribbon with zigzag and armchair edges, and found that the zigzag ribbons have a sharp peak (Van Hove singularity) in the density of states (DOS) at the Fermi level, whereas the armchair ribbons do not have such a singularity (shown Fig. 5.1 **a** and **b**). Furthermore, they applied a Hubbard model with Hartree-Fock mean-field approximation on the graphene ribbons, and found in zigzag ribbons the Stoner instability will trigger ferromagnetic long range order along the edge for infinitesimally small U. Later on, Nakada et al. [Nakada 1996] examined the flat bands of the zigzag ribbon close to the Fermi energy (Fig. 5.1 **a**). They realized that localized electrons are induced by these bands. By varing the width of the graphene ribbons, they found out the nanometer size effect is crucial for determining the relative importance of the edge state. Wakabayashi et al. [Wakabayashi 1998] performed a random phase approximation (RPA) of the Hubbard model on zigzag ribbons to investigate the spin wave modes

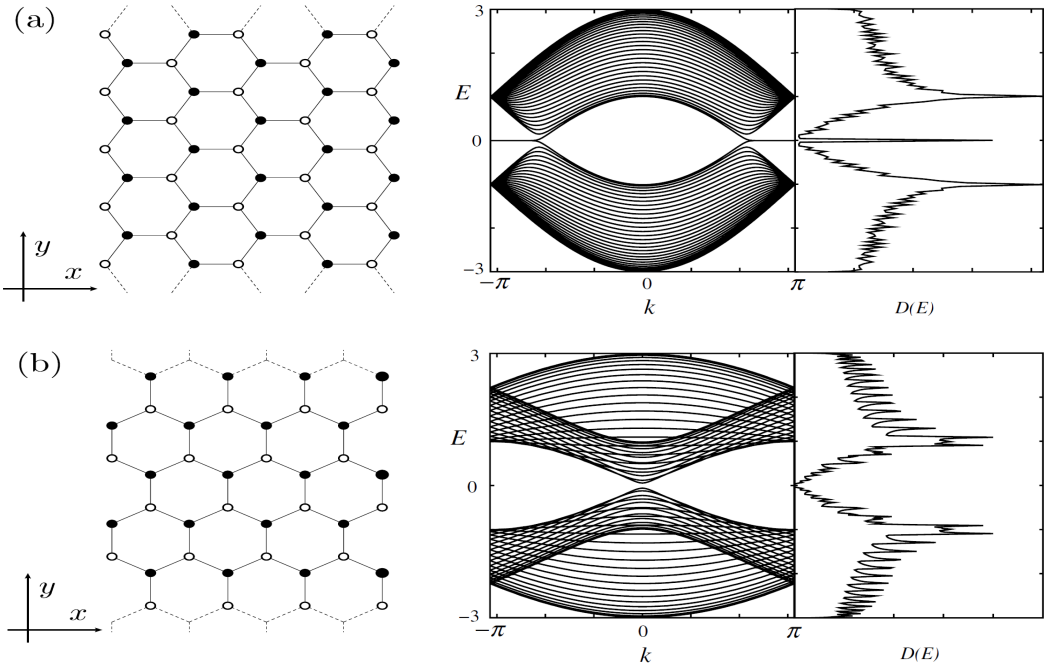

Figure 5.1: Lattice structures, tight-binding dispersions $E(k)$ and density of states $D(E)$ for zigzag **(a)** and armchair **(b)** graphene nanoribbons. The momentum k is normalized by the length of the primitive translation vector, and the energy E is in the unit of the hopping amplitude t. In the zigzag ribbon, flat bands from $2\pi/3$ to π correspond to localized state on the edge. These degenerate bands introduce a divergence (Van Hove singularity) in the DOS at $E = 0$. In armchair ribbon, there is no degeneracy in the entire Brillouin zone (except $k = 0$), the Van Hove singularity is not present.

of the edge magnetic state. At momentum close to $q = 0$ (and 2π), they found a linear spin wave mode, which they associated with the effective antiferromagnetic coupling between the two opposite edges. At higher momentum, a quadratic spin wave dispersion is superposed, which is due to the ferromagnetic ordering of the localized moments in each edge. Hikikara et al. [Hikihara 2003] performed the first DMRG simulation on narrow zigzag ribbon within a Hubbard model description and predicted the magnitude of the interaction driven charge and spin gaps.

Ever since the discovery of graphene, there emerged (and keep emerging) a plethora of works in graphene nanoribbons. Among them, there are first-principle calculations of the band gaps in both zigzag and armchair ribbon as a function of the ribbon width [Son 2006b], DFT and mean-field work concerning the effect of arbitrary termination of the ribbon edge on the magnetic order [Fernández-Rossier 2007, Bhowmick 2008], RPA work on the life time of spin wave excitation on the edge and how the gate voltage and doping will affect it [Culchac 2011]. On the experimental side, the development is even more

intensive, people have succeeded in making graphene nanoribbons with lithographic [Tapaszto 2008], chemical [Datta 2008], sonochemical [Li 2008] methods, and more recently with unzipping of carbon nanotubes [Jiao 2009, Jiao 2010]. Since the graphene ribbon samples are available, people now begin to use STM spectroscopy to study the influence of edge structure on the electronic properties of the graphene ribbons and quantum dots [Ritter 2009], and there is an even move recent work on the STM spectra of chiral Graphene nanoribbons [Tao 2011], where clear spectroscopic signatures of the edge-states on the zigzag edge have been demonstrated.

However, concerning the edge-state magnetism in graphene nanoribbons, we still need to check the reliability of all the mean-field theory (MFT) type approximations [Fujita 1996, Nakada 1996, Wakabayashi 1998, Wakabayashi 1999, Fernández-Rossier 2007, Bhowmick 2008, Jiang 2008b, Yazyev 2010], and how trustworthy the predictions based on them, upon taking the interaction effects into consideration. In a early publication [Feldner 2010], by comparing the MFT with numerical exact results – exact Diagonalization and PQMC – on small graphene (honeycomb lattice) clusters, we have demonstrated that MFT is reliable at least for certain quantities (energy, single particle excitation gap, local magnetization, etc) in the weak-coupling regime where $U/t \leq 1.0$. But on the other hand, we also know that Lieb's theorem predicts there is no net magnetization for bipartite lattice of Hubbard model at half filling [Lieb 1989]. Futhermore, the Mermin-Wagner theorem [Mermin 1966] forbids true long-range order for a ribbon with finite width, since the system is one dimensional. In fact, in a $O(3)$ nonlinear sigma-model treatment of the zigzag ribbon, one can predict a spin gap, i.e., a finite spin-spin correlation length for an even number of zigzag lines, and gapless spin excitations for an odd number of zigzag lines [Yoshioka 2003], and the DMRG work mentioned above found a quite short correlation length in the case of two zigzag lines [Hikihara 2003]. Hence, there are inconsistencies between the theoretical considerations and the recent work on the STM spectra of chiral Graphene nanoribbons [Tao 2011], where Tao et al. observed a clear spectral gap as a signature of edge states on the zigzag edge. In theoretical models, one usually does not take the substrates and intrinsic ripples in graphene into consideration, which might reconcile these inconsistencies.

In view of such puzzling situation, and given the growing experimental effort towards directly probing the magnetism of the graphene nanoribbons, with spin-polarized STM, for instance, we see an urgent calling for an accurate numerical treatment of the Hubbard model description of graphene nanoribbons. In this chapter, we perform PQMC simulations to graphene nanoribbon with zigzag edges, and compare the PQMC results with self-consistent MFT [Feldner 2010]. Our numerically exact results demonstrate that at weak coupling, with realistic ribbon widths, MFT and PQMC are quantitatively comparable. On top of this, we predict a low energy peak in the local spetral function as a dynamical signature of edge-state magnetism. We also confirm other theoretical predictions like the linear magnetic dispersion on the edge arising due to the antiferromagnetic coupling between the edges, the damping effect of the magnetic excitations scattering into particle-hole

continuum. This work has been published in reference [Feldner 2011].

5.2 MFT Results and Experimental Progress

In the MFT, we apply the Hatree-Fock approximation to the original Hubbard Hamiltonian, such that the MFT Hamiltonian is

$$H^{MF} = -t \sum_{\langle i,j\rangle,\sigma} c^\dagger_{i,\sigma} c_{j,\sigma} + U \sum_i \langle n_{i,\uparrow}\rangle n_{i,\downarrow} + U \sum_i n_{i,\uparrow} \langle n_{i,\downarrow}\rangle - U \sum_i \langle n_{i,\uparrow}\rangle \langle n_{i,\downarrow}\rangle. \quad (5.1)$$

It should be noted that the MFT explicitly breaks the SU(2)-symmetry of the Hubbard model. We solve the MFT equations self consistently and compute the ground-state wave function

$$|\Psi_0\rangle = \prod_{\alpha \le N_\uparrow} d^\dagger_{\uparrow\alpha} \prod_{\beta \le N_\downarrow} d^\dagger_{\downarrow\beta} |0\rangle, \qquad \text{with} \qquad d_{\sigma,\alpha} = \sum_i Q^*_{\sigma,\alpha i} c_{\sigma,i}, \quad (5.2)$$

where $Q_{\sigma,\alpha i}$ is the matrix of eigenvectors of H^{MF}, and the one-particle spectrum $\varepsilon_{\sigma,\alpha}$ of the MF Hamiltonian H^{MF}. With these quantities we can compute the ground state energy,

$$E_0 = \sum_\sigma \langle 0| \prod_{i \le N_\sigma} d_{\sigma,i} \left(-t \sum_{\langle i,j\rangle,\sigma} c^\dagger_{i,\sigma} c_{j,\sigma} + U \sum_{i,\sigma} n_{i,\sigma} \langle n_{i,\sigma'}\rangle\right) \prod_{i \le N_\sigma} d^\dagger_{\sigma,i} |0\rangle - U \sum_i \langle n_{i,\uparrow}\rangle \langle n_{i,\downarrow}\rangle \quad (5.3)$$

and the local density

$$\langle n_{\sigma,i}\rangle = \sum_{\alpha \le N_\sigma} Q^*_{\sigma,\alpha i} Q_{\sigma,i\alpha}\,, \quad (5.4)$$

the local magnetization

$$\langle S^z_i \rangle = \frac{1}{2}(\langle n_{\uparrow,i}\rangle - \langle n_{\downarrow,i}\rangle), \quad (5.5)$$

as well as the spin correlation function

$$\begin{aligned} \langle S^z_i S^z_j \rangle \;=\; & \frac{1}{4}\Bigg(\sum_{\sigma=\uparrow,\downarrow} \sum_{\alpha=1}^{N_\sigma} \sum_{\beta\neq\alpha}^{N_\sigma} Q_{\sigma,j\alpha} Q_{\sigma,i\beta} \left\{ Q^*_{\sigma,\alpha j} Q^*_{\sigma,\beta i} - Q^*_{\sigma,\beta j} Q^*_{\sigma,\alpha i} \right\} \\ & - \langle n_{j\uparrow}\rangle \langle n_{i\downarrow}\rangle - \langle n_{j\downarrow}\rangle \langle n_{i\uparrow}\rangle \Bigg). \end{aligned} \quad (5.6)$$

Self-consistency requires that the expectation values $\langle n_{\sigma,i}\rangle$ entering Eq. 5.1 are equal to the expression Eq. 5.4 derived from this Hamiltonian. We solve this condition iteratively using suitable initial conditions with given numbers of electrons N_σ. To overcome convergence problems, instead of the ground state, in the first iteration, we use a thermal state compatible with the Fermi-Dirac distribution at a given temperature [Cabra 2004]. In this case the average density is computed as:

$$\langle n_{\sigma,i}\rangle = \sum_{\alpha \in \Omega_\sigma} Q^*_{\sigma,\alpha i} Q_{\sigma,i\alpha} \quad (5.7)$$

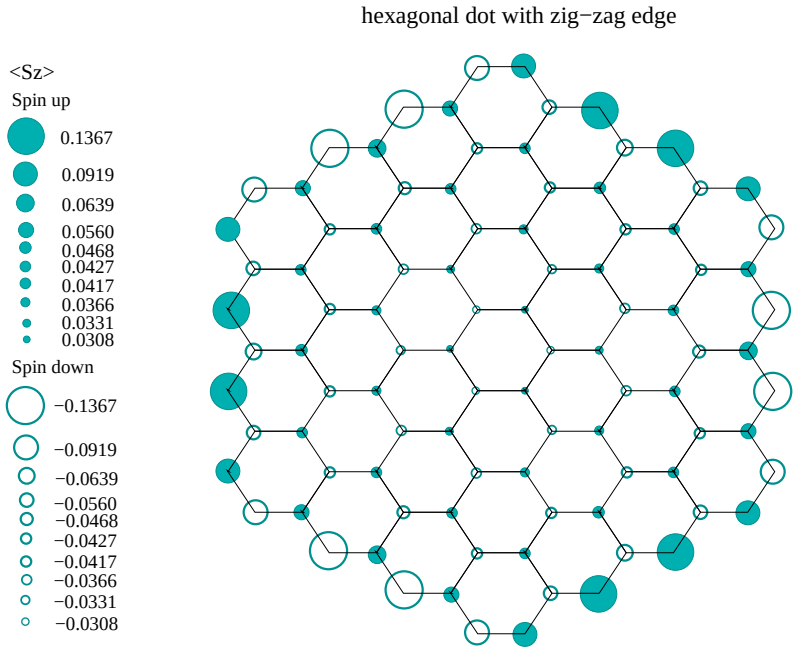

Figure 5.2: Edge magnetization of a graphene quantum dot (at half filling and $U = 2.0t$), the radii of the circles denote the magnitude of local magnetization moment $\langle S^z \rangle$.

where Ω_σ is a set of N_σ single-particle states chosen randomly with probability $n(\varepsilon_{\sigma,\alpha}) = 1/(1 + e^{[\beta(\varepsilon_{\sigma,\alpha} - \bar{\varepsilon})]})$.

We test our MFT by appling it to the 2D honeycomb lattice and find a Mott transition at the literature value $U_c \approx 2.23\,t$ [Sorella 1992], where the system goes from a paramagnetic semimetal to an insulator with antiferromagnetic order. The asymptotic behavior of the Néel order parameter and the single-particle gap is numerically consistent with linear behavior in $U - U_c$ for $U > U_c$, i.e., associated critical exponent β equal to one. This unusual mean-field exponent reflects the unusual density of states which is linear close to the Fermi energy (see chapter 4.2).

For finite size graphene structure with zigzag edge, like ribbons or dots, our MFT shows a nonzero local magnetization on the edge for infinitesimally small U, consistent with previous works [Fujita 1996, Wakabayashi 1998]. For example, Fig. 5.2 show the local magnetisation ($\langle S^z \rangle$) for a dot of hexagonal shape of 96 sites at $U = 2t$, the ferromagnetic order along the zigzag edge is well developed. On the other hand, systems with armchair edges do not show specific magnetic properties and follow an evolution closer to 2D system with periodic boundary conditions.

Before going to the PQMC data on zigzag ribbons, let us elaborate a bit more on the recent experimental breakthrough by Tao et al. in chiral graphene ribbon [Tao 2011]. They use carbon nanotube unzipping methods [Kosynkin 2009, Jiao 2010] to chemically produce variations of graphene nanoribbons of different width, length, chirality, and substrate. Figure 5.4 **a** and **b** show the STM topog-

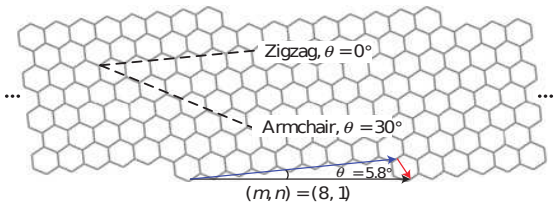

Figure 5.3: Schematic drawing of $(8,1)$ chiral graphene nanoribbon. The chiral vector (m,n) connecting crystallographcically equivalent sites along the edge defines the edge orientation of the ribbon (black arrow). The blue and red arrows are the projection of the $(8,1)$ vector onto the basis vectors of the graphene lattice. Adapted from Ref. [Tao 2011].

raphy and the structural model of a $(8,1)$ chiral ribbon (a schematic drawing is shown in Fig. 5.3). Note that the chiral vector (m,n) connects crystallographically equivalent sites along the edge, and the vector defines the edge orientation of the graphene nanoribbon. Zigzag and armchair edges have corresponding chiral angles of $\theta = 0°$ and $\theta = 30°$, respectively, whereas the $(8,1)$ edge has an chiral angle of $\theta = 5.8°$ (see Fig. 5.3). The local electronic structure of the chiral ribbon is measured by using sub-nm-resolved scanning tunnelling spectroscopy, in which dI/dV measurements reflect the energy-resolved local density of states (LDOS). In Fig. 5.4 **c** and **d**, very close to the ribbon edge, Tao et. al. observe two peaks that rise up within the elastic tunnelling region (that is at energies below the phonon-assisted inelastic onset of large-scale graphene sheets, which is of ~ 130 meV) and the two peaks straddle zero bias, the gap that splits the two peaks is $\Delta = 23.8 \pm 3.2$ meV. These STM measurements reveal the presence of the edge states along the zigzag edge of graphene nanoribbons. Tao et al. associate these spectroscopic features with an interaction driven, 1D spin-polarized edge state, which is not observed in similar experiments for graphite edges, armchair nanoribbons, and comparatively less ordered graphene edges.

5.3 Static Spin-Spin Correlation on the Edge

Now we are ready to present our PQMC simulation and MFT results. The geometry of the graphene nanoribbon with zigzag edges is depicted in the inset of Fig. 5.5. We employ periodic boundary conditions at the armchair edge and open boundary conditions at the zigzag edge. L and W denote the length and the width of the ribbon, respectively. L is measured in units of lattice vector $\mathbf{a}_1 = (\sqrt{3}, 0)$ and W is the number of zigzag legs of the ribbon. The intersite distance between carbon atoms is set to unity.

As has been discussed in the previous sections, MFT for the 2D periodic honeycomb lattice yields a transition from a semimetal to an antiferromagnet at $U_c/t = 2.23$ [Sorella 1992, Feldner 2010] whereas PQMC reveals a metal-insulator transition at $U_{c1}/t = 3.5(1)$ and a further nonmagnetic insulator-antiferromagnetic

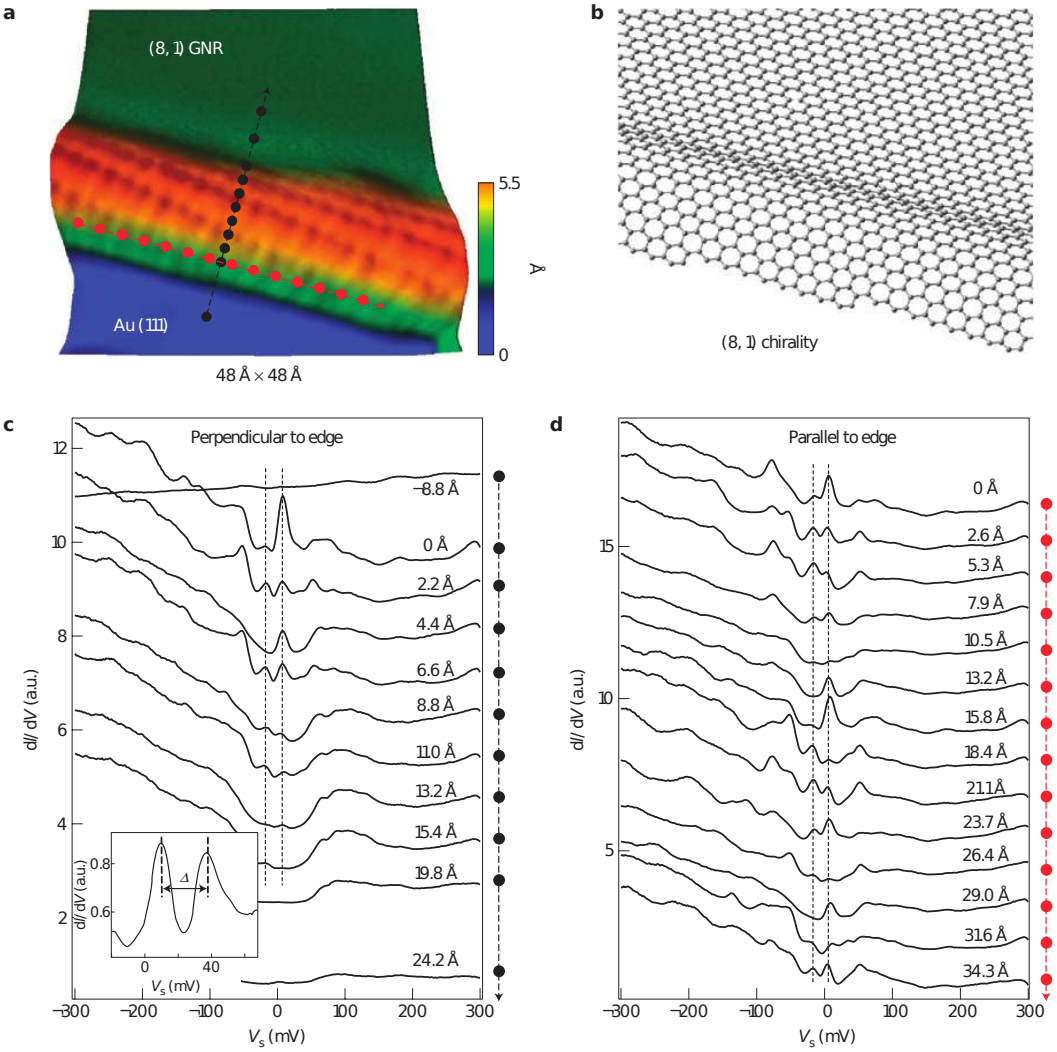

Figure 5.4: **a**, Atomically resolved topography of the terminal edge of an $(8,1)$ chiral graphene nanoribbon. **b**, Structural model of the $(8,1)$ graphene nanoribbon edge shown in **a**. **c**, dI/dV spectra (LDOS) of the nanoribbon edge shown in **a**, measured at different points (black dots) along a line perpendicular to the ribbon edge shown in **a**. Inset shows a higher resolution dI/dV spectrum for the edge of a $(5,2)$ graphene nanoribbon. The dashed lines are guides to the eye. **d**, dI/dV spectra measured at different points (red dots) along a line parallel to the ribbon edge shown in **a**. Taken from Ref. [Tao 2011].

insulator transition at $U_{c2}/t = 4.3(1)$ [Meng 2010]. In this work, we focus on the interaction range $U/t \leq 2$ since we are interested in the behavior of the system in the weak-coupling regime.

The inset of Fig. 5.5 shows the MFT result for the local magnetization at the edge of a $W = 4$, $L = 6$ ribbon at $U/t = 2$ and illustrates the edge-state mag-

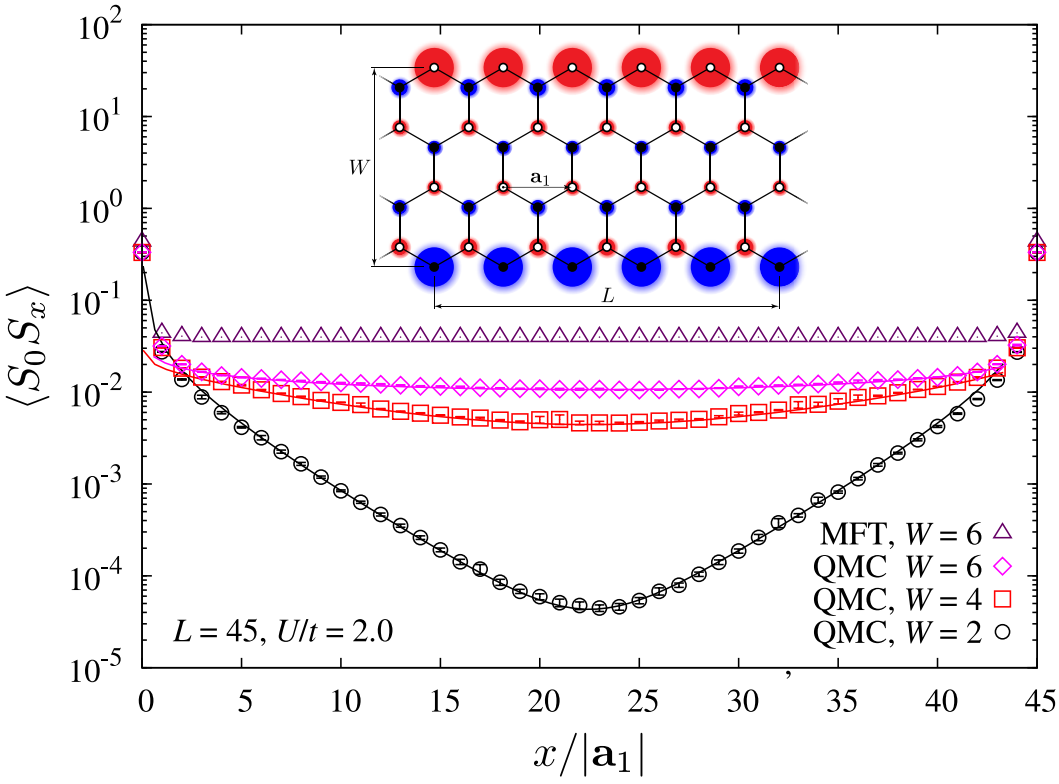

Figure 5.5: Real-space spin-spin correlation function along the zigzag edge of ribbons. Points are the PQMC and MFT data and lines are the fits using Eq. (5.8). Inset: Geometry of the graphene nanoribbon with zigzag edges, $L = 6$, $W = 4$, and lattice size $N = 2 \times L \times W = 48$. Red and blue circles represent the positive and negative values of the local magnetization $\langle S_i^z \rangle = \frac{1}{2}\langle n_{i,\uparrow} - n_{i,\downarrow} \rangle$, calculated from MFT at $U/t = 2$. Radii are proportional to the magnitude.

netism which is expected for weak Coulomb interactions $U/t > 0$ [Fujita 1996, Wakabayashi 1998, Wakabayashi 1999, Fernández-Rossier 2007, Bhowmick 2008, Jiang 2008b, Yazyev 2010]. This is reflected by the MFT result for the spin-spin correlation function which is shown by triangles for $W = 6$, $L = 45$, and $U/t = 2$ in the main panel of Fig. 5.5: the correlation function rapidly approaches a constant value as a function of distance x along the edge with very little dependence on the width W of the ribbon (not shown).

In contrast, the PQMC results for the static spin-spin correlation function shown in the main panel of Fig. 5.5 exhibit a clear decay, at least for narrow ribbons with $W = 2$ (circles) and 4 (squares). Note that the rapid decay for $W = 2$ is consistent with a previous DMRG study [Hikihara 2003]. However, as the width increases, the decay becomes slower and the PQMC result for $W = 6$ in Fig. 5.5 (diamonds) is already qualitatively similar to the MFT result.

For a more quantitative analysis we fit the PQMC data for the longest available

ribbons with a function combining exponential and power-law behavior

$$\langle S_0 S_x \rangle = C \left(x^{-\eta} e^{-x/\xi} + (L|\mathbf{a}_1| - x)^{-\eta} \, e^{-(L|\mathbf{a}_1|-x)/\xi} \right) . \tag{5.8}$$

From a fit for $L = 60$ at $W = 2$ we estimate $\xi/|\mathbf{a}_1| = 4.0 \pm 1$ and $\eta = 0.5 \pm 0.3$ and at $W = 4$ the $L = 54$ data yields $\xi/|\mathbf{a}_1| = 15 \pm 4$ and $\eta = 0.2 \pm 0.15$. At $W = 6$ it is no longer possible to distinguish the correlation length from infinity or the exponent η from zero for the largest available system size within our study ($L = 45$). Indeed, the $W = 6$ PQMC data can equally well be fitted by predictions based on a correlation length. We thus arrive at a picture similar to even-leg spin ladders [Dagotto 1996] or integer spin-S quantum chains [Todo 2001]: ribbons with even W have a finite spin-spin correlation length [Yoshioka 2003], but the correlation length rapidly grows with W, such that for practical purposes it can be considered long ranged for $W \gtrsim 6$. In this sense, edge-state magnetism is found already for ribbons of moderate widths. In order to check if MFT becomes also quantitatively accurate for wider ribbons, one would need to go beyond the system sizes which we can presently access by PQMC.

5.4 Spectral Functions: $A(\omega)$ and $A(q,\omega)$

Since the ferromagnetic behavior at the edges remains fluctuating in a proper treatment of the Hubbard model, we now turn to the dynamic properties. The local single-particle spectral function $A(\omega)$ is a particularly important observable since it can be measured in scanning tunneling microscopy (STM) experiments [Niimi 2006, Ugeda 2010, Tao 2011]. It is defined as

$$A(\omega) = \Im \int_{-\infty}^{\infty} d(t-t') \; e^{i\omega(t-t')} i \langle T[c_i(t) c_i^\dagger(t')] \rangle, \tag{5.9}$$

where $\Im$ denotes the imaginary part, and T is the time ordering operator. The momentum-resolved single-particle spectral function is defined as

$$A(q,\omega) = \Im \int_{-\infty}^{\infty} d(t-t') \; e^{i\omega(t-t')} \frac{1}{L} \sum_{i,j} e^{iq(i-j)} i \langle T[c_i(t) c_j^\dagger(t')] \rangle, \tag{5.10}$$

where i, j are sites along the edge within the same sublattice, the sum runs from $i = 1$ to L where L is the number of unit cells the edge contains.

Previous theoretical studies of the interplay of edge-state magnetism and spectral functions of graphene ribbons are restricted to density-functional approaches [Jiang 2008b, He 2010] with an inherent mean-field type approximation. Here with PQMC simulations, we firstly measure the momentum-resolved Green's function at the ribbon edge in imaginary time $G(q,\tau)$, and then apply a stochastic analytical continuation scheme [Sandvik 1998, Beach 2004] to rotate $G(q,\tau)$ on the τ-axis to $A(q,\omega)$ on the ω-axis. Finally, the local spectral function $A(\omega)$ is obtained by integration over the momentum q along the ribbon direction. In this way, we obtain the spectral function with the full many-body physics taken into consideration,

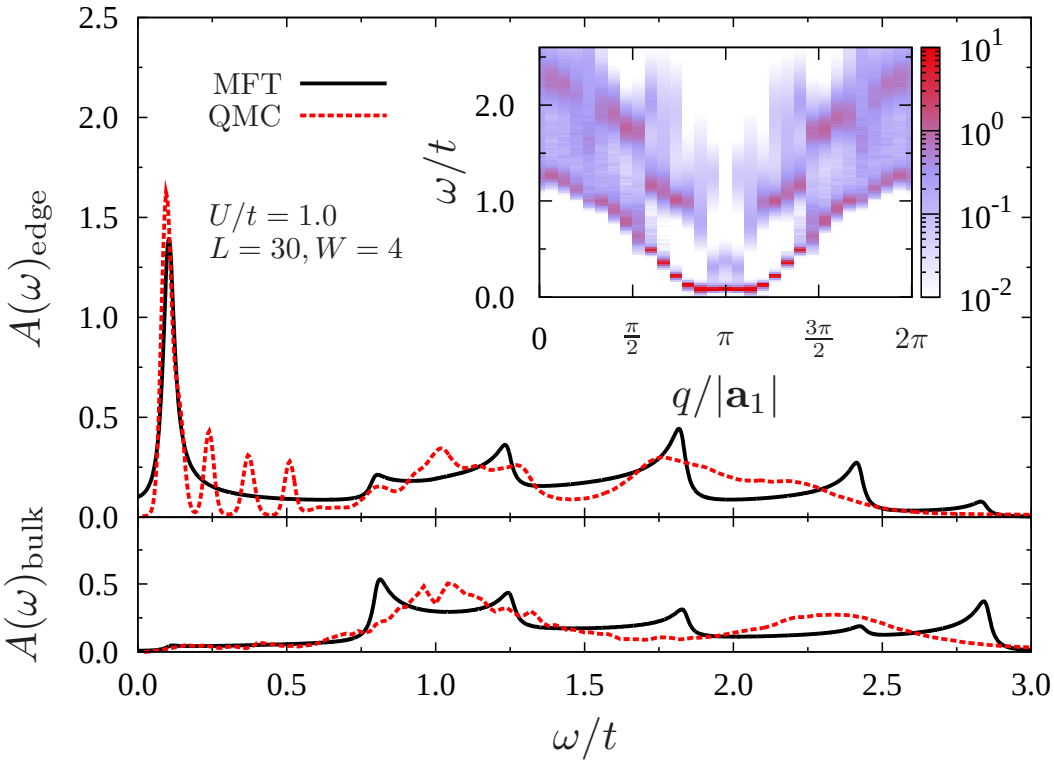

Figure 5.6: Spectral functions of a width $W = 4$ ribbon at $U/t = 1$. PQMC data is for a ribbon of length $L = 30$, whereas results from MFT correspond to the thermodynamic limit. The main panel shows the local spectral function $A(\omega)$ subject to a Lorentzian broadening $\Delta\omega = 0.02\,t$. Note the prominent low-energy peak in $A(\omega)_{\rm edge}$ at $\omega/t \approx 0.1$ which is absent in $A(\omega)_{\rm bulk}$. The inset shows PQMC results for the momentum-resolved spectral function $A(q, \omega)$ along the zigzag edge.

and our data provide the numerically exact benchmark for all the mean-field type approximations, including those of our own.

Fig. 5.6 shows the PQMC single-particle spectral function both on the zigzag edge $A(\omega)_{\rm edge}$ and inside the bulk $A(\omega)_{\rm bulk}$, for ribbon of width $W = 4$ at $U/t = 1$. The MFT spectral function corresponds to a ribbon in the thermodynamic limit. The local spectral functions in the main panel were subjected to a Lorentzian broadening of $\Delta\omega = 0.02\,t$, both in PQMC and MFT. $A(\omega)_{\rm edge}$ exhibits a dominant low-energy peak at $\omega/t \approx 0.1$ which is absent in $A(\omega)_{\rm bulk}$. This peak can be traced to a flat region of a single-particle dispersion visible in $A(q, \omega)_{\rm edge}$ (compare the inset in Fig. 5.6). The agreement between MFT and PQMC is excellent for this low-energy peak and the overall agreement is also good at higher energies. The three additional sharp features in the PQMC result for $A(\omega)_{\rm edge}$ in the region $0.2 < \omega/t < 0.6$ can be traced to a finite-size momentum discretization effect and are reproducible in MFT if the latter is also restricted to a finite ribbon of length $L = 30$. We conclude

that the agreement between MFT and PQMC for $A(\omega)$ is remarkable even at a quantitative level, at least for weak interactions $U/t \lesssim 1$.

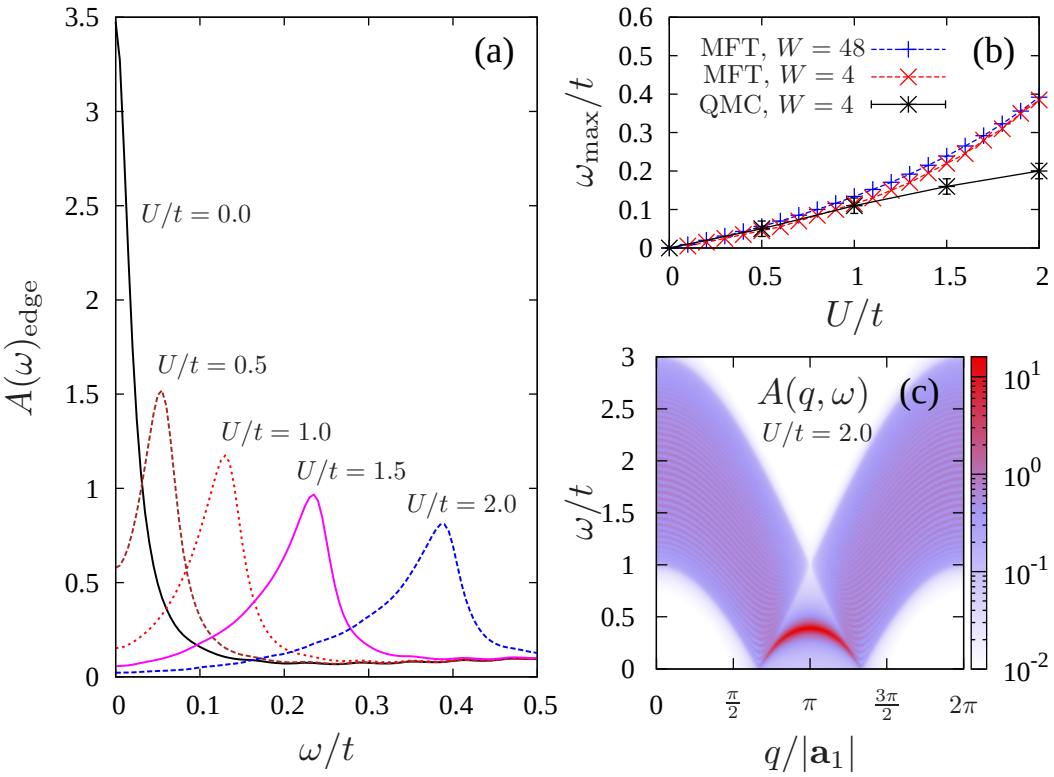

Figure 5.7: (a) Single-particle spectral function $A(\omega)_{\text{edge}}$ for several values of U/t and a ribbon of width $W = 48$. (b) Comparison of the position ω_{max} of the maximum of $A(\omega)_{\text{edge}}$ between MFT for $W = 4$, 48 and PQMC for $W = 4$ and $L = 30$. (c) $A(q,\omega)_{\text{edge}}$ for a ribbon with $W = 48$ at $U/t = 2$.

Having gained confidence in the accuracy of the MFT results for $A(\omega)$, we use it to analyze a bigger and more realistic system with $W = 48$, corresponding to a graphene nanoribbon of 10 nm width. The evolution of the low-energy peak on the edge with the Coulomb repulsion is shown in Fig. 5.7(a). The energy ω_{max} corresponding to the maximum intensity of the spectral function increases with the Coulomb repulsion U and is located at $\omega_{\text{max}} = 0$ only for $U = 0$, i.e., the non-interacting system. In combination with the fact that this peak exists only on the ferromagnetic edge (compare Fig. 5.6) we conclude that it is a clear dynamic signature of edge-state magnetism. Fig. 5.7(b) demonstrates that ω_{max} is insensitive to the actual width of the ribbon and confirms that MFT is accurate for $U/t \lesssim 1$ (the fact that MFT becomes less accurate as one approaches the mean-field phase transition at $U_c/t = 2.23$ [Sorella 1992, Feldner 2010] is not surprising).

The MFT $A(q,\omega)$ shown in Fig. 5.7(c) for $U/t = 2$) reveals that the feature at ω_{max} can be traced to the maximum of a single-particle band at $q/|\mathbf{a}_1| = \pi$ where

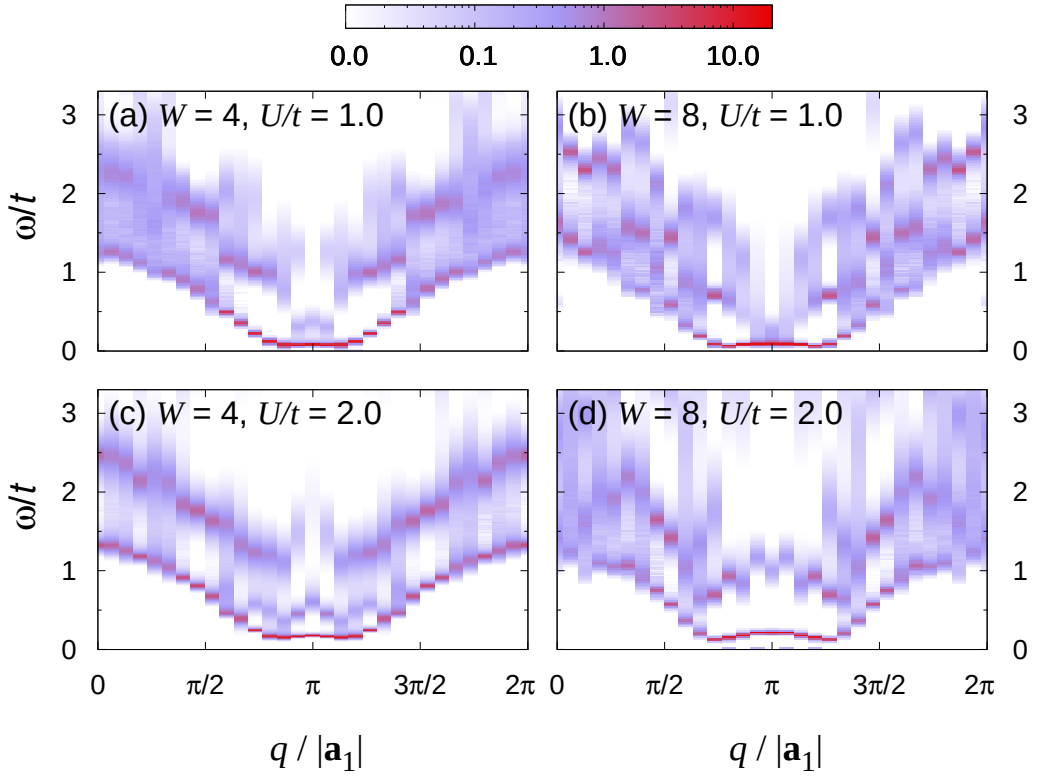

Figure 5.8: PQMC $A(q,\omega)$ for a $L = 30$ ribbon, at different widths $W = 2$ and 4 and different interaction strengths $U/t = 1$ and 2. From (a) to (b), and from (c) to (d), as the width of the ribbon doubled, one observe the flat band gap around $q/|\mathbf{a}_1| = \pi$ begin to bend down around $q/|\mathbf{a}_1| = 2\pi/3$ and $4\pi/3$, forming the "banana" mode.

large matrix elements and a Van Hove singularity combine to yield a maximum intensity of the local spectral function. The true single-particle gap Δ_{sp} is located in the vicinity of $q/|\mathbf{a}_1| = 2\pi/3$ and $4\pi/3$. For the $W = 48$ ribbon shown in Fig. 5.7 it is only $\Delta_{sp}/t = 0.037$ for $U/t = 2$, resulting in a fill-in of spectral weight in the local density of states below the 'pseudo-gap' $\omega_{\max}$ (compare Fig. 5.7(a)). The value of the single-particle gap Δ_{sp} depends strongly on the width of the ribbon; for the $W = 4$ ribbon shown in Fig. 5.6 it is quite close to the pseudo-gap $\omega_{\max}$. Note that the data in Fig. 5.7(a) is subjected to a broadening $\Delta\omega = 0.02t$. With a higher energy resolution, one would observe further features, in particular another Van Hove singularity at Δ_{sp}, albeit with a much smaller weight than at $\omega_{\max}$.

The change of the band shape from from a flat gap at $\omega_{\max}$ around $q/|\mathbf{a}_1| = \pi$ in Fig. 5.6 (inset) to the linear closing at $q/|\mathbf{a}_1| = 2\pi/3$ and $4\pi/3$ in Fig. 5.7 (c) deserves more attention, we explore further on that both in PQMC and MFT. As shown in Fig. 5.8 and Fig. 5.9, for the ribbons of width $W = 4$ the single-particle dispersion around $q = \pi$ is indeed flat, but when the width is doubled, the dispersion

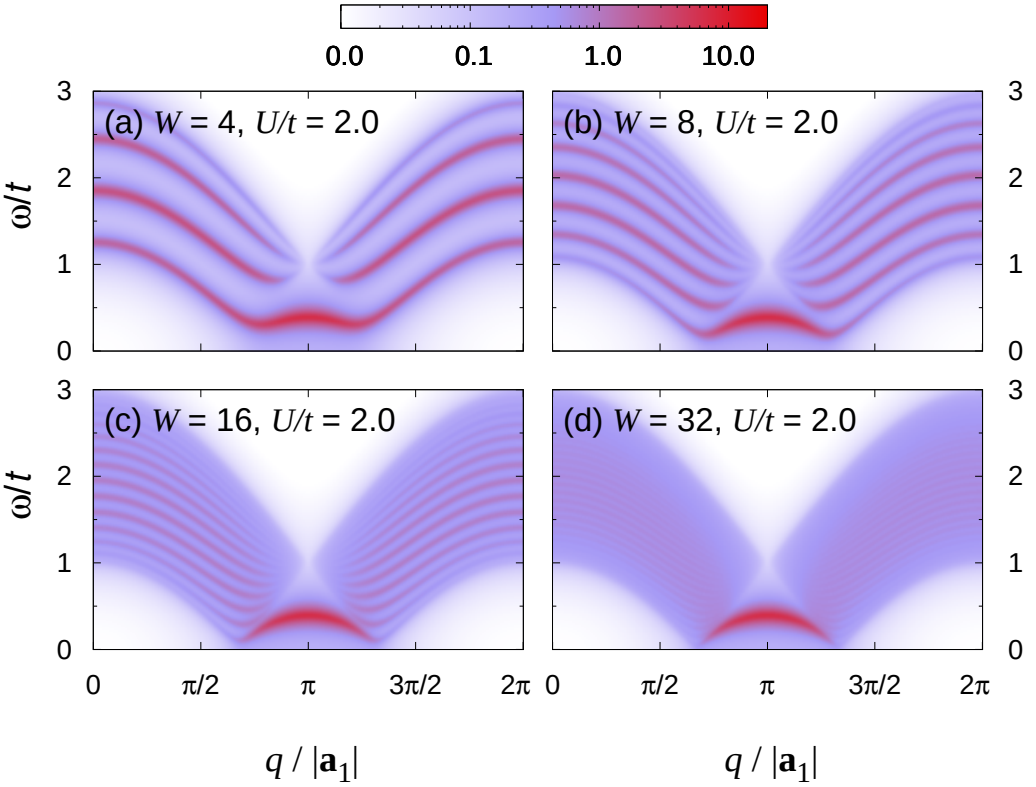

Figure 5.9: MFT $A(q,\omega)$ at different widths and $U/t = 2$. One can see the closing of the band gap with the ribbon width around $q/|\mathbf{a}_1| = 2\,\pi/3$ and $4\,\pi/3$. Such closing comes from the projection of the two Dirac points K and K' in the disperion of graphene sheet.

begins to bend down around $q = 2\pi/3$ and $q = 4\pi/3$. We realized that as the ribbon become wider, the dispersion will reveal more components of its counterpart in 2D Graphene sheet. The two closing points of the banana mode are actually the projection of the two Dirac points $K = (\frac{2\pi}{3\sqrt{3}}, \frac{2\pi}{3})$ and $K' = (-\frac{2\pi}{3\sqrt{3}}, \frac{2\pi}{3})$ in the 2D Brillouin zone.

5.5 Spin Spectral Function $S(q,\omega)$

Another probe to reveal the peculiar magnetic properties of zigzag nanoribbons is provided by the spin spectral function $S(q,\omega)$ on the edge. The momentum-resolved spin spectral function (dynamic structure factor) is defined as

$$S(q,\omega) = \int_{-\infty}^{\infty} dt\; e^{i\omega t} \frac{1}{L} \sum_{i,j} e^{iq(i-j)} \langle S_i^z(t) S_j^z(0) \rangle, \tag{5.11}$$

where i, j are sites on the edge belonging to the same sublattice.

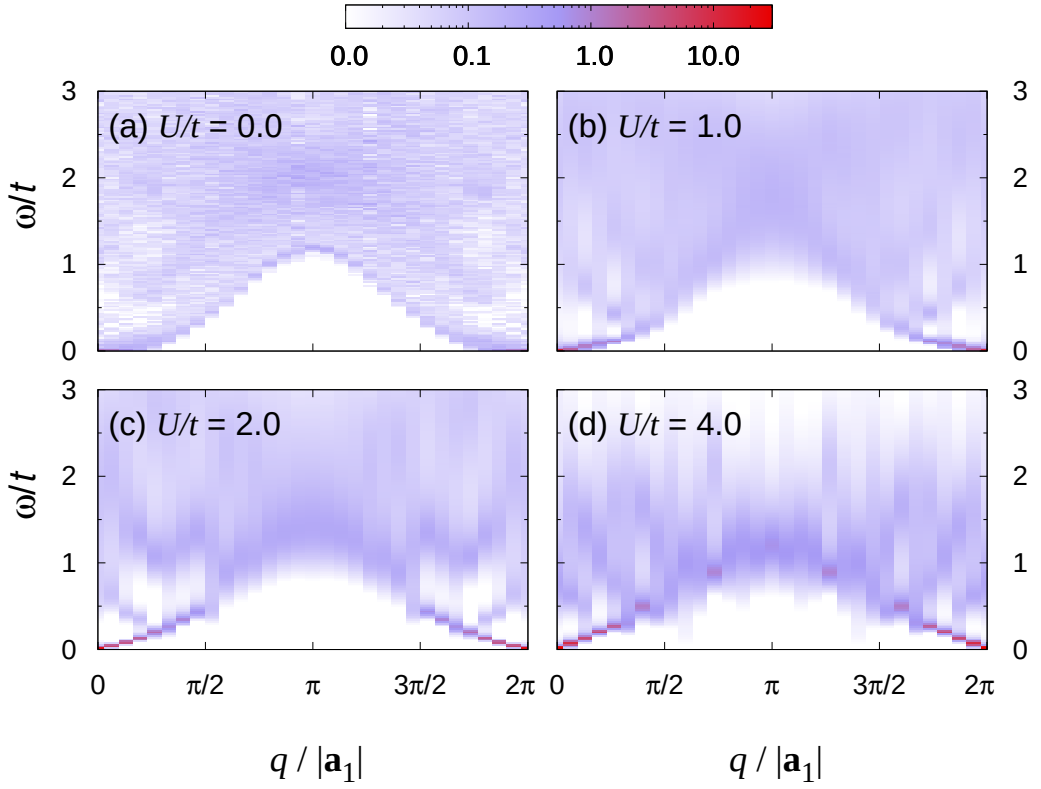

Figure 5.10: PQMC $S(q,\omega)$ for a $L = 30$ $W = 4$ ribbon, at different interaction strengths.

From the enhanced ferromagnetic correlations along the zigzag edge at finite values of U, one might expect $S(q,\omega)$ to exhibit collective spin-wave (magnon) excitations characteristic of a ferromagnetic background, with a quadratic low-energy dispersion relation near $q = 0$. However, as pointed out in Refs. [Wakabayashi 1998, Culchac 2011], the magnetic excitations are affected by the antiferromagnetic coupling between the two edges of the nanoribbon that is mediated by the bulk conduction electrons. These antiferromagnetic correlations result in a linear contribution to the dispersion at small wave vectors (see also Ref. [You 2008]). Furthermore, for energies entering the particle-hole continuum, the collective modes can decay into strongly damped Stoner modes [Culchac 2011].

Our PQMC data in Fig. 5.10 for a $L = 30, W = 4$ ribbon, indeed exhibt the linear, magnon-like dispersion along the edge. Compared with the corresponding evolution in the single particle spectra (Fig. 5.8 (a) and (c)), we can even confirm in a quantitative level, the threshold energy $\omega_{\rm th}$ of the approximately linear magnonlike excitations is twice of corresponding single particle gap $\omega_{\rm max}$. Magnetic excitations above the threshold energy are all damped into the particle-hole continuum. For example, in Fig. 5.10 (b), $U/t = 1$, the $\omega_{\rm th}/t = 0.18 \pm 0.04$ corresponds to the energy up to a wave vector $\mathbf{q}/|\mathbf{a}_1| = \frac{\pi}{3}$, and one can read the $\omega_{\rm max}/t = 0.1 \pm$

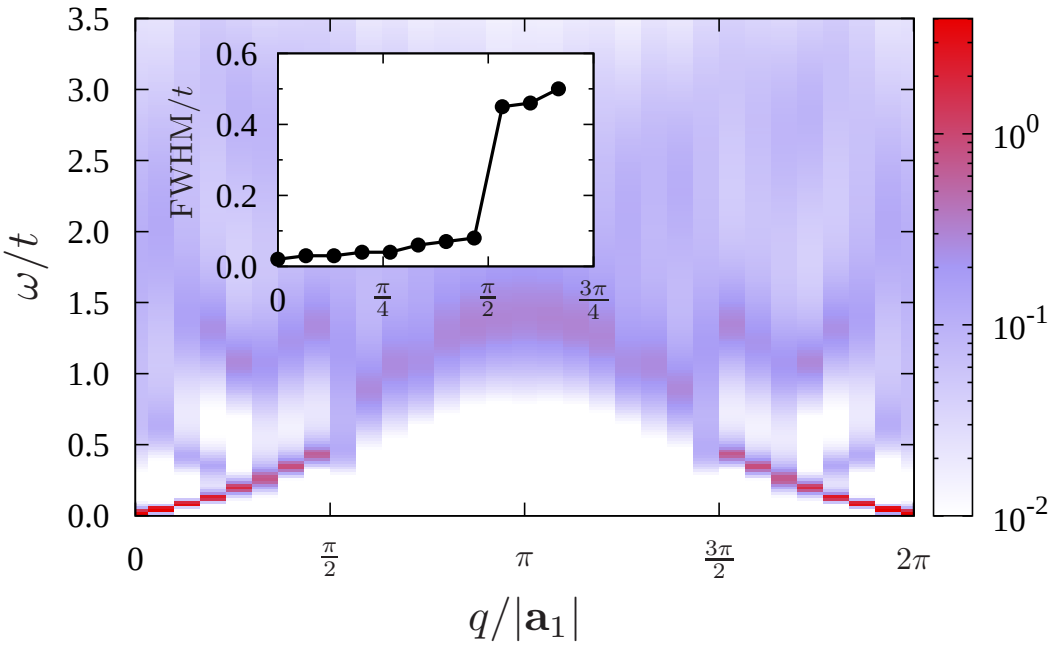

Figure 5.11: PQMC results for the spin spectral function $S(q,\omega)$ along the edge of a zigzag ribbon with $L = 30, W = 4$ and $U/t = 2$. The inset shows the linewidth (FWHM) of the dominant mode in $S(q,\omega)$ as a function of momentum q.

0.02 from Fig. 5.8 (a). Similarly, at $U/t = 2$, Fig. 5.11 exhibits an approximately linearly dispersing sharp mode up to a wave vector $q/|\mathbf{a}_1| \approx 0.5\,\pi$ with a threshold energy $\omega_{th}/t = 0.42 \pm 0.04$, compatible with twice the corresponding single-particle gap of $\omega_{\max}/t = 0.2 \pm 0.02$ from Fig. 5.8 (c). The inset of Fig. 5.11 shows the corresponding evolution of the linewidth (FWHM) of this low-energy mode that drastically increases beyond $q/|\mathbf{a}_1| \approx 0.5\,\pi$.

5.6 Summary and Outlook

To sum up this chapter, we have investigated the static as well as dynamic properties of graphene nanoribbons with zigzag edges, using approximation-free PQMC simulations and MFT of the Hubbard model. Upon closer inspection, true ferromagnetic long-range order at the zigzag edge [Fujita 1996, Wakabayashi 1998, Wakabayashi 1999, Fernández-Rossier 2007, Bhowmick 2008, Jiang 2008b, Yazyev 2010] of a finite-width ribbon turns out to be absent [Lieb 1989, Mermin 1966, Yoshioka 2003, Hikihara 2003], yet there are strong ferromagnetic correlations which are essentially long range but for the narrowest ribbons. We have also identified a dominant low-energy peak in the local spectral function as a dynamic signature of edge-state magnetism, thus providing a theoretical guide for further STM and spin-resolved STM experiments. The agreement between PQMC

and MFT for the local spectral function is remarkably accurate for weak Coulomb interactions, $U/t \leq 2$, justifying a description of realistic geometries within a MFT framework. In particular, we have demonstrated that the position of the dominant low-energy peak at the zigzag edge of a nanoribbon is controlled mainly by the Coulomb interaction U such that STM experiments can be used to deduce the appropriate U value for graphene. Last but not least, we have presented PQMC results for the dynamic spin structure factor at the zigzag edge of ribbon and demonstrated the presence of approximately linearly dispersing low-energy collective spin-wave excitations [Wakabayashi 1998] that decay upon entering the particle-hole continuum [Culchac 2011].

Table 5.1 and Table 5.2 summarize the PQMC spectral functions $A(q,\omega)$ and dynamic spin structure factors $S(q,\omega)$ along the zigzag ribbon edge. All the dynamic properties we have discussed in this chapter, i.e., low-energy peak in $A(\omega)$, closing of the band gap at $q/|\mathbf{a}_1| = \frac{2\pi}{3}$ and $\frac{4\pi}{3}$, linear magnonlike excitations underneath the particle-hole continuum and their damping effect, can all be found in these two tables.

As for future steps, there has been a MFT investigation of the dependence of the edge magnetic moments and the energy splitting on the chirality angle θ [Yazyev 2011]. We are planning to perform PQMC simulations for such generic chiral graphene ribbons, to discuss both the influence of the chirality angle θ on the local spectral function and the spatial decay of the magnetic correlations into the bulk. Moreover, how the edge states will be affected by the presence of other types of terminating edges and defects is also an interesting question. There are MFT studies predicting the robustness of the edge state magnetism, that zigzag edges longer than three to four repeating unit cells are always magnetic, irrespective of other edges (regular polygnoal edges of nanodots and irregular shapes) [Bhowmick 2008], PQMC can also be applied in this direction to verify the claims.

Last but not least, atomic vacancies have strong impact on the electronic and magnetic properties of graphene ribbons, dots and other graphene related materials. There have been STM experiments that measured the electronic resonance at the Fermi energy around an isolated vacancy on a graphene surface [Ugeda 2010]. An algebrical decay in real space $(1/r^2)$ in the LDOS of the vacancy induced bound state is found in the experiment. In the same spirit, the edge of the graphene ribbons might also be viewed as a vacancy, so whether the edge states also follow the algebrical decay into the bulk can well be studied within our PQMC scheme, in fact, our first set of the data in this direction indeed supports an powerlaw decay $(1/r^2)$ of the edge states into to bulk.

Table 5.1: Summary of the PQMC spetral functions $A(\mathbf{q},\omega)$ for $L = 30$ ribbons.

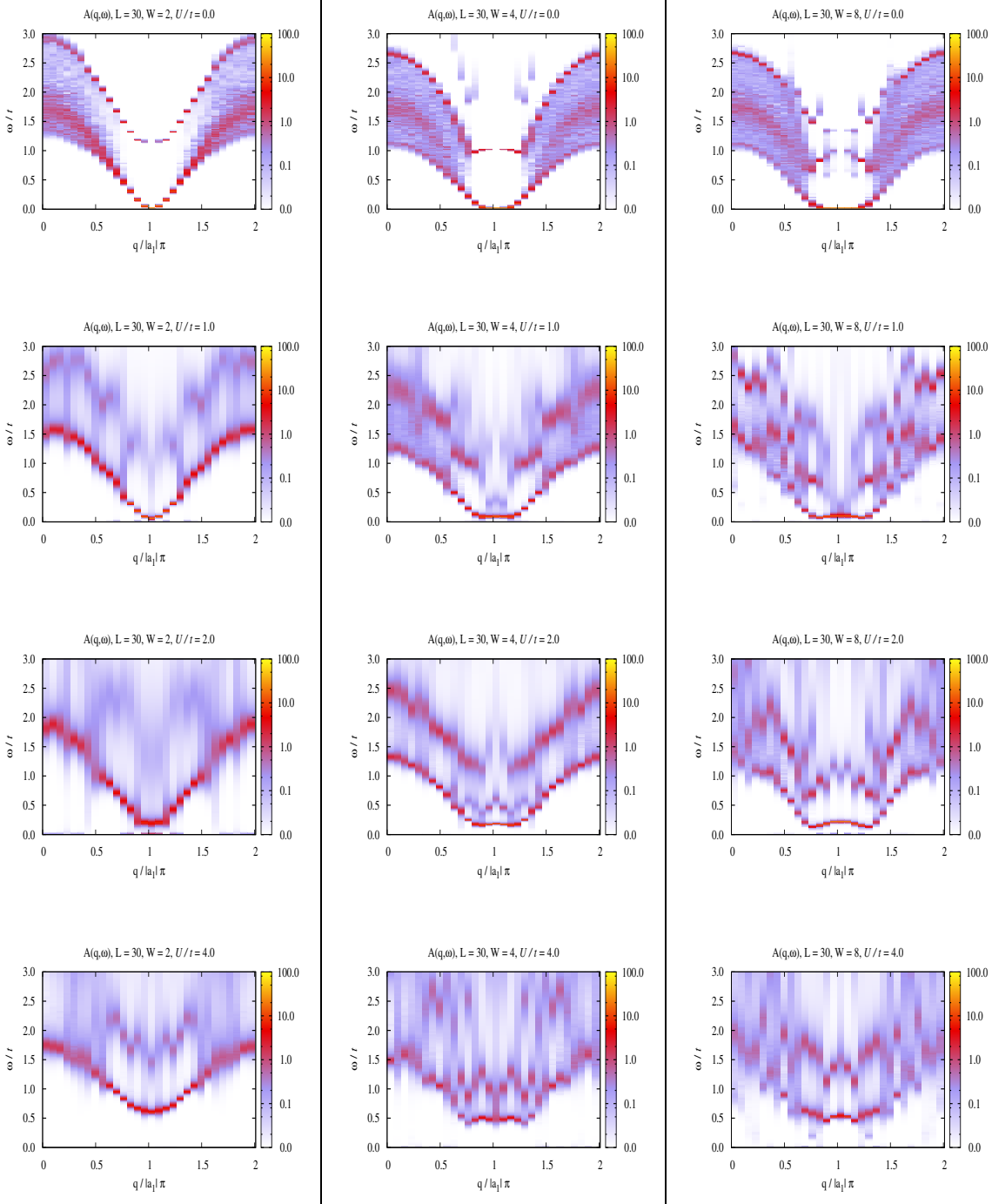

Table 5.2: Summary of the PQMC spectral function $S(\mathbf{q},\omega)$ for $L = 30$ ribbons.

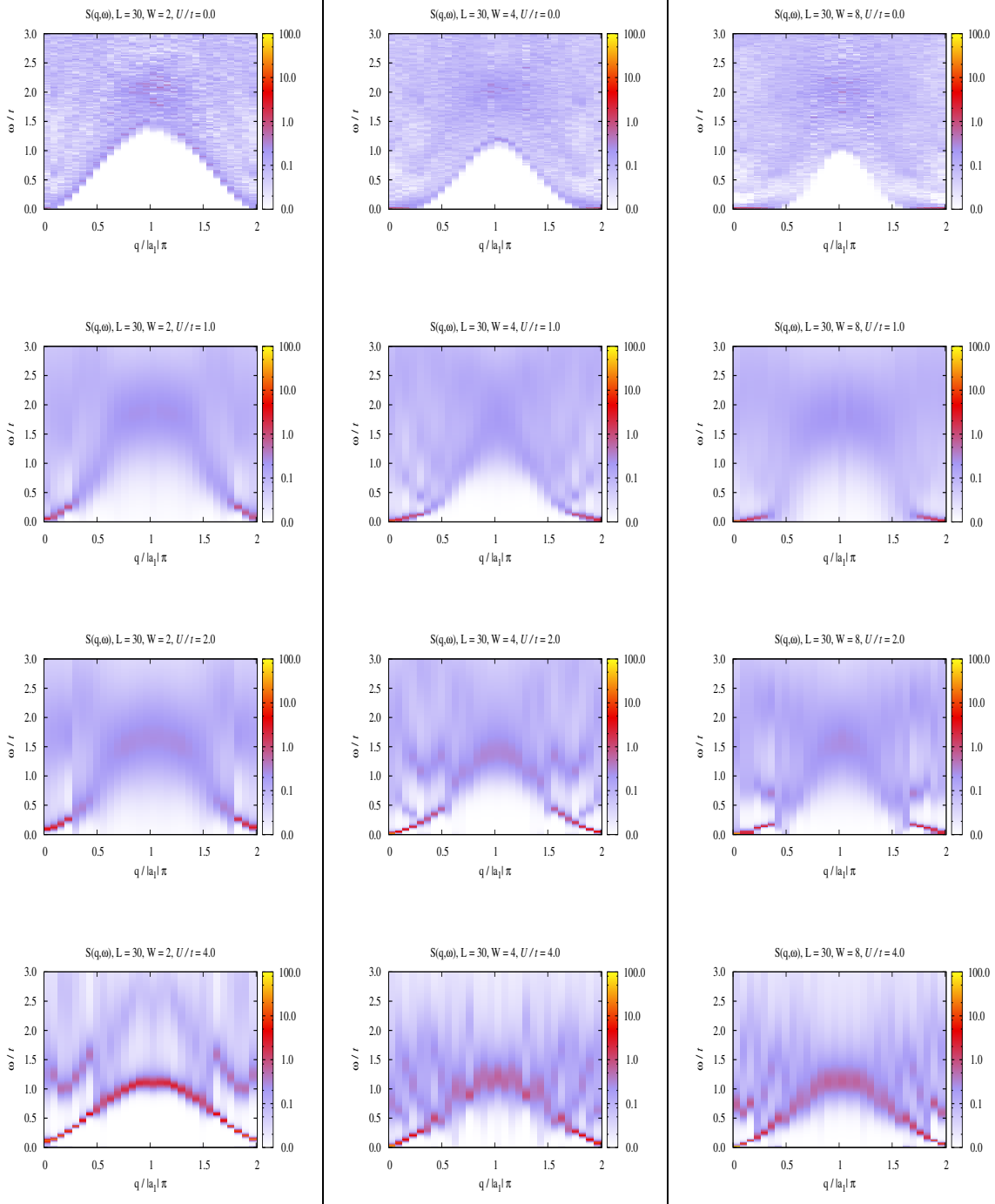

Chapter 6

Conclusion

Throughout this thesis, all the chapters have their own section with summary and outlook, so here we briefly outline the summaries together.

Chapter 2 introduces the two QMC methods we have employed in this thesis, SSE QMC and PQMC. While SSE QMC is applied widely in quantum spin (bosonic) systems, the PQMC is the standard method of choice for strongly correlated fermionic lattice models. Although the QMC methods have their own complications, for instance, the construction of the directed operator loop in SSE QMC and the numeric stabilization scheme in PQMC, they are nevertheless *exact* within errorbars. As we explained the Chapter 1, QMC simulations provide the benchmark for the other theoretical approaches that attempt to deal with strong correlated electron systems like mean field approximations or perturbative methods.

In Chapter 3 we applied the SSE QMC to a model of frustrated quantum magnetism – the spin-1/2 easy-axis Heisenberg model on the Shastry-Sutherland lattice. We explored the ground state phase diagram of the model. Away from the highly degenerate Ising limit, the quantum fluctuations first select a dimer triplet phase as the ground state and furthermore a superfluid phase, where the off-diagonal long range order is developed. The quantum phase transitions between them are characterized in the 3D XY university class. Upon applying an external magnetic field, the magnetization process of the model shows regions where the local magnetic moment increases continuously, these regions correspond to a superfluid of the magnetic triplon excitations. And there are also two magnetization plateaus in the magnetization process, which are two distinctively crystalline phases of the triplon excitations. The 1/3 magnetic plateau persists down to the Ising limit, but the 1/2 plateau is a purely quantum phenomenon that the crystalline order is selected by quantum fluctuations from the degenerate Ising limit.

In Chapter 4, we considered the half-filled Hubbard model on the 2D honeycomb lattice, the structure of graphene. At weak coupling, the relativistic dispersion of the massless Dirac fermions and their vanishing density of states close to the Fermi energy make the system stable against magnetic instabilities. Meanwhile, the low coordination number induces strong quantum fluctuations which, in interplay with the sparse energy density around the Fermi level, suggests that correlation effects are important here. Indeed, our PQMC simulations with careful finite size scaling analysis in this chapter revealed that, in the intermediate coupling regime an unexpected quantum spin liquid emerges. Such a quantum spin liquid is characterized as a RVB liquid with a finite spin gap to all magnetic excitations. The nature of this quantum spin liquid triggers many proposals and intensive discussions, we are

currently working along the directions of determining the phase transition between the QSL and topological band insulator, and the possible topological order in the form of ground state degeneracy in this QSL state.

Chapter 5 is more experimentally motivated, where we employed the PQMC to graphene nanoribbons, the honeycomb lattice in 1D with open edges. We would like to provide insights for the correlation effects on the edge states, which currently attract intensive experimental attention in graphene electronics, especially in direct probing the edge-state magnetism in nanoribbons with zigzag edge. Based on our PQMC data, we verified that the Coulomb interaction opens a gap in the local density of states on the edge. The corresponding dominant peak in the spectral function is hence a dynamic signature of the edge-state magnetism. Furthermore, the magnetic excitations along the zigzag edge for finite ribbon sample develop interesting magnon modes in that not only the ferromagnetic ordering along one edge is present, but the interaction-mediated antiferromagnetic coupling across the ribbon sample is also clearly visible. We have compared our PQMC results carefully with a self-consistent mean-field theory of the model, and numerically confirmed that at weak coupling, the mean-field theory correctly captures the essential features in the dynamical properties of the system.

Bibliography

[Abendschein 2008] A. Abendschein and S. Capponi. *Effective Theory of Magnetization Plateaux in the Shastry-Sutherland Lattice.* Phys. Rev. Lett., vol. 101, page 227201, 2008. (Cited on pages 32, 48, 51 and 52.)

[Affleck 1988] Ian Affleck and J. Brad Marston. *Large-n limit of the Heisenberg-Hubbard model: Implications for high-Tc superconductors.* Phys. Rev. B, vol. 37, no. 7, pages 3774–3777, Mar 1988. (Cited on page 58.)

[Albuquerque 2011] A. F. Albuquerque, D. Schwandt, B. Hetenyi, S. Capponi, M. Mambrini and A. M. Läuchli. *Phase Digram of a Frustrated Quantum Antiferromagnet on the Honeycomb Lattice: Magnetic Order versus Valence-Bond Crystal formation.* arXiv:1102.5325, 2011. (Cited on pages 88 and 97.)

[Alet 2005] F. Alet, S. Wessel and M. Troyer. *Generalized directed loop method for quantum Monte Carlo simulations.* Phys. Rev. E, vol. 71, page 036706, 2005. (Cited on pages 1 and 17.)

[Alet 2006] F. Alet, A. M. Walczak and M. P. A. Fisher. *Exotic quantum phases and phase transtions in correlated matter.* Physica A, vol. 369, pages 122–142, 2006. (Cited on page 57.)

[Anderson 1973] P. W Anderson. *Resonating valence bonds: A new kind of insulator?* Mater. Res. Bull., vol. 8, page 153, 1973. (Cited on pages 57, 71 and 92.)

[Anderson 1987] P. W Anderson. *The Resonating Valence Bond State in La_2CuO_4 and Superconductivity.* Science, vol. 235, page 1196, 1987. (Cited on pages 3, 55, 57, 71 and 96.)

[Andreev 1984] A. F. Andreev and I. A. Grishchuk. *Spin nematics.* Sov. Phys. JETP, vol. 60, page 267, 1984. (Cited on page 91.)

[Ashcroft 1976] Neil W. Ashcroft and N. David Mermin. Solid state physics. W. B. Saunders Company, Philadelphia, 1976. (Cited on pages 21 and 68.)

[Assaad 1993a] F. F. Assaad, W. Hanke and D. J. Scalapino. Phys. Rev. Lett., vol. 71, page 1915, 1993. (Cited on page 29.)

[Assaad 1993b] F. F. Assaad, W. Hanke and D. J. Scalapino. *Flux quantization in the two-dimensional repulsive and attractive Hubbard models.* Phys. Rev. Lett., vol. 71, no. 12, page 1915, Sep 1993. (Cited on page 80.)

[Assaad 1994] F. F. Assaad, W. Hanke and D. J. Scalapino. *Temperature derivative of the superfluid density and flux quantization as criteria for superconductivity in two-dimensional Hubbard models.* Phys. Rev. B, vol. 50, no. 17, page 12835, Nov 1994. (Cited on page 80.)

[Assaad 1996] F. F. Assaad and M. Imada. J. Phys. Soc. of Jpn, vol. 65, page 189, 1996. (Cited on page 29.)

[Assaad 1998] F. F. Assaad. *SU(2)-spin invariant auxiliary field quantum Monte Carlo Algorithm for Hubbard modes.* arXiv:cond-mat/9806307, 1998. (Cited on page 20.)

[Assaad 2002] F.F. Assaad. *Quantum Monte Carlo Methods on Lattices: The Determinantal Approach.* In J. Grotendorst, D. Marx and A. Muramatsu, editeurs, Quantum Simulations of Complex Many-Body Systems: from Theory to Algorithms, FZ-Jülich, 2002. NIC Series, Vol. 10. (Cited on page 18.)

[Assaad 2005] F. F. Assaad. *Phase diagram of the half-filled tow-dimensional SU(N) Hubbard-Heisenberg model: A quantum Monte Carlo study.* Phys. Rev. B, vol. 71, page 075103, February 2005. (Cited on pages 20 and 29.)

[Assaad 2008] F. F. Assaad and H. G. Evertz. Computational many-particle physics, lecture notes in physics 739. Springer-Verlag, Berlin, 2008. (Cited on pages 1, 18 and 29.)

[Azuma 1994] M. Azuma, Z. Hiroi, M. Takano, K. Ishida and Y. Kitaoka. *Observation of a Spin Gap in $SrCu_2O_3$ Comprising Spin-1/2 Quasi-1D Two-Leg Ladders.* Phys. Rev. Lett., vol. 73, no. 25, pages 3463–3466, Dec 1994. (Cited on page 56.)

[Balents 2002a] L. Balents, M. P. A. Fisher and S. M. Girvin. *Fractionalization in an easy-axis Kagome antiferromagnet.* Phys. Rev. B, vol. 65, page 224412, 2002. (Cited on page 34.)

[Balents 2002b] L. Balents, M. P. A. Fisher and S. M. Girvin. *Fractionalization in an easy-axis Kagome antiferromagnet.* Phys. Rev. B, vol. 65, page 224412, 2002. (Cited on page 60.)

[Balents 2010] Leon Balents. *Spin liquids in frustrated magnets.* Nature, vol. 464, pages 199–208, March 2010. (Cited on pages 1, 3, 57, 58 and 59.)

[Balibar 2010] Sebastien Balibar. *The enigma of supersolidity.* Nature, vol. 464, pages 176–182, Mar 2010. (Cited on page 1.)

[Beach 2004] K. S. D. Beach. *Identifying the maximum entropy method as a special limit of stochastic analytic continuation.* cond-mat/0403055v1, 2004. (Cited on page 107.)

[Bercx 2008] Martin Bercx. Magnetic field induced semimetal-to-canted-antiferromagnet transition on the honeycomb lattice. Master's thesis, Universität Würzburg, 2008. (Cited on page 18.)

[Bhowmick 2008] S. Bhowmick and V. B. Shenoy. *Edge state magnetism of single layer graphene nanostructures.* J. Chem. Phys., vol. 128, page 244717, 2008. (Cited on pages 99, 100, 101, 106, 113 and 114.)

[Blankenbecler 1981] R. Blankenbecler, D. J. Scalapino and R. L. Sugar. Phys. Rev. D, vol. 24, page 2278, 1981. (Cited on page 18.)

[Bonnes 2011] Lars Bonnes and Stefan Wessel. *Supersolid polar molecules beyond pairwise interactions.* Phys. Rev. B, vol. 83, no. 13, page 134511, Apr 2011. (Cited on page 34.)

[Byers 1961] N. Byers and C. N Yang. *Theoretical Considerations Concerning Quantized Magnetic Flux in Superconducting Cylinders.* Phys. Rev. Lett., vol. 7, page 46, 1961. (Cited on page 80.)

[Cabra 2004] D. C. Cabra and G. L. Rossini. *Numerical Jordan-Wigner approach for two-dimensional spin systems.* Phys. Rev. B, vol. 69, page 184425, 2004. (Cited on page 102.)

[Cahangirov 2009] S. Cahangirov, M. Topsakal, E. Aktürk, H. Şahin and S Ciraci. *Two- and One-Dimensional Honeycomb Structures of Silicon and Germanium.* Phys. Rev. Lett., vol. 102, page 236804, 2009. (Cited on pages 71 and 96.)

[Capriotti 1999] Luca Capriotti, Adolfo E. Trumper and Sandro Sorella. *Long-Range Néel Order in the Triangular Heisenberg Model.* Phys. Rev. Lett., vol. 82, no. 19, pages 3899–3902, May 1999. (Cited on page 56.)

[Castro Neto 2009] A. H. Castro Neto, F. Guinea, N. M. R. Peres, K. S. Novoselov and A. K. Geim. *The electronic properties of graphene.* Rev. Mod. Phys., vol. 81, page 109, 2009. (Cited on pages 70, 96 and 99.)

[Cépas 2001] O. Cépas, K. Kakurai, L. P. Regnault, T. Ziman, J. P. Boucher, N. Aso, M. Nishi, H. Kageyama and Y. Ueda. *Dzyaloshinski-Moriya Interaction in the 2D Spin Gap System $SrCu_2(BO_3)_2$.* Phys. Rev. Lett., vol. 87, no. 16, page 167205, Oct 2001. (Cited on page 32.)

[Chayes 1989] J. T. Chayes, L. Chayes and S. A Kivelson. *Valence bond ground states in a frustrated two-dimensional spin-1/2 Heisenberg antiferromagnet.* Commun. Math. Phys., vol. 123, page 53, 1989. (Cited on page 95.)

[Chen 2008] Gang Chen and Leon Balents. *Spin-orbit effects in $Na_4Ir_3O_8$: A hyper-kagome lattice antiferromagnet.* Phys. Rev. B, vol. 78, no. 9, page 094403, Sep 2008. (Cited on page 64.)

[Chen 2009] Y. L. Chen, J. G. Analytis, J.-H. Chu, Z. K. Liu, S.-K. Mo, X. L. Qi, H. J. Zhang, D. H. Lu, X. Dai, Z. Fang, S. C. Zhang, I. R. Fisher, Z. Hussain and Z.-X. Shen. *Experimental Realization of a Three-Dimensional Topological Insulator, Bi_2Te_3.* Science, vol. 438, page 178, 2009. (Cited on page 70.)

[Chubukov 1992] Andrey Chubukov. *Order from disorder in a kagomé antiferromagnet.* Phys. Rev. Lett., vol. 69, no. 5, pages 832–835, Aug 1992. (Cited on page 2.)

[Clark 2010] B. K. Clark, D. A. Abanin and S. L. Sondhi. *Nature of the spin liquid state of the Hubbard model on honeycomb lattice.* arXiv:1010.3011, 2010. (Cited on pages 4, 88, 95 and 97.)

[Culchac 2011] F. J. Culchac, A. Latgé and A. T. Costa. *Spin waves in zigzag graphene nanoribbons and the stability of edge ferromagnetism.* New J. Phys., vol. 13, page 033028, Mar 2011. (Cited on pages 100, 112 and 114.)

[Dagotto 1994] Elbio Dagotto. Rev. Mod. Phys., vol. 66, page 763, 1994. (Cited on pages 55 and 56.)

[Dagotto 1996] Elbio Dagotto and T. M. Rice. *Surprises on the way from One-to Two dimensions.* Science, vol. 271, page 618, 1996. (Cited on pages 55 and 107.)

[Damascelli 2003] Andrea Damascelli, Zahid Hussain and Zhi-Xun Shen. *Angle-resolved photoemission studies of the cuprate superconductors.* Rev. Mod. Phys., vol. 75, no. 2, pages 473–541, Apr 2003. (Cited on page 74.)

[Damle 2006] K. Damle and T. Senthil. *Spin Nematics and Magnetization Plateau Transition in Anisotropic Kagome Magnets.* Phys. Rev. Lett., vol. 97, page 067202, 2006. (Cited on page 34.)

[Datta 2008] S. S. Datta, D. R. Strachan, S. M. Khamis and A. T. C. Johnson. *Crystallographic etching of few-layer graphene.* Nano Lett., vol. 8, pages 1912–1915, 2008. (Cited on page 101.)

[Dell'Aringa 1997] S. Dell'Aringa, E. Ercolessi, G. Morandi, P. Pieri and M. Roncaglia. *Effective Actions for Spin Ladders.* Phys. Rev. Lett., vol. 78, no. 12, pages 2457–2460, Mar 1997. (Cited on page 56.)

[Dorier 2008] J. Dorier, K. P. Schmidt and F. Mila. *Theroy of Magnetization Plateaux in the Shastry-Sutherland Model.* Phys. Rev. Lett., vol. 101, page 250402, 2008. (Cited on pages 32, 48, 51 and 52.)

[Drut 2009] Joaquín E. Drut and Timo A. Lähde. *Critical exponents of the semimetal-insulator transition in graphene: A Monte Carlo study.* Phys. Rev. B, vol. 79, no. 24, page 241405, 2009. (Cited on page 71.)

[Duan 2003] L.-M. Duan, E. Demler and M Lukin. *Controlling Spin Exchange Interactions of Ultracold Atoms in Optical Lattices.* Phys. Rev. Lett., vol. 91, page 090402, 2003. (Cited on page 71.)

[Eccleston 1994] R. S. Eccleston, T. Barnes, J. Brody and J. W. Johnson. *Inelastic Neutron Scattering from the Spin Ladder Compound* $(VO)_2P_2O_7$. Phys. Rev. Lett., vol. 73, no. 19, pages 2626–2629, Nov 1994. (Cited on page 56.)

[Evenbly 2010] G. Evenbly and G. Vidal. *Frustrated Antiferromagnets with Entanglement Renormalization: Ground State of the Spin-12 Heisenberg Model on a Kagome Lattice*. Phys. Rev. Lett., vol. 104, no. 18, page 187203, May 2010. (Cited on page 61.)

[Fazekas 1974] P. Fazekas and P. W Anderson. *On the ground state properties of the anisotropic triangular antiferromagnet*. Philos. Mag., vol. 30, page 432, 1974. (Cited on pages 57, 71 and 92.)

[Fazekas 1999] Patrik Fazekas. Lecture notes on electron correlation and magnetism. World Scientific, Singapore, 1999. (Cited on pages 55 and 57.)

[Feldbacher 2001] M. Feldbacher and F. F. Assaad. *Efficient calculation of imaginary-time-displaced correlation functions in the projector auxiliary-field quantum Monte Carlo algorithm*. Phys. Rev. B, vol. 63, page 073105, 2001. (Cited on pages 22, 25 and 29.)

[Feldner 2010] H. Feldner, Z. Y. Meng, A. Honecker, D. Cabra, S. Wessel and F. F. Assaad. *Magnetism of finite graphene samples: Mean-field theory compared with exact diagonalization and quantum Monnte Carlo simulations*. Phys. Rev. B, vol. 81, page 115416, 2010. (Cited on pages 101, 104 and 109.)

[Feldner 2011] Hélène Feldner, Zi Yang Meng, Thomas C. Lang, Fakher F. Assaad, Stefan Wessel and Andreas Honecker. *Dynamical Signatures of Edge-State Magnetism on Graphene Nanoribbons*. Phys. Rev. Lett., vol. 106, no. 22, page 226401, May 2011. (Cited on page 102.)

[Fernández-Rossier 2007] J. Fernández-Rossier and J. J. Palacios. *Magnetism in graphene nanoislands*. Phys. Rev. Lett., vol. 99, page 177204, 2007. (Cited on pages 99, 100, 101, 106 and 113.)

[Fouet 2001] J.B. Fouet, P. Sindzingre and C. Lhuillier. *An investigation of the quantum* J_1-J_2-J_3 *model on the honeycomb lattice*. Eur. Phys. J. B, vol. 20, no. 2, pages 241–254, 2001. (Cited on page 88.)

[Fujita 1996] Mitsutaka Fujita, Katsunori Wakabayashi, Kyoko Nakada and Koichi Kusakabe. *Peculiar Localized State at Zigzag Graphite Edge*. J. Phys. Soc. Jpn., vol. 65, pages 1920–1923, 1996. (Cited on pages 99, 101, 103, 106 and 113.)

[Furukawa 2001] N. Furukawa. *Antiferromagnetism of the Hubbard Model on a Layered Honeycomb Lattice - Is MgB2 a Nearly-Antiferromagnetic Metal?* J. Phys. Soc. Jpn., vol. 70, no. 1483, 2001. (Cited on page 77.)

[Gabani 2007] S. Gabani, S. Matas, P. Priputen, K. Flachbart, K. Siemensmeyer, E. Wulf, A. Evdokimova and N. Shitsevalova. *Magnetic structure and phase diagram of TmB_4*. arXiv:0712.0519, 2007. (Cited on page 32.)

[Giamarchi 2008] T. Giamarchi, C. Rüegg and O. Tchernyshyov. *Bose-Einstein condensation in magnetic insulators*. Nature Physics, vol. 4, pages 198 – 204, 2008. (Cited on page 57.)

[Haldane 1988] F. D. M Haldane. *Model for a Quantum Hall Effect without Landau Levels: Condensed-Matter Realization of the 'Parity Anomaly'*. Phys. Rev. Lett., vol. 61, page 2015, 1988. (Cited on pages 80 and 87.)

[Hasan 2010] M. Z. Hasan and C. L. Kane. *Colloquium: Topological insulators*. Rev. Mod. Phys., vol. 82, no. 4, pages 3045–3067, Nov 2010. (Cited on page 96.)

[Hasenbusch 1999] M. Hasenbusch and T. Török. J. Phys. A, vol. 32, page 6361, 1999. (Cited on page 40.)

[Hastings 2004] M. B. Hastings. *Lieb-Schultz-Mattis in higher dimensions*. Phys. Rev. B, vol. 69, no. 10, page 104431, Mar 2004. (Cited on page 92.)

[He 2010] H. Y. He, Y. Zhang and B. C. Pan. *Tuning electronic structure of graphene via tailoring structure: theoretical study*. J. Appl. Phys., vol. 107, page 114322, 2010. (Cited on page 107.)

[Heidarian 2005] D. Heidarian and K. Damle. Phys. Rev. Lett., vol. 95, page 127206, 2005. (Cited on page 34.)

[Helton 2007] J. S. Helton, K. Matan, M. P. Shores, E. A. Nytko, B. M. Bartlett, Y. Yoshida, Y. Takano, A. Suslov, Y. Qiu, J.-H. Chung, D. G. Nocera and Y. S. Lee. *Spin Dynamics of the Spin-1/2 Kagome Lattice Antiferromagnet $ZnCu_3(OH)_6Cl_2$*. Phys. Rev. Lett., vol. 98, no. 10, page 107204, Mar 2007. (Cited on pages 63 and 64.)

[Henley 1989] Christopher L. Henley. *Ordering due to disorder in a frustrated vector antiferromagnet*. Phys. Rev. Lett., vol. 62, no. 17, pages 2056–2059, Apr 1989. (Cited on page 2.)

[Herbut 2009] I. F. Herbut, V. Juricic and O. Vafek. *Relativistic Mott criticality in graphene*. Phys. Rev. B, vol. 80, no. 7, page 075432, Aug 2009. (Cited on page 70.)

[Hermele 2005] Michael Hermele, T. Senthil and Matthew P. A. Fisher. *Algebraic spin liquid as the mother of many competing orders*. Phys. Rev. B, vol. 72, no. 10, page 104404, Sep 2005. (Cited on pages 71, 72 and 80.)

[Hermele 2007] Michael Hermele. *SU(2) gauge theory of the Hubbard model and application to the honeycomb lattice*. Phys. Rev. B, vol. 76, no. 3, page 035125, 2007. (Cited on pages 71, 72 and 80.)

[Hikihara 2003] T. Hikihara, X. Hu, H. H. Lin and C. Y. Mou. *Ground-state properties of nanographite system with zigzag edges.* Phys. Rev. B, vol. 68, page 035432, 2003. (Cited on pages 99, 100, 101, 106 and 113.)

[Hirsch 1985a] J. E. Hirsch. Phys. Rev. Lett., vol. 54, page 1317, 1985. (Cited on page 19.)

[Hirsch 1985b] J. E. Hirsch. Phys. Rev. B, vol. 31, page 4403, 1985. (Cited on page 20.)

[Hohenadler 2011] M. Hohenadler, T. C. Lang and F. F. Assaad. *Correlation Effects in Quantum Spin-Hall Insulators: A Quantum Monte Carlo Study.* Phys. Rev. Lett., vol. 106, no. 10, page 100403, Mar 2011. (Cited on page 96.)

[Honerkamp 2008] C. Honerkamp. *Density waves and Cooper pairing on the honeycomb lattice.* Phys. Rev. Lett., vol. 100, page 146404, April 2008. (Cited on pages 3, 71, 72, 80 and 85.)

[Hwang 2007] Chi-Ok Hwang, Jin Min Kim, Seung-Yeon Kim and Daeseung Kang. *Ising antiferromagnets in a nonzero uniform magnetic field.* J. Stat. Mech.: Theor. Exp., page L05001, 2007. (Cited on page 52.)

[Imai 2008] T. Imai, E. A. Nytko, B. M. Bartlett, M. P. Shores and D. G. Nocera. *^{63}Cu, ^{35}Cl, and ^{1}H NMR in the $S = 1/2$ Kagome Lattice $ZnCu_3(OH)_6Cl_2$.* Phys. Rev. Lett., vol. 100, no. 7, page 077203, Feb 2008. (Cited on pages 63, 64 and 65.)

[Isaev 2009] L. Isaev, G. Ortiz and J. Dukelsky. *Local Physics of Magnetization Plateaux in the Shastry-Sutherland Model.* Phys. Rev. Lett., vol. 103, no. 17, page 177201, Oct 2009. (Cited on pages 32, 48, 51 and 52.)

[Isakov 2006a] S. V. Isakov, Y. B. Kim and A. Paramekanti. *Spin liquid phase in a $S = 1/2$ quantum magnet on the kagome lattice.* Phys. Rev. Lett., vol. 97, page 207204, 2006. (Cited on pages 34 and 60.)

[Isakov 2006b] S. V. Isakov, S. Wessel, R. G. Melko, K. Sengupta and Yong Baek Kim. *Valence Bond Solids and Their Quantum Melting in Hard-Core Bosons on the Kagome Lattice.* Phys. Rev. Lett., vol. 97, page 147202, 2006. (Cited on page 34.)

[Isakov 2007] S. V. Isakov, A. Paramekanti and Y. B. Kim. *Exotic phase diagram of a cluster charging model of bosons on the kagome lattice.* Phys. Rev. B, vol. 76, page 224431, 2007. (Cited on page 60.)

[Isakov 2011] S. V. Isakov, M. B. Hastings and R. G. Melko. *Topological Entanglement Entropy of a Bose-Hubbard Spin Liquid.* arXiv:1102.1721, 2011. (Cited on page 60.)

[Itou 2007] T. Itou, A. Oyamada, S. Maegawa, M. Tamura and R. Kato. *Spin-liquid state in an organic spin-1/2 system on a triangular lattice, $EtMe_3Sb[Pd(dmit)_2]_2$*. J. Phys.: Condens. Matter, vol. 19, page 145247, 2007. (Cited on pages 63 and 64.)

[Itou 2008] T. Itou, A. Oyamada, S. Maegawa, M. Tamura and R. Kato. *Quantum spin liquid in the spin-1/2 triangular antiferromagnet $EtMe_3Sb[Pd(dmit)_2]_2$*. Phys. Rev. B, vol. 77, no. 10, page 104413, Mar 2008. (Cited on pages 68 and 69.)

[Itou 2009] T. Itou, A Oyamada, S Maegawa, M Tamura and R Kato. *^{13}C NMR study of the spin-liquid state in the triangular quantum antiferromagnet $EtMe_3Sb[Pd(dmit)_2]_2$*. J. Phys. Conf. Ser., vol. 145, page 012039, 2009. (Cited on page 68.)

[Jain 2000] J. K. Jain. *The composite fermion: A quantum particle and its quantum fluids*. Physics Today, vol. 53, pages 39–45, Apr 2000. (Cited on page 58.)

[Jiang 2008a] H. C. Jiang, Z. Y. Weng and D. N. Sheng. *DMRG Numerical Study of the Kagome Antiferromagnet*. Phys. Rev. Lett., vol. 101, page 117203, 2008. (Cited on page 61.)

[Jiang 2008b] J. Jiang, W. Lu and J. Bernholc. *Edge States and Optical Transition Energies in Carbon Nanoribbons*. Phys. Rev. Lett., vol. 101, no. 24, page 246803, 2008. (Cited on pages 99, 101, 106, 107 and 113.)

[Jiao 2009] L.Y. Jiao, L. Zhang, X. R. Wang, G. Diankov and H. J. Dai. *Narrow graphene nanoribbons from carbon nanotubes*. Nature, vol. 458, pages 877–880, 2009. (Cited on page 101.)

[Jiao 2010] L.Y. Jiao, X. R. Wang, G. Diankov, H. L. Wang and H. J. Dai. *Facile synthesis of high-quality graphene nanoribbons*. Nature Nanotech, vol. 5, page 321, Apr 2010. (Cited on pages 101 and 103.)

[Jordens 2008] R. Jordens, N. Strohmaier, K. Gunter, H. Moritz and T. Esslinger. *A Mott insulator of fermionic atoms in an optical lattice*. Nature, vol. 455, page 204, 2008. (Cited on page 71.)

[Kageyama 1999] H. Kageyama, K. Yoshimura, R. Stern, N. V. Mushnikov, K. Onizuka, M. Kato, K. Kosuge, C. P. Slichter, T. Goto and Y. Ueda. *Exact Dimer Ground State and Quantized Magnetization Plateaus in the Two-Dimensional Spin System $SrCu_2(BO_3)_2$*. Phys. Rev. Lett., vol. 82, page 3168, 1999. (Cited on page 31.)

[Kane 2005] C. L. Kane and E. J Mele. *Quantum spin Hall effect in Graphene*. Phys. Rev. Lett., vol. 95, page 226801, 2005. (Cited on pages 4, 71, 72, 87 and 96.)

[Karbach 1997] M. Karbach, G. Müller, A. H. Bougourzi, A. Fledderjohann and K. H. Mütter. Phys. Rev. B, vol. 55, page 12510, 1997. (Cited on page 55.)

[Karbach 1998] M. Karbach, K. Hu and G. Muller. *Introduction to the Bethe ansatz II.* Computers in Physics, vol. 12, pages 565–573, 1998. (Cited on page 55.)

[Kartsovnik 2004] M. V. Kartsovnik. *High Magnetic Fields: A Tool for Studying Electronic Properties of Layered Organic Metals.* Chem. Rev., vol. 104, pages 5737–5782, 2004. (Cited on page 66.)

[Keren 1994] A. Keren, L. P. Le, G. M. Luke, W. D. Wu, Y. J. Uemura, Y. Ajiro, T. Asano, H. Kuriyama, M. Mekata and H. Kikuchi. *Muon spin relaxation measurements in kagomé lattice system* $SrCr_8Ga_4O_{19}$. Hyperfine Interact., vol. 85, no. 1, pages 181–186, December 1994. (Cited on page 63.)

[Kitaev 2006] A. Kitaev. *Anyons in an exactly solved model and beyond.* Ann. Phys., vol. 321, pages 2–111, 2006. (Cited on page 55.)

[Kivelson 1987] S. A. Kivelson, D. S. Rokhsar and J. P Sethna. *Topology of the resonating valence-bond state: Solitons and high-Tc superconductivity.* Phys. Rev. B, vol. 35, page 8865, 1987. (Cited on pages 71, 92 and 96.)

[Kodama 2002] K. Kodama, M. Takigawa, M. Horvatić, C. Berthier, H. Kageyama, Y. Ueda, S. Miyahara, F. Becca and F. Mila. *Magnetic Superstructure in the Two-Dimensional Quantum Antiferromagnetic* $SrCu_2(BO_2)_2$. Science, vol. 298, pages 395–399, 2002. (Cited on page 32.)

[Kopnin 2008] N. B. Kopnin and E. B Sonin. *BCS superconductivity of Dirac electrons in graphene layers.* Phys. Rev. Lett., vol. 100, page 246808, 2008. (Cited on page 96.)

[Kosynkin 2009] D. V. Kosynkin, A. L. Higginbotham, A. Sinitskii, J. R. Lomeda, A. Dimiev, B. K. Price and J. M. Tour. *Longitudinal unzippling of carbon nanotubes form graphene nanoribbons.* Nature, vol. 458, page 872, Apr 2009. (Cited on page 103.)

[Kurosaki 2005] Y. Kurosaki, Y. Shimizu, K. Miyagawa, K. Kanoda and G. Saito. *Mott Transition from a Spin Liquid to a Fermi Liquid in the Spin-Frustrated Organic Conductor* $\kappa - (ET)_2Cu_2(CN)_3$. Phys. Rev. Lett., vol. 95, no. 17, page 177001, Oct 2005. (Cited on pages 63 and 67.)

[Lang 2010] Thomas C. Lang. *Quantum Monte Carlo methods and strongly correlated electrons on honeycomb structures.* PhD thesis, Julius-Maximilians-Universität Würzburg, 2010. (Cited on pages 4, 18, 57, 66 and 70.)

[Läuchli 2002] Andreas Läuchli, Stefan Wessel and Manfred Sigrist. *Phase diagram of the quadrumerized Shastry-Sutherland model.* Phys. Rev. B, vol. 66, page 014401, 2002. (Cited on page 37.)

[Läuchli 2011] A. M. Läuchli, J. Sudan and E. S. Sørensen. *Ground-State Energy and Spin Gap of Spin-1/2 Kagome Heisenberg Antiferromagnetic Clusters: Large Scale Exact Diagonalization Results.* arXiv:1103.1159, 2011. (Cited on page 61.)

[Lee 2005] S.-S. Lee and P. A Lee. *U(1) Gauge Theory of the Hubbard Model: Spin Liquid states and possible application to κ-(BEDT-TTF)$_2$Cu$_2$(CN)$_3$.* Phys. Rev. Lett., vol. 95, page 036403, 2005. (Cited on pages 66, 71, 72 and 80.)

[Lee 2006] Patrick A. Lee, Naoto Nagaosa and Xiao-Gang Wen. *Doping a Mott insulator: Physics of high-temperature superconductivity.* Rev. Mod. Phys., vol. 78, no. 1, pages 17–85, Jan 2006. (Cited on pages 55 and 71.)

[Lee 2007] S.-H. Lee, H. Kikuchi, Y. Qiu, B. Lake, Q. Huang, K. Habicht and K. Kiefer. *Quantum-spin-liquid states in the two-dimensional kagome antiferromagnets ZnxCu4-x(OD)6Cl2.* Nature Materials, vol. 6, page 853, 2007. (Cited on page 31.)

[Lee 2008a] Hunpyo Lee, Gang Li and Hartmut Monien. *Hubbard model on the triangular lattice using dynamical cluster approximation and dual fermion methods.* Phys. Rev. B, vol. 78, page 205117, 2008. (Cited on pages 59, 66 and 71.)

[Lee 2008b] Patrick A. Lee. *An End to the Drought of Quantum Spin Liquids.* Science, vol. 321, pages 129–130, 2008. (Cited on pages 55 and 58.)

[Lee 2009] K. L. Lee, K. Bouadim, G. G. Batrouni, F. Hébert, R. T. Scalettar, C. Miniatura and B. Grémaud. *Attractive Hubbard model on a honeycomb lattice: Quantum Monte Carlo study.* Phys. Rev. B, vol. 80, no. 24, page 245118, Dec 2009. (Cited on page 77.)

[Levin 2006] Michael Levin and Xiao-Gang Wen. *Detecting Topological Order in a Ground State Wave Function.* Phys. Rev. Lett., vol. 96, no. 11, page 110405, Mar 2006. (Cited on page 60.)

[Li 2008] Xiaolin Li, Xinran Wang, Li Zhang, Sangwon Lee and Hongjie Dai. *Chemically Derived, Ultrasmooth Graphene Nanoribbon Semiconductors.* Science, vol. 319, pages 1229–1232, 2008. (Cited on page 101.)

[Lieb 1989] Elliott H. Lieb. *Two theorems on the Hubbard model.* Phys. Rev. Lett., vol. 62, no. 10, pages 1201–1204, Mar 1989. (Cited on pages 92, 101 and 113.)

[Limelette 2003] P. Limelette, P. Wzietek, S. Florens, A. Georges, T. A. Costi, C. Pasquier, D. Jérome, C. Mézière and P. Batail. *Mott Transition and Transport Crossovers in the Organic Compound κ-(BEDT-TTF)$_2$Cu[N(CN)$_2$]Cl.* Phys. Rev. Lett., vol. 91, no. 1, page 016401, Jul 2003. (Cited on page 67.)

[Lindgren 1974] Ingvar Lindgren. *The Rayleigh-Schrödinger perturbation and the linked-diagram theorem for a multi-configurational model space.* J. Phys. B: Atom. Molec. Phys., vol. 7, no. 18, page 2441, 1974. (Cited on page 43.)

[Löw 2009] U. Löw. *Properties of the two-dimensional spin-1/2 Heisenberg model on a honeycomb lattice with interlayer coupling.* Condensed Matter Physics, vol. 12, page 497, 2009. (Cited on page 56.)

[Lu 2010a] Yuan-Ming Lu and Ying Ran. *Spin liquids on a honeycomb lattice: Projective Symmetry Group study of Schwinger fermion mean-field theory.* arXiv:1005.4229, 05 2010. (Cited on page 92.)

[Lu 2010b] Yuan-Ming Lu and Ying Ran. *Z_2 spin liquid and chiral antiferromagnetic phase in Hubbard model on the honeycomb lattice: duality between Schwinger-fermion and Schwinger-boson representations.* arXiv:1007.3266, 2010. (Cited on pages 92 and 97.)

[MacDonald 1988] A. H. MacDonald, S. M. Girvin and D. Yoshioka. *$\frac{t}{U}$ expansion for the Hubbard model.* Phys. Rev. B, vol. 37, no. 16, page 9753, Jun 1988. (Cited on page 95.)

[MacDonald 1990] A. H. MacDonald, S. M. Girvin and D. Yoshioka. *Reply to "Comment on 't/U expansion for the Hubbard model"'.* Phys. Rev. B, vol. 41, no. 4, page 2565, Feb 1990. (Cited on page 95.)

[Mahan 1990] Gerald D. Mahan. Many-particle physics. Plenum Press, New York, 2nd édition, 1990. (Cited on pages 20 and 25.)

[Melko 2005] R. G. Melko, A. Paramekanti, A. A. Burkov, A. Vishwanath, D. N. Sheng and L. Balents. Phys. Rev. Lett., vol. 95, page 127207, 2005. (Cited on page 34.)

[Melko 2010] Roger G. Melko, Ann B. Kallin and Matthew B. Hastings. *Finite-size scaling of mutual information in Monte Carlo simulations: Application to the spin- 1/2 XXZ model.* Phys. Rev. B, vol. 82, no. 10, page 100409, Sep 2010. (Cited on page 60.)

[Mendels 2007] P. Mendels, F. Bert, M. A. de Vries, A. Olariu, A. Harrison, F. Duc, J. C. Trombe, J. S. Lord, A. Amato and C. Baines. *Quantum Magnetism in the Paratacamite Family: Towards an Ideal Kagomé Lattice.* Phys. Rev. Lett., vol. 98, no. 7, page 077204, Feb 2007. (Cited on pages 63 and 64.)

[Meng 2007] Zi Yang Meng. Quantum monte carlo studies of the anisotropic shastry-sutherland quantum antiferromagnet. Master's thesis, Universität Stuttgart, November 2007. (Cited on pages 8, 17 and 34.)

[Meng 2008] Zi Yang Meng and S. Wessel. *Phases and magnetization process of an anisotropic Shastry-Sutherland model.* Phys. Rev. B, vol. 78, no. 224416, 2008. (Cited on page 34.)

[Meng 2010] Z. Y. Meng, T. C. Lang, S. Wessel, F. F. Assaad and A. Muramatsu. *Quantum spin liquid emerging in two-dimensional correlated Dirac fermions.* Nature, vol. 464, pages 847–851, April 2010. (Cited on pages 70 and 105.)

[Mermin 1966] N. D. Mermin and H. Wagner. Phys. Rev. Lett., vol. 17, page 1133, 1966. (Cited on pages 101 and 113.)

[Metropolis 1953] N. Metropolis, A. Rosenbluth, M. Rosenbluth, A. Teller and E. Teller. J. Chem. Phys., vol. 21, page 1087, 1953. (Cited on pages 8 and 23.)

[Misguich 2001] G. Misguich, T. Jolicoeur and S. M. Girvin. Phys. Rev. Lett., vol. 87, page 097203, 2001. (Cited on pages 32 and 48.)

[Miyahara 1999] Shin Miyahara and Kazuo Ueda. *Exact Dimer Ground State of the Two Dimensional Heisenberg Spin System $SrCu_2(BO_3)_2$.* Phys. Rev. Lett., vol. 82, no. 18, pages 3701–3704, May 1999. (Cited on page 31.)

[Miyahara 2000] Shin Miyahara and Kazuo Ueda. *Superstructures at magnetization plateaus in $SrCu_2(BO_3)_2$.* Phys. Rev. B, vol. 61, no. 5, pages 3417–3424, Feb 2000. (Cited on page 48.)

[Miyahara 2003a] Shin Miyahara, Federico Becca and Frederic Mila. *Theory of spin-density profile and lattice distortion in the magnetization plateaus of $SrCu_2(BO_3)_2$.* Phys. Rev. B, vol. 68, page 024401, 2003. (Cited on page 48.)

[Miyahara 2003b] Shin Miyahara and Kazuo Ueda. *Theory of the orthogonal dimer Heisenberg spin model for $SrCu_2(BO_3)_2$.* J. Phys.: Condens. Matter, vol. 15, pages R327–R366, 2003. (Cited on pages 2, 31, 33, 37 and 51.)

[Moessner 2001a] R. Moessner and S. L. Sondhi. *Resonating Valence Bond Phase in the Triangular Lattice Quantum Dimer Model.* Phys. Rev. Lett., vol. 86, no. 9, pages 1881–1884, Feb 2001. (Cited on page 57.)

[Moessner 2001b] R. Moessner, S. L. Sondhi and E Fradkin. *Short-ranged resonating valence bond physics, quantum dimer models, and Ising gauge theories.* Phys. Rev. B, vol. 65, page 024504, 2001. (Cited on page 92.)

[Moessner 2008] R. Moessner and K. S. Raman. *Quantum dimer models.* arXiv:0809.3051, 2008. (Cited on pages 92 and 94.)

[Momoi 2000a] Tsutomu Momoi and Keisuke Totsuka. *Magnetization plateaus as insulator-superfluid transitions in quantum spin systems.* Phys. Rev. B, vol. 61, no. 5, pages 3231–3234, 2000. (Cited on pages 31 and 48.)

[Momoi 2000b] Tsutomu Momoi and Keisuke Totsuka. *Magnetization plateaus of the Shastry-Sutherland model for $SrCu_2(BO_3)_2$: Spin-density wave, supersolid, and bound states.* Phys. Rev. B, vol. 62, no. 9, pages 15067–15078, 2000. (Cited on pages 31 and 48.)

[Motrunich 2005] Olexei I. Motrunich. *Variational study of triangular lattice spin-1/2 model with ring exchanges and spin liquid state in κ-$(ET)_2Cu_2(CN)_3$.* Phys. Rev. B, vol. 72, no. 4, page 045105, July 2005. (Cited on page 66.)

[Muñoz-Rojas 2009] F. Muñoz-Rojas, J. Fernández-Rossier and J. J. Palacios. *Giant magnetoresistance in ultrasmall Graphene based devices.* Phys. Rev. Lett., vol. 102, page 136810, 2009. (Cited on page 99.)

[Nakada 1996] Kyoko Nakada, Mitsutaka Fujita, Gene Dresselhaus and Mildred S. Dresselhaus. *Edge state in graphene ribbons: Nanometer size effect and edge shape dependence.* Phys. Rev. B, vol. 54, pages 17954–17961, 1996. (Cited on pages 99 and 101.)

[Nam 2007] Moon-Sun Nam, A. Ardavan, S. J. Blundell and J. A. Schlueter. *Fluctuating superconductivity in organic molecular metals close to the Mott transition.* Nature, vol. 449, pages 584–587, 2007. (Cited on pages 65 and 95.)

[Niimi 2006] Y. Niimi, T. Matsui, H. Kambara, K. Tagami, M. Tsukada and Hiroshi Fukuyama. *Scanning tunneling microscopy and spectroscopy of the electronic local density of states of graphite surfaces near monoatomic step edges.* Phys. Rev. B, vol. 73, no. 8, page 085421, Feb 2006. (Cited on page 107.)

[Nikolic 2003] P. Nikolic and T. Senthil. *Physics of low-energy singlet states of the Kagome lattice quantum Heisenberg antiferromagnet.* Phys. Rev. B, vol. 68, no. 21, page 214415, Dec 2003. (Cited on page 61.)

[Nojiri 2003] H. Nojiri, H. Kageyama, Y. Ueda and M. Motokawa. *ESR Study on the Excited State Energy Spectrum of $SrCu_2(BO_3)_2$ – A Central Role of Multiple-Triplet Bound States.* J. Phys. Soc. Jpn., vol. 72, pages 3243–3253, 2003. (Cited on page 32.)

[Norman 2011] M. R. Norman, F. Wang and D. H. Lee. *Special Section: Superconductivity.* Science, vol. 332, pages 189–204, April 2011. (Cited on page 1.)

[Okamoto 2007] Yoshihiko Okamoto, Minoru Nohara, Hiroko Aruga-Katori and Hidenori Takagi. *Spin-Liquid State in the $S = 1/2$ Hyperkagome Antiferromagnet $Na_4Ir_3O_8$.* Phys. Rev. Lett., vol. 99, no. 13, page 137207, Sep 2007. (Cited on pages 63, 64 and 65.)

[Okamoto 2009] Yoshihiko Okamoto, Hiroyuki Yoshida and Zenji Hiroi. *Vesignieite $BaCu_3V_2O_8(OH)_2$ as a Candidate Spin-1/2 Kagome Antiferromagnet.* J. Phys. Soc. Jpn., vol. 78, page 033701, 2009. (Cited on page 63.)

[Onizuka 2000] K. Onizuka, H. Kageyama, Y. Narumi, K. Kindo, Y. Ueda and T. Goto. *1/d Magnetization Plateau in $SrCu_2(BO_3)_2$ - Stripe Order of Excited Triplets.* J. Phys. Soc. Jpn., vol. 69, no. 4, pages 1016–1018, 2000. (Cited on page 31.)

[Paiva 2005] Thereza Paiva, R. T. Scalettar, W. Zheng, R. R. P. Singh and J. Oitmaa. *Ground-state and finite-temperature signatures of quantum phase transitions in the half-filled Hubbard model on a honeycomb lattice.* Phys. Rev. B, vol. 72, no. 8, page 085123, Aug 2005. (Cited on pages 72, 76 and 77.)

[Pauling 1960] L Pauling. The Nature of the Chemical Bond. Cornell University Press, 1960. (Cited on page 88.)

[Pollock 1987] E. L. Pollock and D. M. Ceperley. *Path-integral computation of superfluid densities.* Phys. Rev. B., vol. 36, no. 16, pages 8343–8352, 1987. (Cited on pages 18 and 37.)

[Powell 2011] B. J. Powell and Ross H. McKenzie. *Quantum frustration in organic Mott insulators: from spin liquids to unconventional superconductors.* Rep. Prog. Phys., vol. 74, page 056501, April 2011. (Cited on pages 57, 64, 65, 66, 67 and 71.)

[Pratt 2010] F. L. Pratt. *Using Shubnikov-de Haas data to estimate the magnetic frustration parameter t'/t in the spin-liquid system κ-$ET_2Cu_2(CN)_3$.* Physica B: Condensed Matter, vol. 405, pages S205–S207, 2010. (Cited on page 66.)

[Pratt 2011] F. L. Pratt, P. J. Baker, S. J. Blundell, T. Lancaster, O. Kawamura, C. Baines, Y. Shimizu, K. Kanoda, I. Watanabe and G. Saito. *Magnetic and non-magnetic phases of a quantum spin liquid.* Nature, vol. 471, page 612, 2011. (Cited on pages 63, 68 and 95.)

[Press 1992] W. H. Press, S. A. Teukolsky, W. T. Vetterling and B. P. Flannery. Numerical recepies in c. Cambridge University Press, Cambridge, UK, 1992. (Cited on pages 22, 24 and 27.)

[Raghu 2008] S. Raghu, X.-L. Qi, C. Honerkamp and S.-C Zhang. *Topological Mott Insulators.* Phys. Rev. Lett., vol. 100, page 156401, 2008. (Cited on pages 3, 71, 72, 80, 85 and 87.)

[Rantner 2002] W. Rantner and X.-G. Wen. *Spin correlations in the agebraic spin liquid: Implications for high T_c superconductors.* Phys. Rev. B, vol. 97, page 144501, 2002. (Cited on page 58.)

[Read 1991] N. Read and Subir Sachdev. *Large-N expansion for frustrated quantum antiferromagnets.* Phys. Rev. Lett., vol. 66, no. 13, pages 1773–1776, Apr 1991. (Cited on page 58.)

[Renyi 1961] A. Renyi. *Proceedings of the 4th Berkeley Symposium on Mathematical Statistics and Probabilities.* volume 1, page 547, Berkeley, CA, 1961. University of California Press. (Cited on page 60.)

[Reuther 2011] J. Reuther, D. A. Abanin and R. Thomale. *Magnetic order and paramagnetic phases in the quantum J_1-J_2-J_3 honeycomb model.* arXiv:1103.0859, 2011. (Cited on pages 4, 88, 95 and 97.)

[Ritter 2009] K. A. Ritter and J. W. Lyding. *The influence of edge structure on the electronic properties of graphene quantum dots and nanoribbons.* Nature Materials, vol. 8, pages 235–242, 2009. (Cited on page 101.)

[Rokhsar 1988] D. S. Rokhsar and S. A Kivelson. *Superconductivity and the Quantum Hard-Core Dimer Gas.* Phys. Rev. Lett., vol. 61, page 2376, 1988. (Cited on pages 92 and 94.)

[Romhányi 2011] Judit Romhányi, Keisuke Totsuka and Karlo Penc. *Effect of Dzyaloshinskii-Moriya interactions on the phase diagram and magnetic excitations of $SrCu_2(BO_3)_2$.* Phys. Rev. B, vol. 83, no. 2, page 024413, Jan 2011. (Cited on page 32.)

[Ryu 2009] S. Ryu, C. Mudry, C.-Y. Hou, and C Chamon. *Masses in graphene-like two-dimensional electronic systems: topological defects in order parameters and their fractional exchange statistics.* Phys. Rev. B, vol. 80, page 205319, 2009. (Cited on page 80.)

[Sandvik 1991] A. W. Sandvik and J. Kurkijärvi. Phys. Rev. B, vol. 43, page 5950, 1991. (Cited on page 5.)

[Sandvik 1997] Anders W. Sandvik. *Finite-size scaling of the ground-state parameters of the two-dimensional Heisenberg model.* Phys. Rev. B, vol. 56, no. 18, pages 11678–11690, Nov 1997. (Cited on pages 5 and 56.)

[Sandvik 1998] A. W. Sandvik. *Stochastic method for analytic continuation of quantum Monte Carlo data.* Phys. Rev. B, vol. 57, page 10287, 1998. (Cited on page 107.)

[Sandvik 1999] A. W. Sandvik. *Stochastic series expansion method with operator-loop update.* Phys. Rev. B, vol. 59, page R14157, 1999. (Cited on pages 5 and 10.)

[Scalapino 1981] D. J. Scalapino and R. L. Sugar. *Monte Carlo calculations of coupled boson-fermion systems. II.* Phys. Rev. B, vol. 24, page 4295, 1981. (Cited on page 18.)

[Scalettar 1993] R. T. Scalettar, A. Moreo, E. Dagotto, L. Bergomi, T. Jolicoeur and H. Monien. *Ground-state properties of the Hubbard model on a C_{60} cluster.* Phys. Rev. B, vol. 47, no. 18, pages 12316–12319, May 1993. (Cited on pages 72 and 76.)

[Schneider 2008] U. Schneider, L. Hackermüller, S. Will, Th. Best, I. Bloch, T. A. Costi, R. W. Helmes, D. Rasch and A. Rosch. *Metallic and Insulating Phases of Repulsively interacting Fermions in a 3D optical lattice.* Science, vol. 322, page 1520, 2008. (Cited on pages 1 and 71.)

[Schollwöck 2004] U. Schollwöck, J. Richter, D.J.J. Farnell and R.F. Bishop. Quantum magnetism, lecture notes in physics 645. Springer-Verlag, Berlin, 2004. (Cited on page 1.)

[Sebastian 2008] S. E. Sebastian, N. Harrison, P. Sengupta, C. D. Batista, S. Francoual, E. Palm, T. Murphy, H. A. Dabkowska and B. D. Gaulin. *Fractalization drives crystalline states in a frustrated spin system.* Proceedings of the National Academy of Sciences of the United States of America, vol. 105, pages 20157–20160, 2008. (Cited on pages 2, 31, 33, 48, 51 and 52.)

[Senthil 2004] T. Senthil, A. Vishwanath, L. Balents, S. Sachdev and M. P . A. Fisher. *Deconfined Quantum Critical Points.* Science, vol. 303, page 1490, 2004. (Cited on page 58.)

[Shao 1996] Jun Shao and Dongsheng Tu. The jackknife and bootstrap, springer series in statistics. Springer-Verlag, New York, 1996. (Cited on page 27.)

[Shastry 1981] B. Sriam Shastry and Bill Sutherland. *Exact Ground State of a Quantum Mechenical Antiferromagnet.* Physica (Amsterdam), vol. 108B, pages 1069–1070, 1981. (Cited on pages 2, 31, 34, 35 and 36.)

[Sheng 2005] D N Sheng and Leon Balents. *Numerical evidences of fractionalization in an easy-axis two-spin heisenberg antiferromagnet.* Phys. Rev. Lett., vol. 94, no. 14, page 146805, April 2005. (Cited on page 34.)

[Shimizu 2003] Y. Shimizu, K. Miyagawa, K. Kanoda, M. Maesato and G. Saito. *Spin Liquid State in an Organic Mott Insulator with a Triangular Lattice.* Phys. Rev. Lett., vol. 91, no. 10, page 107001, Sep 2003. (Cited on pages 63, 64, 67, 71 and 95.)

[Si 2010] Qimiao Si and Frank Steglich. *Heavy Fermions and Quantum Phase Transitions.* Science, vol. 329, no. 5996, pages 1161–1166, Sep 2010. (Cited on page 1.)

[Siemensmeyer 2008] K. Siemensmeyer, E. Wulf, H.-J. Mikeska, K. Flachbart, S. Gabani, S. Matas, P. Priputen, A. Evdokimova and N. Shitsevalova. *Fractional Magnetization Plateaus and Magnetic order in the Shastry-Sutherland magnet TmB_4.* Phys. Rev. Lett., vol. 101, pages 177201–177204, 2008. (Cited on pages 32, 33, 47 and 51.)

[Singh 2007] Rajiv R. P. Singh and David A. Huse. *Ground state of the spin-1/2 kagome-lattice Heisenberg antiferromagnet.* Phys. Rev. B, vol. 76, no. 18, page 180407, Nov 2007. (Cited on page 61.)

[Singh 2008] Rajiv R. P. Singh and David A. Huse. *Triplet and singlet excitations in the valence bond crystal phase of the kagome lattice Heisenberg model.* Phys. Rev. B, vol. 77, no. 14, page 144415, Apr 2008. (Cited on page 61.)

[Singha 2011] A. Singha, M. Gibertini, B. Karmakar, S. Yuan, M. Polini, G. Vignale, M. I. Katsnelson, A. Pinczuk, L. N. Pfeiffer, K. W. West and V. Pellegrini. *Two-Dimensional Mott-Hubbard Electrons in an Artifical Honeycomb Lattice.* Science, vol. 332, pages 1176–1179, Jun 2011. (Cited on pages 71 and 96.)

[Son 2006a] Y.-W. Son, M. L. Cohen and S. G. Louie. *Energy Gaps in Graphene Nanoribbons.* Phys. Rev. Lett., vol. 97, page 216803, 2006. (Cited on page 99.)

[Son 2006b] Y.-W. Son, M. L. Cohen and S. G. Louie. *Half-metallic graphene nanoribbons.* Nature, vol. 444, page 347, 2006. (Cited on pages 99 and 100.)

[Sorella 1989a] S. Sorella, S. Baroni, R. Car and M. Parinello. Europhys. Lett., vol. 8, page 663, 1989. (Cited on page 22.)

[Sorella 1989b] S. Sorella, E. Tosatti, S. Baroni, R. Car and M. Parinello. Int. J. Mod. Phys B, vol. 1, page 993, 1989. (Cited on page 22.)

[Sorella 1992] S. Sorella and E. Tosatti. *Semi-metal-Insulator Transition of the Hubbard Model in the Honeycomb Lattice.* Europhys. Lett., vol. 19, no. 8, pages 699–704, August 1992. (Cited on pages 72, 76, 77, 103, 104 and 109.)

[Stern 2010] Ady Stern. *Non-Abelian states of matter.* Nature, vol. 464, pages 187–193, March 2010. (Cited on page 58.)

[Sun 2009] Gao-Yong Sun and Su-Peng Kou. *Anomalous Spin Dynamics of Hubbard Model on Honeycomb lattice.* arXiv:0911.3002, 2009. (Cited on page 88.)

[Suzuki 1976] M. Suzuki. Comm. Math. Phys., vol. 51, page 183, 1976. (Cited on page 19.)

[Suzuki 2009] Takahumi Suzuki, Yusuke Tomita and Naoki Kawashima. *Magnetic properties of the spin- 12 XXZ model on the Shastry-Sutherland lattice: Effect of long-range interactions.* Phys. Rev. B, vol. 80, no. 18, page 180405, Nov 2009. (Cited on page 52.)

[Suzuki 2010] T. Suzuki, Y. Tomita, N. Kawashima and P. Sengupta. *Finite-temperature phase transition to the $m = 1/2$ plateau phase in the spin-1/2 XXZ model on the Shastry-Sutherland lattices.* Phys. Rev. B, vol. 82, no. 21, page 214404, Dec 2010. (Cited on pages 4 and 52.)

[Swendsen 1987] R. Swendsen and J.-S. Wang. Phys. Rev. Lett., vol. 58, page 86, 1987. (Cited on page 12.)

[Syljuåsen 1997] Olav F. Syljuåsen, Sudip Chakravarty and Martin Greven. *Correlation Lengths in Quantum Spin Ladders.* Phys. Rev. Lett., vol. 78, no. 21, pages 4115–4118, May 1997. (Cited on page 56.)

[Syljuåsen 2002] O. F. Syljuåsen and A. W. Sandvik. *Quantum Monte Carlo with directed loops.* Phys. Rev. E, vol. 66, page 046701, 2002. (Cited on pages 1, 5, 8, 10, 14 and 16.)

[Takigawa 2008] M. Takigawa, S. Matsubara, M. Horvatić, C. Berthier, H. Kageyama and Y. Ueda. *NMR Evidence for the Persistence of a Spin Superlattice Beyond the* 1/8 *Magnetization Plateau in* $SrCu_2(BO_3)_2$. Phys. Rev. Lett., vol. 101, no. 3, page 037202, Jul 2008. (Cited on page 32.)

[Tamura 2006] Masafumi Tamura, Akiko Nakao and Reizo Kato. *Frustration-Induced Valence-Bond Ordering in a New Quantum Triangular Antiferromagnet Based on* $[Pd(dmit)_2]$. J. Phys. Soc. Jpn., vol. 75, page 093701, 2006. (Cited on page 31.)

[Tao 2011] Chenggang Tao, Liying Jiao, Oleg V. Yazyev, Yen-Chia Chen, Juanjuan Feng, Xiaowei Zhang, Rodrigo B. Capaz, James M. Tour, Alex Zettl, Steven G. Louie, Hongjie Dai and Michael F. Crommie. *Spatially Resolving Spin-split Edge States of Chiral Graphene Nanoribbons.* Nature Phys. (in press), 2011. (Cited on pages 101, 103, 104, 105 and 107.)

[Tapaszto 2008] L. Tapaszto, G. Dobrik, R. Lambin and L. P. Biro. *Tailoring the atomic structure of graphene nanoribbons by scanning tunneling microscope lithography.* Nature Nanotechnol., vol. 3, pages 397–401, 2008. (Cited on page 101.)

[Thijssen 2003] J. M. Thijssen. Computational physics. Cambridge University Press, Cambridge, UK, 2003. (Cited on page 14.)

[Tocchio 2009] Luca F. Tocchio, Alberto Parola, Claudius Gros and Federico Becca. *Spin-liquid and magnetic phases in the anisotropic triangular lattice: The case of* κ-$(ET)_2X$. Phys. Rev. B, vol. 80, no. 6, page 064419, 2009. (Cited on page 66.)

[Todo 2001] Synge Todo and Kiyoshi Kato. *Cluster Algorithms for General-S Quantum Spin Systems.* Phys. Rev. Lett., vol. 87, no. 4, page 047203, 2001. (Cited on page 107.)

[Trauzettel 2007] Björn Trauzettel, Denis V. Bulaev, Daniel Loss and Guido Burkard. *Spin qubits in graphene quantum dots.* Nature Physics, vol. 3, pages 192–196, 2007. (Cited on page 99.)

[Trotter 1959] H. F. Trotter. Proc. Am. Math. Soc., vol. 10, page 545, 1959. (Cited on page 19.)

[Troyer 2005] M. Troyer and U.-J. Wiese. *Computational Complexity and Fundamental Limitations to Fermionic Quantum Monte Carlo Simulations.* Phys. Rev. Lett., vol. 94, no. 17, page 170201, 2005. (Cited on page 33.)

[Uchoa 2007] B. Uchoa and A. H Castro Neto. *Superconducting States of Pure and Doped Graphene.* Phys. Rev. Lett., vol. 98, page 146801, 2007. (Cited on pages 3, 71, 72 and 80.)

[Ugeda 2010] M. M. Ugeda, I. Brihuega, F. Guinea and J. M. Gómez-Rodríguez. *Missing atom as a source of Carbon magnetism.* Phys. Rev. Lett., vol. 104, page 096804, 2010. (Cited on pages 107 and 114.)

[Vaezi 2010] Abolhassan Vaezi and Xiao-Gang Wen. *Phase diagram of the Hubbard model on honeycomb lattice.* arXiv:1010.5744, 2010. (Cited on page 97.)

[Vaezi 2011] Abolhassan Vaezi and Xiao-Gang Wen. *Gauge theory of the Hubbard model on honeycomb lattice and its instanton effect.* arXiv:1101.1662, 2011. (Cited on page 97.)

[Wakabayashi 1998] K. Wakabayashi, M. Sigrist and M. Fujita. *Spin wave mode of edge-localized magnetic states in nanographite zigzag ribbons.* J. Phys. Soc. Jpn., vol. 67, pages 2089–2093, 1998. (Cited on pages 99, 101, 103, 106, 112, 113 and 114.)

[Wakabayashi 1999] K. Wakabayashi, M. Fujita, H. Ajiki and M. Sigrist. *Electronic and magnetic properties of nanographite ribbons.* Phys. Rev. B, vol. 59, page 8271, 1999. (Cited on pages 99, 101, 106 and 113.)

[Wang 2010] Fa Wang. *Schwinger boson mean field theories of spin liquid states on a honeycomb lattice: Projective symmetry group analysis and critical field theory.* Phys. Rev. B, vol. 82, no. 2, page 024419, Jul 2010. (Cited on page 97.)

[Wannier 1950] G. H. Wannier. *Antifferomagnetism. The Triangular Ising Net.* Phys. Rev., vol. 79, pages 357–364, 1950. (Cited on page 36.)

[Weinberg 2005] S. Weinberg. The Quantum Theory of Fields, Vol. 1: Foundations. Cambridge University Press, 2005. (Cited on page 70.)

[Wen 1991] X. G. Wen. *Mean-field theory of spin-liquid states with finite energy gap and topological orders.* Phys. Rev. B, vol. 44, no. 6, pages 2664–2672, Aug 1991. (Cited on pages 3 and 92.)

[Wen 2002] Xiao-Gang Wen. *Quantum orders and symmetric spin liquids.* Phys. Rev. B, vol. 65, no. 16, page 165113, Apr 2002. (Cited on page 58.)

[Wessel 2001] Stefan Wessel. *Critical Properties of Quantum Spin Liquids.* PhD thesis, University of Southern California, 2001. (Cited on page 56.)

[Wessel 2005] S. Wessel and M. Troyer. Phys. Rev. Lett., vol. 95, page 127205, 2005. (Cited on page 34.)

[White 1989] S. R. White, D. J. Scalapino, R. L. Sugar, E. Y. Loh, J. E. Gubernatis and R. T. Scalettar. *Numerical study of the two-dimensional Hubbard model.* Phys. Rev. B, vol. 40, no. 1, page 506, 1989. (Cited on pages 20 and 22.)

[White 1994] S. R. White, R. M. Noack and D. J. Scalapino. Phys. Rev. Lett., vol. 73, page 886, 1994. (Cited on page 56.)

[Wolff 1989] Ulli Wolff. *Collective Monte Carlo Updating for Spin Systems.* Phys. Rev. Lett., vol. 62, no. 4, pages 361–364, Jan 1989. (Cited on page 12.)

[Xu 2010] Cenke Xu and Subir Sachdev. *Majorana Liquids: The Complete Fractionalization of the Electron.* Phys. Rev. Lett., vol. 105, no. 5, page 057201, Jul 2010. (Cited on page 97.)

[Xu 2011] Cenke Xu and Leon Balents. *Quantum Phase Transitions around the Staggered Valence Bond Solid.* arXiv:1103.1638, Mar 2011. (Cited on page 97.)

[Yamashita 2008] Satoshi Yamashita, Yasuhiro Nakazawa, Masaharu Oguni, Yugo Oshima, Hiroyuki Nojiri, Yasuhiro Shimizu, Kazuya Miyagawa and Kazushi Kanoda. *Thermodynamic properties of a spin-1/2 spin-liquid state in a κ-type organic salt.* Nat. Phys., vol. 4, no. 6, pages 459–462, 06 2008. (Cited on pages 63 and 68.)

[Yamashita 2009] Minoru Yamashita, Norihito Nakata, Yuichi Kasahara, Takahiko Sasaki, Naoki Yoneyama, Norio Kobayashi, Satoshi Fujimoto, Takasada Shibauchi and Yuji Matsuda. *Thermal-transport measurements in a quantum spin-liquid state of the frustrated triangular magnet κ-(BEDT-TTF)$_2$Cu$_2$(CN)$_3$.* Nat. Phys., vol. 5, page 44, 2009. (Cited on pages 63, 68, 69 and 95.)

[Yamashita 2010] Minoru Yamashita, Norihito Nakata, Yoshinori Senshu, Masaki Nagata, Hiroshi M. Yamamoto, Reizo Kato, Takasada Shibauchi and Yuji Matsuda. *Highly Mobile Gapless Excitations in a Two-Dimensional Candidate Quantum Spin Liquid.* Science, vol. 328, page 1246, 2010. (Cited on pages 63, 68 and 69.)

[Yan 2011] Simeng Yan, D. A. Huse and S. R. White. *Spin-Liquid Ground State of the S=1/2 Kagome Heisenberg Antiferromagnet.* Science, vol. 332, pages 1173–1176, 2011. (Cited on pages 61, 62, 63 and 71.)

[Yang 2010] Hong-Yu Yang, Andreas M. Läuchli, Frédéric Mila and Kai Phillip Schmidt. *Effective Spin Model for the Spin-Liquid Phase of the Hubbard Model on the Triangular Lattice.* Phys. Rev. Lett., vol. 105, no. 26, page 267204, Dec 2010. (Cited on pages 59, 71 and 95.)

[Yazyev 2008] O. V. Yazyev and M. I. Katsnelson. *Magnetic correlations at Graphene edges: Basis for novel spintronics devices.* Phy. Rev. Lett., vol. 100, page 047209, 2008. (Cited on page 99.)

[Yazyev 2010] Oleg V. Yazyev. *Emergence of magnetism in graphene materials and nanostructures.* Rep. Prog. Phys., vol. 73, no. 5, page 056501, 2010. (Cited on pages 99, 101, 106 and 113.)

[Yazyev 2011] O. V. Yazyev, R. B. Capaz and S. G. Louie. *Theory of Magnetic Edge states in Chiral Graphene Nanoribbons.* arXiv:1102.4886, 2011. (Cited on page 114.)

[Yoshioka 2003] H. Yoshioka. *Spin excitation in nano-graphite ribbons with zigzag edges.* J. Phys. Soc. Jpn., vol. 72, pages 2145–2148, 2003. (Cited on pages 101, 107 and 113.)

[Yoshioka 2009] Takuya Yoshioka, Akihisa Koga and Norio Kawakami. *Quantum Phase Transitions in the Hubbard Model on a Triangular Lattice.* Phys. Rev. Lett., vol. 103, no. 3, page 036401, Jul 2009. (Cited on pages 59 and 66.)

[You 2008] Jhih-Shih You, Wen-Min Huang and Hsiu-Hau Lin. *Relativistic ferromagnetic magnon at the zigzag edge of graphene.* Phys. Rev. B, vol. 78, no. 16, page 161404, Oct 2008. (Cited on page 112.)

[Zhang 2009] Haijun Zhang, Chao-Xing Liu, Xiao-Liang Qi, Xi Dai, Zhong Fang and Shou-Cheng Zhang. *Topological insulators in Bi_2Se_3, Bi_2Te_3 and Sb_2Te_3 with a single Dirac cone on the surface.* Nat. Phys., vol. 97, page 438, 2009. (Cited on page 70.)

[Zhitomirsky 2002] M. E. Zhitomirsky. *Field-Induced Transitions in a Kagome Antiferromagnet.* Phys. Rev. Lett., vol. 88, no. 5, page 572041, 2002. (Cited on page 51.)

[Zhou 2008] Yi Zhou, Patrick A. Lee, Tai-Kai Ng and Fu-Chun Zhang. *$Na_4Ir_3O_8$ as a 3D Spin Liquid with Fermionic Spinons.* Phys. Rev. Lett., vol. 101, no. 19, page 197201, Nov 2008. (Cited on page 64.)

Curriculum Vitae

Zi Yang Meng
born in Xi'an, Shaanxi, June 23th 1982
China

Education

[02/2008 – 06/2011] Doctoral-study of theoretical condensed matter physics at the Institut für Theoretische Physik III, Universität Stuttgart; advisor Prof. Stefan Wessel.

[10/2005 – 11/2007] Master of Science in Physics, Universität Stuttgart;
Master Thesis: *Quantum Monte Carlo Studies of the Anisotropic Shastry-Sutherland Quantum Antiferromagnet*
advisor Priv.-Doz. Dr. Stefan Wessel, Ph. D.

[06/2004 – 06/2005] Bachelor Thesis at the Group of Theoretical Computation in Condensed Matter Physics, Department of Physics, University of Science and Technology of China;
Bachelor Thesis: *Diffusion of the Dangling Bonds in Hydrogenated Amorphous Silicon: an ab-initio Study*
advisor Prof. Bicai Pan.

[09/2000 – 07/2005] Bachelor of Science in Physics, University of Science and Technology of China

[07/2000] College Entrance Exam in China, major in mathematics, physics and chemistry

[09/1994 – 07/2000] Xi'an, Xi Guang School (middle and high school).

Stuttgart, 4. June 2011
Zi Yang Meng

List of publications

The listed publications have been printed in peer-reviewed journals and proceedings:

[1] H. Feldner, Z. Y. Meng, T. C. Lang, A. Honecker, S. Wessel and F. F. Assaad Dynamical Signatures of Edge-State Magnetism on Graphene Nanoribbons. *Phys. Rev. Lett.* **106**, 226401 (2011).

[2] Z. Y. Meng, T. C. Lang, S. Wessel, F. F. Assaad and A. Muramatsu Quantum spin liquid emerging in two-dimensional correlated Dirac fermions. *Nature* **464**, 847 (2010).

[3] H. Feldner, Z. Y. Meng, A. Honecker, D. Cabra, S. Wessel and F. F. Assaad Magnetism of finite graphene samples: Mean-field theory compared with exact diagonalization and quantum Monnte Carlo simulations. *Phys. Rev. B*, **81**, 115416 (2010).

[4] Z. Y. Meng, T. C. Lang, S. Wessel, F. F. Assaad and A. Muramastsu Spin-Liquid phase in the Hubbard model on the honeycomb lattice. *HPC in Science and Engineering'10* Stuttgart (HLRS), 5 (2010).

[5] Z. Y. Meng and S. Wessel Phases and magnetization process of an anisotropic Shastry-Sutherland model. *Phys. Rev. B* **78**, 224416 (2008).

This paper is in preparation:

[1] T. C. Lang, Z. Y. Meng, S. Wessel, F. F. Assaad and A. Muramatsu. Phase diagram of the SU(N) Hubbard-Heisenberg model on the honeycomb lattice: a QMC study. To be submitted to *Phys. Rev. Lett.*.